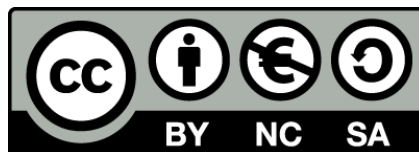




UNIVERSITAT<sub>DE</sub>  
BARCELONA

## Functional organization and network resilience in self-organizing clustered neuronal cultures

Sara Teller Amado



Aquesta tesi doctoral està subjecta a la llicència **Reconeixement- NoComercial – Compartir Igual 4.0. Espanya de Creative Commons.**

Esta tesis doctoral está sujeta a la licencia **Reconocimiento - NoComercial – Compartir Igual 4.0. España de Creative Commons.**

This doctoral thesis is licensed under the **Creative Commons Attribution-NonCommercial-ShareAlike 4.0. Spain License.**

# **Functional organization and network resilience in self-organizing clustered neuronal cultures**



UNIVERSITAT DE  
BARCELONA

**Sara Teller Amado**

Departament d'Estructura i Constituents de la Matèria  
Universitat de Barcelona

PhD Advisor

**Jordi Soriano Fradera**

PhD Tutor

**Jaume Casademunt Viader**

*Tesis presentada dins del Programa de Doctorat en Física*

Facultat de Física

November 2015



A mis padres,



*“ The brain struggling to understand the brain is society trying to explain  
itself.”*

Colin Blakemore



## **Acknowledgements**

Por fin ha llegado el momento que más deseaba, estar escribiendo estas palabras, lo que significa que esta tesis ya está casi finalizada y que dentro de nada empezaré a ver la luz después de meses intensos de esfuerzo. Pese a este sobreesfuerzo que ahora mismo me tiene en condiciones mínimas, me gustaría decir que me siento realizada más que nunca, no sólo por tener ya la tesis escrita, sino por todo lo aprendido en cada paso que he dado. Recuerdo cuando empecé que tuve que lidiar con el problema de tomar mis propias decisiones y tener mi propia inventiva. Ahora odio el ‘haz esto así porque sí’. Más tarde, tuve que combatir con la frustración de acabar los días viendo como las neuronas una y otra vez morían, viendo como diseños experimentales que parecían ideales luego no servían. Y sí, creo que ahí, desarrollé una paciencia extraordinaria que ha sido clave para el resto de la tesis (y para la vida en sí). Después vino la parte más estimulante de la tesis, poder tratar con los datos experimentales y sacarles todo ‘el jugo’ posible. Aunque encontrar las herramientas matemáticas ideales o crear los programas para estudiar estos datos de forma adecuada ha requerido un gran esfuerzo, a la vez ha sido un gran aprendizaje. Luego, luchar con los miedos e inseguridades de si realmente se está haciendo todo correctamente o si se podría hacer mejor. Aunque todo esto vale la pena, cuando ves que al final las cosas salen, que tu nombre, que tu trabajo se ve por fin publicado en una revista, y sientes máximo orgullo de poder aportado tu granito de arena en el mundo de la ciencia en general, pero sobretudo en el campo de la neurociencia en particular. Así que pese a este sobreesfuerzo final en esta última etapa, no

cambiaría por nada el haber realizado ESTA tesis. Y digo ésta, porque me siento afortunada del tema en concreto del estudio realizado. Mis clústeres de neuronas han ido trabajo tras trabajo desvelando interesantes propiedades que me han ido cautivando más y más, y que hacen que hoy en día me fascinen.

Igualment tot aquest estudi no el podria haver aconseguit sense la teva gran ajuda, Jordi. Gràcies per la teva gran paciència amb mi, per sempre rebrem amb un somriure a la cara, per ajudar-me en tot el que has pogut, però sobretot gràcies per la teva gran motivació, perquè gràcies a això m'has ensenyat que un pot passar-s'ho bé treballant, que tot pot ser molt 'guai' (encara que és una pena no poder escriure 'guai' en un paper, no?).

I gràcies en Jaume, gràcies pel vot de confiança que vas fer amb mi. Gràcies en general pel teu suport, i en especial, pels teus ànims amb la meva eterna batalla entre l'anglès i jo.

També volia agrair a tota la gent amb la que he col·laborat i que han fet aquesta tesis sigui possible. En especial, en Àlex Arenas, gràcies per ensenyar-me la teva enriquidora forma de fer ciència, i per donar-me les eines per començar a 'volar' jo sola. Gràcies també en Sergi, per resoldre sempre tots els meus dubtes. I gràcies a la Clara, per fer que les discussions de resultats pugui ser una part estimulants i divertida.

Gràcies Mònica per tota la teva ajuda, thanks Bogachan for rich discussions and effort. Gràcies en Jordi Andilla, gràcies per ser tan proper i alhora ensenyar-me tant. Gracias también a Pablo Loza, por contar con nosotros para desarrollar este bonito proyecto experimental.

Gracias también en particular, a Marta Nieto y a Juan Segovia por la gran paciencia al enseñarme métodos experimentales. Y por último, también me gustaría agradecerle a Gorka Zamora todas las provechosas discusiones que he tenido a su lado.

També m'agradaria agrair al grup de Física No Líneal i Consolidar. Gràcies a ells he après a presentar la meva recerca i saber discutir-la. També volia

agraïr als que formen el departament d'ECM i els d'astro. En especial aquells, que tants cop m'heu parat pel passadís per preguntar-me: com ho portes? i després sentir: 'Tranquila, ja queda poc'.

També volia agrair als meus companys de despatx (sí, encara que sé que casi no he estat). En especial, volia agrair a en Xavier Orlandi, per sempre resoldrem tots els dubtes quan ho he necessitat. Gràcies per la teva gran paciència i entrega.

Gràcies també a tu Eli. Gràcies per donar-li vida al laboratori. Gràcies per sempre preocupar-te de que no faltés de res, però sobretot gràcies per poc a poc anar-te obrint a mi i deixar-me compartir al teu costat. Gràcies Lluís també. Encara que hagi entrat 'nou' relativament i que la meitat del temps m'has vist estresada cap amunt i cap avall, m'emporto les grans converses filosòfiques que en petits breaks hem tingut i que m'han donat a pensar per dies.

Gracias a las del baile, por siempre tenerme una sonrisa preparada cuando entro por la puerta, y por preocuparos tanto por mi en estos últimos meses. Y en especial gracias al baile en sí, por haber hecho que al salir por esa puerta me sienta reconfortada y llena de energía para seguir trabajando.

Gracias también a Mariana, por sus horas de inglés hablando de mi tesis y por su constante apoyo.

Gràcies també els amics de la carrera, en especial, a tú bixeta pels teus ànims i per la teva gran bondat. Gracias a toda la gente del master. Però sobretot gràcies a vosaltres, els que encara hi sou en el meu dia a dia. Gràcies per estar a l'hora de dinar, a l'hora de berenar (sí, encara que la majoria de vegades no baixés). Gràcies perquè heu fet que en aquests cinc anys anar a treballar sigui també estar amb els meus AMICS. Gracias Juan, por tus grandes historias, gracias Camilo por tu chispa, gracias Piu por tu sentido crítico, gracias Pacheco, por tu gran fortaleza y a la vez gran corazón, gracias Mario por tu espíritu inquieto y emprendedor, gràcies Maria per preocupar-te per mi sempre tant. Gràcies Palau per les teves 'breus' però gran aportacions,

per mai perdre el bon humor que et caracteriza i sobretot per estar quan t'he necessitat. Y gracias a tí, en especial, David Frigola, gracias por estos más de 10 años a mi lado, gracias por tu ayuda incondicional, por tus miradas de comprensión, y por tus 'abrazos' para darme ánimos en los momentos clave. Sabes que una parte de esta tesis es gracias a ti.

Y gracias a mis pulis, a los míos. Sin su especial apoyo ahora no estaría escribiendo estas líneas. Gracias Lorena por estar siempre ahí, y por transmitirme paz cuando lo he necesitado. Gràcies Emma pel teu positivisme. Gracias Rakel por tus constantes ánimos y reflexiones. Gràcies Ione per la teva fidelitat i recolçament. Gracias Fresi por enseñarme que nunca es tarde para luchar por lo que quieres. Gràcies Hel·lena per ensenyar-me altres formes de veure la vida. Gracias Ana por tu fuerza y apoyo. Pero sobretodo gracias a tí, Franc. Gracias por ser más que un amigo, por valorarme y confiar en mí más que yo en mi misma.

Gracias a vosotros familia. Gracias Silvia por crecer (en todos los sentidos) a mi lado. Gracias a mis padres, primero, por ser siempre exigentes conmigo, gracias por que ha hecho que ahora esté donde esté. Después en especial, gracias papá por tenerme tanto respeto y siempre confiar en mí. Y sobre todo gracias a ti, mamá. Gracias por tu incondicional apoyo, sé que siempre puedo contar contigo.

I ja per últim, et volia agrair a tu, Ferran, per tantes coses que podria fer una altra tesis (i no és el què vols, no?). Però reduiré dien-te que gràcies en especial pel teu amor, gràcies perquè ha estat el motor del meu dia a dia en aquests anys de tesis i sobretot en aquests últims dies durs. En fí, gràcies per sempre ser-hi. Sense tú en especial, no hauria aconseguit arribar fins aquí.

# Table of contents

<b>1</b>	<b>Introduction</b>	<b>1</b>
1.1	Introduction . . . . .	1
1.1.1	From single neurons to neuronal circuits . . . . .	1
1.1.2	Neuronal circuits and complex networks . . . . .	3
1.1.3	The brain as a complex network . . . . .	6
1.1.4	Graph theory and brain networks . . . . .	9
1.1.5	Network resilience and brain disorders . . . . .	10
1.1.6	The need of <i>in vitro</i> approaches: neuronal cultures . . . . .	13
1.1.7	Homogeneous cultures . . . . .	16
1.1.8	Patterned cultures . . . . .	18
1.1.9	Clustered cultures: appealing complex organization in a dish . . . . .	20
<b>2</b>	<b>Experimental Setup and Procedure</b>	<b>27</b>
2.1	Culture preparation . . . . .	27
2.1.1	Clustered cultures . . . . .	28
2.2	Glass-PDMS structure preparation . . . . .	32
2.3	Experimental setup . . . . .	35
2.3.1	Calcium imaging . . . . .	36
2.3.2	Calcium Imaging versus MEAs . . . . .	37
2.4	Experimental procedure . . . . .	40
2.4.1	Experiments at Jordi Soriano's Lab . . . . .	42

2.5	Pharmacology . . . . .	45
2.5.1	Blocking Inhibitory connections . . . . .	45
2.5.2	Blocking Excitatory connections . . . . .	46
2.5.3	Chemical preparation for $A\beta$ and $M-A\beta$ . . . . .	47
2.6	Experiments at ICFO's Lab . . . . .	48
<b>3</b>	<b>Analysis tools and Methods</b>	<b>57</b>
3.1	Data analysis in neuronal cultures . . . . .	58
3.1.1	From fluorescence signal to data . . . . .	58
3.1.2	Ignition firing times . . . . .	60
3.1.3	Reliability in detecting the clusters' ignition times . . . . .	62
3.2	Firing sequences . . . . .	65
3.2.1	Firing sequences' identification . . . . .	66
3.3	Community detection . . . . .	67
3.3.1	Applying hierarchical clustering to find the dynamical modules . . . . .	70
3.3.2	Optimum threshold for community detection . . . . .	72
3.4	Complex Networks . . . . .	75
3.4.1	Basic concepts . . . . .	75
3.4.2	Our effective connectivity inference method . . . . .	77
3.4.3	Effective connectivity . . . . .	78
3.4.4	Comparison with alternative effective network constructions . . . . .	81
3.4.5	Network properties . . . . .	86
3.4.6	Hubs and Rich Club . . . . .	91
<b>4</b>	<b>RESULTS I : Modular Organization and Effective Connectivity</b>	<b>97</b>
4.1	Firing sequences . . . . .	98
4.1.1	Validity of firing sequences . . . . .	102
4.2	Functional organization . . . . .	103
4.2.1	Functional organization sensitivity . . . . .	106

4.3	Effective connectivity characterization . . . . .	111
4.3.1	Analysis of the effective networks . . . . .	112
4.3.2	Assortativity . . . . .	119
4.3.3	Rich-Club properties . . . . .	123
4.3.4	Hubs . . . . .	126
4.3.5	Robustness of our effective connectivity inference method . . . . .	129
4.3.6	Topological and dynamical modules . . . . .	137
4.3.7	Top links mapping and small world properties . . . .	137
4.3.8	Identification of the clusters that initiate spontaneous activity . . . . .	142
4.4	Discussion of the Results . . . . .	146
<b>5</b>	<b>Results II: Network resilience</b>	<b>151</b>
5.1	Global network damage . . . . .	152
5.2	Local physical damage . . . . .	161
5.2.1	Random cluster deletion . . . . .	162
5.2.2	'Hub' deletion . . . . .	168
5.2.3	Initiators damage . . . . .	172
5.3	Discussion . . . . .	177
5.3.1	Assortativity, resilience, and network circuitry . . .	177
5.3.2	On recovery mechanisms upon CNQX degradation .	179
5.3.3	The importance of the hubs in our experiments . . .	180
5.3.4	Network performance upon random and targeted damage . . . . .	181
5.3.5	Network damage and the brain . . . . .	182
5.3.6	Network response upon attack and resilience . . . .	184
5.3.7	Potential descriptor of network damage . . . . .	185
<b>6</b>	<b>Results III: Clustered networks as an <i>in vitro</i> model for Alzheimer</b>	<b>187</b>
6.1	Biochemical context . . . . .	188

6.2	Experimental system . . . . .	189
6.3	Experimental Results . . . . .	191
6.3.1	Spontaneous activity upon M-A $\beta$ action . . . . .	191
6.3.2	Disruption of the structure of network communities due to M-A $\beta$ complex . . . . .	196
6.3.3	Loss of integration-segregation balance upon M-A $\beta$ damage . . . . .	203
6.3.4	Clustered networks exhibit higher resistance to M- A $\beta$ damage compared to homogeneous ones. . . . .	206
6.4	Discussion . . . . .	208
<b>7</b>	<b>Work in progress</b>	<b>211</b>
7.1	Anatomical and functional connectivities . . . . .	211
7.2	Mapping structural connectivity in clustered networks . . . . .	212
7.3	Functional vs. cluster-to-cluster structural connectivity . . . . .	218
7.4	Towards engineering clustered neuronal networks . . . . .	224
<b>8</b>	<b>Conclusions</b>	<b>229</b>
<b>9</b>	<b>Resumen en castellano</b>	<b>237</b>
9.1	Introducción . . . . .	237
9.2	Métodos experimentales . . . . .	239
9.3	Métodos teóricos . . . . .	241
9.4	Resultados y conclusiones . . . . .	242
	<b>References</b>	<b>245</b>

# Chapter 1

## Introduction

### 1.1 Introduction

#### 1.1.1 From single neurons to neuronal circuits

Neuronal networks are an example of an important paradigm shift in neuroscience. Single neurons, considered since Ramón y Cajal the structural and functional units of the nervous system, are now viewed as the constituents of a much more fundamental building block: the *neuronal circuits*. They shape in great measure the functionality of the brain, from simple motor tasks to complex abstract thinking (Yuste, 2015).

An individual neuron responds to particular stimulus in a on-off manner that pictures its dynamical non-linearity and complexity. However, this inherent behavior does not confer a neuron a predominant role in a neuronal circuit. Indeed, the single-neuron conceptual framework started to lose popularity by 1930, when multi-neuron imaging technologies were brought to light and brain spontaneous activity started to be measured (Fox and Raichle, 2007). This emergent activity is characterized by the coherent activation of large neuronal assemblies in the absence of stimuli, and cannot be explained from a single-neuron perspective. More importantly, individual neurons never

seem to respond identically to the same stimulus (Gross and Kowalski, 1999), and the activation of a single neuron often leads to the activation of an entire population (Feldt et al., 2011). Thus, one of the big assertions of modern neuroscience is that information is distributed in cell assemblies rather than encoded by single cells, although the nature of coding or the information processing in these neuronal circuits remains unclear.

Cortical columns are considered the minimum functional element in the brain (DeFelipe et al., 2012; Mountcastle, 1997). These cortical columns are characterized by a dense, highly organized population of neurons that are vertically arranged across the horizontal discrete layers in the cortex. The connectivity pattern features groups of neurons more densely connected among them than to neurons constituting cortical columns, altogether shaping a connectivity profile in the form of *modules*.

The topological organization of the connections among neuronal populations is one of the key ingredients for information processing. The architecture of the underlying neuronal circuitry can indeed substantially constrain the resulting dynamics (Sporns et al., 2000, 2004). Additionally, the connectivity of the circuit can be tuned by neuronal dynamics in a *plastic* manner. The strength of the connections can be reinforced or weakened, as well as the number and location of synapses. Thus, a neuronal circuit can be seen as a hard-wired but tunable system where dynamics may continuously modify the synaptic coupling strengths, shaping activity patterns that may in turn reshape the physical connections. In this sense, the relationship between connectivity and functionality is not straightforward since the dynamic elements that are the neurons, coupled through the network, may in principle give rise to very diverse activity patterns with few modifications in circuitry wiring and neuronal dynamics.

In this line, the studies presented in this thesis are framed along this neuronal circuit level. Our scenario is simplified: living neuronal networks in the form of *neuronal cultures* that shape a topological connectivity that

resemblances cortico–cortical connectivity structures. Neuronal cultures offer a suitable platform to study in a more precise —and accessible— manner the dynamics, connectivity, and information processing capabilities among neuronal populations; and to shed light on the intricate interplay between anatomical connectivity and the repertoire of activity patterns that emerge in the system.

### 1.1.2 Neuronal circuits and complex networks

A characteristic feature of a Complex System is the emergence of a rich collective behavior in an ensemble of coupled dynamical elements. In other words, the resulting system exhibits much richer features than the sum of its parts, being the interactions between the elements the hallmark of the arising collective behavior.

Uncovering the complexity of a neuronal circuit, and ultimately the human brain, is obviously a challenging task that has gathered extraordinary support along the last 50 years from modern *network science* (Stam, 2014). This branch of knowledge has become a powerful tool in describing complex systems in fields as diverse as social, technological, and biological sciences, and using a combination of theoretical tools that include graph theory, non-linear dynamics, noise theory and concepts from statistical physics.

The main scheme of graph theory —also known as complex network theory— (Alon, 2007; Barrat et al., 2008; Dorogovtsev and Mendes, 2003; Estrada, 2011a; Newman, 2010) is the representation of the elements of a system as *nodes* of a network, and their interactions as *links* or connections between elements. The number of links connected to a node is termed *degree*. The *degree distribution*,  $p(k)$ , is the probability to find a node with degree  $k$  randomly chosen. Many complex networks usually present non-Gaussian  $p(k)$ , exhibiting a long tail towards high degrees. The most typical degree distribution exhibited by many complex networks is the ‘scale-free’ distribution and that follows a power law scaling  $p(k) \sim k^{-\gamma}$ . This scaling leads to a high

number of low-degree nodes together with a small number of high-degree ones. The latter are often termed *hubs*, and ensure a high level of global connectivity (Barabási and Albert, 1999; Barabási and Bonabeau, 2003; Grigorov, 2005). Another organization principle that is often shared in different complex systems is the presence of *small-world* attributes. A small-world network shows high clustering among nodes (similar to a regular or a lattice network), combined with short average node-to-node distances as occurs in a random network (Watts and Strogatz, 1998). Moreover, real networks can also be modular, i.e. shaped by highly interconnected nodes that form definite entities known as *modules* or *communities*, and whose interconnectivity is mediated by a few inter-moduli links that govern their integration (Blondel et al., 2008; Newman, 2006). Networks in which modularity dominates are often called *segregated*, and networks in which the whole system is strongly assembled are called *integrated*. This integration-segregation balance has become an important breakthrough for the characterization of neuronal networks and the quantification of their efficiency and robustness.

In the context of neuroscience, this rich mathematical framework has proven to be exquisitely useful for studying the development and evolution of neuronal circuits (Feldt et al., 2011), comprehending network robustness and vulnerability (Achard et al., 2006; Srinivas et al., 2007), as well as understanding the interplay between connectivity and dynamics (Bullmore and Sporns, 2009). For instance, synchronization between neuronal assemblies in the developing hippocampus has been ascribed to the existence of super-connected nodes in a scale-free topology (Bonifazi et al., 2009); efficient information transfer has been associated to circuits with ‘small-world’ features (Latora and Marchiori, 2001), such as in the nematode worm *C. elegans* (Watts and Strogatz, 1998) or the brain cortex (Harriger et al., 2012; Sporns and Zwi, 2004); and the coexistence of both segregated and integrated activity in the brain has been hypothesized to arise from a modular circuit architecture (Hagmann et al., 2008; Meunier et al., 2010).

The analysis of neuronal circuits in terms of network science can take two visions: *structural*, where the nodes are actual neurons (or ensembles of them) and connections are actual anatomical paths; or *functional*, where the nodes are dynamic elements, and connections are statistical relations between them. These two levels of representation can lead to very different networks. Their relationship, though intimate and complementary to one another, is challenging to assess and a vast field of research.

Structural neuronal networks, on the one hand, has been described at different scales. At the microscopic scale, nodes correspond to single neurons, and the anatomical connections to neurites. At the other extreme, at the macroscopic scale, nodes are associated with brain regions and the connections with white matter, the most prominent connectivity highways. The microscale description can be highly complex due to the extensive biological and molecular details, and thus may fail at providing a clear picture of emergent collective phenomena. Conversely, the macroscale studies provide many fundamental insights into large-scale organization, but may result insufficient for a complete understanding of the human brain's functional dynamics and information processing capabilities. The necessary scale that fills the gap between both descriptions is the *mesoscale*, where nodes correspond to neuronal populations, and the links to fibers of axons. In addition, the first signs of emergent functional features occur at this intermediate scale, making the exploration of such systems of extreme importance.

Functional neuronal networks, on the other hand, are based on dynamical observations, as illustrated in Figure 1.1. To be more precise, one can consider *functional* connections when referring to the statistical dependence between neuronal activities without assuming the mechanisms of the mutual relationship; and *effective* connections, when the direct influence that a node exerts on another—or *causal relationship* between the pair-wise activity—is taken into account. The functional or effective connectivity maps can be seen as a good *proxy* of neuronal dynamics. These functional or effective maps

are inferred from neuronal activity data provided by imaging techniques such as functional magnetic resonance imaging (fMRI) or electro-physiological techniques such as electroencephalography (EEG) or magnetoencephalography (MEG). At lower scales, the neuronal firing of single neurons or the events associated to populations of neurons are measured typically through fluorescence calcium imaging (Figure 1.2A-B) or through micro-electrode arrays (MEAs, Figure 1.2D). However, a wide spectrum of techniques have been developed with their advantages and limitations, as summarized in Table 1.1. In particular, calcium imaging techniques have incredibly improved in the last decade thanks to new imaging technologies such as two-photon imaging (Svoboda and Yasuda, 2006) and laser-scanning light-sheet microscopy (Keller et al., 2008). These technologies, combined with new better fluorescence probes and genetic calcium indicators (Tian et al., 2009), have provided incredible advances, for instance the visualization of *in vivo* activity of the zebrafish at single-cell resolution (Ahrens et al., 2013).

### 1.1.3 The brain as a complex network

Mapping the wiring architecture of the brain, as well as comprehending the complex mechanisms that executes, has been one of the most fundamental goals in modern neuroscience (Behrens and Sporns, 2012; Toga et al., 2012). And not only to understand how the brain works but also, ultimately, ourselves (Seung, 2012). These efforts have increased in the last decade with the establishment of two grand initiatives that aim at either simulating or disentangling the whole human connectome at the microscale. The first project to appear was the European ‘Blue Brain Project’ in 2002, which was able to describe the complete connectivity map of a cortical column (Markram, 2006), and that was later extended in 2013 to shape the ‘Human Brain Project’ (Abbott, 2013; Markram, 2012). In parallel, the US administration launched the ‘BRAIN Initiative’ (Insel et al., 2013) to develop new imaging and compu-

FLUORESCENCE IMAGING	Description	Advantages	Limitations
<b>Chemical Calcium Indicators (CCI)</b>	Synthetic dyes. Emitted light upon binding to the free calcium ions inside the cell.	High SNR. Easy and rapid incubation. Spatial resolution (~ $\mu\text{m}$ ). Different types for different preparations. Economical.	Millisecond temporal resolution. Photobleaching. Phototoxicity. Autofluorescence. Short time recordings. Non-cell-class specific. Poor sensitivity?
<b>Genetically Encoded Calcium Indicators (GECI)</b>	Engineered dyes. Emitted light upon calcium influx through molecular conformational changes (e.g. FRET-based)	Non-toxic. Photostability. Long term recordings. Spatial resolution (~ $\mu\text{m}$ ). Cell-class specific. High sensitivity.	Lower SNR compared to CCI. Complicated marker delivery in dye-loading. Most of markers show slow kinetics.
<b>Genetically Encoded Voltage Indicators (GEVI)</b>	Engineered dyes. Emitted light upon voltage membrane changes through molecular conformational changes.	Submillisecond resolution. Non-toxic. Photostability. Long term recordings. Spatial resolution (~ $\mu\text{m}$ ). High sensitivity.	Lower SNR compared to GECI. Mixed signal (LFP). Complicated marker delivery. Non-cell-class specific.
<b>Voltage-sensitive-dyes (VSDs)</b>	Synthetic dyes. Emitted light upon voltage membrane changes through conformational changes.	Microsecond resolution. Spatial resolution (~ $\mu\text{m}$ ).	Lower SNR compared to GECI. Mixed signal. Non-cell-class specific. Photodynamic damage.
TYPICAL ELECTRODES	Description	Advantages	Limitations
<b>Standard Multielectrode Arrays (MEAs)</b>	Device with 64 microelectrodes. Extracellular field potential recordings (LFP).	Submillisecond resolution. Non-invasive. Long term recordings.	Lower SNR compared to CCI. Spatial resolution (~10 cells). Non-cell-class specific. Mixed signal.
<b>High Density MEAs</b>	Device with 512 microelectrodes. Extracellular recordings (LFP)	Time resolution (~ $\mu\text{s}$ ). Non-invasive. Long term recordings.	Lower SNR compared to CCI. Spatial resolution (~100 cells). Non-cell-class specific. Mixed signal.
<b>Multi transistor arrays Based on CMOS</b>	Device with 11,011 microelectrodes. Extracellular recordings (LFP)	Time resolution (~ $\mu\text{s}$ ). Non-invasive. Long term recordings. Better SNR. Better spatial resolution (~1000 cells).	Complicated engineering. Non-cell-class specific. Mixed signal. Expensive.
<b>Patch Clamp</b>	Intracellular recording system.	High temporal resolution. Good cell coupling.	Invasive. Short time recordings. Single-cell.

**Table 1.1 Neuronal activity detection techniques in neuronal circuits.** The list summarizes major achievements in the recording of neuronal activity at the micro and mesoscales. Fluorescence imaging and electrodes technology are reviewed, and their respective advantages and limitations highlighted.

tational resources to image the whole brain *in vivo*, explore its handling of information, and characterize both health and diseased circuits.

These two grand projects are being essential to unify the way in which neuroscience data is recorded and shared, from the molecular level (starting by the gene expression of molecular channels) up to whole-brain activity. Both projects are becoming a central reference for a broad range of specialized databases, interdisciplinary collaborations, improvement of mechanistic models, and interpretation of human functional brain data.

The human brain circuitry, however, contains around  $10^{11}$  neurons and  $10^{14}$  synapses (Herculano-Houzel, 2009; Pakkenberg et al., 2003). Storing such an amount of data is comparable to storing all the worldwide written information until today (Lichtman et al., 2014). Furthermore, the complexity of the human brain not only resides in the high number of neurons and connections, but also in the high spectrum of dynamical processes that can sustain at different temporal and spatial scales (Buzsáki and Draguhn, 2004; Honey et al., 2007b). Thus, the feasibility of these ambitious quests is creating a growing debate.

Despite the high efforts and resources being poured on these enterprises, the necessity to tackle the brain using different approaches is evident. In that sense, two different approaches have emerged, the *top-down* approach that explores the brain at the large-scale, and the *bottom-up* approach that investigates the brain at the micro and mesoscale. The latter uses simple model systems with small size and relative architectural simplicity, but providing a rich behavioral repertoire (Macosko et al., 2009; Sumbre et al., 2008). By combining microscale description with accessible neuronal circuits, mesoscale models provide a better knowledge on the emergence of general neuronal mechanisms that are often disregarded when one dives into biological details.

### 1.1.4 Graph theory and brain networks

Macroscale studies in the brain have revealed many important characteristics in structural as well as functional networks. First graph theoretical analysis were applied to examine the anatomical connection patterns between brain areas in the cat cerebral cortex and monkey (Hilgetag et al., 2000; Scannell et al., 1995; Young, 1993). Later, they started to analyze structural (Gong et al., 2009; He et al., 2007) as well as functional human brain data (Achard et al., 2006). In particular, the topological organization in functional human brain networks is inferred from data measured in healthy human volunteers ‘at rest’, i.e. not performing any particular task, shaping what is known as the *resting state* functional network (Deco et al., 2011; Wang et al., 2009).

Modern network science has pinpointed that this ‘normal brain’ network’s organization is characterized by ‘small–world’ features that shape a cost–efficient configuration that combines strong local connectivity (high clustering) and efficient long distance connections (short path length) (Achard et al., 2006; Bassett and Bullmore, 2009; Sporns, 2011). Moreover, the distribution of the connections (degree distribution) among brain regions seems to follow a near scale free topology, that gives rise to the presence of hubs, i.e. nodes that cope with much of the information flow (Bullmore and Sporns, 2012; Sporns, 2013; van den Heuvel and Sporns, 2013). It has also been seen that these hubs are highly interconnected, shaping a connectivity backbone in the network known as ‘rich club’ core (Sporns, 2013; van den Heuvel and Sporns, 2011; van den Heuvel et al., 2013). It is important to note that hubs in general, and the rich club in particular, handle most of the information traffic in brain networks. Additionally, it has been observed that normal brains present a hierarchical modular dynamics, where each module seems to be associated to specific functions such as motor action or sensory processing (He et al., 2009; Meunier et al., 2010). The interplay between these segregated modules and their integration is believed to result in a correct processing,

synchronization and information flow across the brain, ultimately leading to normal task-related functions and cognition (Sporns, 2013; Stam, 2014).

Another common feature that appears in structural and functional brain networks is a positive ‘assortativity’ (Eguíluz et al., 2005; Hagmann et al., 2008). This network measure evaluates the tendency of nodes with high number of connections (degree) to be connected between them. Thus, positive assortativity reveals the high likelihood of the appearance of a rich club, and in turn a higher robustness to attack (i.e. removal of nodes) as compared to disassortative networks (Newman, 2002, 2003). Hence, the presence of assortative connectivity and rich club traits in the brain networks is highly relevant since it may facilitate redundancy in information processing that ultimately reinforces and stabilizes the network (Fornito et al., 2015; Rubinov and Sporns, 2010a).

Several of these organizational aspects of brain networks have been observed at different human brain scales, different species, and in a wide range of other complex systems. Indeed, as we will see along this thesis, the *clustered neuronal networks* that we investigated share a large number of similarities with functional brain networks, particularly the presence of assortativity and rich club features. These similarities grant the clustered networks as an appealing experimental system not only to deepen in the understanding of brain network organization but also to study network resilience to perturbations and damage.

### **1.1.5 Network resilience and brain disorders**

The continuous improvement in the characterization of healthy brain networks has motivated the study of neurological and psychiatric pathologies from this complex network perspective (Crossley et al., 2014; Fornito et al., 2015; Stam et al., 2007; Stam, 2014; van den Heuvel et al., 2013). The main goal is to understand network changes from healthy brains to diseased ones, and

to create opportunities to develop new diagnostic and therapeutic strategies using network descriptors as markers.

Network resilience has been the subject of strong debate since Barabasi et al. (Albert and Barabási, 2002; Albert et al., 2000) studied ‘attack vulnerability’ in complex networks. Several studies after their seminal paper have adopted this approach to study network resilience under different degrees of damage in complex systems (Crucitti et al., 2004; Doyle et al., 2005; Holme et al., 2002). The study of Albert and Barabasi (Albert et al., 2000) introduced two kinds of perturbations termed ‘random error’ and ‘targeted attack’. Random error is simulated by selecting one node (e.g. a region of the brain) at random and removing it as well as all its links. The largest connected component and the mean path length (or global efficiency) is then reevaluated. The process is repeated incrementally, eliminating at random node after node until the size of the largest component corresponds to a single node. The targeted attack follows the same procedure but the first node to be eliminated is the hub, defined as the node with the largest degree. After hub deletion, the degree of the nodes are reevaluated, and then iteratively removed from the network in order of decreasing degree. The difference between the mean path length before and after every isolated elimination of nodes provides a measure of the centrality of this region to global network topology.

In their study, Barabasi and coworkers concluded that networks with ‘scale free’ degree distribution are more robust under random error than networks with a ‘gaussian-like’ degree distribution (Erdős–Rényi random networks). On the other hand, networks with a scale free distribution seemed to be more vulnerable under targeted attack due to the presence of hubs, whereas the impact of removing high degree nodes in random networks is limited since every node has a ‘small’ connectivity. Posterior several studies in this field have also examined resilience to insult in networks that presented different degree distributions and comparing them with the previous ones, highlighting the indirect link between degree distribution and resilience. It has been shown

that in physical embedded networks such as the brain, the appearance of highly connected nodes is less probable than in scale free networks (Hilgetag and Kaiser, 2004; Sporns and Zwi, 2004; Sporns et al., 2004) since the wiring cost to make long distance connections may be prohibitive. As a result, brain networks are characterized by near scale free distributions and present less hubs. In consequence, these networks are considerable more resilient under hub targeted attacks than scale free ones (Achard et al., 2006).

Computational models of *affected* systems typically consists in simulating on empirically mapped network structures the effects of various structural lesions (Alstott et al., 2009; Honey and Sporns, 2008). Although this integrated approach enables rigorous and testable predictions, more empirical results are needed. To date, few empirical brain studies exists to directly evaluate the effects of such lesions and quantify the changes in the the real functional connectivity (Achard et al., 2006; Warren et al., 2014). It has been theoretically suggested that human brain networks are highly vulnerable under the specific attack of ‘connector hubs’, defined in modular networks as nodes that highly participate with other modules. The deletion of such a central hub can result in a disruption of the hierarchical architecture, affecting the normal balance between integration and segregation (Stam, 2014). This hypothesis has been recently supported empirically in studies showing that the loss in network integration is related with a loss of cognitive domains (Warren et al., 2014).

These studies are essential to understand the development of pathologies after structural lesions as occurs in stroke, traumatic brain injury, cancer or neurodegeneration. For instance, recent findings have indicates that many brain disorders such as Alzheimer’s or Parkinson’s showed damage in highly central nodes, giving rise to a rich club deterioration (Buckner et al., 2009; Crossley et al., 2014; Stam, 2014; van den Heuvel and Sporns, 2013).

In addition, the brain network also presents recovery mechanisms to fight against or restore focal lesions. For instance, by increasing activity in unaffected brain regions, as occurs in patients with stroke(Riecker et al., 2010;

Saur et al., 2006), although a high persistent hyper-activation can lead to degeneration as well (de Haan et al., 2012; Saxena and Caroni, 2011). This compensatory mechanisms can explain the observed increased activity in some brain areas in Alzheimer's disease, Parkinson's, and multiple sclerosis, though at early stages of the disease, with the activity strongly declining at later disease stages (Poudel et al., 2014; Schoonheim and Filippi, 2012; Sperling, 2007).

In this sense, we will see along this thesis that our clustered neuronal cultures are characterized by a functional organization qualitatively similar to the brain, a property that confers them a higher resilience than other network configurations. In this sense, our cultures are an accessible, excellent model system to empirically study the impact of these random and targeted attacks. These studies would lead to better knowledge on the link between the physical neuronal circuit damage and the resulting functional disturbances (i.e. global activity disruptions), as well as to study the recovery mechanisms that can give rise to their final global restoration and stability.

### **1.1.6 The need of *in vitro* approaches: neuronal cultures**

Despite considerable advances, the link between brain connectivity, neuronal activity, and function (or dysfunction) that ultimately give rise to a normal (impaired) behavior and cognition, remains elusive. Understanding this intricate puzzle requires the study of neuronal circuits in simpler systems at a *mesoscale* level. In such systems, not only their complexity is reduced, but also their controllability and manipulation highly increased.

Mesoscale approaches include theoretical models, computational simulations, and experiments in simple living systems, e.g. animal models or *in vitro* preparations in the form of slices or neuronal cultures. The three aspects often work together, reinforcing the validity of the derived tools as well as their applicability (Markram et al., 2015).

*In vitro* neuronal networks are gaining increasing interest given their reasonable number of nodes and connections. Figure 1.2 illustrates different culture preparation and different strategies for measuring activity. These networks are easily manipulable, exhibit rich spontaneous activity, and both neurons and their dynamics can be monitored in detail. The *in vitro* environment also allows highly reproducible pharmacological and chemical manipulations, making it highly attractive to study cellular, connectivity, and molecular aspects related to healthy and diseased neuronal circuits.

The simplest yet highly advantageous *in vitro* system are ‘primary neuronal cultures’. They consist in the isolation of a specific brain tissue, its dissociation into individual cells, and their culturing in an appropriate, nutritious environment. Primary cultures preserve the cellular variety of the original tissue although the initial topology is lost. Both connectivity and spontaneous activity emerge *de novo*, in a fascinating self-organized manner that is still poorly understood.

Three major types of cultured neuronal networks are of particular interest, namely ‘homogeneous’, ‘clustered’, and ‘patterned’ (Figure 1.2). For the first type, neurons are plated on a substrate that contains a layer of adhesive proteins. Neurons firmly adhere to the substrate, leading to cultures with a homogeneous distribution of neurons (Cohen et al., 2008; Orlandi et al., 2013; Tibau et al., 2013; Wagenaar et al., 2006). For the second type, neurons are plated with full motility freedom, swiftly aggregating into small, compact assemblies termed *clusters* that connect to one another (Gabay et al., 2005; Segev et al., 2003a; Shein Idelson et al., 2010; Teller and Soriano, 2013). Finally, for the third type, neurons are anchored in a specific locations following a dictated topological map.

Despite the enormous gap between neurons in the brain and *in vitro*, neuronal cultures are playing an important role in the understanding of brain alterations. They can indeed mimic deficiencies of some brain pathologies, allowing to study the implications of the damage as well as to investigate pos-

sible recovery strategies using pharmacological drugs (Srinivas et al., 2007) or even stimulation (Mazzatenta et al., 2007). In this context, neuronal cultures have assisted in the comprehension of circuit dysfunction in mild traumatic brain injury (Bottlang et al., 2007; Cullen and LaPlaca, 2006; Morrison III et al., 2011; Patel et al., 2012), epilepsy (Srinivas et al., 2007; Sun et al., 2002, 2004) or neurodegenerative diseases, particularly Alzheimer's (Dahlgren et al., 2002b; Hartley et al., 1999). In the enlightening study of Ref. (Patel et al., 2012), for instance, an isotropic mechanical pressure on a dissociated culture was applied to resemble the biomechanics of a *in vivo* deformation in concussions. Interestingly, the authors observed that a mild injury ( $> 35\%$  stretch) caused a widespread effect in the neuronal global dynamics that led to a break down of the initial synchrony into multiple, smaller interconnected functional modules. The versatility of the experiment was such that the network could be nearly completely restored to its pre-injury state. In other investigations, chemical agents were added to model stroke-induced episodes in epilepsy, and where cultures were overexcited under glutamate action. Interestingly, the study of Ref. (Srinivas et al., 2007) found that the exponential degree distribution and small-world features that presented their hippocampal cultures were lost upon glutamate injury. Furthermore, neuronal cultures have been also used as a platform for drug development and testing of toxicity (Frega et al., 2012). It is worth to point out that all these studies facilitated not only the comparison of the dynamics between control and impaired cultures, but also the investigation of the molecular basis of these alterations for reversing them.

In addition of the above disease-oriented investigations, neuronal cultures can provide valuable data for basic theoretical neuroscience research, for instance by combining *in vitro* data with *in silico* models. They are also unique tools to improve imaging technologies, for instance, by helping the interpretation of data provided by electrodes or calcium fluorescence imaging (Ito et al., 2011; Stetter et al., 2012). These neuronal cultures also offer the

possibility to study scaling properties, e.g. by changing the neuronal density or the physical dimensions of the cultures. Interestingly, different studies have been carried out in unidimensional cultures (Figure 1.2E) to study an aspect as fundamental as wave propagation and information coding (Feinerman et al., 2005, 2007; Jacobi et al., 2010) or to build neuromorphic devices (i.e. logical gates) capable of ‘computation’ (Feinerman et al., 2008). At the other extreme, three-dimensional cultures have started to catch attention given their topological proximity to naturally formed circuits, and using glass beads (Pautot et al., 2008), polymers (Lai et al., 2012) or other structures (LaPlaca et al., 2010) as the skeletal supports of the network.

Finally, neuronal cultures are also remarkable platforms to study network response on electrical, chemical, and optical stimulation. Low levels of electrical stimulation have been explored to add noise to a neuronal system, for instance in the study of stochastic resonance or synchronization. And a combination of electrical stimulation and chemical action have been used to devise a theorico-experimental percolation framework for assessing the connectivity of living neuronal circuits (Breskin et al., 2006; Soriano et al., 2008). And, recently, with the introduction of the optogenetics technology (Yizhar et al., 2011), the stimulation or silencing of neurons with light can be precisely controlled, allowing the interrogation of neuronal circuits, the induction of activity patterns, as well as the control of excitability, for instance to stop an epileptiform activity (Tønnesen et al., 2009).

### 1.1.7 Homogeneous cultures

Homogeneous neuronal cultures (Figure 1.2A-C) represent the most standard and most used culture preparation. They have proven highly valuable in addressing questions related to the generation and propagation of spontaneous activity patterns. This is characterized by the collective activation of all the neurons in a short time window, a phenomenon called *network bursts* (Ben-Ari, 2001; Gross and Kowalski, 1999; Kamioka et al., 1996; Streit et al., 2001;

Wagenaar et al., 2006). For sake of clarity, we must specify that a neuron in such preparation elicits upon firing a series of action potentials or *spikes*. A train of such spikes in a neuron is termed *burst*, whereas the collective network activation is the ‘network burst’. Diverse studies showed that this collective activity exhibits a rich repertoire of patterns throughout the time life of the network (Van Pelt et al., 2004; Wagenaar et al., 2006). Additionally, various groups studied the initiation of these spontaneous network bursts, and developed a high variety of theories that include the existence of initiation zones (Feinerman et al., 2007), synchronization of different type of neurons and networks (Segev et al., 2004), or the presence of a small subset of highly active neurons called ‘leader neurons’ (Eckmann et al., 2008, 2010; Ham et al., 2008) or ‘functional hubs’ (Sun et al., 2010).

This spontaneous activity, however, needs to present universal regulatory mechanisms since it has been observed in systems as diverse as the retina (Harris et al., 2002), the hippocampus (Mazzoni et al., 2007), or the spinal cord (Streit et al., 2001). In this line, our research group at the University of Barcelona recently proposed a new scenario (Orlandi et al., 2013) that explains this spontaneous activity as an amplification of the synaptic neuronal noise through the network. The new scenario was unveiled by combining theoretical modeling, simulations and *in vitro* experiments. Although these studies are not the topic of the present thesis, I participated in their development and co-authored the main publication describing the problem (Orlandi et al., 2013).

In addition of the initiation mechanisms, researchers have also studied in detail the propagation characteristics of the network bursts. Some studies observed that they propagate through the network as a circular wave (Maeda et al., 1995; Orlandi et al., 2013), while others claimed that propagation is power law distributed in time (Mazzoni et al., 2007; Pasquale et al., 2008; Pu et al., 2013; Tetzlaff et al., 2010), indicating that the wave propagation occurs in avalanche-like manner and drives the culture towards a critical state. In

particular, these studies have pointed out that the age of the neuronal culture sets different critical regimes, evolving from sub-critical to super-critical and finally reaching the critical one. This criticality was previously shown in brain slices (Beggs and Plenz, 2003, 2004) and has been strongly related with memory and optimal computational capabilities.

Homogeneous culture were also found to support learning (Madhavan et al., 2006, 2007). Following the discovery of plasticity rules in the coupling between single neurons (Bi and Poo, 2001) a network-level analog was found in which path specific potentiation and depression were induced using electrical stimulation (van Pelt et al., 2005). In addition to these plastic changes, a series of regulatory mechanisms constantly tune synapses and intrinsic neuronal excitability to achieve single cells and network-level homeostasis (Shein et al., 2008; Turrigiano and Nelson, 2004). These studies show that neuronal cultures are potential platforms to explore network-level mechanisms important to information processing, activity propagation, memory and learning.

Despite all these important studies, homogeneous cultures have two major imitations. First, the homogeneous organization is markedly different from *in vivo* networks. And, second, the restriction of motility impedes the formation of richer physical circuits which, in turn, could favor a wider spectrum of activity patterns and functional connectivity traits. For instance, homogeneous cultures a cannot support parallel and hierarchical information processing, as observed in the brain (Meunier et al., 2010) and, as we will see, in other culture preparations.

### 1.1.8 Patterned cultures

A much richer repertoire of connectivity and activity patterns can be obtained by facilitating heterogeneity in the distribution of the neurons over the substrate. For instance, modular architectures can arise by sparsely interconnecting small subsets of highly connected neurons. Experimentally,

and boosted by recent advances in cell patterning techniques, a large set of tools have become available for controlling neuronal network architecture (reviewed in Ref.(Wheeler and Brewer, 2010)). However, activity analysis of patterned networks has been poorly addressed, but the continuous developments proves the great potential of such an idea.

In general, patterned cultures emerged to explore the intriguing relationship between connectivity and dynamics (Eckmann et al., 2007; Wheeler and Brewer, 2010). Ideally, by modifying the connectivity of a neuronal culture in a control manner, one can build neuronal circuits with predefined structural architectures, to later ascribe them to functional topological characteristics. Several tools and approaches have been applied to immobilize neurons in specific locations, or to make them grow on predefined areas (Figure 1.2E-I). Some of them include the physical caging of neurons within barriers, biochemical approaches to combine cell-attracting with cell-repelling surfaces, or the patterning of surfaces with lithographic techniques (Gabay et al., 2005; Macis et al., 2007; Shein et al., 2009; Shein-Idelson et al., 2011; Sorkin et al., 2006). In order to guarantee neuronal activity in some sparse network configurations, the majority of these studies used small aggregates of neurons (clusters) rather than single neurons as nodes in the network ((Figures 1.2C and 1.2F-G)). Although high density preparations are better to ensure culture viability—for easily more than a month—, the major requirement in the preparation of patterned cultures is to reach full network maturation while preserving the neurons in their initial locations. Neurons indeed present a high motility that often compromises the quality of patterning(Shein-Idelson et al., 2011) (Figure 1.2). Substantial efforts are poured in this direction, and the most successful technique so far combines micro-contact printing of an adhesion promoter in combination with an agarose repulsive layer. By using such a cell patterning approach, (Marconi et al., 2012) achieved a regular structural configuration that exhibited a functional activity that matched theoretical predictions.

Finally, these patterned networks were used to study scaling properties in homogeneous networks, for instance to investigate the robustness of network bursts under different sizes as well as their self-regulatory nature (Shein Idelson et al., 2010). Interestingly, it was also shown that neuron–glia clusters composed by 40 cells is the smallest network that can show global activity (Shein Idelson et al., 2010), although other groups refined later the experimental procedures to prepare ‘micro–cultures’ consisting of 4 – 30 neurons that were able to exhibit collective spontaneous activity (Cohen and Segal, 2011).

### **1.1.9 Clustered cultures: appealing complex organization in a dish**

When there are not constraints to keep cells at specific locations, neurons spontaneously tend to connect to each other, giving rise to highly packed clusters of neurons and glia that connect with other clusters by bundles of neurites (axons and dendrites). The size of the clusters range between 20 and 120  $\mu\text{m}$  in diameter and can contain several hundred of neurons and glial cells. Typically, these glia cells spatially arrange forming a layer on top of which neurons grow (Shein Idelson et al., 2010).

These *clustered neuronal cultures* were initially studied to comprehend the self-organizing principles behind the formation of the clusters (Segev et al., 2003b; Shefi et al., 2002). Particularly, in biological systems, the characterization of the emergent self–organization of their components is of utmost importance to comprehend the mechanisms of life (Eckmann et al., 2007; Gross and Kowalski, 1999; Van Essen, 1997). Interestingly, the study of (Segev et al., 2003b) showed theoretically that this spontaneous aggregation occurs when the pulling forces exerted by the bundle of neurites overcome the adhesion of the neurons on the substrate. Moreover, this clustered configuration seems to occur without participation of the glia cells and without any activity (Segev et al., 2003b). In line with this characterization, clustered

networks emerged as an attractive platform to study the interplay between morphological and functional connectivity at the mesoscale (Gabay et al., 2005; Macis et al., 2007; Shein et al., 2009; Shein-Idelson et al., 2011; Sorkin et al., 2006). Indeed, the fact that the neurons self-organize into clusters facilitate cell patterning since they provide higher stability and culture viability is much higher.

Studies of individual cluster of neurons, i.e. intra-cluster level, revealed that they present global firing events resembling the network bursts found in homogeneous networks (Segev et al., 2003b; Shein et al., 2008; Shein Idelson et al., 2010; Shein-Idelson et al., 2011), and that appeared to be independent of their size although a minimum number of cells was required (Shein Idelson et al., 2010). In addition, the distribution of the inter-burst intervals was qualitatively similar to homogeneous cultures.

However, the potential property that makes clustered cultures very appealing is that the activity between clusters, i.e. inter-cluster level, is markedly modular, meaning that clusters fire in small groups much more often than as an entire system (Segev et al., 2003a; Shein et al., 2009; Shein Idelson et al., 2010; Shein-Idelson et al., 2011). Activation within a group is concatenated, with a delay from the activation of a cluster to the next one that appears to depend on clusters' size and their coupling strength (Shein-Idelson et al., 2011; Tsai and Chang, 2008). Additionally, the inter-cluster delays are larger than the ones observed between single neuron on homogeneous cultures (Berdondini et al., 2006; Shein-Idelson et al., 2011; Tsai and Chang, 2008; Yvon et al., 2005).

The modular dynamics of these clustered networks is one of their most fascinating properties, and reflect their dynamic repertoire (Raichman and Ben-Jacob, 2008; Shein-Idelson et al., 2011; Tsai and Chang, 2008). (Tsai and Chang, 2008) showed that there exist certain pathways of firing patterns initiated by different master groups, although the dynamic patterns are also conditioned by the spatial configuration of the network. The robustness and

variability of these repeating pathways could be related to memory storage. By decreasing the inter-clusters coupling or lowering their effective firing threshold the repeating pathways remains robust, although the occurrence rate and their temporal persistence varied (Tsai and Chang, 2008).

As outline before, an important aspect is the dynamics of the clustered cultures is that activity can include all the culture or only a part of them. This shapes a network that is not only modular, but also hierarchical (Berdondini et al., 2006; Shein-Idelson et al., 2011; Tsai and Chang, 2008; Yvon et al., 2005). Their investigation therefore provide an interesting insight on the interaction between subnetworks, i.e. the *integration–segregation* balance. This hierarchical topology further elevates the richness and complexity as compared to homogeneous networks.

All these studies showed that clustered cultures are a powerful platforms to investigate information processing at network-level, to study signal propagation between population of cells, and to uncover plasticity and memory mechanisms at mesoscopic scale. These investigations shaped a first powerful reason to investigate these cultures as my thesis project.

From a complex networks perspective these clustered cultures have a unique potential due to the existence of a two-level network, one within a cluster and another between clusters, making them really appealing to study dynamical and topological features of hierarchical as well as modular networks. The possibility of using clustered cultures as *network theory laboratory* shaped the second reason to study such a system.

Indeed, these clustered networks can be seen as a model system to study in a more precise —and accessible— manner the connectivity among neuronal populations, and address how these anatomical connections can shape the repertoire of activity patterns that emerge in the system. Moreover, neuronal cultures in general, and these clustered cultures in particular, are ideal platforms to dive deeper not only in the understanding of the fundamental traits that shape stable activity patterns in neuronal systems, but also in their

resilience to perturbations, a fundamental topic in neuroscience and a very attractive field of research for the physical and network science communities.

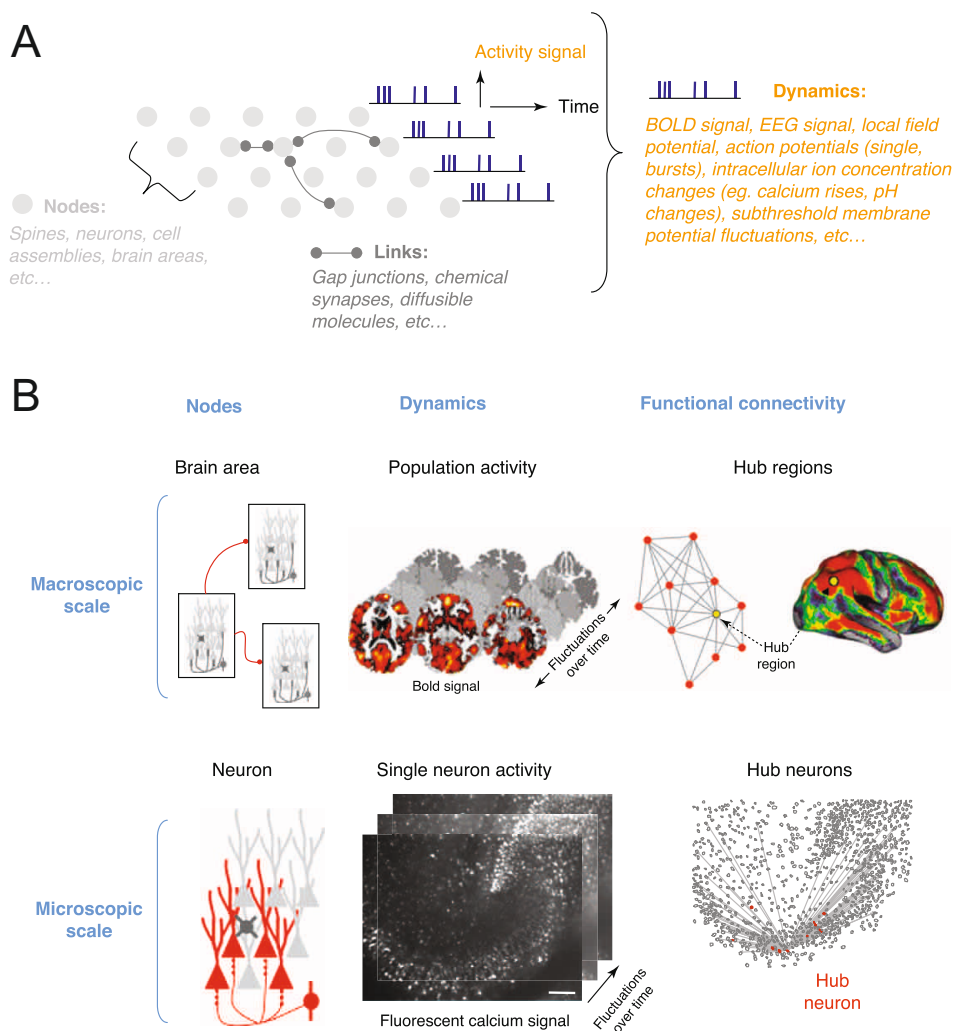


**Fig. 1.1 Complex network theory applied to the analysis of neuronal networks.** **A**, Schematic representation of a neuronal network where nodes represent different neuronal entities (e.g. neurons or assemblies of them) and links represent different communication methods (e.g. chemical synapses). Dynamics characterize the onsets/offsets of a given signal measured for each node as a function of time, and can include action potentials or BOLD signals observed with fMRI. **B**, ‘Scale-free’ topologies are particularly appealing models for neuronal circuits at both the macroscopic (top) and microscopic (bottom) levels. Top panel: fMRI data, allowing for the mapping of correlated activity between distant brain regions from which a functional connectivity network is derived. Candidate hubs are those regions with disproportionately high connectivity. Bottom panel: Multi-neuron calcium imaging enables functional connectivity to be described at the scale of microcircuits. It also enables the identification of hub neurons (red), which are functionally connected to many others (functional links in gray). Adapted from Refs.(Feldt et al., 2011)

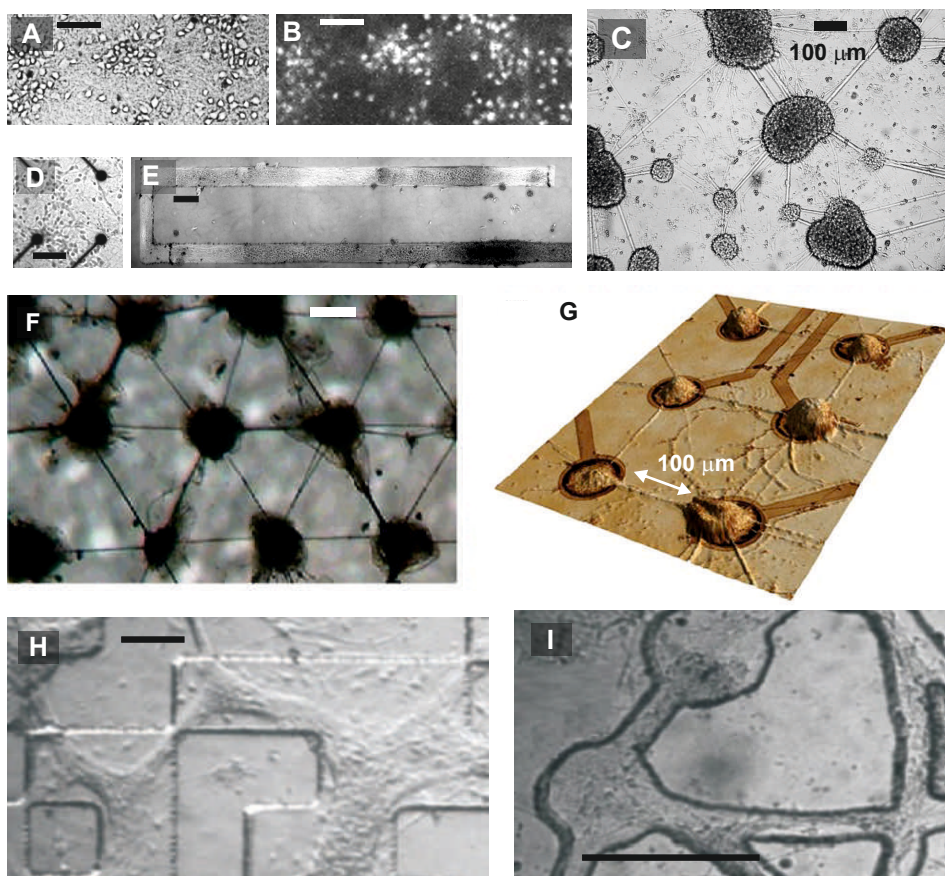


**Fig. 1.2 Neuronal cultures.** **A**, Bright field image of a neuronal network where cover the substrate in a homogeneous manner. Round white objects are neurons. **B**, Corresponding fluorescence image. **C**, Clustered neuronal culture, formed by dense aggregates of neurons (dark objects) interconnected through bundles of neurites (straight lines). **D**, Neurons plated on multi-electrode arrays. Black spots are electrodes. **E**, Unidimensional neuronal culture, formed by patterning neurons along a circuit  $70\ \mu\text{m}$  wide and  $15\ \text{cm}$  long. **F**, Patterned culture in which aggregates of neurons occupy predefined locations. **G**, Alternative patterning in which the aggregates sit over electrodes. **H**, Patterned culture in which neurons grow at the top of a topographical mold. **I**, Patterned culture in which neurons occupy the bottom of patterned formed by interconnected circular traps. Scale bars in all figures are  $100\ \mu\text{m}$ . Panels F and G adapted from Ref. (Wheeler and Brewer, 2010).



# Chapter 2

## Experimental Setup and Procedure

Neuronal cultures, despite their divergence from naturally formed neuronal circuits such as the brain, constitute an advantageous, accessible and highly manipulable neuronal system that have always fascinated the scientific community. They possibly shape one the simplest yet powerful experimental systems to tackle fundamental questions in both neuroscience and physics. This chapter aims at describing the experimental tools, strategies and procedures that we developed to give rise, week after week along 4 years, to the collection of experiments that shape this thesis.

### 2.1 Culture preparation

All the neuronal cultures used in our experiments were prepared at Jordi Soriano's Lab. This lab was a dusty, empty space in January 2009. It needed more than a year and a gigantic effort to take shape, but by May of 2010 we were able for the first time to dissect brains, incubate cultures and measure spontaneous activity in our own space and with our own resources.

The basic protocols and strategies to prepare the neuronal cultures, and that we describe in the following, were ‘imported’ from the laboratory of Elisha Moses at the Weizmann Institute of Science in Israel, the research group where Jordi Soriano spent about 4 years as postdoc. We want to express here our gratitude towards Moses’ group and the Weizmann Institute, whose continuous assistance along 2009 facilitated the birth of our laboratory.

Moses’ group essentially worked with what we call *homogeneous cultures*, and the corresponding original protocols can be found in Refs. (Breskin et al., 2006; Cohen et al., 2010; Soriano et al., 2008). We used the same protocols with minor modifications. The idea of using *clustered cultures* arose from Soriano’s mind and the protocols that we finally used after some refinement were published in Ref. (Teller et al., 2014).

All the experimental procedures were approved by the Ethical Committee for Animal Experimentation of the University of Barcelona in 2010, under order DMAH-5461, and were revised and updated periodically in accordance to the regulations of the Generalitat de Catalunya.

### **2.1.1 Self organizing clustered cultures**

The neurons that we used were dissected from Sprague-Dawley rat embryos at 18 – 19 days of development. In all experiments we used cortical neurons given the relatively easy access and large size of such a brain region, and that allowed us to prepare 24 – 48 cultures simultaneously every week. Additionally, the majority of the cortical neurons are pyramidal cells and therefore the formed networks can be considered homogeneous in neuronal type. This homogeneity also facilitates similar activity patterns in cultures prepared identically.

Neurons in tissues from 18 – 19 day old embryos are weakly connected and therefore easy to dissociate. Gentle pipetting sufficed in all our preparations to isolate the neurons, ruling out the need for aggressive chemical agents such as trypsin, as used regularly by others (Chen et al., 2008; Choi

et al., 1987; Walicke et al., 1986). Pregnant rats were bred at the animal farm of the University of Barcelona, ceased with CO<sub>2</sub> at the same facility and swiftly transported to our laboratory for dissection. For clarity, the different chemicals that we used for the preparation of our cultures are summarized in Table 2.1. The embryonic brains were gently dissected in ice cold L-15 medium. Neuronal cortices were then dissociated by repeated pipetting with gradually narrower pipette tips, and the obtained suspension of dissociated cortical neurons was finally seeded onto 13 mm glass coverslips (Marienfield-Superior) that incorporated 4 circular cavities in a mold of polydimethylsiloxane (PDMS). Details of the preparation and treatment of the PDMS molds are provided in Section 2.2. Cavities were 3 mm in diameter and 1 – 4 mm deep, depending on the experiment. The cavities limited the size of the neuronal networks to convenient dimensions for our imaging system, ultimately ensuring the visualization of neuronal activity in the whole network and with optimum recording conditions. A sketch of the cell culture preparation is provided in Figure 2.1A.

Neurons within each cavity connected to one another to constitute a new network. The glass substrate was clean of impurities and did not contain any adhesive protein, therefore facilitating cell motility and aggregation (Figure 2.1B). This aspect is crucial to create the clustered cultures, a process that arises naturally as a self-organizing mechanism. Indeed, neurons can move freely on the glass substrate. In that condition, the neurites' tension between neurons overcomes the substrate friction, facilitating the neuron's motility and coalescence (de Santos-Sierra et al., 2014; Segev et al., 2003b).

For each dissection we used a multi-well plate of 24 wells containing in each well the identical glass-PDMS structure. Then, each well contained 4 minicultures of 3 mm in diameter each, giving rise to around 100 minicultures per plate, and sharing similar conditions. Neurons were placed on the cavities with a nominal density of 2500 neurons/mm<sup>2</sup> and incubated in *plating medium* at 37 °C, 5% CO<sub>2</sub> and 95% humidity up to day in vitro (DIV) 5. After plating,

Product Name	Description	Provider	Role
L15+2G	L15 enriched with 0.6% glucose and gentamicin	Sigma-Aldrich	Maintains physiological pH conditions before planting
MEM+3G	Essential Medium Eagle's-L-glutamate enriched with gentamicin, glutamate and glucose	Sigma-Aldrich	Main buffer for cell culturing and development
Plating Medium	MEM+3G with 5% of foetal calf serum (FCS), 5% of horse serum (HS), and 0.1% B27	FCS and HS, Invitrogen B27, Sigma-Aldrich	Neuronal growth
Chenging Medium	MEM+3G with 0.5% Uridine, and 10% HS	FUDR and Uridine, Sigma-Aldrich	Limits glia cell division
Final medium	MEM+3Gwith 10% HS	HS Invitrogen	Maintains a proper enviroment to keep cultures healthy for long time
EM	500ml DDW with 128mM NaCl, 1mM CaCl <sub>2</sub> , 1mM MgCL <sub>2</sub> , 45 mM sucrose, 10mM glucose, and 0.01M Hepes; pH 7.4	-	Recording solutions i.e. pH-stable buffer for actual experiments

**Table 2.1 Cell culture and recording solutions.** The table summarizes the different culture media used for preparation and maintenance of the cultures, as well as for recording activity. We also include the manufacturer of the product and the role of the different products.

the absence of adhesive proteins on the glass substrate rapidly favored cell-cell attachment and, gradually, the formation of islands of highly compact neuronal assemblies or clusters that minimized the surface contact with the substrate. By DIV 2 the culture encompasses dozens of small aggregates that coalesced and grew in size as the culture matured. By DIV 4 – 5, neuronal clusters exhibited spontaneous activity and connections between them were visible. At this stage of development, clusters also anchored at the surface of the glass. Their number and position remained stable although they continued growing and developing connections along the next 2 weeks (Figure 2.2).

Clustered cultures were maintained for about 3 weeks, as follows. At DIV 5 the plating medium was switched to *changing medium* to limit glial cell division, and from DIV 8 onwards cultured in *final medium* with a periodic fluid replacement every three days.

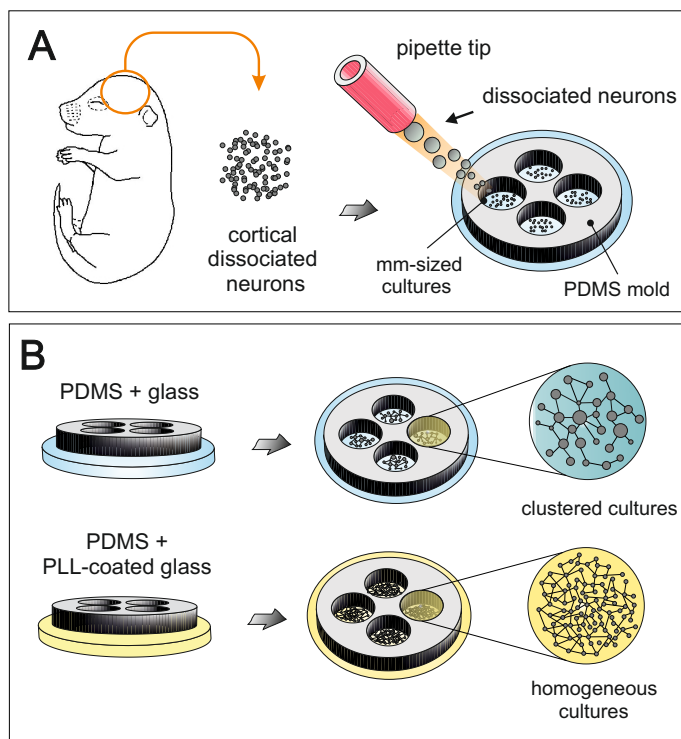


**Fig. 2.1 Culture preparation.** **A**, Cortices from embryonic rat brains were dissected and neurons dissociated by pipetting. Neurons were then suspended in plating medium and seeded onto previously prepared PDMS–glass structures 13 mm in diameter, and containing 4 cavities, each 3 mm in diameter. **B**, Each culture well contained 4 networks, which could be neatly isolated by adjusting the height of the PDMS walls. Two main cultures could be prepared. In the absence of the adhesive protein PLL (top), neurons moved and aggregated, shaping the clustered configuration. The coating of the glasses with PLL (bottom) gave rise to the homogeneous networks.

For sake of clarity, culture preparation and maintenance in homogeneous cultures were identical as described for the clustered ones, i.e. we used the same nominal neuronal density for plating, we included PDMS pierced molds to restrict neuronal growth in cavities of 3 mm in diameter, and we refreshed the culture medium in the same manner. The crucial difference resides in the fact that, prior plating, the PMS–glass structure was treated overnight with poly-L-lysine (PLL) to provide a coating of adhesive protein. Glasses were then washed 3 times with double distilled water (DDW) to remove

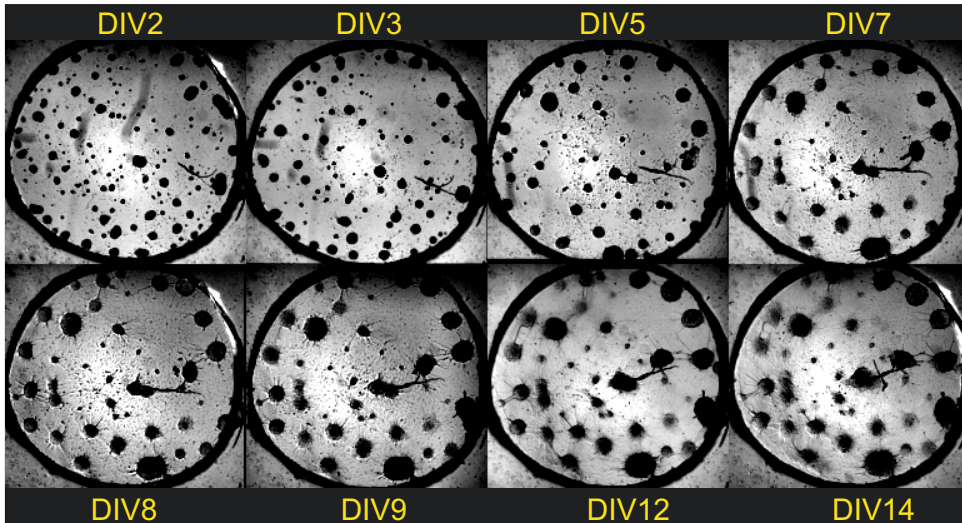


**Fig. 2.2 Culture development.** The images show different stages of a representative clustered culture, from DIV= 2 to 14. By DIV= 2 – 4, the culture encompasses several dozens of small, disconnected neuronal assemblies. Around DIV= 5 – 7 these small assemblies merge into one another shaping recognizable clusters, which grow in size and create pairwise inter-connections. Clusters anchor to the substrate at this stage of development, remaining at similar positions although along the next 2 weeks they continue growing and developing connections.

residual PLL. The adhesive protein anchors the neurons onto the substrate, restricting their motility and therefore preserving the initial homogeneous neuronal spatial distribution.

## 2.2 Glass-PDMS structure preparation

PDMS is a silicon-based polymer that is transparent and non-toxic. At the beginning of the thesis this polymer was used as a mold to control the neuronal connectivity and later just to restrict the size of our cultures. The glass-PDMS structure preparation used for the latter case is described below.

First, prior plating, glasses were treated in 70% nitric acid during 2 h, later washed 2 times in DDW, sonicated in ethanol for 30 min, and finally dried with a methane gas torch.

In parallel, we prepared the PDMS mold. We used the PDMS Sylgard 184 Silicone Elastomer Kit provided by Dow Corning (Midland, MI, USA). This kit has two components; a resin (base) and a hardener (curing agent). Both components were briskly mixed in a small beaker in a concentration 10:1 (typically 30mg of the resin with 3mg of the hardener) until they were completely merged. The viscous mixture was carefully spread over a 100 mm diameter petri dish to achieve a large area and a homogeneous layer. The amount of PDMS poured depended on the desired thickness of the mold, typically in the range 2 – 4 mm. The PDMS dish was either left overnight at room temperature or heated at 80 °C during 2 h in an oven. Once the PDMS film hardened, it was pierced with a stainless steel puncher of 13 mm in diameter, and that corresponds to the same diameter as the cover glasses used for culturing.

Cavities in the PDMS were next obtained by piercing the film with a puncher (Integra-Miltex) of 3 mm in diameter. The reason to restrict the cavities in diameters of 3 mm was primarily to fit 2 – 4 minicultures (depending on the study) in the field of view under optimal recording conditions, as described later. Finally, the PDMS molds were placed on the glass coverslips and autoclaved at 105 °C achieving a highly adhesion between the combined structures. This process both sterilized the PDMS while strongly bonding it to the glass.

The thickness of the PDMS film was set to satisfy specific experimental conditions while balancing culture preparation efficiency, imaging quality, and healthy neuronal network development. Two experimental conditions shaped the work in this thesis:

- *Standard biochemical environment experiments.* Are those in which we simply monitored spontaneous activity in the cavities. The buffer used upon recording of activity was the same in all cavities and therefore *thin* PDMS films sufficed.

- *Specific, perturbative biochemical environment experiments.* Are those in which different chemical agents were applied in each cavity during recording of activity. This procedure required the cavities to be independent, in order to prevent the spread of these chemical agents to other mini-cultures, and therefore *thick* PDMS layers were required.

To fine tune the thicknesses  $H$  of the PDMS film, the options that we finally explored and their use are the following:

- $H < 1$  mm. The PDMS attached firmly to the glass, but the neurons on the top of the PDMS connected to the ones within the cavities, effectively producing a single network in the 13 mm diameter PDMS-glass structure. Although we tested the idea of peeling off the PDMS from the glass before the actual measurements to isolate the networks in the cavities, the procedure resulted in the damage of most of the clusters. Hence, these thicknesses were excluded from the preparation protocol.
- $1 < H < 2$  mm. The PDMS attached firmly to the glass and, more importantly, the neurons at the top of the PDMS and the ones at the cavities evolved independently, shaping independent networks. This thickness range was therefore used as the optimum one for the standard experiments. In these experiments, the PDMS film was left in the culture during recording.
- $2 < H < 4$  mm. Autoclaving was not sufficient to keep PDMS and glass firmly bond, requiring an additional oxygen plasma treatment to ensure firm attachment. Such thicknesses, however, were not necessary for standard experiments, but were the basis for the specific, perturbative biochemical environment ones.
- $H \simeq 4$  mm. Oxygen plasma treatment of the PDMS before autoclaving significantly increased the binding strength with the glass. Treatment

was carried out in the facilities of the Institute for Bioengineering of Catalonia (IBEC). Plating was successful and networks within the cavities neatly developed. This procedure was the one finally used for the specific, perturbative biochemical environment experiments, assuring that each cavity had walls sufficiently high to preserve its own solution.

- $H > 5$  mm. PDMS-glass binding was strong upon oxygen plasma treatment, but the neurons did not develop properly within the cavities, possibly due to inefficient flow of nutrients in such a deep structure. Cultures were inviable and typically died after 4 days *in vitro*. These thicknesses also made difficult the recording of activity, since the walls of the cavities not perfectly aligned with the objective masked the neurons. We therefore excluded such heights from experiments.

## 2.3 Experimental setup

Spontaneous neuronal activity in our experiments was monitored using the technique known as *em* Fluorescence Calcium Imaging (Rocheffort et al., 2008; Smetters et al., 1999). This experimental technique allows the detection of neuronal firing by the indirect monitoring of calcium transients through a calcium sensitive probe, as described in detail in the review of Ref. (Grienberger and Konnerth, 2012). This technique was the main activity monitoring technique used in Moses' lab (Breskin et al., 2006), and was implemented in our lab upon the creation of Soriano's group. The technique is very versatile, and has been extensively used both *in vitro* (Breskin et al., 2006; Orlandi et al., 2013) and *in vivo* (Ahrens et al., 2013).

### 2.3.1 Calcium fluorescence imaging

$\text{Ca}^{+2}$  ions are involved in important cell functions such as contraction, secretion, neuronal activity and plasticity. In particular, when a neuron fires there is a high intake of  $\text{Ca}^{+2}$  ions inside the cell (100 times higher compared to the free calcium concentration at rest (Berridge et al., 2000)). By using calcium sensitive indicators that binds to the intracellular free calcium ions one can detect, through a properly tuned optical system, the onset of neuronal firing. A typical fluorescence signal of neuronal firing is characterized by a sharp increase of about few milliseconds upon neuronal depolarization (rapid influx of calcium ions through the voltage-gated  $\text{Ca}^{+2}$  channels) followed by a slower decay of about few seconds during hyperpolarization (outflow of these ions through a slow pumping process).

Two kinds of calcium indicators have a widespread use, namely the chemical indicators and the genetically encoded ones (GECI) (Knöpfel, 2012). The former are small molecules that modify their fluorescent properties upon binding with calcium ions, ultimately emitting fluorescence light. The latter are genetically modified molecules that incorporate a GFP (or its variants) with other molecules that, at binding to calcium ions, experience conformational changes that enable the fluorescence emission. In particular, throughout this thesis we used the chemical calcium indicator Fluo-4-AM (Invitrogen) (Gee et al., 2000; Paredes et al., 2008). Compared to others chemical indicators, Fluo-4 presents a high light intensity that results into a high signal to noise ratio (SNR). This overall quality makes Fluo-4 one of the most extensively used probes to detect neuronal activity, both in neuronal cultures (Ganguly et al., 2001; Orlandi et al., 2013; Tibau et al., 2013) and in brain slices (Carrillo-Reid et al., 2008; Ikegaya et al., 2004). Figure 2.3 illustrates typical fluorescence images from our experiments, together with representative activity traces.

In general, the binding of the indicators to the calcium ions is much faster than the unbinding, a feature that makes relatively easy to capture the onset time of firing, but *not* repeated activity events such as spike trains, as

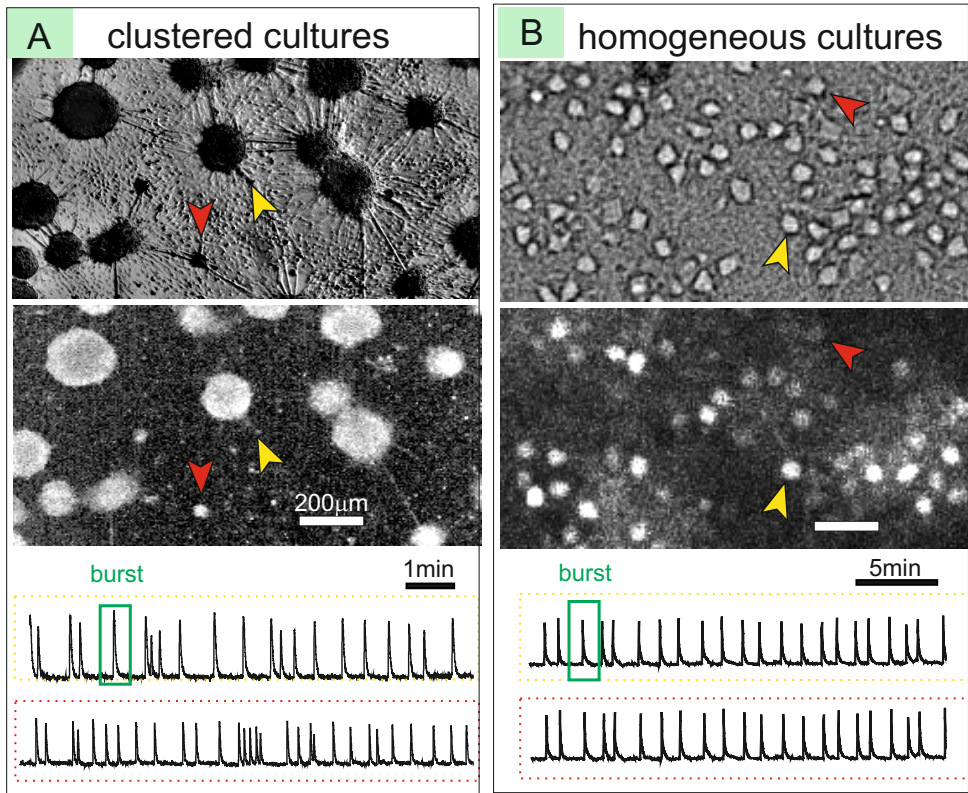


**Fig. 2.3 Calcium Imaging in our neuronal cultures.** **A**, Bright field image of a clustered culture (top), its corresponding calcium fluorescence signal (center), and two representative fluorescence traces (bottom) of the neuronal clusters marked with yellow and red arrows. **B**, Equivalent representation for a homogeneous neuronal network. Scale bars apply to all images.

illustrated in Figure 2.3. Then, by using a high speed camera, one can easily distinguish those onset times by detecting the sharp rise in the fluorescence signal.

### 2.3.2 Calcium Imaging versus MEAs

First, it is important to point out that there exist a number of techniques—in addition to calcium imaging—to detect neuronal firing. All techniques have their advantages and limitations, but the final choice for one or another

depends on the experimental system and the particular aspect that one is interested to explore. Here we briefly review the importance multi-electrode arrays (MEAs) as alternative approach to calcium imaging *in vitro*.

We must remark first that fluorescence calcium imaging allows the visualization of calcium dynamics in a relatively simple and straightforward manner, and subsequent data processing (e.g. to infer the onset of neuronal activity events) is relatively simple. However, the temporal resolution of this technique is limited by the calcium dynamics and the indicator kinetics, and typically falls in the 5 – 20 ms range. This rules out the fine detection of single spikes.

MEAs, on the contrary, allow for a much finer temporal resolution, and has been applied to both brain slices (Beggs and Plenz, 2003; Carmeli et al., 2013) and dissociated neurons (Bettencourt et al., 2007; Downes et al., 2012; Raichman and Ben-Jacob, 2008). A standard MEAs is constituted by 64 microelectrodes with  $30\mu\text{m}$  in diameter that are spatially arranged in a  $8\times 8$  grid with a typically spacing of  $200\mu\text{m}$ . This experimental system provides extracellular electrical signals (local field potentials, LFP) from single neurons or population of cells that have been plated on the microelectrodes substrate. The main advantage of this technology is its high temporal resolution, in the range 10 – 100  $\mu\text{s}$ , that allows for accurate spike detection. MEAs also offer long recordings, being ideal for monitoring network development. However, compared to Calcium Imaging, the major drawback of MEAs is its poor spatial resolution, which is limited by the number of recording electrodes. In addition, it is difficult to ensure that a single neuron is precisely located at the electrode. Indeed, several neurons often pack together and slightly far from the electrode; or crossing neurites attach to the electrodes. Hence, MEAs data requires strong data processing algorithms to unveil which neuron fired and where it was located, a difficult problem known as ‘spike sorting’ (see review (Lewicki, 1998)).

The relevance of MEAs in producing fine data has motivated the development of denser MEAs to overcome their poor spatial resolution. Two remarkable examples are the high-density MEAs (Ito et al., 2014), with 512 recording sites and that can access about 100 neurons simultaneously; and the multi-transistor arrays-based on complementary semiconductor–metal–oxide (CMOS) technology, with about 10.000 recording sites (Hierlemann et al., 2011). Nevertheless, these devices are not widely spread due to their difficult fabrication, high cost, demanding data storage and challenging analysis.

Calcium Imaging is not absent of difficulties. Experiments may be affected by both photo-damage, i.e. the damage of neuronal cells due to the fluorescence light; and photobleaching, i.e. the gradual alteration and degradation of the fluorescence probe to such a extent that it is unable to fluoresce. Both aspects can be minimized by running short experiments or using a weak light, but the quality of the measurements can be compromised. Additionally, chemical indicators require the incubation of the culture in the presence of the indicator and a solvent, typically DMSO, which deteriorates the health of the culture at long term and, effectively, limits its use to only one experiment. MEAs do not have these experimental limitations, making it very suitable for long recordings.

In our case, it is clear that MEAs could have been advantageous, in particular to monitor the development of the clustered cultures from an ensemble of independent neurons to the set of interconnected clusters. We could have also used GECI instead of Fluo-4 to circumvent the toxicity of DMSO. GECI are non-chemically invasive since, when binding to the calcium ions, the conformational changes that they experience result into actual fluorescence. GECI are typically incorporated into the cells through viral transduction shortly after plating. No further treatment is required, and cultures can be measured several times.

Our choice for chemical indicators was essentially economic and practical, since the newly formed Soriano's lab had very limited resources. Chemical

indicators are cheap, simple to manipulate, and do not require extremely sensitive optical systems to obtain good recordings. Additionally, Soriano's long expertise with these indicators ensured that we could obtain good quality data and results in a reasonable time, ultimately making this thesis possible. As we will see along this thesis, our measurements using these fluorescence markers provided very interesting results whose many open questions can be explored in the future using GECI or MEAs.

## 2.4 Experimental procedure

We here describe the experimental systems and the steps that we followed to carry out the different sets of experiments. In all experiments we measured spontaneous activity, i.e. the default dynamics that neuronal cultures exhibit. Spontaneous activity was typically measured at *day in vitro* (DIV) 5 – 16, i.e. covering about two weeks of development. Cultures started to degrade by DIV 25, and therefore we did not use cultures older than 3 weeks in our experiments. We performed typically two kinds of experiments, namely *standard experiments* and *resilience experiments*. Standard experiments consisted of recording the spontaneous activity of the clustered cultures without any kind of perturbation, while in resilience experiments we applied a physical or biochemical damage to prove the network resilience. Table 2.2 summarizes the procedures in these experiments.

Although most of the experiments were carried out in Soriano's laboratory, a number of specific experiments were carried at the nearby Institute for Photonic Sciences (ICFO, Castelldefels). The experimental systems used, as well as the goals of the research, were different in one or another facility, and are described in the following when required.

STANDARD EXPERIMENTS	Experimental Procedure	# expts	fps
E + I / E	20 min recording (E+I) 40 min recording with [bic]=40uM (E only)	35	100-83 (2MNC)
E	50-60 min recording with [bic]=40uM (E only)	25	100-83 (2MNC)
RESILIENCE EXPERIMENTS			
Physical Damage			
Physical Damage	20-30 min recording (E+I) 40 min recording after physical damage (E+I)	40	100-83 (2MNC)
Biochemical Damage			
CNQX Degradation	20 min recording with [bic]=40uM and [APV]=20uM 15 min recording with increasing [CNQX] (30, 60, 120, 300, 600, 1000, 2000 nM)	15	83 (2MNC)
Photodamage	3-4 h recording with high intensity light (E+I)	10	50 (4MNC)
Damaging chemical agents involved in Alzheimer Disease	20-30 min recording with [bic]=40uM 40 min recording after the application of the chemical agents	15	50 (4MNC)

**Table 2.2 Performed experiments** This Table classifies the kind of experiments and their respective procedures performed along this thesis. (2MNC indicates 2-MINICULTURES configuration; 4MNC indicates 4-MINICULTURES configuration.)

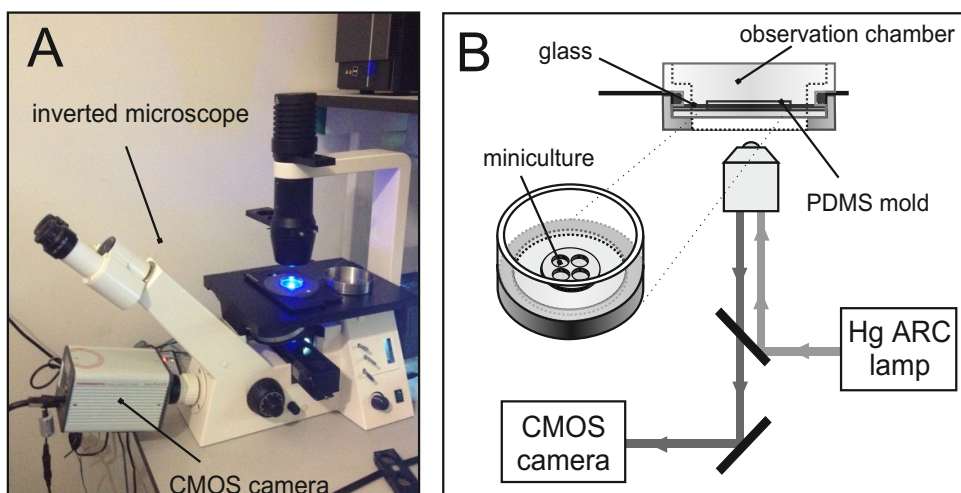


**Fig. 2.4 Experimental setup at Jordi Soriano's Lab.** **A**, Standard configuration used in most of the experiments, showing the inverted microscope and the attached CMOS camera. The culture to be studied sits in the center of the  $x-y$  stage and appears blue due to the excitation light for fluorescence. **B**, Detailed sketch of the experimental system. The observation chamber contains 4 minicultures and is filled with EM. An arc lamp excites the fluorescence with a wavelength of 485 nm (blue). Fluorescence light is emitted at 520 nm (green), which is captured by the camera.

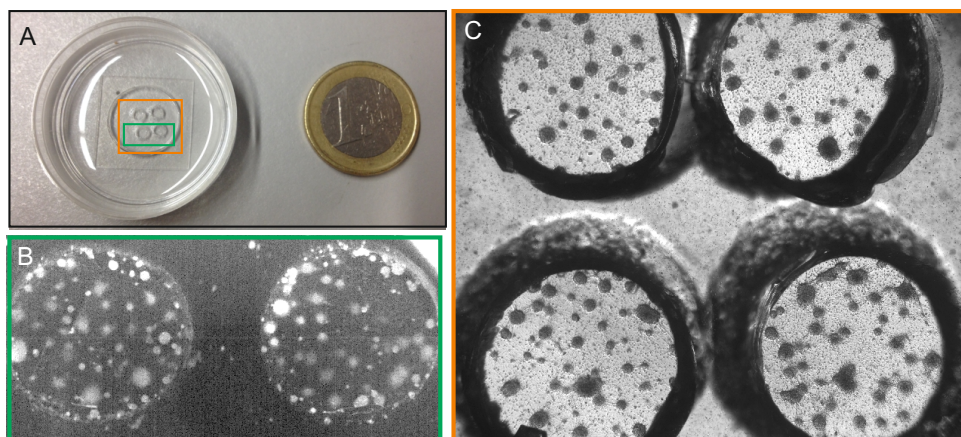
### 2.4.1 Experiments at Jordi Soriano's Lab

Figure 2.4 shows the optical system and the common procedures in Soriano's laboratory. Prior to recording, the glass coverslip containing the 4 minicultures within the PDMS cavities (Figure 2.5A) was transferred from the culture plate to a 30 mm diameter petri dish (Corning) that contained a pH-stable medium for the actual recordings (*external medium*, EM, see Table 2.1). The culture was then incubated in the presence of Fluo-4. The chemical indicator came as powder in stocks of 50  $\mu\text{g}$ , and was dissolved in DMSO (1  $\mu\text{l}$  of DMSO per  $\mu\text{g}$  of Fluo-4) prior use. We used 3  $\mu\text{l}$  of Fluo4 solution in a volume of 2 ml EM (1  $\mu\text{g}/\text{ml}$  of Fluo4 per ml of EM), which was gently spread across the culture using an orbital shaker (Termo-Fischer) at 40 rpm. After incubation, the culture was moved to an *observation chamber* filled with 4 ml EM, and consisting of a 30 mm diameter, special petri dish that contained at the bottom a circular crevice 14 mm in diameter and 500  $\mu\text{m}$  deep. The culture was placed in the crevice in such a way that rested at its walls, hence remaining stable for the subsequent recording. The chamber was finally moved to the microscope, and left 5 min in darkness for stabilization. The PDMS pierced mold was usually left in contact with the glass during both incubation and the actual experiment to minimize accidental damage to the aggregates during the manipulation of the cultures.

The observation chamber was mounted on Zeiss Axiovert inverted microscope coupled with a high speed CMOS camera (Hamamatsu Orca Flash 2.8), as illustrated in Figure 2.4. All experiments were carried out at 26°C using a thermostat (Scientifica). Depending on the objective of the experiment and ultimately in the number of minicultures simultaneously recorded, we used two optimized settings that are described below.

- 2-MINICULTURES

This configuration was typically used for recording at the highest camera speeds. To simultaneously visualize two minicultures in the field of



**Fig. 2.5 Observation chamber and imaging configurations.** **A**, Picture of the observation chamber compared to 1 euro coin. On the center one can observe the glass–PDMS mold structure showing the 4 cavities, each 3 mm in diameter. **B**, Fluorescence image of 2 clustered networks in the ‘2-MINICULTURES’ configuration. **C**, Bright filed image of 4 clustered networks using ‘4-MINICULTURES’ configuration.

view we used an objective of 2.5X in the microscope combined with a 0.32X optical zoom in the camera. By using this configuration we were able to record at 83 – 100 frames per second (fps), i.e. 12 – 10 ms between consecutive frames. These settings provided a field of view of  $7.6 \times 3.4$  (width x height)  $\text{mm}^2$ . We note that high camera acquisition rates required the reduction of pixel lines, and therefore high fps inevitable implied the access to only 2 minicultures. Each frame was acquired as 8-bit grey-scale images, a size of  $940 \times 400$  pixels, and a spatial resolution of  $8,51 \mu\text{m}/\text{pixel}$ . (Figure 2.5B). This configuration shaped those experiments where the precise onset time was very important for subsequent analysis. Concretely, we used these settings to carry out the *standard experiments* and some *resilience experiments*. This configuration was particularly appropriate for the *physical damage* experiments, allowing the simultaneous recording (with high temporal resolution) of the damaged culture and the control one one.

- 4-MINICULTURES

This configuration involved an objective of 2.5X combined with a 0.32X optical zoom with acquisition speeds in the range 45 – 50 fps (22 – 20 ms interval). These settings covered a field of view of  $8.2 \times 6.1$  mm<sup>2</sup> and allowed the simultaneous recording of 4 mini-cultures (Figure 2.5C). Individual frames were acquired as 8-bit grey-scale images, a size of  $960 \times 720$  pixels, and a spatial resolution of  $8.51 \mu\text{m}/\text{pixel}$ . This configuration was tailored for the majority of the *biochemical damage* experiments. Especially, in the experiments dedicated to study the damaging role of biochemical agents involved in Alzheimer's disease, this configuration was ideal since one cavity (i.e. a miniculture) was left as control while the others were dosed with specific chemical agents.

The settings in all these configurations were optimized to have a good balance between three main factors: image quality, sufficient time resolution, and minimum light intensity. The latter was particularly important to minimize photo-damage and photo-bleaching, allowing recordings of about 2 – 3 h with the neuronal culture in healthy conditions. However, we normally limited most of our experiments to about 1 h of recording since we had to balance also the duration of the experiments with the amount of data to store and process. The combination of high acquisition speeds, e.g. in the 83 – 100 fps range, and high resolution images (every single frame occupying about 0.5 MB) resulted in large data files of about 150 GB per hour. Data had to be saved in a solid state disk of 500 GB during acquisition and then transferred to other disks for analysis. The analysis itself required the conversion of the acquired image sequences from the specific Hamamatsu format to individual frames, which doubled the data in the hard drive. Hence, a single experiment recorded for 1h required a total of 300 GB, which would increase to 900 GB for a longer, 3 h recording for instance, totally beyond our possibilities.

Measurements in homogeneous cultures were carried out in the same way, with the only difference that the recording speed was increased to 100 – 150 fps to take into account the fast propagation of activity fronts in

these preparations, as observed for instance in the study of our partners in Ref. (Orlandi et al., 2013).

## 2.5 Pharmacology

We applied different drugs to the neuronal cultures depending on the study to be carried out, although in the majority of the cases we targeted excitatory and inhibitory connections. All the pharmacological protocols described here were used identically in clustered and homogeneous cultures. Table 2.3 summarizes the set of the basic neurotransmitter receptors present in our neuronal cultures, the antagonists used in our experiments, and their major action.

Neurotransmitter	Antagonist	Action
AMPA-glutamate	CNQX	Reduces excitation
NMDA	APV	Block non-glutamate excitation
GABA <sub>A</sub>	Biscuculline	Blocks inhibition

**Table 2.3** Basic neurotransmitter receptors present in neuronal cultures, their respective antagonists applied in our experiments, and their major action.

### 2.5.1 Blocking Inhibitory connections

Neuronal cultures encompass both excitatory and inhibitory connections, a connectivity blueprint that we refer as ‘E+I’. Neurotransmitters bind to chemical receptors at the post-synaptic neuron, exciting or inhibiting it depending on the excitatory or inhibitory nature of the receptors. In our experiments we typically left the excitatory NMDA<sup>1</sup> and AMPA<sup>2</sup> receptors active whereas the inhibitory GABA<sup>3</sup> receptors were blocked. We denote this latter group

<sup>1</sup>N-methyl-D-aspartate

<sup>2</sup> $\alpha$ -amino-3-hydroxy-5-methyl-4-isoxazolepropionic acid

<sup>3</sup> $\gamma$ -Aminobutyric acid

as ‘E-only’ connectivity blueprint. We performed the experiments in such excitation-only configuration for simplicity in analysis, since the inhibitory connections play a complex role within neuronal dynamics that it is still unknown.

For neuronal cultures above DIV 6 we applied 40  $\mu$ l of the antagonist bicuculline (Sigma) to block the inhibitory synapses. We left active inhibitory synapses for experiments with  $\text{DIV} < 6$  since at this early stages of development GABA has a depolarizing effect and therefore an excitatory action (Ganguly et al., 2001; Soriano et al., 2008; Tibau et al., 2013). At higher days *in vitro* a phenomenon known as ‘GABA switch’ occurs, and GABA takes its standard inhibitory role. As reference, in the cortex there are 80% excitatory neurons and 20% inhibitory ones (Soriano et al., 2008).

Once the drug was applied, we waited 5 min for the drug to take effect before starting the recordings.

### 2.5.2 Blocking Excitatory connections

In other experiments we studied the decay in spontaneous activity as a result of progressively weakening the neuronal network by blocking the NMDA and AMPA excitatory receptors. We first blocked NMDA receptors, which comprises about 20% of the excitatory receptors, with 20  $\mu$ M of the antagonist APV<sup>4</sup> (Sigma). Later on we gradually applied CNQX<sup>5</sup> (Sigma), an AMPA-glutamate receptor antagonists in excitatory neurons. For  $[\text{CNQX}] = 0$  the connectivity strength between neurons is maximum. As  $[\text{CNQX}]$  is administered, the efficacy of excitatory connections steadily diminishes, which is accompanied by a reduction in spontaneous activity. High CNQX concentrations lead to a complete halt in activity. In the measurements we used CNQX concentrations in the range 0 – 2000 nM, in quasi-logarithmic

---

<sup>4</sup>2-amino-5-phosphonovaleric acid

<sup>5</sup>6-cyano-7-nitroquinoxaline-2,3-dione

steps (see Table 2.2) . We left the culture unperturbed for 5 min after each CNQX application for the drug to dissolve and act on the neurons.

### 2.5.3 Chemical preparation for A $\beta$ and M-A $\beta$

The experiments of network affectation upon magnetite, amyloid- $\beta$  (A $\beta$ ) and magnetite-amyloid- $\beta$  complex (M-A $\beta$ ), oriented to study Alzheimer's disease *in vitro*, were carried out in collaboration with Prof. J. Samitier's group at IBEC. Their team prepared the chemicals (described next), while all the experiments were conducted in our laboratory.

The synthesis of magnetite-A $\beta$ 42 complex was carried out by mixing 12.5  $\mu$ mol iron (III) chloride hexahydrate (FeCl<sub>3</sub>-6H<sub>2</sub>O) (Sigma) and 6.25  $\mu$ mol Iron (II) chloride tetrahydrate (FeCl<sub>2</sub>-4H<sub>2</sub>O) (Sigma) in 10  $\mu$ l of DDW and added to 0.04  $\mu$ mol of lyophilized A $\beta$ 42. The pH was adjusted afterwards to physiological conditions with 2.6  $\mu$ l of 7.2 M ammonium hydroxide (Sigma). The solution was sonicated at 37°C for 30 min to minimize aggregation and self-fibrilization of the A $\beta$ 42 Dahlgren et al. (2002a); Sato et al. (2006). To remove side products from the magnetite-A $\beta$ 42 complex, the solution was washed with consecutive cleaning steps with 1 ml ethanol and 1 ml DDW. Between washing steps, unattached amyloid and other side products were separated from the magnetite-A $\beta$ 42 complex using a neodymium magnet. The sample was next mixed with 1 ml ethanol and centrifuged at 2400 rpm for 2 min. The liquid was next removed and the sample was kept redissolved in RS for its use in the experiments. The final concentrations were 12.5 mM for Fe<sup>3+</sup>, 6.25 mM for Fe<sup>2+</sup>, and 10  $\mu$ M for the A $\beta$ 42 peptide. These values are similar to the ones reported in brains of AD patients (Bishop and Robinson, 2003; Kuo et al., 1996).

## 2.6 Experiments at ICFO's Lab

By January 2012 we started a collaboration with the group of Pablo Loza at the Institute for Photonic Sciences in Castelldefels, Barcelona. The goal of the collaboration was to monitor the changes in spontaneous activity upon physical damage, and using state of the art optical tools. However, at the beginning of the collaboration we found important technical problems, most notably the lack of a sufficiently sensitive camera for the recording of activity, the lack of a dedicated computer for data acquisition and analysis, and the difficulties in building an adequate culture chamber for the cultures to be both monitored and damaged in a control manner. Initial experiments failed and the collaboration was put at hold for two years to address all technical aspects. Collaboration restarted by January 2014, and improvements included a redesign of the experimental setup; a new, highly sensitive Hamamatsu Orca Flash 4.0; a workstation; and an improved culture chamber with the requirements that we needed, and that allowed both the monitoring of activity for long time with neurons in healthy conditions and the possibility to act neatly on the culture. The experimental setup and procedure describe here corresponds to this final configuration. We note that all the process of the design and setup of the experimental systems was developed together between Soriano's and Loza's groups.

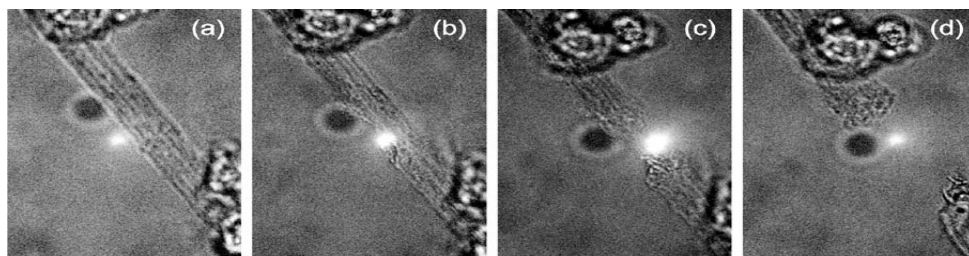


**Fig. 2.6 Removal of connections through laser ablation.** From left to right, different stages of the operation to remove the bundle of connections between two clusters. The bright spot is the laser beam. The entire procedure needs about 5 min.

As we said, the main objective of these experiments was to physically damage a neuronal culture to study the changes in spontaneous dynamics after the physical attack. Although we initially considered as target the cutting of connections between clusters of neurons, we experienced important difficulties. First, the connections between clusters were not well defined in most of the cases, with bundle of axons spreading everywhere or highly tangled. This made difficult to ensure the full disconnection of two clusters after the destruction of links (see Figure 2.6). And secondly, the physical connectivity could be more complex than the one would initially assess by visual inspection, e.g. connections could cross more than one cluster. Conversely, to silence a given cluster is much easier for two reasons. First, they are very clear morphologically (they appear as well defined spheres); and second one can immediately ensure that they have become silent after damage since they will be strongly bright in fluorescence and inactive.

### **Culture Preparation**

In all the experiments at ICFO we used clustered cultures following the identical culture preparation as described in Section 2.1. We performed all the culture preparation in Soriano's lab. Normally, about 14 PDMS-glass combined structures were prepared, containing each 4 minicultures with a diameter of 3 mm. By DIV 7 – 14 the best neuronal cultures were transported from Soriano's lab to ICFO in a portable incubator with appropriate physiological conditions to maintain them healthy during the trip, which lasted about 30 min. At ICFO, neuronal cultures were immediately moved into an incubator with identical settings as ours.

### **Experimental Setup**

We used again the Calcium Imaging approach to monitor the spontaneous activity of clustered cultures. In this case, the fluorescence signal was detected using a multimodal microscope (developed by ICFO itself) coupled with a

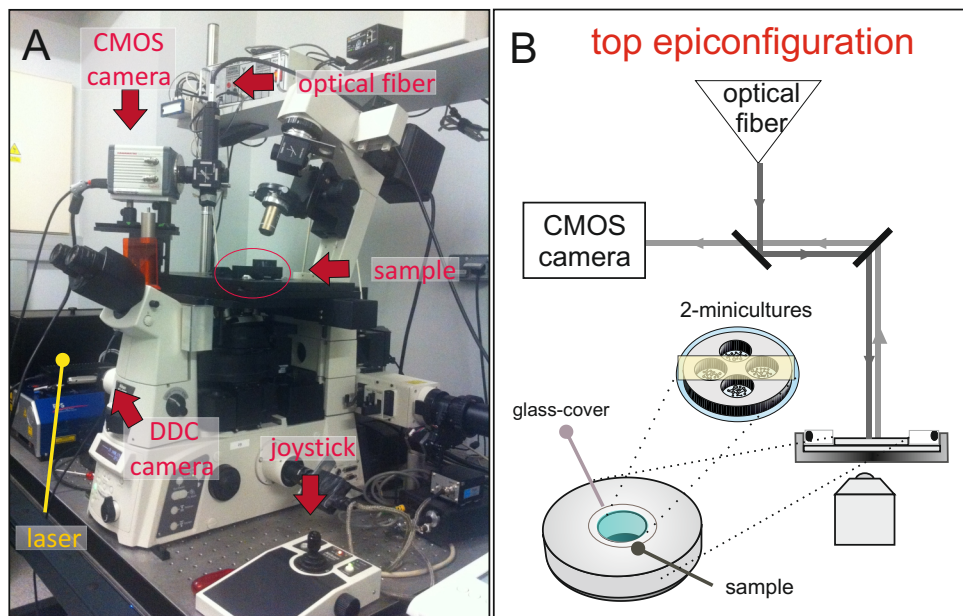


**Fig. 2.7 Experimental setup at ICFO's Lab.** **A**, Multimodal microscope at ICFO's lab, highlighting its main components. **B**, Detailed sketch of the 'top epi onfiguration', suited for spontaneous activity fluorescence recordings in 2 minicultures (yellow band). The observation chamber is closed and sealed with a glass cover to prevent medium evaporation.

high speed CMOS camera (Hamamatsu Orca Flash 4, USB3 mode) providing high quantum efficiency of collection and large field of view (see Figure 2.7). The multimodal microscope is an extension of a confocal microscope (Nikon C1) that allows two-photon fluorescence, and nonlinear photoablation allowing accurate nano-surgery by optical manipulation and stimulation. To carry out the experiments, we set the microscope in three different configurations that we called 'top EPI configuration', 'bottom EPI configuration', and 'laser configuration'.

- 'Top EPI configuration'. The multimodal microscope was modified to implement an epifluorescence microscope in an upright configuration. Mercury lamp (Nikon ND16) lamp was used guided by a liquid optical fiber into the EPI-illumination port. The fluorescence filter set was a dichroic mirror (FF 509 FDI) with a green filter and a blue bandpass filter

(HQ470/40X). We used the top EPI configuration to record spontaneous activity through calcium fluorescence imaging of 2-minicultures. The frames were imaged with  $254 \times 534$  pixels ( $3.5 \times 6.5$  mm<sup>2</sup>), at 16 bits grey levels, allowing recordings at 83-100 fps acquisition.

- 'Bottom transmission configuration'. The mercury lamps were used as the upright bright field transmission lamp in the 'bottom transmission configuration'. The optical fiber was moved from the top port for the 'top EPI configuration' to the standard EPI port for the 'bottom transmission configuration'. In this case, we selected the TRITC filter (green light). This configuration was used to acquire bright field images of the 4 minicultures, which provided an evaluation of the clusters or connections to be cut using the upright path.
- 'Laser configuration'. The uniqueness of this setup lays in the use of a Ti-sapphire laser (Mira Optima 900-F, Coherent) either to ablate some connections between clusters or damage the clusters themselves. That laser is an infrared 'ultra short pulsed' (in the order of the fs) with 400mW enabled for ablation (more details in the 'Laser adapted for ablation' section). In the 'laser configuration' we used a water immersion objective of 25x (Olympus) with 1.05 NA (Numerical Aperture).

## Experimental Procedure

The experimental procedure in these experiments was similar to the one previously described in Section 2.4, with only a modification in the observation chamber. Thus, a combined PDMS-glass structure containing 4 minicultures was selected and placed in a petri dish containing 1.5 ml of EM with  $2\mu\text{l}$  of Fluo4. After 25 min of incubation, the medium in the system was switched to 2 ml of fresh EM, and finally placed into the ICFO-dedicated observation chamber (see Figure 2.7).

The observation chamber was built at the machine shop of the University of Barcelona, following our design and guidelines (Figure 2.8). Different configurations were tested until we achieved the most suitable one for our experiments. The final one that we used was formed by two elements. The top one was manufactured in Teflon and contained a wide circular aperture in its center, creating a cylindrical hole 15 mm in diameter and 5 mm deep. The bottom one was a stainless steel structure that incorporated a 5 mm deep cavity with a diameter of 15 mm except just at its basis, which was designed as a 100  $\mu\text{m}$  thick crevice with an opening of 11 mm in diameter. Such a design provided a ring of 3 mm in diameter where the culture sits, and accompanied of a silicone ring to seal the chamber (Figure 2.8).

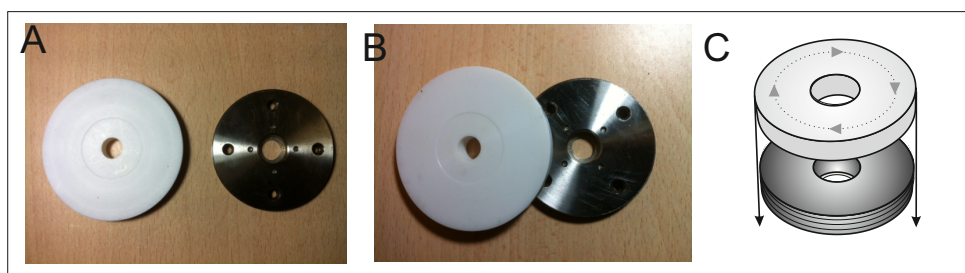


**Fig. 2.8 Observation chamber at ICFO's Lab. (A-B)** Pictures of the device, showing the Teflon part and the stainless steel one. **C**, Final configuration. The culture is placed at the bottom of the stainless steel structure and over a silicone ring. The device is then screwed to the Teflon part, the central cavity filled with EM, and the top opening sealed with a glass coverslip to prevent evaporation.

The glass with the PDMS was carefully placed over the silicone ring, the whole metal structure rapidly screwed with the Teflon part, and finally the chamber filled with 2 ml of EM. During the whole process we took special care to maintain the culture always in contact with EM. Finally, we covered the top hole with a glass coverslip 30 mm in diameter to prevent medium evaporation.

Prior recording, the observation chamber was transferred to the microscope and left in darkness for 5 minutes for stabilization. Then, we changed

the microscope to the 'bottom EPI configuration' to capture a high resolution, bright field snapshot of the 4 minicultures. The optical system was next changed to prepare the 'top EPI configuration' that permitted to excite the sample with fluorescence light. In this step, we selected the 2 most active minicultures. We then adjusted the settings in the camera to image only 2 minicultures. One of the minicultures was left as control and the other was the targeted one.

The next steps in the experiment depended on the special role of the targeted cluster. We considered 3 distinct actions.

1. **RANDOM ATTACK.** We recorded spontaneous activity along 20 – 30 min in the 2 minicultures before destroying a neuronal cluster randomly chosen.
2. **INITIATOR ATTACK.** In these experiments we were interested to attack the cluster that most frequently initiated activity. To proceed, we recorded in two blocks. First, during 10 – 15 min and immediately after for another 15 – 10 min. During the second recording, we swiftly analyzed the first one to rapidly identify which was the cluster that more frequently initiated the spontaneous activity.
3. **HUB ATTACK.** In a similar manner we recorded in two blocks, 10 – 15 min each, and identified the clusters with a special connectivity feature that we call 'hub'. Then, again, during the second second measurement we analyzed the initial data to identify the cluster to be targeted.

The third step of the experimental procedure consisted in destroying with the laser the chosen cluster. In order to do that we changed the configuration of the microscope to the 'laser configuration'. In this part, while maintaining the laser blocked, we located visually the target cluster and moved the stage (x-y plane) and the z-plane until it is correctly focused. At this high magnification, this step sometimes became complicated since the image seen in the ocular

were inverted and rotated. We often needed to open the previously taken bright field image to invert and rotate it, facilitating the search throughout the culture for the target cluster. Once it located and on focus, we switched from the ocular to a second camera. This camera was a DCC 1545M (Thor Labs) coupled to the microscope and was used to observe the target cluster together with the laser (as a point in the screen). Then, with the assistance of a joystick, the laser was finely positioned in the  $x - y$  plane and  $z$  axis, and the entire cluster gradually damaged. In order to compensate the chromatic aberration of the objective, it was necessary to move the laser along the  $z$  axis, to focus the laser in the sample plane ensuring full damage. We typically needed about 10 min to complete the task.

Finally, we reconfigured the setup in the same manner as in the second step ('top EPI configuration') and then both the damaged culture and the control one were recorded for additional 30 – 40 min. All experiments were carried out at room temperature (20°C).

### **Laser adapted for ablation**

The multiphoton microscope is used as ablation system. Basically, the laser beam size is adapted to fit the steering galvanometric mirrors and then magnified to overfill slightly the pupil of the 25x objective. A variable attenuator controls the necessary power to switch between the imaging and the ablation modes. The typical power in a two photon microscope is about 30-70mW, whereas for ablation is used up to 700mW. The percentage of light transmittance depends on the wavelength and the objectives used but it is typically in the range of 35-40%. In that sense, when the measured power was about 600 mW the actual power in the sample plane was about 200mW. Between the attenuators there was a shutter that allows the control of the exposure time of the laser.

The advantages of using ultra short pulsed lasers is the significant light intensity per time that provide per pulse. High irradiance ( $10^8 W/mm^2$ ) in

the focal volume produces local ablation and the apparition of plasma. The infrared wavelength (800nm) provides high tissue penetration. The ultrashort pulses reduces the energy on the sample in the order of nanojoules that minimizes collateral damages and presents lower dependency with the material absorption coefficient helping to a deeper penetration into the sample.



# Chapter 3

## Analysis tools and Methods

Once described the experimental preparation and procedure in the previous chapter, we here focus on characterizing the neuronal dynamics of these clustered networks. They generally present a *modular* dynamics in which group of clusters are activated in a sequential manner. This behavior contrasts with the one observed in more standard neuronal networks where neurons cover uniformly the substrate, and whose dynamics is characterized by the activation of all the neurons in a short time window (*bursting*).

In the present chapter we describe the algorithms to convert the raw fluorescence images to time series of cluster's activity, which are subsequently processed to obtain the ignition times of each neuronal cluster. We then describe our methodology to construct the functional connectivity of the network and the mathematical resources to characterize its topological features. Finally, we describe the tools to identify those group of clusters that shape the dynamical modules (or *communities*) in the network, i.e. groups of clusters that frequently fire together.

All these analysis tools shape the core resources to analyze and characterize the most prominent dynamics features of these self-organizing systems.

## 3.1 Data analysis

The spontaneous activity of our neuronal cultures was monitored using fluorescence calcium imaging, a technique that reveals neuronal firing events as a sharp rise in the fluorescence signal, i.e. a sudden increase in the clusters' brightness during recording. The collected fluorescence images were the raw information from which individual clusters' fluorescence traces were computed and, finally, their train of firing episodes determined.

### 3.1.1 From fluorescence signal to data

To better understand the process of obtaining the fluorescence time series, we first describe the methodology used in more standard homogeneous networks, as illustrated in Figure 3.1. We note that although our research primarily focused on the clustered networks, we often compared the dynamic behavior of homogeneous and clustered ones, and therefore it is important to describe the analysis tools in both systems.

The original recordings of fluorescence signal were first converted into individual frames using the Hokawo 2.5 software (provided by the camera vendor, Hamamatsu). As seen in Fig. 3.1A-C, single neurons were manually identified and selected as *Regions of Interest* (ROIs) over the images to, later, simply evaluate the gray intensity in the region along the entire collection of frames using Matlab or C++ libraries. These libraries were part of the resources already in use in Soriano's lab. Each ROI covered an area of typically  $10 \times 10 \mu\text{m}$ , i.e. a single neuron. In the culture of Fig. 3.1A, about 3000 neurons were monitored. A typical experiments contained on the order of a hundred thousand images, and therefore the process of scanning all neurons to evaluate their gray level, and extend it to all the images, required about 4 hours.

An example of the obtained individual neuronal traces is shown in Fig. 3.1D. This basic dataset was named *raw fluorescence signal* and was characterized

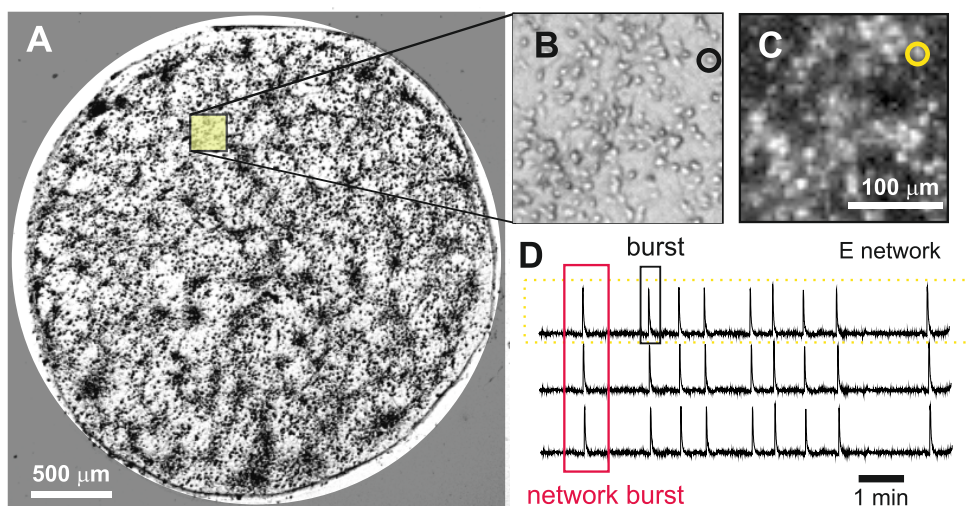


**Fig. 3.1 From fluorescence signal to data in homogeneous cultures.** **A**, Highly contrasted bright field image of a homogeneous culture (miniculture) 3 mm in diameter and containing  $\simeq 3000$  neurons. Black spots are neurons. **B**, Zoom into of a small region. The black circle marks an individual neuron. **C**, The same region in fluorescence. Bright spots are firing neurons. The yellow circle depicts the same neuron is an bright field, and that would correspond to a Region of Interest (ROI). **D**, Representative fluorescence traces from three ROIs. The black box marks a single burst (train of spikes), whereas the bigger pink box highlights a network burst, i.e the collective activation of the neurons in the network.

by a noisy baseline interrupted by sharp increases that corresponded to a fast train of spikes termed *burst*. Upon activation, fluorescence rose and peaked in about 10 ms, to slowly decay back to the baseline in few seconds. As can be seen in the example of Fig. 3.1D, neurons in this homogeneous preparation spontaneously activated together in a short time window, an event known as *network burst*.

The raw fluorescence signal,  $\tilde{F}$ , contained artifacts. The typical (though not common) artifact was a small yet steady increase of the fluorescence baseline due to photo-bleaching or neuronal deterioration. This artifact was abundant in the first experiments in our laboratory, but it was gradually reduced and minimized by recording the experiments with highly attenuated light and by shortening the experiments as much as possible. This artifact was

corrected by detrending the signal, i.e. by fitting a straight line to the baseline and subtracting it from the data. The detrended signal was then normalized as  $F(t) \equiv \Delta\tilde{F}/F_0 = (\tilde{F} - F_0)/F_0$ , with  $F_0$  the baseline fluorescence level, to remove the background brightness of the neurons.

This procedure was identical for the clustered networks, with the difference that the number of ROIs was on the order of 40. An example of data analysis for the clustered networks is provided later.

### 3.1.2 Determination of ignition firing times

The detection of firing events in neuronal networks from fluorescence recordings is a task that is routinely applied by many research groups. In our group in particular, the work of Orlandi *et al.* (Orlandi et al., 2013) —focused on the problem of understanding the generation of spontaneous activity in homogeneous neuronal cultures— already provided a series of analysis tools that have served as basis for analyzing the experiments with clusters. In that work, a custom-made software was developed in order to detect the precise onset times of neuronal firings, and used the data to determine the propagation velocity of activity fronts. Although we developed our own analysis algorithms for this thesis, the methodology used in that work, and that is briefly described next, was used as a benchmark to create our algorithm as well as to crosscheck the reliability in resolving the clusters' ignition times.

#### Ignition firing times in homogeneous cultures

The determination of the neurons' ignition times was carried out by using the sub-frame resolution method described in (Orlandi et al., 2013). In this method, each bursting episode of a neuron was first coarsely detected by identifying those data points in the fluorescence signal whose derivative and amplitude are above a given threshold. Then, as illustrated in Figure 3.2A, the finer analysis consisted of carrying out two linear fits on the data, one

comprising the data points preceding the detected burst, and another one encompassing the points during the fast rise in fluorescence. The crossing point of the two lines provided the onset time of neuronal activation. This process was next extended to all neurons (Figure 3.2A). Since the position of the ROIs was known, the analysis of the onset times unveiled the spatio-temporal features of the network bursts. For the particular case of the experiments in Ref. (Orlandi et al., 2013), it was observed that activity traveled in the form of a circular wave at about 20 mm/s (Figure 3.2).

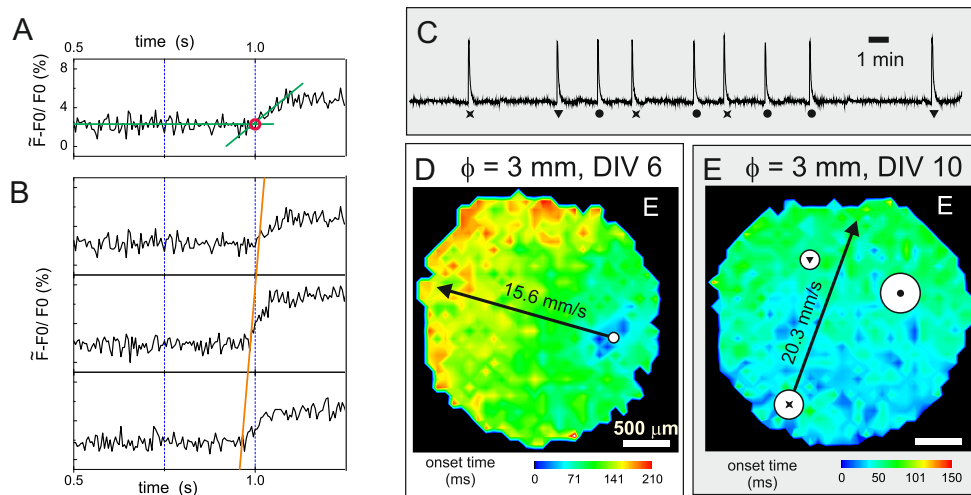


**Fig. 3.2 Determination of ignition firing times and wave propagation in homogeneous cultures.** **A**, Example of a fluorescence signal of an individual neuron. The red circle marks the ignition time detected applying the subframe resolution method, i.e. the crossing point of linear fits before firing and during the high rise in fluorescence. **B**, Fluorescence traces of three neurons. The thick blue line connects the measured onset times, and illustrates the delay between neurons' activations. **C**, Fluorescence signal averaged over 500 neurons, where peaks correspond to network bursts. The symbols below each network burst identify its initiation in a specific area over the culture. **D-E**, Example of the propagation of a spontaneous network burst in a homogeneous minicultures 3 mm in diameter, 'E-only' conditions, and at different developmental stages. The analysis of the onset times of neuronal firing provides the average velocity and the initiation point of the front (white circles). The fronts advance as a circular wave at about 20 mm/s. **E**, Another example highlighting the initiation points of the bursts shown in **C**. For clarity, nearby initiations are grouped defining the nucleation sites. Three main initiation sites are identified. The size of the circles is proportional to the relative occurrence of nucleation events at each site.

### Ignition firing times method in clustered cultures

Clustered networks presented bursting events that were different in comparison to the typical homogeneous bursts, specifically a much higher firing amplitude given the large number of neurons in the clusters. Such a characteristic greatly facilitated the analysis, and we developed our own algorithm but following some of the guidelines used in the previous approach. First of all, the raw fluorescence signal  $\tilde{F}$  was detrended and next smoothed out using a moving average window 500 ms wide. The fluorescence baseline  $F_0$  was then evaluated by discarding the data points with an amplitude two times above the SD of the signal. Fluorescence signal normalization was finally carried out to obtain  $F(t)$ . The onset times were calculated as those points of the fluorescence signal that were 2 SD above the baseline and avoiding to take two consecutive bursts within a narrow time window of 300 ms. Moreover, those detected points that does not show a slower decay of a minimum 50ms wide were also excluded (an example of the procedure is shown in Figure 3.3).

#### 3.1.3 Reliability in detecting the clusters' ignition times

Three major tests were carried out to assess the reliability of our experimental procedure and detection algorithm. In a first one, we measured spontaneous activity at 200 fps, i.e. twice the standard recording speed, but used stronger light to compensate for the lower exposure time. We next analyzed the data, re-sampled the image sequence down to 100 fps and compared the results with the original acquisition. We observed that the accuracy in resolving the onset times at 200 fps improved only by about 15% as compared to 100 fps, which did not justify the excess of light and the associated damage to the neurons.

In a second test, we measured spontaneous activity in a culture using identical light settings but considering different acquisition rates, namely 100, 150, and 200 fps. We then selected trains of clusters' activations that were

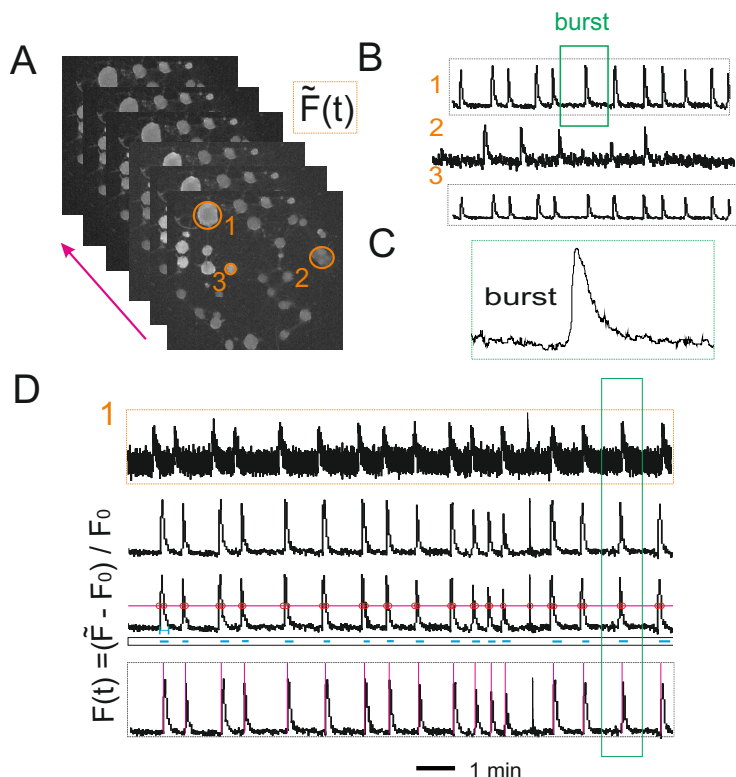


**Fig. 3.3 Fluorescence signal analysis and determination of onset times in clustered neuronal cultures.** **A**, Sketch illustrating the conversion of the recording into individual frames using the Hokawo 2.5 software. Orange circles depict three distinct ROIs that correspond to single neuronal clusters. **B**, Fluorescence traces of the three ROIs. Cluster #1 and #2 display a similar activity, while cluster #3 only fires concurrently with the other in a small number of occasions. This behavior is characteristic of modular dynamics. The green box encompasses a cluster's burst. **C**, Detail of the marked burst. **D**, Data analysis work flow. The first, top panel, highlighted in an orange contour, is smoothed with the moving average method using a window of 500 ms (second panel). The signal is then detrended and normalized as  $F(t) \equiv \Delta\tilde{F}/F_0 = (\tilde{F} - F_0)/F_0$ , with  $F_0$  the fluorescence at rest. The detected bursts (third panel) fulfill the following three requirements: (a) the peaks are superior to 2SD of the mean fluorescence signal (red line); (b) nearby wrong detections are avoided by considering a window of 300 ms below which another firing is not accepted; and (c) the width of the burst have to be at least 500 ms (blue boxes) to prevent camera errors to be taken as bursts. The correct final onset time detections are marked as pink lines (fourth panel).

as similar as possible in all three measurements, and compared the results. We observed that only in the few cases where the clusters fired with strong amplitudes the increased speed enhanced detection, and again by 15%. For the rest of the cases, the higher speeds actually worsened the analysis due to the poorer signal-to-noise ratio. We concluded that the balance between acquisition speed, good signal-to-noise ratio and healthy neurons imposed severe constraints in our experimental procedure, as illustrated in Figure 3.4. Hence, most of the experiments were limited to 1 h acquisition at 83 fps with the minimum light exposure.

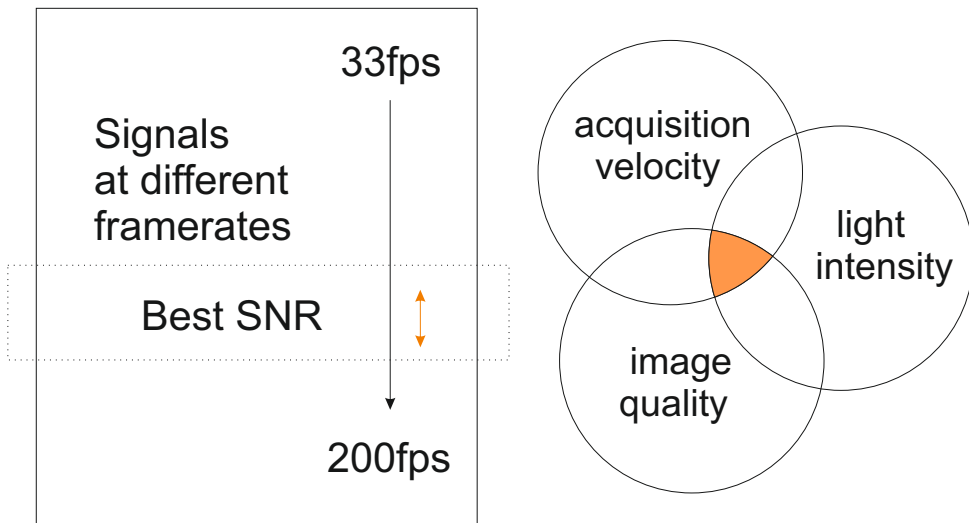


**Fig. 3.4 Experimental constraints.** **A**, Fluorescence traces at three different frame rates and identical camera settings. The optimum condition that satisfies good detection of onset times and good signal are in the range 83 – 100 fps. **B**, Sketch illustrating the need for balancing high frame rates, low light intensity and good image quality, altogether showing the very small flexibility in tuning our experiments.

Finally, in a third test, we used the sub-frame resolution analysis introduced above to evaluate the importance of finer ignition time values. Two straight lines were fitted at the vicinity of each initially detected cluster's firing event. A first fit included the 100 points of the background signal that preceded ignition, and a second one extended to the 10 points that correspond

to the fast rise in fluorescence. The crossing value of the two lines provided an onset time that refined the initially measured value. The better accuracy increased the discrimination of co-activations that were initially identified as simultaneous (which were actually rare, by 5%), but overall the additional effort did not provide a significant difference in the identification of the ignition times of clusters' activation.

## 3.2 Firing sequences

Homogeneous cultures display a nearly periodic episodes of collective neuronal firing known as *network bursts*. As we have outlined before, these network bursts are actually activity fronts that initiate in specific regions of the network and propagate as a circular wave throughout the entire neuronal network (Orlandi et al., 2013).

Clustered networks behave very differently. Indeed, events that one could initially associate as *network bursts* actually corresponded to concatenated activations of a fractions of the total number clusters. For this reason, and to avoid confusion, we call *firing sequences* to these collective activation events. As sketched in Fig. 3.5, these firing sequences involved a small group of clusters that were activated sequentially in a short time window, and with a pattern of activation that could often repeat along the entire recording. However, one could also observe interesting variations, in both the number of participating clusters and the timing within them, that made the problem highly fascinating. The adequate identification and treatment of these sequences is crucial for identifying the two key features of the networks, namely the characteristic dynamical modules and the functional connectivity map.

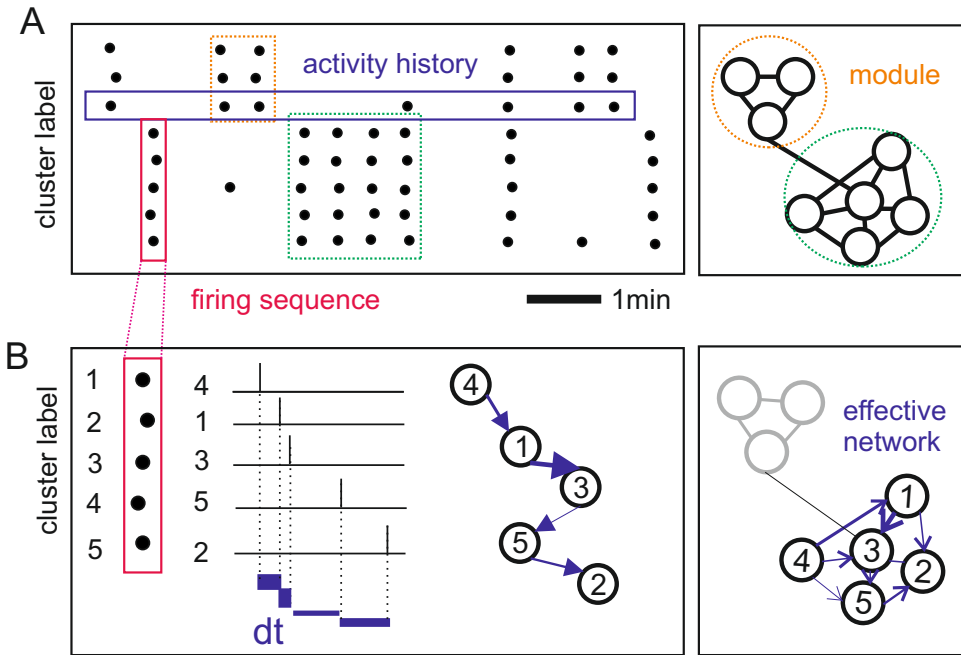


**Fig. 3.5 Conceptual representation of Functional Organization.** **A**, The left panel shows a typical raster plot, where every dot marks the firing events of each cluster. Rows of the raster plot (blue outline) represent the activity history of every cluster, i.e. the temporal structure of their firing events. Columns in the raster plot (pink outline) define the firing sequences, i.e. the downstream clusters' activations. The right panel sketches the group of clusters that frequently fire together (green and orange dashed boxes), i.e. share similar activity histories, and thus shape characteristic modules. **B**, The left panel details a firing sequence, formed by five clusters that have fired together in a narrow time window. After ordering the sequence as a function of time, the effective network (a directed and weighted graph) is built by weighting the links according to the time delays in activation. The smaller  $dt$  (blue bands), the higher the weight of the links in the network (arrows). The right panel shows the concept of functional organization, picturing both links between clusters and their presence into a given module.

### 3.2.1 Firing sequences' identification

The identification of firing sequences can become a difficult task since different groups of clusters get activated at different times. Hence, two or more groups could be treated as a single one if the time window for a firing sequence to occur was arbitrarily large. Hence, to prevent such a problem, we

used a cut-off of 200 ms, and assumed that two clusters that had fired above this value were not influenced by one another. This cut-off was determined from measuring the time delay between clusters' consecutive activations,  $t_p$ , in control experiments recorded at high acquisition rates (200 fps or higher). We observed that  $t_p$  varied in the range  $10 \lesssim t_p \lesssim 100$  ms, and took as cut-off two times the maximum time delay. Other studies in clustered networks provided similar results (Tsai and Chang, 2008; Yvon et al., 2005). Interestingly, these times are fairly large compared to the eventual scale of signal integration-propagation between single neurons (on the order of few ms), and therefore the observed delay times are related with the integration time of the intra-clusters information processing.

On the other hand, we must note that for homogeneous cultures the typical time delay between single neurons during the activity wave propagation (as shown for instance in Figure 3.2D-E) is around 5 ms, a value that is in agreement with other studies (Mason et al., 1991; Swadlow, 1994). Hence, when analyzing the topological traits of homogeneous cultures as compared with clustered ones, we used two times this value, 10ms, as a cut-off to identify the corresponding sequences, i.e. network bursts.

### 3.3 Community detection

Groups of clusters that repeatedly participate in the same firing sequences share the same *history*, i.e. they shape persistent, coherent activations that we call dynamical modules or communities (Figure 3.5). The dynamics of the clustered network was complex, shaping groups of active clusters that varied in size, from two units to the entire network.

Two steps were considered to properly assess the neuronal clusters that formed the characteristic communities. First, we performed the hierarchical clustering algorithm (Fortunato, 2010; Kaufman and Rousseeuw, 2009) to group together those clusters with high similarity in their activity history.

Next, we applied a threshold using Variation of Information (Karrer et al., 2007; Meilă, 2003) to establish the most representative communities in the network.

We must note that several community detection methods have been proposed in order to find the characteristic communities in a network (as reviewed in Refs. (Fortunato, 2010; Newman, 2012)). These methods can consider spectral properties of matrices, information-theoretic measures, random walks, and many other approaches. Hence, the community concept (also known as *module* or *cluster* in the literature) does not have a unique and well established definition. For instance, one can talk about dynamical modules or topological modules (as we will see later) and indeed the meaning of what these modules represent, their calculation, and ultimately the units that integrate them (in our case neuronal clusters) may be completely different in both cases. Thus, each algorithm is good at finding communities according to its own definition, and with the objective to fulfill necessary requirements or to fit specific problems.

For instance, well known strategies to data clustering based on principal component analysis (PCA) or independent component analysis (ICA) are difficult to implement in our study. They are indeed multidimensional scaling approaches that work properly when the variables present a strong statistical independence among them. Additionally, the hierarchy of modules that present our neuronal clusters gives rise to complex dependencies, both within and between modules, that makes difficult to correctly classify them with this kind of algorithms. Other methodologies need ‘a priori’ the number of modules to address them, as occurs with the K-mean algorithm (Kanungo et al., 2002), and therefore we could not use such a construction since we did not know them in advance.

### **Agglomerative hierarchical clustering**

Hierarchical clustering encompasses an entire family of techniques that aim at discovering the most natural group division. This algorithm is easily applied

to a network where very little is known about its organizational community structure (Fortunato, 2010). This methodology is agglomerative in the sense that it begins from single elements (clusters in our case) that are iteratively merged into composites, i.e. *groups* of clusters, depending on their similarity until all the elements (the whole network) is grouped as a unique family. We note that such a construction is a bottom–up evaluation.

The starting point of any hierarchical method is the definition of a matrix that shows the distances or similarities between pairwise variables. Once this distance matrix is set, the agglomerative clustering begins, joining in each step the two closest elements (or composites) with the smallest distance or high similarity. For instance, if we imagine that two elements A and B are the most similar, then they would be the first to be grouped. Later, that conjoined elements A and B would be removed from the total set of variables N, and the process would be repeated by replacing them for a composite AB that would represent them. The distances between this composite AB and all other remaining variables (N-1) would be then computed. The algorithm again would search the next most similar pairwise association that could correspond in that example to two new elements or the composite AB with a new element. In that way, the process would be repeated until just only one element remains. The order of the grouping formation is important and can be nicely represented as a hierarchical tree or dendrogram, whose depths indicate the steps at which these objects have been combined.

Hierarchical clustering methods differ between them depending on the particular measure of similarity used, and on the rules set to group similar elements (linkage criterion). There are indeed a variety of metrics (e.g. Euclidean distance, cosine similarity, or Jaccard distance) to calculate the distance matrix, and there also exists different linkage methods to evaluate the ‘smallest’ distance (or ‘highest’ similarity) between the objects (e.g. single linkage, complete linkage, or average linkage). However, we observed

that selecting one method or another did not change the final community arrangement, as we will see in the Results chapter.

### 3.3.1 Applying hierarchical clustering to find the dynamical modules

The hierarchical clustering method was applied to organize the neuronal clusters that have fired in a similar way along time, i.e. they share similar activity histories, to later differentiate the characteristic communities or dynamical modules applying a threshold. An overview of the methodology is illustrated in Figure 3.6. To proceed, we carried out the following steps. First, a coactivation matrix  $X$  containing  $N \times M$  elements was initially considered, where  $N$  accounted for the number of variables (neuronal clusters) and  $M$  for the number of distinct observations (firing sequences). Once all the sequences in a given measurement were established, the elements were set to  $X_{ij} = 1$  if cluster  $i$  had participated in the sequence  $j$ , and  $X_{ij} = 0$  otherwise. At the end of the construction, the rows of the matrix  $X$  (with length  $M$ ) reflected the activity history of a given cluster. A silent cluster contained all the elements of its row equal to zero.

Jaccard metrics (Karrer et al., 2007; Kaufman and Rousseeuw, 2009) was next used to calculate the pairwise similarity between the activity history of the clusters in the network. If  $A$  and  $B$  are any two rows of the matrix  $X$ , the *Jaccard similarity*  $J(A, B)$  provides a score that indicates the similarity in the history of  $A$  and  $B$ .

$$J(A, B) = \frac{|A \cap B|}{|A \cup B|} \quad (3.1)$$

In the sense used in this study, the Jaccard similarity calculates the number of concurrent activations in the two clusters respect to all the occurrences where at least one of the clusters had fired [see Equation (3.1)]. If  $A$  and  $B$  had

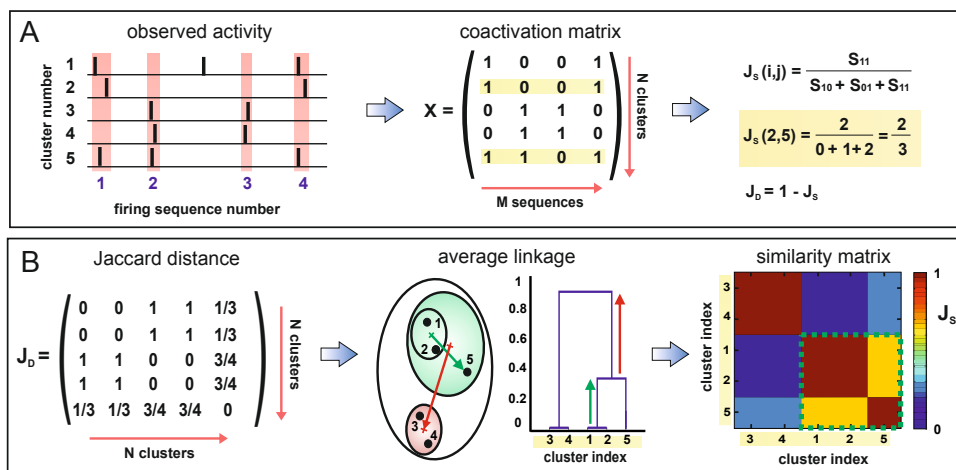


**Fig. 3.6 Communities' analysis methodology.** **A**, Schematic representation of spontaneous activity traces for 5 clusters. All those clusters that fire concurrently in a short time window define a sequence (pink bars). Clusters that fire independently are discarded. Sequences shape the  $X$  matrix, where each column corresponds to a sequence, and each row represents the activity history of a cluster. Two or more clusters that share a similar history are more likely bound and would constitute a community. The degree of similarity between all pairs of clusters ( $i, j$ ) is established through the Jaccard's similarity measure  $J(i, j)$ , from which the Jaccard's matrix distance  $D = 1 - J_s$  is determined. Clusters #1 and #2 are identical in history and provide  $J(1, 2) = 1$ , but both are also similar to #5 (yellow bands), with  $J(1, 5) = J_s(2, 5) = 2/3$ . **B**,  $J$  is a symmetric matrix that reflects the relative closeness of all pairs of clusters, which can be sketched as spatial groups or in the form of a dendrogram. Clusters #3 and #4 have identical histories and form a unique community. Clusters #1 and #2 also shape a community, but they are sufficiently close to cluster #5 to constitute together a higher, more representative group. The number of communities is formally set by selecting a threshold in the dendrogram. Any threshold along the red arrow would maintain two communities. Once a threshold is set, the similarity matrix is ordered to visually highlight the communities in the network.

no common activations (i.e.  $A$  and  $B$  have all elements as 0), then  $J(A, B) = 0$ ; and if  $A = B$  (all elements equal) then  $J(A, B) = 1$ .

Using the *Jaccard distance*  $D = 1 - J$ , which was evaluated through the average linkage method (Statistical Toolbox package, Matlab), the arrangement of the grouping of neuronal clusters is established. The procedure can be better illustrated in the dendrogram form. At the bottom level we would have the neuronal clusters forming a community by themselves. At gradually

higher levels, several neuronal clusters could be combined forming higher-order communities. Finally, at the top level, all neuronal clusters would be grouped together forming a single community. Once the dendrogram was completed, the matrix  $J$  was ordered according to the obtained index (found along the bottom of the dendrogram). This matrix representation is convenient, since it visually highlights those groups of clusters that shape distinct communities in the network.

### **3.3.2 Optimum threshold for community detection**

A variety of algorithmic methods have been developed to find the optimum threshold that identify the relevant modules. The majority of them use the optimization of the modularity function (Newman, 2006), such as the simulated annealing (Kirkpatrick, 1984), or the ‘Louvain method’ (Blondel et al., 2008). These methodologies will be discussed later within the Results chapter. In our work, we took advantage of the Variation of Information method, and that is described in the next section, to identify this optimum threshold.

We should remark that we have tested other community detection methods with PCA and the Louvain methods, and observed a very similar structure in the organization of the communities. Again, we refer to the Results chapter for examples.

#### **Community detection normalization**

Despite the variety of methods, the selection of the best threshold is, intuitively, a relatively straightforward task since one can easily appreciate the characteristic communities by a visual inspection of the dendrogram. However, since most of the cases we need to compare the changes in modules’ organization across measurements, it is a fundamental step to properly normalize the distances of the hierarchical tree.

Normalization of the Jaccard similarity matrix was established by analyzing which pairwise similarities were statistically significant, i.e. by comparing the similarity values with a null hypothesis using the z-score. This procedure is important to neglect, for instance, those clusters that were frequently active but that fired in an independent manner. The z-score measure calculates how much the distance deviates from the random case, and in ‘standard deviation’ units.

Our null model consisted in a series of 500 surrogates of the matrix  $X$  in which its rows were random reshuffles of the original data. We note that this reshuffling preserved the number of firings of each cluster. Each surrogate provided a corresponding Jaccard distance matrix  $S$ . The distance matrix of z-score values,  $Z$ , was next computed as

$$Z_{ij} = \frac{D_{ij} - \langle S_{ij} \rangle}{\sigma_{ij}^S}, \quad (3.2)$$

where  $\sigma_{ij}^S$  is the standard deviation of the family of surrogate values  $S_{ij}$ .  $\tilde{Z} = Z / \max\{Z\}$  was finally computed  $\tilde{Z} \in [0, 1]$ .

### Variation of Information as a threshold

The analysis of  $\tilde{Z}$  in the form of a dendrogram gave a visual representation of the arrangement of the clusters into communities. To provide representative communities in the network a threshold  $d$  in this dendrogram was set. The larger the threshold, the smaller the number of communities. The optimum value for the threshold was obtained through the computation of the Variation of Information, and provided the minimum yet significant number of communities in the system that was not the trivial case of a single community.

The variation of information, VI, is an information-theoretic measure that compares the distance between two groups, i.e. classification of elements,  $X$

and  $Y$  (Karrer et al., 2007; Meilă, 2003)). It is computed as:

$$\begin{aligned} \text{VI}(X, Y) = H(X|Y) + H(Y|X) = & - \sum_N P(x, y) \log(P(x, y)/P(y)) \\ & - \sum_N P(x, y) \log(P(x, y)/P(x)), \quad (3.3) \end{aligned}$$

where  $H(X|Y)$  is the conditional entropy, the information needed to describe  $X$  known  $Y$ . In our case, the two partitions  $X$  and  $Y$  correspond to the set of communities that appear at different thresholds  $d_X$  and  $d_Y$  of the  $\tilde{Z}$  distance. Hence, two partitions  $X$  and  $Y$  obtained at different thresholds and that have the same set of communities would result in  $\text{VI} = 0$ . We scanned  $\text{VI}$  as a function of the threshold  $d$  in steps of 0.01.

Each threshold provided a partition  $X$  containing  $n$  moduli, and constructed as a vector of integers where each value labels the module where a cluster belongs to. For instance, in the example of Figure 3.6 a threshold  $d = 0.75$  provided  $n = 2$  moduli and  $X = \{2, 2, 1, 1, 2\}$ . Labels ‘1’ and ‘2’ denote the community index, with clusters  $\{3, 4\}$  shaping the community #1, and clusters  $\{1, 2, 5\}$  the community #2.

For the actual experimental data, we computed  $\text{VI}$  between a partition at a threshold  $d_i$  and all the other partitions at  $d \neq d_i$ , and computed the average value,  $\text{MVI}_i$ .

Finally, to identify which threshold  $d_i$  provided the most significant partition, we plotted the difference  $\Delta\text{MVI} = \text{MVI}(d_{i+1}) - \text{MVI}(d_i)$  for gradually higher  $d_i$ . A jump in  $\Delta\text{MVI}$  indicated that a small variation in the threshold led to a significant change in the structure of communities. Our choice of the optimum threshold  $d_{\text{th}}$  was set as the highest jump in  $\Delta\text{MVI}$  that provided at least two communities.

## 3.4 Complex Networks

A complex network is the representation of the interactions between the elements of a system in terms of nodes (elements) and links (interactions) in a graph (Boccaletti et al., 2006; Dorogovtsev and Mendes, 2002; Estrada, 2011b; Newman, 2010). The analysis of such resulting abstraction of the system, the network, provides clues about regularities that can be connected with certain functionalities, or even be related to organization mechanisms that help to understand the rules behind the system's complexity.

Neuronal circuits are particularly appealing to be represented in terms of complex networks (Bullmore and Sporns, 2009; Sporns, 2011; Sporns et al., 2004; Stam and Reijneveld, 2007). In this context, three major modalities of complex networks can be defined. *Structural* connectivity corresponds to the anatomical description of neuronal circuits; *functional* connectivity is related to the statistical dependence between neuronal activity; and *effective* (or directed functional) connectivity takes into account the causal interactions between neuronal activities.

### 3.4.1 Basic concepts

A network or graph is usually defined by a connectivity (*adjacency*) matrix  $A$  that contains  $n \times n$  entries, where  $n$  corresponds to the number of nodes and the entries denote links. The matrix is *binary* for most brain network studies, with each element set as  $a_{ij} = 1$  if a link exists between the nodes  $i$  and  $j$ , or  $a_{ij} = 0$  otherwise. The matrix is called *weighted* when a real number  $w_{ij}$  is associated to the link between the nodes  $(i, j)$  and that reflects their coupling strength. Depending on the direction of the link, one can consider *directed* networks for uni-directional links, e.g. information flow solely from  $i$  to  $j$ ; or *undirected* networks for bi-directional links. For the latter case, the matrix would be symmetrical,  $a_{ij} = a_{ji}$ . Illustrative examples of different network constructions are shown in Fig 6.10.

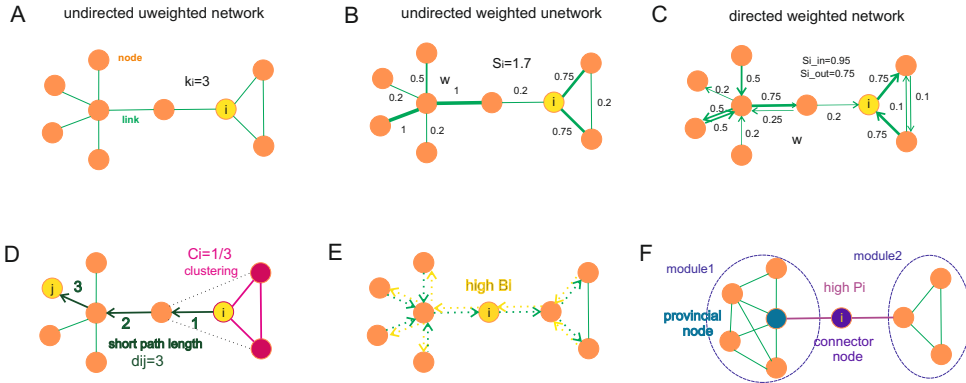


**Fig. 3.7 Basic concepts in complex networks.** The panels show different network representations of networks and key concepts. **A**, An undirected and unweighted network. The node degree  $k_i$  is the number of links that possess a given node  $i$ . **B**, An undirected and weighted network where every link has an specific weight. The weighted version of the degree is termed strength  $S$ . **C**, A directed and weighted network. The connections here are not only weighted but also have a direction. The nodal strength have two components:  $S_{in}$  is the sum of the weights of the in-going links that receive a node; and  $S_{out}$  counts the weight of its out-going links. **D**, The clustering coefficient of a given node counts the number of neighbors of this node that also are neighbors between them (triangle), respect to all possible triangles. The short path length  $d_{ij}$  is the minimum number of ‘steps’ (links) to navigate from nodes  $i$  to  $j$ . **E**, The nodal betweenness  $B_i$  corresponds to the number of shortest paths that pass through a given node  $i$ . **F** Modules are defined as the set of nodes that are more densely connected among them (blue outline) than to other nodes in other modules. The participation coefficient  $P_i$  of a node takes into account the number of links distributed to other modules respect to the number total of links of such node  $i$ . A *connector node* is defined as a node that presents high number of links connecting to different modules, while a *provincial node* is ascribed to a node that has a high number of links within its own module.

Theoretical network studies to date have typically used symmetrical measures of statistical association between nodes  $i$  and  $j$ , most notably correlation, covariance, spectral coherence or mutual information, to construct undirected, *functional* networks. A recent extension of this construction consists in considering asymmetrical measures of causal association to generate directed, *effective* networks. The latter requires the establishment of a ‘cause and effect’ criterion to determine the direction of the interactions. Hence, effective networks normally rely on information-theoretic approaches such as Granger Causality (De Vico Fallani et al., 2014; Granger, 1969),

Transfer Entropy (Schreiber, 2000), or are based on Bayesian constructions (Mishchenko et al., 2011), as occurs for instance in the ‘dynamical causal modeling’ (Mechelli et al., 2003)). The development of such methods in neuronal circuits is nowadays a highly active area of research (Singh and Lesica, 2010; Stetter et al., 2012) that has even promoted international competitions for the development of new mathematical frameworks.

In this spirit to introduce new measures for effective connectivity inference, in one of the flagship publications of this thesis (Teller et al., 2014) we introduced a novel theoretical framework to render the corresponding effective networks of our datasets using the propagation of activity between clusters as a measure of ‘causality’. We note that ‘causality’ here has to be understood as propagation of delayed activations.

### 3.4.2 Our effective connectivity inference method

The sequences of clusters’ activations, as analyzed in Section 3.2.1, convey information on the degree of causal influence between any pair of clusters in the network. Our realistic effective network construction takes into account these possible influences from the upstream connected clusters, and where the weight is established by the time delay in activation. This weighted treatment of the interaction between clusters is the major novelty and the backbone of our model (Teller et al., 2014).

Specifically, the interaction between any two neuronal clusters follows the principle of causality, i.e. the firing of cluster  $j$  immediately after cluster  $i$  eventually implies that cluster  $i$  has induced the activity of  $j$  at that particular time. The likelihood of this relation between clusters is weighted according to its frequency along the full observational time, allowing to an statistical validation. Indeed, cluster  $i$  could induce the activity of various clusters, if all of them activate in a physically plausible short time window after cluster  $i$ . Such a construction is illustrated in Figure 3.8.

### 3.4.3 Effective connectivity

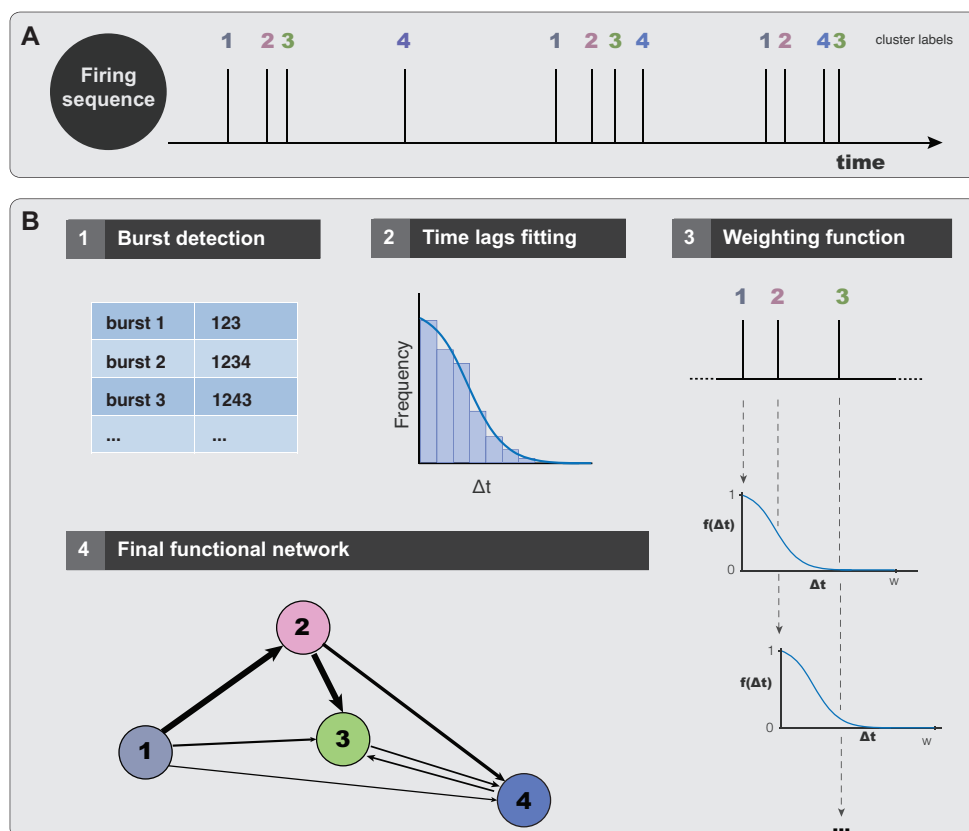


**Fig. 3.8 Sketch of the construction of the effective network.** **A**, Schematic representation of the experimental data, with 12 firing events for four different clusters. **B**, Stages of the method to construct the directed effective network. (1) The first step consists in detecting the onset times in each sequence. Firings that are separated by more than 200 ms are not considered part of the same sequence. (2) Calculation of the time lags  $\Delta t$  between consecutive firings inside the sequences. The frequency distribution of time lags is next fitted to a Gaussian distribution  $f(\Delta t) \sim \exp(-(\Delta t)^2/c)$ , finally providing the variance  $c$  that will be specific for each culture. (3) Weighting procedure example for the first sequence. Cluster #1 can activate #2 and #3. The weight of the links  $1 \rightarrow 2$  and  $1 \rightarrow 3$  depends on the time differences between clusters' activation, and is given by the function  $f(\Delta t)$  determined by the previous fitting. Hence, weight  $w_{1 \rightarrow 2} \simeq 0.6$ , and  $w_{1 \rightarrow 3} \simeq 0$ . Cluster #3 can be activated as well by cluster #2, with  $w_{2 \rightarrow 3} \simeq 0.2$ . (4) Schematic representation of the resulting effective connectivity network. The width of the connections is proportional to the weight of the links for clarity.

To construct the effective networks for each studied culture we proceeded as follows. As a first step, we defined the distinct firing sequences using the cut-off of 200 ms (for clustered cultures) previously introduced in Section 3.2. Once all the firing sequences were detected, we computed the frequency distribution  $f(\Delta t)$  of time lags  $\Delta t$  between pairs of consecutive firings. This frequency distribution presented a good fit to a universal Gaussian decay ( $y \sim e^{-x^2/c}$ ) in all the analyzed cultures, although the variance  $c$  was specific for each culture. More importantly, the distribution informs about the characteristic times expected between two consecutive firings within the same sequence, and hence it is a good proxy of the causal influence of a cluster on another. We used this information to weight the causal influence of firing propagation.

The second and last step in the construction of the effective networks consisted in linking the interactions within each firing sequence, and weighting them according to the previous frequency distribution (Figure 3.8B). We considered that every cluster influences other clusters (posterior in time) within a firing sequence and, the larger the time after a cluster has fired the lower the influence in the activation of another cluster. The weights were reinforced every time the same pair of clusters' sequence was observed. The analysis was then extended to all observed firing sequences, and the final weight value of the effective link  $w_{ij}$  between clusters  $(i, j)$  was established as the sum of all computed weights. We finally obtained a peer-to-peer activation map that was our *proxy* of the effective network.

For homogeneous cultures we proceeded identically to construct the effective networks, with the only difference that the cut-off time corresponded to 10 ms.

### **Null model**

Weak and non-significant links in the effective network may represent spurious connections that mask the topology of strong and significant connections.

To overcome this problem, noisy and non-casual connectivity values can be filtered out by thresholding and normalizing the drawn effective network with respect to a random connectivity matrix. The resulting effective connectivity map exhibits a map of the significant connections, and with the weights normalized to allow systematic comparisons between networks at different experimental conditions.

Shuffling datasets (Beggs and Plenz, 2004; Rolston et al., 2007) are the most common way to create a null model without the need of assumptions on the behavior of the data. There exist different methods depending on which features are randomly permuted and which ones are preserved. The higher the number of statistical features that are maintained, the more stringent the null model will be.

In the context of neuroscience, one of the typical null models consists in reshuffling the timing of activity events, i.e. a random permutation of the firing episodes of each neuron. We note that such a construction preserves the index of the neurons and the firing rate, but breaks the firing structure. An alternative randomization consists in swapping the neurons' indexes while maintaining the temporal structure. This null model retains both the structure of firing events in the dataset and the number of firings per neuron, but alters the firing rate of each neuron. This method is illustrated in Figures 3.9A-B and is the method applied to create the surrogates in our study.

The procedure that we applied to create the null model is as follows. First, we constructed a matrix of  $N \times 2$  elements, where  $N$  is the total number of firings. The first column of the matrix stores the onset firing times values detected in the recording, while the second one stores their corresponding cluster index. The second column was then permuted without repetition, effectively shaping a first surrogate. This process was then repeated to obtain 500 surrogates.

Once the surrogates were generated, we computed the  $z$ -score for the weights  $w_{ij}$  as

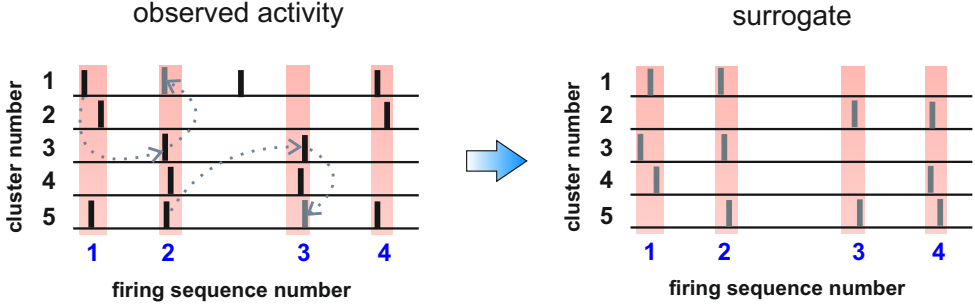


**Fig. 3.9 Construction of the null model.** The left panel shows the original activity histories for 5 clusters. The null model consists in taking the actual firing events between clusters (black bars) and randomly assigning them to another cluster (blue bars). The right panel shows the results after several permutations. The reshuffling produces a *surrogate* that preserves the temporal structure of activations in the network, but altering the activations history of each cluster.

$$Z_{ij} = \frac{w_{ij} - \langle w_{ij}^S \rangle}{\sigma_{ij}^S}, \quad (3.4)$$

where  $\langle w_{ij}^S \rangle$  is the mean weight between  $i$  and  $j$  provided for the 500 surrogates of the null model, and  $\sigma_{ij}^S$  the corresponding standard deviation.

We note that the  $z$ -score effectively provided the normalized weights between all the effective connected clusters in the network, and we therefore used  $W_{ij} \equiv Z_{ij}$  to refer to the matrix of normalized weights. Those links with a high  $W$  score appeared frequently and therefore their clusters were strongly connected. At the other extreme, negative  $W$  scores reflected those links that were less connected than in a random configuration and therefore had to be disregarded.

### 3.4.4 Comparison with alternative effective network constructions

Other metrics have been proposed besides our model to infer the functional or effective connectivity *in vitro* (Bettencourt et al., 2007; Garofalo et al., 2009;

Ito et al., 2011, 2014; Marconi et al., 2012; Salinas and Sejnowski, 2001; Shimono and Beggs, 2014; Stetter et al., 2012). Widely used strategies include cross correlation (CC), Mutual information (MI) and Transfer Entropy (TE). In particular, MI and TE are information theoretic measures that are both sensitive to linear and non-linear interactions between any pair of neuronal activities. CC, on the contrary, just captures first order, linear interactions. For instance, in the special case of a three-body system, where a neuron  $i$  is driving the dynamics of a neuron  $j$  and  $k$ , which in principle are not connected, the three methodologies would detect a relationship for  $(i, j)$  and  $(i, k)$ , but only TE and MI would also provide a relationship for  $(j, k)$ .

An additional important aspect, however, is that MI and CC are in principle unable to detect the directionality of information flow, i.e. they are unable to provide an effective connectivity. For this reason, TE has emerged as the most useful tool to infer the causal interactions from neuronal time series (Garofalo et al., 2009; Ito et al., 2011; Orlandi et al., 2014; Shimono and Beggs, 2014; Stetter et al., 2012).

With these alternative constructions in mind, we found important to cross-check the robustness of our computed effective networks. We therefore carried out MI and TE reconstructions in our experimental datasets. We found that the resulting networks were largely in agreement with the ones extracted using our method, as we describe in detail in the Results chapter. For completeness, we next describe the mathematical framework of MI and TE.

### **Time delayed mutual information**

Mutual information (Hlaváčková-Schindler et al., 2007) is a particular case of the Kullback-Leibler divergence (Kullback and Leibler, 1951), an information-theoretic measure of the distance between two probability distributions. The mutual information between two stochastic variables  $X$  and  $Y$  provides an estimation of the amount of information gained about  $X$  when  $Y$  is known.

Let us indicate by  $\{s_\ell^{(i)}\}$  the time series corresponding to the  $i$ -th cluster, with  $\ell = 1, 2, \dots, L$  and  $L$  the total number of time frames involved in the observation process. The time series adopted for the successive analysis are obtained by mapping the observed train of cluster activations to another time series termed *walk*<sup>1</sup>, defined as

$$x_\ell^{(i)} = \sum_{l=1}^{\ell} [s_l^{(i)} - \langle s_\ell^{(i)} \rangle]. \quad (3.5)$$

For the specific case of our analysis, the mutual information between two time series  $X = \{x_\ell^{(i)}\}$  and  $Y = \{x_\ell^{(j)}\}$ , corresponding to two different clusters, is interpreted as the amount of correlation between the dynamics of cluster  $i$  and  $j$ . In general, the time scale of the correlation between two time series is not known *a priori*. Such a time scale corresponds to the time delay required to maximize the gain of information. Therefore, in the spirit of Fraser and Swinney (Fraser and Swinney, 1986), we define the time delayed mutual cross information between  $\{x_\ell^{(i)}\}$  and  $\{x_\ell^{(j)}\}$  as

$$I(x^{(i)}, x^{(j)}; \tau) = - \sum_{\mu, \nu} p_{\mu\nu}^{(i,j)}(\tau) \log \frac{p_{\mu\nu}^{(i,j)}(\tau)}{p_\mu^{(i)} p_\nu^{(j)}}, \quad (3.6)$$

where  $\mu$  and  $\nu$  are indices running over some partition of the observed time series. In Equation. 3.6,  $p_\mu^{(i)}$  indicates the probability to find a value of time series  $\{x_\ell^{(i)}\}$  in the  $\mu$ -th interval,  $p_\nu^{(j)}$  is the probability to find a value of time series  $\{x_\ell^{(j)}\}$  in the  $\nu$ -th interval, whereas  $p_{\mu\nu}^{(i,j)}$  denotes the joint probability to observe a firing from the  $i$ -th cluster falling in the  $\mu$ -th interval and a firing from the  $j$ -th cluster falling in the  $\nu$ -th interval exactly  $\tau$  time frames later.

For the sake of simplicity, we adopt the more concise notation  $I_{ij}(\tau) = I(x^{(i)}, x^{(j)}; \tau)$  to indicate the time delayed mutual cross information. In order to gain the highest amount of information about the dynamics of cluster  $i$  by

---

<sup>1</sup>That procedure transforms the discret time series to a continuous one gaining in statistics

observing cluster  $j$ , we consider only the maximum value  $I_{ij}^{\max} = \max_{\tau}[I_{ij}(\tau)]$  of  $I_{ij}(\tau)$  with respect to the time delay  $\tau$ .

### Generalized transfer entropy

Transfer Entropy (Hlaváčková-Schindler et al., 2007; Schreiber, 2000) is an information theoretic measure that quantifies the statistical coherence between different time series. Transfer entropy follows the principle of Granger Causality, i.e. A causes B if A can be better predicted from past values of A and B rather than A alone. Given two discrete time series X and Y, the Transfer Entropy can be evaluated by computing the corresponding Kullback entropy:

$$TE_{Y \rightarrow X} = \sum p(x_{n+1}, x_n^{(k)}, y_n^{(l)}) \log \frac{p(x_{n+1} | x_n^{(k)}, y_n^{(l)})}{p(x_{n+1} | x_n^{(k)})}, \quad (3.7)$$

where  $p$  denotes the transition probability conditioned to the past  $k$  and  $l$  observations of the temporal series X and Y.

Mathematically, TE can be interpreted as a measure of the deviation from the generalized Markov property, expressed as

$$p(x_{n+1} | x_n^{(k)}) = p(x_{n+1} | x_n^{(k)}, y_n^{(l)}). \quad (3.8)$$

We note that the Markov property is only valid when transitions of X do not depend statistically on past values of Y, i.e. the knowledge of the past values of Y has no effect on the predictability of X. The fulfillment of this property would therefore result in  $TE = 0$ . Higher  $TE$  scores indicate that the Markov property does not hold and there is an information flow from Y to X, or a gain in the information of X given the evolution of Y.

TE is a mathematical formalism with continuous expansion. For neuroscience applications, Stetter (Stetter et al., 2012) and coworkers introduced an extension of TE, termed Generalized Transfer Entropy (GTE), aimed at

reconstructing the connectivity in a neuronal network known solely the fluorescence time series of their containing neurons. The authors used realistic numerical simulations —inspired in homogeneous neuronal cultures— to generate neuronal fluorescence traces, assess the effective connectivity between all pairs of neurons in the context of GTE, and then evaluate the accuracy of the formalism in replicating the underlying network structure.

The novelty of GTE is the restriction of the TE analysis to a selected dynamic regime. This restriction is achieved by establishing a threshold  $g$  in the fluorescence signal that restricts the range of fluorescence values to study. GTE is expressed as

$$GTE_{Y \rightarrow X} = \sum p(x_n, x_{n-1}^{(k)}, y_{n-1+S}^{(k)} | g_n < g) \log \frac{p(x_n | x_{n-1}^{(k)}, y_{n-1+S}^{(k)}, g_n < g)}{p(x_n | x_{n-1}^{(k)}, g_n < g)}, \quad (3.9)$$

where  $g_n < g$  indicates the restriction of the data points to only those that fall within a range of fluorescence values. In our case we selected high fluorescence levels and that correspond to strong clusters' firing, i.e. we selected those fluorescence levels above a threshold that is much higher than the noisy fluorescence signal of the clusters at rest. The Markov order  $k$  is related with the 'causality' time window, i.e. the maximum time bin to expect the clusters to be influenced to one another. For the clustered networks we set  $k = 10$ , a value that approximately corresponds to the cut-off time of 200 ms for clusters' interactions previously inferred.  $S$  accounts for 'same bin interactions', and can be set to either 1 or 0 to accept or reject the connectivity between two clusters when they fire in the same time bin.

$GTE_{ij}$  scores of clusters  $(i, j)$  quantify the strength of an effective link from a cluster  $i$  to cluster  $j$ , i.e. the future fluorescence of  $j$  is better predicted by considering the past fluorescence of  $i$  in addition to the past of  $j$  itself.

### 3.4.5 Network properties

There exist a wide range of network measures (Rubinov and Sporns, 2010b) aim at characterizing the architecture of the network, i.e. its topology or the way in which nodes are linked throughout the network. The majority of these network topological descriptors have their binary, weighted, directed and undirected extensions, depending on the characteristics of the links under study. In this Section we describe the network attributes to our directed and weighted functional networks. The definitions of all the measures used in this thesis are provided in Table 3.1. Some of this network measures are calculated using the ‘Radatools’ software package (<http://deim.urv.cat/~sergio.gomez/radatools.php>), and others using the Brain Connectivity Toolbox in Matlab (Rubinov and Sporns, 2010b). In order to compare these measures across experiments, they were standardized using the  $z$ -score. The representation in terms of  $z$ -score allowed the values in each studied experimental network realization to be properly scaled and therefore facilitated comparison between experiments.

#### Degree and strength

Typically, the *degree*  $k_i$  of a node is the number of neighbors (links) of the node  $i$ . In directed graphs,  $k_i$  is defined as the sum of ingoing (in-degree,  $k_i^{in}$ ) and outgoing (out-degree  $k_i^{out}$ ) links in node  $i$ . The *degree distribution*,  $P(k)$  includes the node degrees  $k_i$  of all the nodes, which gives the probability that a randomly selected node possesses exactly  $k$  links. The first moment of the degree distribution  $\langle k \rangle$  (mean degree) and the second moment  $\langle k^2 \rangle$  (degree variance) are widely used to define important topological aspects of a network. In particular, the mean degree of a network is commonly used as a density measure, and is often interpreted as the ‘wiring cost’ of the network. The second moment measures the fluctuation of the connectivity distribution.

The weighted variant of the degree is the strength  $S$ , which is defined in a similar manner but taking into account the weight of the links. The

Network properties	Definition (weighted and directed networks)
Basic notation	N: total set of nodes; n: number of nodes.
Weighted links	Normalized weights $0 \leq w_{ij} \leq 1$ and $l = \sum_{i,j \in N} w_{ij}$ is the number of links.
Strength	Out-strength $S_i^{out} = \sum_{j \in N} w_{ij}$ in-strength $S_i^{in} = \sum_{j \in N} w_{ji}$ Strength $S_i = S_i^{out} + S_i^{in}$
Number of triangles	$t_i = \frac{1}{2} \sum_{j,h \in N} ((w_{ij} + w_{ji})(w_{ih} + w_{hi})(w_{jh} + w_{hj}))^{1/3}$
Clustering Coefficient	$C = \frac{1}{n} \sum_{i \in N} C_i = \frac{1}{n} \sum_{i \in N} \frac{t_i}{(S_i^{out} + S_i^{in})(S_i^{out} + S_i^{in} - 1) - 2 \sum_{j \in N} w_{ij} w_{ji}}$ Where $C_i$ is the clustering coefficient of node $i$ . (Onella 2005, Fagiolo 2007, Rubinov 2010)
Shortest path length (distance) applying Dijkstra's algorithm	$d_{ij} = \sum_{a_{ij} \in g_{i \rightarrow j}} \left( \frac{1}{w_{ij}} \right)$ Where $g_{i \rightarrow j}$ is the directed shortest weighted path from $i$ to $j$
Characteristic path length	$L = \frac{1}{n} \sum_{i \in N} L_i = \frac{1}{n} \sum_{i \in N} \frac{\sum_{j \in N, j \neq i} d_{ij}}{n-1}$ Where $L_i$ is the average distance between node $i$ and all the others.
Global efficiency	$E_G = \frac{1}{n} \sum_{i \in N} E_i = \frac{1}{n} \sum_{i \in N} \frac{\sum_{j \in N, j \neq i} d_{ij}^{-1}}{n-1}$ Where $E_i$ is the efficiency of node $i$ .
Local Efficiency	$E_{loc} = \frac{1}{n} \sum_{i \in N} E_{loc,i} = \frac{1}{n} \sum_{i \in N} \frac{\sum_{j,h \in N, j \neq i} (w_{ij} + w_{ji})(w_{ih} + w_{hi}) ([d_{jh}(N_i) + d_{hj}(N_i)])^3}{(S_i^{out} + S_i^{in})(S_i^{out} + S_i^{in} - 1) - 2 \sum_{j \in N} w_{ij} w_{ji}}$ Where $E_{loc,i}$ is the local efficiency of node $i$ and $d_{jh}(N_i)$ is the length of the shortest path between $j$ and node $h$ , that contains only neighbors of $i$ .
Modularity Index (Newman 2006, Leicht and Newman 2008)	$Q = \frac{1}{l} \sum_{i,j \in N} \left( w_{ij} - \frac{S_i^{out} S_j^{in}}{l} \right) \delta_{m_i, m_j}$ Where $m_i$ is the module containing node $i$ , and $\delta_{m_i, m_j} = 1$ if $m_i = m_j$ and 0 otherwise.
Assortativity	$\rho^{pw} = \frac{\sum_{ij} w_{ij} (S_i^{out} - \langle S^{out} \rangle_i) (S_j^{in} - \langle S^{in} \rangle_j)}{\sqrt{\sum_i S_i^{out} (S_i^{out} - \langle S^{out} \rangle_i)^2} \sqrt{\sum_j S_j^{in} (S_j^{in} - \langle S^{in} \rangle_j)^2}}$
Betweenness centrality	$b_i = \frac{1}{(n-1)(n-2)} \sum_{h,j \in N, h \neq j, h \neq i, j \neq i} \frac{\rho_{hj}(i)}{\rho_{hj}}$ Where $\rho_{hj}$ is the number of shortest paths between $h$ and $j$ , and $\rho_{hj}(i)$ is the number of shortest paths between $h$ and $j$ that pass through $i$ .
Participation coefficient	$y_i = 1 - \sum \left( \frac{S_i^{out}(m)}{S_i^{tot}} \right)^2$
Rich Club	$\phi_{s_r}^{unc} = \frac{W_{s_r}}{W_{s_r}^{unc}}, W_{s_r}^{unc} = \langle s \rangle \frac{\sum_{i \in V_{s_r}} \sum_{j \in V_{s_r}} S_i^{out} S_j^{in}}{N \langle s \rangle^2 - \langle S^{out} S^{in} \rangle}$

**Table 3.1** Summary of the definitions used for the calculation of the different network properties along this thesis. All expressions use directed and weighted versions of graphs.

total strength of a node  $i$ ,  $S_i$ , is defined as the sum of all its neighboring link weights (see Figure 6.10 and Table 3.1).

### Characteristic path length and global efficiency

The distance or *shortest path*,  $d_{ij}$ , is defined as the minimum number of links that have to be crossed to travel from node  $i$  to node  $j$  in the network (Figure 6.10). The *characteristic path length*,  $L$ , also known as *average short path length*, is defined as the mean of shortest paths over all pair of nodes, i.e. the mean of geodesic lengths over all couple of nodes. Its average inverse is called *global efficiency*. Global efficiency,  $G_{eff}$ , is becoming more successful to measure functional integration since it can be well evaluated in disconnected networks, while the short path length in these cases diverges ( $d_{ij} = \infty$ ). Both measures indicate the global information flow (global network communication) of a network, i.e. its traffic capacity.

### Clustering and Local Efficiency

The *clustering coefficient*,  $C_i$ , corresponds to the number of triangles around an individual node divided by the maximum possible triangles, which in practice is equal to counting the number of neighbors of a node that are also neighbors between them (Figure 6.10). High clustering implies high segregation. The *local efficiency*,  $L_{eff}$ , is a good alternative measure of the clustering coefficient. The local efficiency of a node  $i$  is the average global efficiency of such node in the local subgraphs (graph formed by the neighbors of node  $i$ ). This topological descriptor shows how efficient is the communication between neighbors.

### Assortativity

One of the widely used measure to reflect network resilience is the *assortativity coefficient*. Newman (Newman, 2002) defined that measure as the *Pearson* correlation between the degrees of every pair linked nodes in the network.

Thus, networks with high positive assortativity coefficient would mean that nodes with the same degree tend to be interconnected. Networks containing many nodes with high degree are likely to present a resilient core, i.e. high-degree nodes are interconnected. On the other hand, networks with negative assortative mixing (disassortative) tend to show high-degree nodes connected with low-degree ones, becoming more vulnerable networks.

Based on the weighted and directed nature of our networks, we proposed a new measure of assortativity (Teller et al., 2014) that considers the strengths instead of the degrees to carry out the correlation of every pair of linked nodes. The measure also takes into account the weight of the link from node  $i$  to node  $j$ , since links with higher weight have a large contribution to the correlation.

### Generalization of assortativity to directed weighted networks

In directed unweighted networks, for every paired linked of nodes assortativity measures the degree-degree correlation between them. The directed assortative coefficient,  $\rho^P$ , would be the *Pearson* correlation between  $k_i^{out}$  of node  $i$  and  $k_j^{in}$  of node  $j$ , as defined in Ref. (Newman, 2003).

Incorporating the weight could be crucial since high-degree nodes can be connected to a majority of low-degree ones (apparently a disassortative network) but concentrating the largest fraction of their strength only on the nodes with high degree. Then, the network could be considered assortative in an effective way, just because the most relevant links in term of weights are linking high-degree nodes.

Then the final directed and weighted assortativity measure,  $\rho^{PW}$ , is a modification of the defined Newman (Newman, 2003) directed assortativity, but using the strengths instead of the degrees and including the weight that

carries each linked paired nodes.

$$p^{PW} = \frac{\sum_{i,j} w_{ij} (s_i^{out} - \langle s^{out} \rangle_E) (s_j^{in} - \langle s^{in} \rangle_E)}{\sqrt{\sum_i s_i^{out} (s_i^{out} - \langle s^{out} \rangle_E)^2} \sqrt{\sum_j s_j^{in} (s_j^{in} - \langle s^{in} \rangle_E)^2}}, \quad (3.10)$$

where  $E$  scans all the links in the network, and  $\langle s^{out} \rangle_E = \frac{1}{\sum_{(i,j) \in E} w_{ij}} \sum_{(i,j) \in E} w_{ij} s_i^{out}$  and  $\langle s^{in} \rangle_E = \frac{1}{\sum_{(i,j) \in E} w_{ij}} \sum_{(i,j) \in E} w_{ij} s_j^{in}$ .

Litvak *et al.* (Litvak and Van Der Hofstad, 2013) showed that in disassortative networks the magnitude of the standard assortativity decreases with network size, a difficulty that was solved by replacing the Pearson correlation with the Spearman correlation, thus obtaining a *Spearman assortativity*,  $\rho^S$ . Spearman rank correlation is calculated in the same way as the Pearson correlation but substituting the values (in this case, the strength of the nodes) by their respective ranks, i.e. their position when the values are sorted in ascending order. This leads us to define the *Spearman weighted assortativity*  $\rho^{SW}$  as the Spearman weighted correlation.

The estimation of the error in the assortativity value (for any of the previous variants) can be computed in several ways, for instance through the jackknife method, the bootstrap algorithm, or by using the Fisher transformation (Efron; Newman, 2003). In our calculation, we used the bootstrap algorithm, and considered 1000 random samples of the data.

## Modularity index

A network can present topological modules or communities, as we have seen in Section 3.3. These topological modules are defined as sets of nodes that are more densely connected among each other than with nodes in other modules. Hence, the modularity index (Newman, 2006),  $Q$ , is the most applied measure to quantify how well the network can be subdivided in that non-overlapping

modules, and by maximizing the number of links within the module while minimizing the number of inter-modular links.

### 3.4.6 Hubs and Rich Club

Complex networks have been widely applied to uncover key organizational features of network topology and to make predictions about the different roles that the nodes can exhibit. In particular, in the past few years a great interest has concentrated on nodes called *hubs*. However, there no exist a unified definition of a hub, but it is commonly agreed that they play a crucial role in fast transport and efficient integration of information across the network. In the context of the brain, those hubs are likely to occupy a central position in the organization of a network and to display a strong influence in neuronal communication and integrative brain function (van den Heuvel and Sporns, 2013).

#### Centrality measures

In order to identify these hubs in a network, several centrality measures have been proposed, that variously assess how important or influential a node is within a network with different criteria. Here, we will focus on some of them.

The *centrality degree* is one of the most common and the simplest measure of centrality. Nodes with high degree are nodes that interact, structurally or functionally, with many others in the network. For instance, in some social networks where nodes are referred to a person and the links to the relationships (or acquaintances) among them, a hub (defined as the node with high degree) would be a ‘politician’ or a ‘celebrity’. However, this measure does not take into consideration the global structure of the network and just captures the local behavior around a node.

The *eigenvector centrality* measure (also known as *pagerank centrality*) is similar in meaning as the degree centrality, but it takes nto account the degree

of the other nodes that are connected with a given node, therefore extending to global features of the graph, and weighting the influence of their neighbors. Following the social example, a person can be more influential when the people that he or she knows is also more influential. Mathematically, the eigenvector centrality is calculated as the first eigenvector of the adjacency matrix that corresponds to the largest eigenvalue (Lohmann et al., 2010).

However, the eigenvector centrality has been recently seen (Martin et al., 2014) to be problematic in small networks due to a bias that can appear around central nodes, i.e. a localization effect. Qualitatively, that localization arises because a hub with a high eigenvector centrality gives high centrality to its neighbors, which in consequence turns it back again and inflate the hub's centrality.

In addition, although a node might be really important because it is connected to many others, it might not be in a position where other nodes can easily reach them. In such a case, the 'important' node would be unable to access resources such as information or knowledge to the global network. To capture this feature, other centrality approaches are based on the idea that hubs are central nodes that participate in many short paths within the network, and therefore are responsible for information flow.

One of these centrality measures is the *closeness centrality* which is evaluated as the inverse of average shortest path lengths between a given node and the rest of the network. A limitation of this measure is the lack of applicability to networks with disconnected components since it diverges. To overcome such limitation, the measure known as *betweenness centrality* has been introduced, and corresponds to the number of shortest paths that pass through a given node (see Figure 6.10). Then, nodes with high values of betweenness centrality participate in a large number of shortest paths, asserting a control over the flow information.

In modular networks, the idea of a hub can also be related with its role in integrating communities or modules. In this line, Guimera and Amaral

(Guimera and Amaral, 2005) defined the *within-module degree z-score*  $z_i$ , a measure that captures the node role within the module and the *participation coefficient*  $P_i$ , a measure that expresses the distribution of links' node across all modules in a network. The nodes with high within-module degree and low participation coefficient are known as *provincial hubs*. These nodes display an important role within the communities helping to modular segregation.

On the other hand, nodes with high degree but also with high participation coefficient are known as *connector hubs* and are likely to facilitate global inter-modular integration. However, the participation coefficient defined by Guimera and Amaral assumes that all communities are of the same size. For this reason, in our study we evaluated the participation coefficient for every possible partition in the network and averaged the final result. To proceed, we carried out a thresholding (with steps of 0.1) in the Jaccard Similarity matrix, a procedure similar as 'cutting' the dendrogram. Thus, for every threshold, a particular partition was obtained. In each partition the participation coefficient (in the weighted version) was calculated for every cluster. Finally, the final nodal participation coefficient corresponded to the average of all the previous participation coefficient values obtained in each partition. In this manner, the size of the different communities was taken into account.

Overall, one can indeed notice that different meanings and descriptors have been appeared to define a hub. Currently studies have been using a combination of the centrality measures (like a 'hubness' score) to get a better identification and interpretation of the nodes' role in the network. Actually, ranking the nodes according to the different criteria are often correlated, then aggregating rankings is a powerful mechanism to improve the distinction of the hubs. For instance, in (van den Heuvel et al., 2010) ascribed as hubs the nodes that present high nodal strength, high nodal betweenness, low shortest path length, and low clustering coefficient. In the same line, (Schroeter et al., 2015), addressed as 'hub score' the average of the nodal strength, betweenness centrality, local efficiency and the participation coefficient. Hubs

in both cases were finally assigned to the nodes that presented scores above of the 20% within each category, e.g. the top 20% of the ‘hubness’ ranking. This latter definition has been the one applied in this thesis.

### Rich Club Analysis

When nodes with high strength are more highly connected between them than one would expect by chance then they create a backbone in the network that is called Rich Club phenomenon. The rich-club analysis computes the degree-degree (or weight-weight) correlation distributions respect to a null model of non-correlated degrees (or weights). We first introduce the formulation for the calculation of rich-club in weighted networks as presented in (Serrano, 2008), and afterwards we will extend it to the case of weighted directed networks.

The rich-club score is calculated as follows

$$\phi_{s_T}^{unc} = \frac{W_{s_T}}{W_{s_T}^{unc}} \quad (3.11)$$

where  $\phi_{s_T}$  is the rich-club score relative to the uncorrelated null case,  $W_{s_T}$  is the sum of the weights of the links of the subgraph formed only by those nodes whose strengths are higher than  $s_T$ ,

$$W_{s_T} = \sum_{i \in \mathcal{V}_{s_T}} \sum_{j \in \mathcal{V}_{s_T}} w_{ij} \quad (3.12)$$

and  $W_{s_T}^{unc}$  is the corresponding value in the case of uncorrelated strengths, being

$$W_{s_T}^{unc} = \langle s \rangle \frac{\sum_{i \in \mathcal{V}_{s_T}} \sum_{j \neq i \in \mathcal{V}_{s_T}} s_i s_j}{N \langle s \rangle^2 - \langle s^2 \rangle} \quad (3.13)$$

The term  $v_{s_T}$  designates the subset of nodes  $i$  such that  $s_i > s_T$ .  $N$  is the total number of nodes in the network, and  $\langle s \rangle$  and  $\langle s^2 \rangle$  are the first and second moments of the strength distribution. The ratio  $\phi_{s_T}$  is calculated for all values of  $s_T$ , and ranges from the minimum value of strength in the network to the maximum. This ratio indicates the presence or absence of a rich–club in the network: a network shows a rich–club effect when the high values of  $s_T$  give a ratio above 1.

To calculate this ratio on our networks that not only are weighted but also directed we need to adapt the former formulation considering the in–strength,  $s^{in}$ , and out–strength,  $s^{out}$ , of each node. Indeed, in the directed formulation, Equations (3.11) and (3.13) remain unchanged. However,  $v_{s_T}$  must be redefined as

$$v_{s_T} = \{i \mid s_i^{in} + s_i^{out} > 2s_T\} \quad (3.14)$$

and the term  $W_{s_T}^{\text{unc}}$  becomes

$$W_{s_T}^{\text{unc}} = \langle s \rangle \frac{\sum_{i \in v_{s_T}} \sum_{j \in v_{s_T}} s_i^{out} s_j^{in}}{N \langle s \rangle^2 - \langle s^{out} s^{in} \rangle} \quad (3.15)$$

where the averages are calculated over the total  $N$  nodes in the network as  $\langle s \rangle = \frac{1}{N} \sum_i s_i^{out} = \frac{1}{N} \sum_i s_i^{in}$  and  $\langle s^{out} s^{in} \rangle = \frac{1}{N} \sum_i s_i^{out} s_i^{in}$ .

This formulation allows us to calculate the rich–club coefficient for weighted directed networks. Note that for an undirected network where  $s^{out} = s^{in}$  we would recover the expression in (Serrano, 2008).

### Statistical significance tests

We used along the thesis Student’s t-test for clustered cultures, and the Kolmogorov-Smirnov test to compare homogeneous and clustered networks

since the two culture types had different number of experimental realizations. In all the statistical results, the p-value  $p$  is indicated as \* for  $p < 0.05$ , and \*\* for  $p < 0.005$ .

# Chapter 4

## RESULTS I : Modular Organization and Effective Connectivity

As we have seen, clustered cultures display a self-sustained spontaneous activity characterized by the fast activation of aggregates of neurons *clusters* in a sequential manner *firing sequences*. These neuronal clusters often participate within the same firing sequences, shaping persistent coherent activations that we called *communities*. As we have described in the Methods Section, we unveiled the structure of these communities by comparing the history of activations of a given cluster with all the other clusters' histories, finally grouping the clusters according to the most prominent categories. We computed this analysis by considering a hierarchical clustering construction, and using the 'Jaccard similarity' as a measure of the resemblance in cluster's histories. Typically, we observed that the emergent dynamics displays a hierarchical modularity, where small communities appertain to higher ones.

We also introduced that the detailed analysis of the firing sequences in the context of a novel mathematical framework forged the effective connectivity of the clustered networks. Our framework naturally captured the intrinsic

dynamics of our networks, and is based on the use of the time delays between any two clusters' activations —within a firing sequence— to ascribe and weight the effective coupling between them. This framework gave similar results to other approaches such as Mutual Information or Transfer Entropy, as it was simpler to apply and computationally cheap.

In this chapter we will analyze in detail the functional organization of the network in the context of our actual experiments. We will first deepen in the characterization of the communities and the functional networks, and next we will investigate the topological properties of the inferred networks.

## 4.1 Firing sequences

As described in Chapter 2, neurons were dissociated and seeded homogeneously on a glass substrate. Cultures were limited to circular areas 3 mm in diameter for better control and full monitoring of network behavior (Figure 4.1A). The lack of adhesive proteins in the substrate rapidly favored cell-to-cell attachment and aggregation, giving rise to clustered cultures that evolved quickly. We measured dynamics already at DIV 5, and studied cultures up to DIV 16. Inhibitory connections were blocked in most of the experiments to operate in a biochemical scenario as simple as a possible. Network dynamic behavior was therefore solely molded by excitation.

The clustered networks —at the developmental stage at which we investigated them— contain around 30 clusters that display rich spontaneous activity. Although the spatial arrangement of the clusters and their interconnectivity varied from an experimental realization to another one, their dynamics presented similar features. The spontaneous activity was monitored through fluorescence calcium imaging (Figure 4.1B) and recorded for typically 1 hour, which provided sufficient statistics in firing events while minimizing culture degradation due to photo-damage. The analysis of the images at the end of

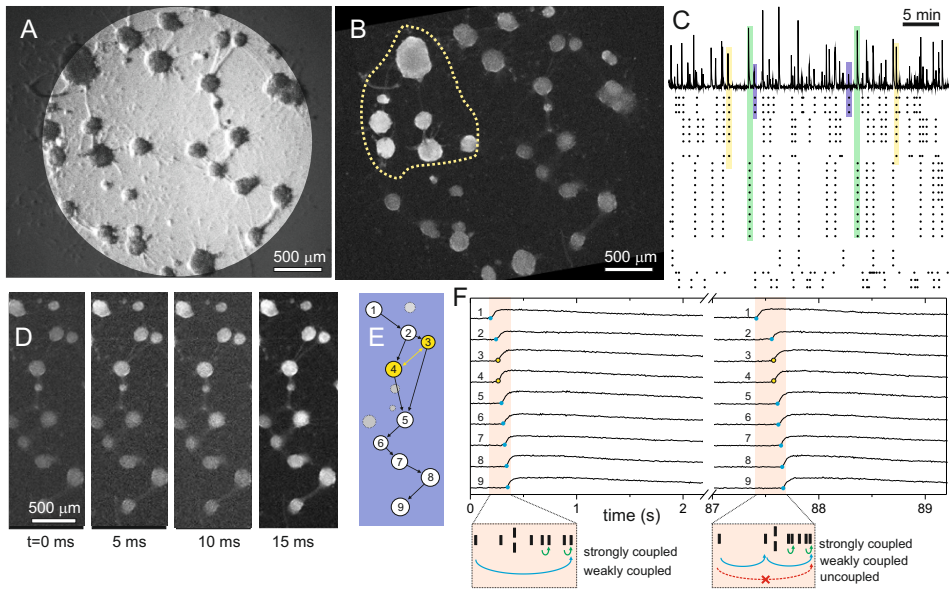


**Fig. 4.1 Representative experiment in clustered neuronal networks.** **A**, Bright field image of a clustered culture at *day in vitro* 14. Dark circular objects are aggregates of neurons (clusters), and filaments are visible physical connections between them. **B**, Corresponding fluorescence image, integrated over 50 frames ( $\approx 0.5$  s). Bright clusters at the top-left corner are firing ones. A group of clusters that are active together in a short time window define a firing sequence (yellow outline). **C**, Spontaneous activity in the network. The top plot shows the average fluorescence signal of the clustered network shown in **B**, and along 40 min of recording. The sharp peaks in fluorescence correspond to the fast sequential ignition of a group of clusters. The bottom raster plot shows the clusters that ignite along the recording. Different color bars remark repeated firing sequences, and highlights the tendency for the clusters to activate in specific groups. **D**, Example of a particular firing sequence in a region of the network containing 13 clusters. From left to right, the progress of cluster's activation is revealed by the increase in fluorescence signal of the downstream connected clusters. **E**, Order of activation (black arrows) according to the analysis of the fluorescence signal. The clusters marked in yellow are those that fire simultaneously within experimental resolution. The ones in gray are clusters that do not participate in the firing sequence, and either fire independently or remain silent. **F**, Detail of the fluorescence traces for the 9 participating clusters along two different firing sequences, illustrating the accuracy in resolving the time delay in the activation of the clusters. The two firing sequences contain the same clusters, but the activation sequences are slightly different. Blue dots mark the ignition time, and yellow dots signal the clusters that fired simultaneously. The bottom orange boxes depict the final activation sequences. In the construction of the directed functional network, the influence of a cluster on another is conditioned by the time span between their activations. Close activations result in strong couplings (green arrows); far activations in weak ones (blue). Any two clusters whose activations are above 200 ms are considered functionally uncoupled (red).

the measurement provided the variations in fluorescence intensity for each cluster and the corresponding onset times of firing (Figure 4.1C).

The spontaneous activity of these clustered neuronal cultures is characterized by the fast cascades of clusters' activation that we call 'firing sequences'. An illustrative example is shown in Figure 4.1D-F, which depicts representative fluorescence images and the traces of 9 clusters along two consecutive firing sequences. The first sequence corresponds to the images and sketch of Figure 4.1E. The orange box at the bottom of the plot indicates the relative activation time of each cluster within the window, with two clusters treated as simultaneous.

To introduce the construction of the effective network that is described later, we note that, intuitively, the firing of cluster #9 is most likely caused by #8 and therefore both clusters are (functionally) strongly coupled. At the other extreme, cluster #1 most likely did not trigger #9, and therefore their mutual coupling is very weak. For the second burst, we note that the activation sequence is very similar, but the relative delay times differ, therefore modifying the cluster's coupling strengths. Indeed, cluster #1 and #9 are now functionally disconnected given their long temporal separation. The above sequences of clusters' activations, extended to all the clusters and firing sequence episodes of the monitored culture, convey information on the degree of causal influence between any pair of clusters in the network. For instance, cluster #5 in Figures 4.1E-F can fire because of the first order influence of clusters #3 and #4, but also because of the second and third order influences of clusters #2 and #1, respectively. We observed that the time spanned between two consecutively firing clusters typically ranged between 10 and 100ms (Figure 4.2A). Therefore, we used two times the maximum value as a cut-off to separate a given firing sequence from the preceding one. We considered that above this value there is no casual activation between consecutive clusters' firings.

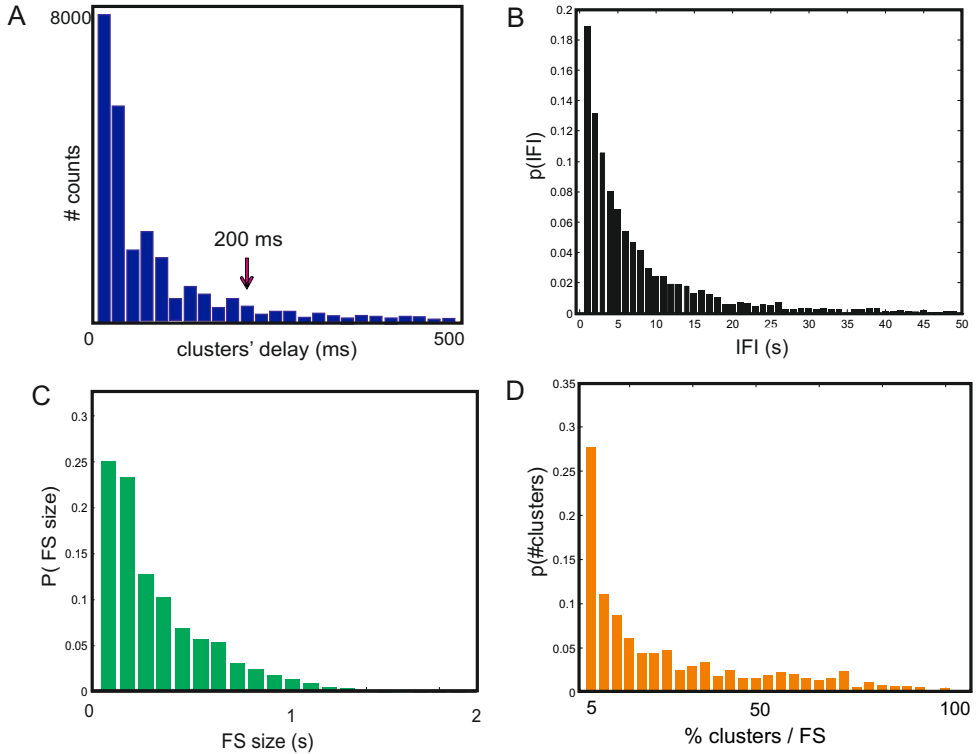


**Fig. 4.2 Time delays and occurrence of firing sequences.** **A**, Distribution of the cluster's activation delay times up to 500 ms. The arrow depicts the value of 200 ms used as cut-off. The probability of consecutive clusters' activations over this cut-off is about 1%. **B**, Probability distribution of the time interval between firing sequences (IFI), which is exponential-like. The temporal separation between consecutive firing sequences typically occurs in the range 1 – 15 s. **C**, Probability distribution of the duration of the firing sequences, which follows an exponential distribution as well, with the mean around 100 – 150 ms. **D**, Distribution of the number of clusters that encompass a firing sequence. Although two-cluster activations appear often, the typical size of a firing sequence is around 20 clusters.

A typical recording provided on the order of 100 – 200 firing sequences ( $\simeq 3$  firing sequences/min). Firing sequences are typically separated in time by 1 – 15 s. The probability distribution of the time intervals between these firing sequences (*inter-firing interval*, IFI) follows an exponential distribution rather than a Gaussian distribution as occurs in homogeneous cultures (Figure 4.2A). Firing sequences in our clustered networks generally last 150 ms (Figure 4.2C) and encompass between 2 and 20 clusters (Figure 4.2D).

### 4.1.1 Validity of firing sequences

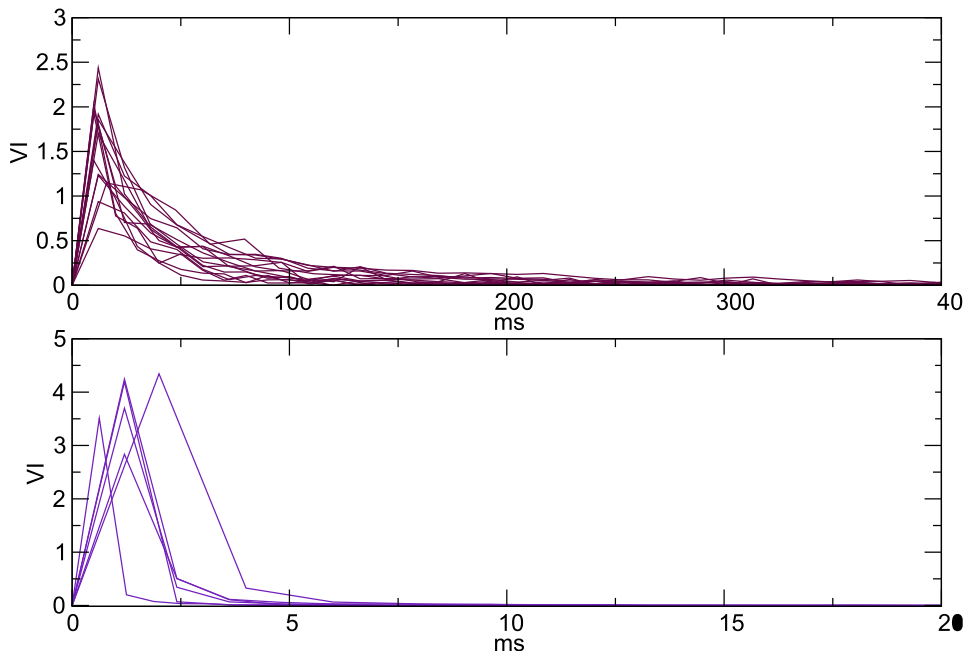


**Fig. 4.3 Sensitivity of the functional network construction to the cut-off times.** The plots show the Variation of Information (VI) between the grouping of bursts at a certain cut-off value and the previous one, and for clustered networks (top) and homogeneous ones (bottom). Each grouping is the set of bursts found at a certain value of the cut-off. The cut-off values were investigated in the range 0 – 1000 ms. The analysis shows that 200 ms for clustered cultures and 10 ms for homogeneous ones are values for which VI is already stabilized.

The cut-off determines the end of a sequence and therefore its variation modifies the set of firing sequences chosen. The cut-off was set to 200 ms for clustered cultures and to 10 ms for homogeneous ones. To assess the sensitivity of the grouping of firing sequences to the cut-off, in (Teller et al., 2014) we computed the Variation of Information (VI) between the grouping of firing sequences at a certain cut-off value and the previous one.

The variation of information (Karrer et al., 2007; Meilă, 2003) is an information-theoretic measure that compares the distance between two groups, i.e. partitions of elements X and Y (see Section 3.3.2). In our specific case, each partition corresponds to the set of firing sequences (or network bursts for homogeneous cultures) found at a certain value of the cut-off. We screened the cut-off values from 0 to 1000ms and finally observed that 10ms for homogeneous and 200ms for clustered cultures are values for which VI was already stabilized (Figure 4.3). Thus, the modification of the cut-off within the stabilization region does not change the grouping of clusters in each burst, and therefore the derived functional networks, as well as the corresponding network measures, remain the same.

## 4.2 Functional organization

The observation that the firing sequences repeated along the recording indicated that groups of clusters tended to participate in the same activity sequence, although the precise sequence of activation could vary. One can observe a typical raster plot of a representative experiment in Figure 4.4A. Two firing sequences with similar pattern of clusters' activation are indicated with green and orange boxes. In addition, these small groups often also participated within a major group that involved practically the entire network (blue box).

By comparing the history of activations of each cluster (i.e. the rows of the raster plot) one can assess which clusters exhibited a high degree of

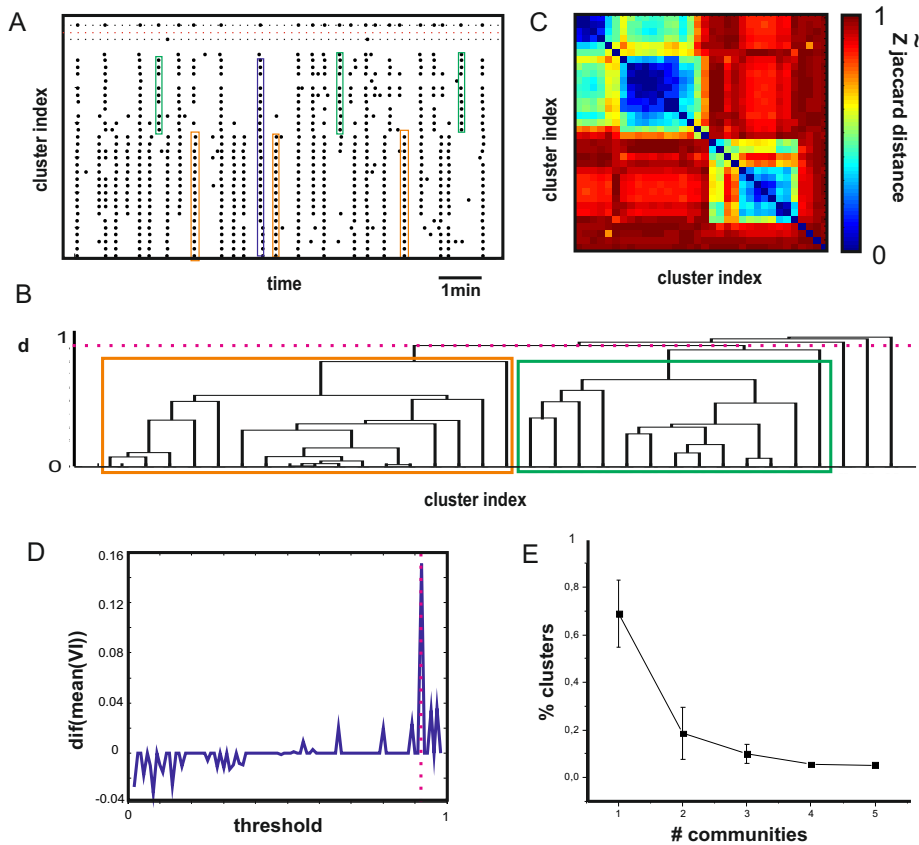


**Fig. 4.4 Functional Organization.** **A**, Raster plot of spontaneous activity in a typical experiment with strong modular behavior, meaning that clusters tend to fire in groups following a functional structure that frequently repeats (vertical color boxes). Dots in the raster plot mark a cluster firing event. The green and orange boxes mark two characteristic firing sequences that are repeated along the recording, whereas the blue box highlights a firing sequence that almost comprises the entire network. Horizontal dotted lines indicate clusters that fire independently. **B**, Corresponding dendrogram of the similarity between the activity history of the clusters using the Jaccard metrics (as a similarity measure) and the average linkage criterion (as a method to group the clusters depending on their similarity values in the hierarchical construction). The dashed line indicates the threshold for the optimal set of communities. Color boxes indicate the two most representative communities, color coded as in the raster plot. **C**, Equivalent representation in the form of a distance matrix  $\tilde{Z}$ , clearly depicting the two characteristic communities. The matrix was arranged according to the clusters' indexing inferred from the dendrogram. **D**, Mean difference  $\Delta \text{VI}$  between pairwise consecutive partitions using VI as a function of the threshold  $d_i$ . The vertical dashed line indicates the optimal threshold. **E**, Fraction of clusters that shape the characteristic communities averaged over  $N = 18$  experiments, showing that typically about 70% of the clusters in a network the biggest community, followed by other 20% that configure a second community.

coherence and therefore shaped the characteristic dynamical communities in the network. In a formal manner, we carried out the agglomerative hierarchical construction using the ‘Jaccard’ metrics (see Section 3.3.1). This measure computes the number of common activations between two clusters respect to all the occurrences where either one cluster or the other had fired. This definition is convenient since it excludes those events where both clusters have remained silent. Once the distance (or the similarity) matrix is obtained, a  $z$ -score test is implemented with 500 surrogates. The final, normalized Jaccard distance matrix  $\tilde{Z}$  (Figure 4.4C) can be conveniently represented using a dendrogram, a hierarchical tree representation (Figure 4.4B). This construction shows the cluster index along the  $x$ -axis, while the  $y$ -axis shows their dynamical similarity  $d$ . The cluster index can be used to sort the  $\tilde{Z}$  matrix and visualize better which clusters are more similar (or have a shorter distance). The value of  $d$  of the dendrogram depicts the depth in which pairwise clusters have been grouped.

A threshold has to be applied in dendrogram to establish the number and structure of the communities in the network. Such a ‘threshold’ effectively means to set a particular value  $d_i$ . The optimal threshold was obtained by computing the Variation of Information. We proceeded by evaluating the mean of all pairwise VI,  $\Delta\text{MVI}$ , scanned along all possible thresholds  $d_i$ , and next identified the maximum value that marks the optimal partition. That partition should give the minimum number of communities in the network with the richest information content, and excluding the trivial case of a single community. For instance, in the experiment shown in Figure 4.4D, a sharp jump in  $\Delta\text{MVI}$  was observed at  $d_i=0.93$ . By applying this threshold in the dendrogram, we found two characteristic communities and that are marked in orange and green (Figure 4.4B). Clusters that were not included in any community were considered as ‘independent’ clusters—they are indicated with a horizontal dotted line in the raster plot. These clusters might be structurally disconnected and they just activate randomly. Additionally,

we can notice in the grouping of clusters represented in the dendrogram of Figure 4.4B that those clusters that fire together in a small community tend to participate within a major community, giving rise to a hierarchical structure of modules and submodules.

Indeed, the clusters presented a modular dynamics where the number of communities could vary, for instance along the developmental day *in vitro*. As we explained in the Chapter 2, these clustered cultures start displaying spontaneous activity by  $DIV=5$ . At this early stage of development, small groups of typically 2 – 3 clusters (and that are physically close) tend to get activated together; forming segregated small communities. At middle stages of the development,  $6 \lesssim DIV \lesssim 15$ , the culture is sufficiently mature for all the connections to be established, giving rise to stable number of 2 – 3 distinct communities. In general we observed that about 70% of the clusters participated in a big community, other 20% shaped a second community, and the remaining 10% comprised clusters that were either totally disconnected from the rest of the network or cliques of 2 – 3 clusters that formed a third or more communities (Figure 4.4E). At higher stages of development,  $DIV \gtrsim 14$ , the number of communities stabilized around 1 – 2, and it was even frequent to observe a global coherent behavior where nearly all the clusters were activated as a single community.

### 4.2.1 Robustness of the inferred functional organization

#### Comparison with other hierarchical constructions

We tested other metrics to evaluate the sensitivity of our approach to the definition of distance. We investigated the *euclidean distance*, *cosine similarity* and *cross correlation*, and found very small differences as found compared to the Jaccard metrics. More specifically, as we can observe in Figure 4.5A, the Pearson correlation coefficient between the values of the  $\tilde{Z}$  evaluated by the Jaccard metrics and by the cosine similarity metrics provided  $r = 0.98$  for the

representative experiment of Figure 4.4. Nearly negligible variations were detected in the similarity values using one metrics or the other. Additionally, by evaluating the equation  $\psi = (\text{Jacc} - \text{Cos})/(\text{Jacc} + \text{Cos})$  (Figure 4.5B), we can easily visualize that the small differences appeared at low similarity distances, i.e. where the 'more similar clusters' are grouped, and therefore the arrangement of the established communities remained untouched. Indeed, we computed the VI between our final partition, i.e. the clusters that form the communities using the Jaccard metrics, with respect to the partitions that resulted from applying the other metrics, and always obtained 0, i.e. no difference.

We also analyzed the sensitivity of the results to other linkage criteria different than our 'average linkage', and tested for instance the 'single linkage' one. This linkage joins two clusters or 'composites' that have the minimum distance between them. We obtained similar results using the average linkage or the single one. AS shown in Figure 4.5C, the Pearson correlation fit between the  $\tilde{Z}$  values using one linkage criterion or the other for the experiment of Figure 4.4 provided  $r = 0.98$ . Again, the small differences were found at the first steps of the hierarchical construction (Figure 4.5D-E). Once the threshold was applied, the clusters that formed the distinct communities were identical independently of the linkage criterion taken.

### **Comparison with other community detection algorithms**

We compared our clusters' organization in communities, as obtained using the VI for threshold selection, with other approaches such as the 'Louvain' method (Blondel et al., 2008) or the principal component analysis, PCA (Jolliffe, 2002).

The 'Louvain' methods proceeds as follows. In a first phase of computation, each neuronal cluster is assigned to be a community by itself, and therefore there are initially as many communities as number of clusters. Then, for each cluster  $i$ , the algorithm considers its neighbors  $j$  and evaluates the

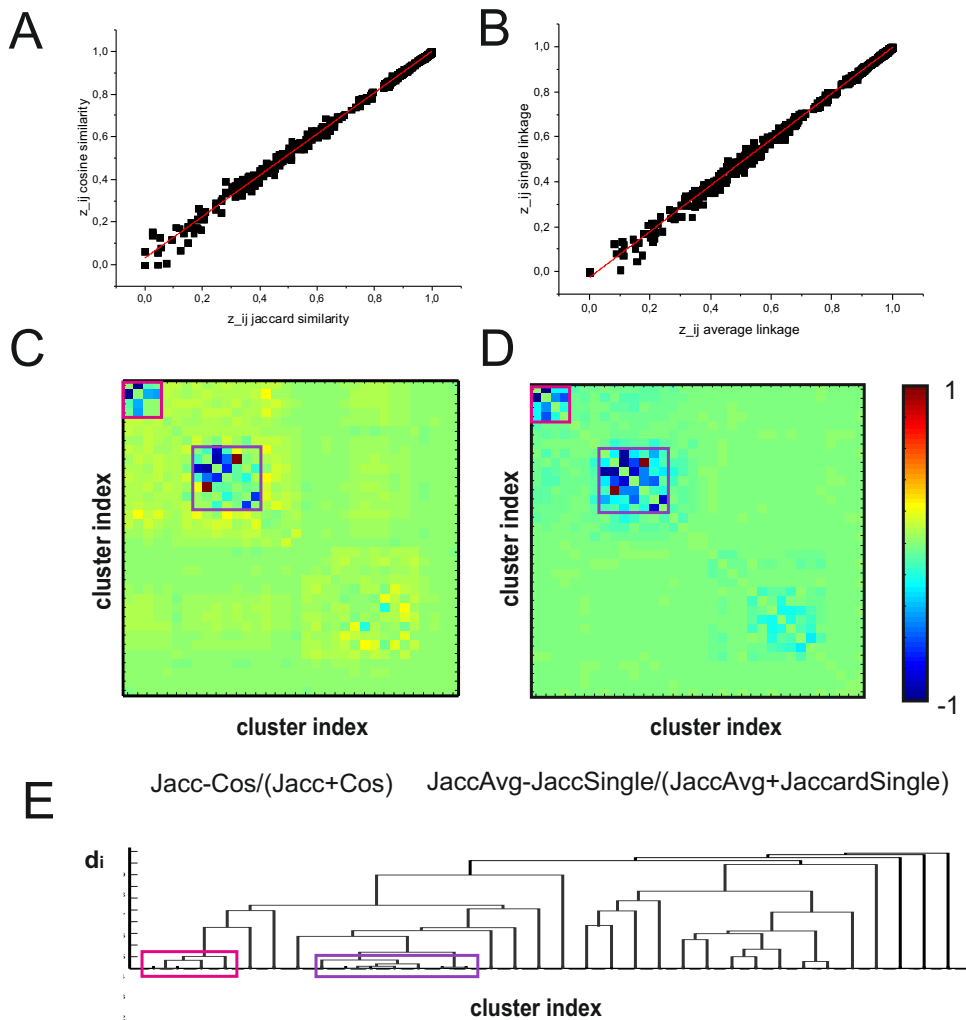


**Fig. 4.5 Comparison with other hierarchical constructions.** **A**, Comparison of the  $\tilde{Z}$  similarity values between the ‘Jaccard’ (abbreviated *Jacc*) and ‘cosine similarity’ (abbreviated *Cos*) metrics. The good Pearson correlation between them ( $r = 0.98$ ) highlights their excellent agreement in characterizing the network traits. **B**, Comparison of the  $\tilde{Z}$  similarity values between an analysis using the ‘average linkage’ criterion and the ‘single linkage’ one. The good fit ( $r = 0.98$ ) reflects the validity of any of the two methods. **C-D**, Evaluation of the similarity values differences using  $\psi = (Jacc - Cos) / (Jacc + Cos)$ , for either the single or average linkage.  $\psi = 0$  when the similarity values using one metrics or the other are equal ( $Jacc = Cos$ ). At the other extremes, for  $Cos = 1$  and  $Jacc = 0$  then  $\psi = -1$ ; and for  $Jacc = 1$  and  $Cos = 0$  then  $\psi = 1$ . Only small differences are found, which essentially affected only the submodules grouped at the lowest part of the dendrogram. **E**, Dendrogram built using the Jaccard similarity with average linkage. Boxes are colored according to the above matrices, and highlight the small observed differences.

gain in modularity that would result by removing the cluster  $i$  from its community and grafting it into the community of the cluster  $j$ . When the gain is positive, the cluster  $i$  is then placed into the community of cluster  $j$ . This process is iteratively repeated until no improvement in modularity is achieved, giving rise to a set of communities. Then, in a second phase of computation, the algorithm creates a network where the ‘nodes’ are the previously found communities and the links between these ‘nodes’ are the sum of the weights between connected clusters within the inferred communities. The first phase is then called again, so that communities gradually contain more clusters. The whole process is iteratively repeated until the community structure is stabilized and the maximum of modularity is reached. A remarkable feature of this algorithm is its hierarchical nature since, in every step, a hierarchy of communities within communities is built. The resolution parameter  $\gamma$  informs about the level within the hierarchy. In our experiments, for  $\gamma = 0$  all the clusters formed a single community, and for  $\gamma > 2$  each cluster formed isolated communities.

We next calculated the VI and the MI between each resulting partition in the Louvain method (screening  $0 \leq \gamma \leq 2$ ) with our optimal partition. We observed that there is always a well-defined range in  $\gamma$  values that minimizes and maximizes the VI and the MI. The final  $\gamma$  used to identify the ‘Louvain’ characteristic modules belonged to that range. We observed slight differences in the classification of modules by applying our method and the Louvain one (VI  $\simeq 0.04$ , MI  $\simeq 0.93$ ). These differences are associated to the classification of the ‘independent’ clusters. These clusters tend to be grouped at the last level in the hierarchical construction (the top values in the dendrogram). More specifically, we calculated in Figure 4.6A the VI and the MI between the partitions obtained by the Louvain approach and our method, and for diverse Louvain resolution parameters  $\gamma$  of the representative experiment of Figure 4.4. We observed that there was always a range (in this case,  $0.6 \simeq \gamma \simeq 1$ ) where the difference is minimum. The clusters’ arrangement in this range was

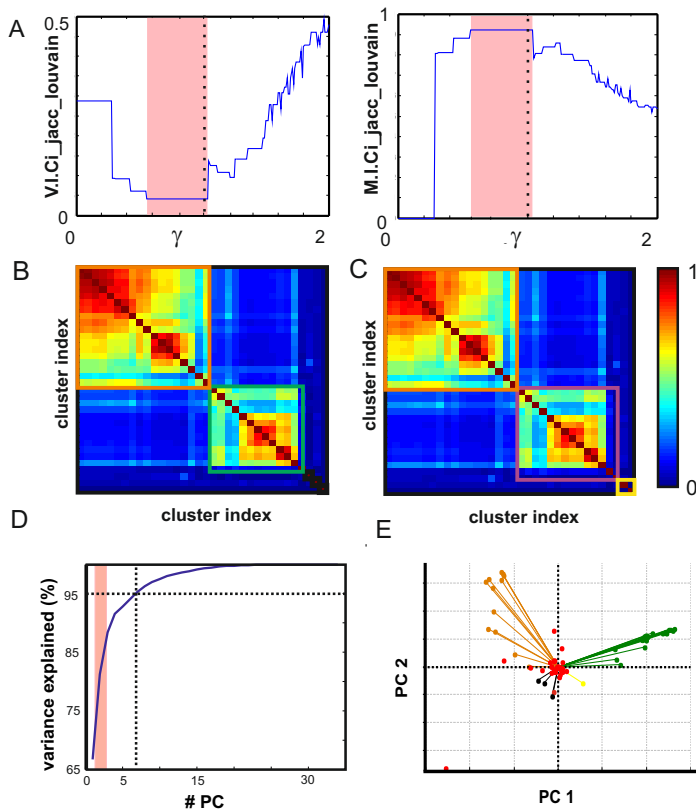


**Fig. 4.6 Other community detection methods.** **A**, VI between the optimal partition using the Jaccard metrics (Figure 4.4) and Louvain partitions at gradually higher resolution limit parameter  $\gamma$ . VI is minimum in the region  $0.6 \leq \gamma \leq 1$  and therefore in this interval the two partitions practically coincide. **B**, Similar results can be found by evaluating the MI. For the same  $\gamma$  range both partitions are very similar and MI is maximum. **C**, Comparison of the derived similarity matrices. Left corresponds to the Jaccard construction shown in Figure 4.4, with the two main communities outlined with color boxes together with independent clusters (black). Right corresponds to the Louvain construction with  $\gamma = 1$ . Cluster indexing is the same as the Jaccard one. The grouping of clusters into communities is practically the same except for two independent clusters that appear as a third community (bottom-right yellow outline). **D**, Cumulative distribution of the variance as a function of the number of principal components (PCs). The first principal component by itself explains less than 80% of the variance content, which is not sufficient. 85% can be reached by including the second principal component (pink rectangle). The dashed lines mark the number of principal components required to explain the 95% of the information, 6 in our case, which is impractical to represent in a plot. **E**, Data contents of the two first principal components. The colored dots are the coefficients of the main PCs into the projected PC space. The direction and length of the vectors reflect the contribution of each cluster to the two PCs. The colors code the distinct communities according to the classification found above. The derived arrangement of communities differ from our method solely in the independent clusters, which are grouped as a third community (black dots), and in a cluster that now appears as independent (yellow)

similar (Figure 4.6C) to the obtained with our method (Figure 4.6B). In particular, the clusters' pattern in the first community (orange box in Figure 4.6B) was exactly the same (orange box in Figure 4.6C), and the arrangement of clusters within the second community (green box in Figure 4.6B) was nearly identical (purple box in Figure 4.6C). As we stressed before, the small differences resided in the distribution of the 'independent clusters' within the communities (black boxes in Figure 4.6B).

Finally, concerning PCA analysis, we applied this algorithm to the similarity matrix of the representative experiment, and plotted the values on the principal component space (Figure 4.6E) to identify the different communities. Although PCA did not allow to represent all the information in just in 2-3 principal components (Figure 4.6D), the final community structure of the two main principal component slightly differs with respect to the functional organization achieved with our method. In particular we obtained similar grouping of clusters in communities except n one (colored in yellow, Figure 4.6E).

We conclude that the final functional organization using these techniques is practically the same as ours, with small differences that appear in the assignment of the clusters with lower similarity values (the top of the dendrogram, high  $d_i$ ) and that correspond to the independent clusters. These clusters are indeed the ones that have erratic behavior and exhibit poor firing.

### 4.3 Characterization of the effective connectivity

The effective connectivity matrix was constructed using the method based on the analysis of the time delays between clusters' activations. Briefly, sequences were first identified by using a cut-off of 200 ms, ruling out any causal influence between consecutive clusters' activations above this threshold. Then, all the clusters that participated within a firing sequence were pair-wise linked with a weighting function that depended on the time delay between

clusters' activations. The shorter the time delay, the stronger the weight of the link. Additionally, when the time delay between clusters' activations was either too short for detection or activation occurred simultaneously, clusters' inter-relation was treated as a bi-directional link, since no 'causality' could be inferred. This simultaneous events occurred rarely, by 5% of the cases. Finally, the total weight of the link was established as the sum of all the computed weights in all the observed firing sequences. The final connectivity layout was both directed and weighted, i.e. shaping strictly speaking an effective connectivity map.

### 4.3.1 Analysis of the effective networks

We carried out measurements in 15 different clustered networks, and labeled them with capital letters as networks 'A' – 'O'. In order to compare their properties with the ones from cultures with a distinct structure, we applied the same analysis to 6 cultures characterized with a homogeneous distribution of neurons, and labeled them as networks 'P' – 'U'. We computed the effective networks of the 15 ('A' to 'O') realizations of clustered cultures, as well as the 6 ('P' to 'U') homogeneous ones, and analyzed their major topological traits. Firstly, for each culture we obtained the number of nodes, the number of edges, the average degree of the networks, and its average strength. The investigated networks and their main topological measures are summarized in Table 4.1. Although young cultures display a richer activity, in general all networks presented a similar number of nodes and a comparable effective connectivity.

Three representative examples of the investigated effective networks for the clustered configuration are shown in Figure 4.7. The position of the nodes and their size are the same as the actual clusters for easier comparison. Edges in the directed network are both color and thickness coded to highlight their importance, with darker colors corresponding to the highest weights. This representation revealed those pairs of clusters that maintained a persistent

Culture type	Network	DIV	burst rate (min <sup>-1</sup> )	Number of nodes	Number of edges	Average degree	Average strength	Assortativity Pearson (wh)	Assortativity Spearman (wh)
<b>Clustered</b>									
	A	5	7.35	38	544	14.32	33.71	0.642 ± 0.044	0.605 ± 0.036
	B	6	6.80	34	1044	30.71	131.94	0.404 ± 0.040	0.449 ± 0.035
	C	6	6.55	29	762	26.28	142.45	0.440 ± 0.036	0.425 ± 0.041
	D	7	2.99	27	471	17.44	32.53	0.442 ± 0.064	0.414 ± 0.063
	E	7	0.87	29	660	22.76	22.83	0.402 ± 0.043	0.396 ± 0.045
	F	8	0.85	32	750	23.44	12.89	0.317 ± 0.064	0.287 ± 0.057
	G	8	0.79	35	395	11.29	4.99	0.528 ± 0.086	0.553 ± 0.063
	H	9	1.17	32	722	22.56	30.99	0.355 ± 0.061	0.377 ± 0.052
	I	10	3.19	27	486	18.00	81.88	0.460 ± 0.046	0.478 ± 0.046
	J	12	2.42	24	456	19.00	97.32	0.326 ± 0.049	0.322 ± 0.046
	K	13	1.28	19	252	13.26	38.27	0.729 ± 0.062	0.699 ± 0.051
	L	14	3.40	17	116	6.82	28.25	0.586 ± 0.076	0.552 ± 0.077
	M	14	1.40	25	205	8.20	16.71	0.356 ± 0.084	0.309 ± 0.087
	N	14	1.86	26	437	16.81	30.63	0.698 ± 0.060	0.664 ± 0.061
	O	14	4.91	29	391	13.48	38.77	0.372 ± 0.069	0.364 ± 0.061
<b>Homogeneous</b>									
	P	6	3.30	814	453812	557.51	41.24	0.059 ± 0.005	0.055 ± 0.005
	Q	8	4.10	589	243606	413.59	27.66	0.038 ± 0.007	0.036 ± 0.007
	R	10	0.27	562	35379	62.95	2.46	0.112 ± 0.023	0.125 ± 0.023
	S	15	1.05	1107	239517	216.37	9.47	0.111 ± 0.008	0.107 ± 0.008
	T	16	0.47	694	274278	395.21	24.89	0.077 ± 0.007	0.067 ± 0.006
	U	16	0.78	703	155643	221.40	10.34	0.040 ± 0.009	0.037 ± 0.009

**Table 4.1 Network measures of clustered and homogeneous cultures.** The table shows the major topological descriptors of the functional networks investigated, 15 corresponding to a clustered neuronal organization and 6 to a homogeneous one. Average degree refers to the mean number of connections per node, and the average strength to the mean weight per node. All the cultures were maintained and studied identically (see Methods). Experiments covered almost 10 days of development *in vitro* (DIV). All clustered cultures were strongly assortative, while the homogeneous ones tended to be weakly assortative, or neutral.

causality relationship over time. Nodes are also color coded according to their strength, i.e. the total weight of the in- and out-edges.

The effective networks exhibited some interesting features. First, there were groups of nodes that formed tightly connected communities. These topological communities actually reflected the most frequent firing sequences or the dynamical modules (see Section 4.3.6). Second, nodes preferentially connected to neighboring ones with some additional long-range connectivity, and often following paths that were not the major physical connections. As an example, the network 'H' in Figure 4.7 shows effective connectivity paths that are very different from its major structural connections. This indicates that the structural connectivity of the network cannot be assessed from just an examination of the most perceivable processes. And third, we observed that there was no correlation between the width of the physical connections and their weight, or the size of the nodes and their strength, indicating that the dynamical traits of the network cannot be inferred from its physical configuration, stressing the importance of our functional study.

We also calculated the total strength distribution for all the clustered experiments normalizing first the effective connectivity by its maximum weight (Figure 4.8A). The distribution presents a group of clusters with nearly negligible strengths, meaning that their frequency of participation was very low. In principle, one can think that these clusters presented just low firing rates and that they co-activated just few times with others. That is one possibility but it could exist many others. Discarding possible 'false detections' in the analysis of the data, which is rare given the generally good signal-to-noise ratio, we conjecture two other explanations. First, these clusters could be 'independent' units, i.e. clusters that were structurally disconnected from the network and that fired in an independent way, either randomly or periodically. And, second, these clusters could operate as modules' connectors, i.e. clusters that were responsible for integrating different segregated modules. On the other hand, the strength distribution also shows a high spectrum of nodes with

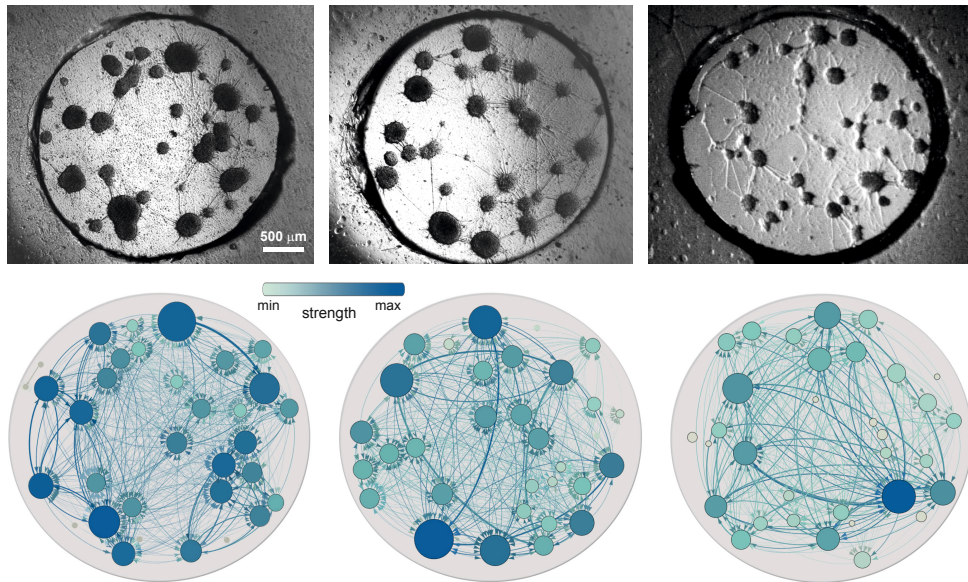


**Fig. 4.7 Neuronal cultures and effective networks.** Top: Bright field images of 3 representative neuronal cultures at different *days in vitro*. Bottom: Corresponding effective networks obtained from the directed and weighed construction described in Methods. From left to right, the pictures correspond to the cultures labeled D, H and O in Table 4.1. Only active clusters are used in the construction of the functional network. The size of the nodes is similar to the ones observed in the cultures, and facilitates the comparison of the functional network with the real culture. In the functional networks, the edges are both color and thickness coded according to their weight, while the nodes are only color coded according to their strength. The darker the color, the higher the value.

low and medium strength and few nodes with remarkable high strengths. The latter could be related to the existence of hubs in the network.

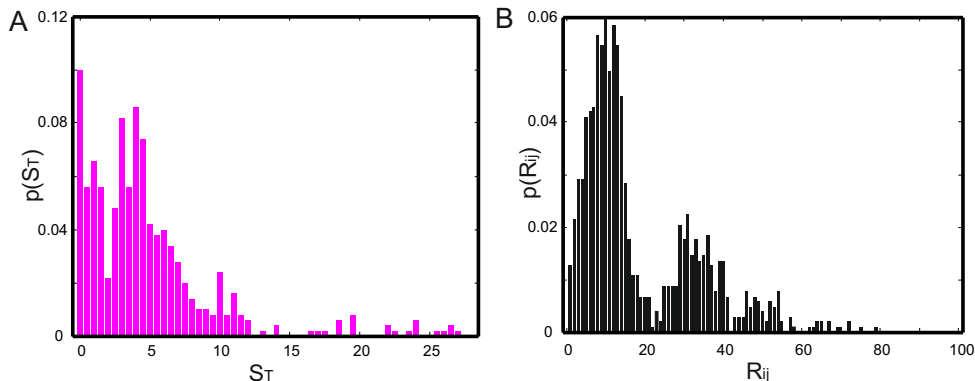


**Fig. 4.8 Strength distribution and real distance pairwise distribution.** **A**, Probability distribution function of strengths. They are calculated from the effective matrix and normalized by the maximum. No null model is introduced in this calculation. **B**, Probability distribution function of physical distances over the substrate (in pixels), as obtained from the analysis of the ROIs.

Finally, another interesting observation arises from the examination of the histogram of the physical distance between interacting clusters (Figure 4.8B). The histogram is characterized by the presence of a number of peaks. Indeed, the highest peak and that corresponds to short distances, is associated to the large number of nodes that preferentially connect to their nearest neighbors. However, other peaks at well established larger distances are also very clear. This feature indicates that clusters connect to second and further neighbors, and that the distance between connected units is maintained. Hence, we conclude that the apparent random clusters' configuration has some structural order for which we do not have an explanation, but that clearly drives the clusters to organize and develop following a characteristic distance over the substrate.

### Significance test and normalization

As we commented before, independent clusters that fired randomly or periodically within the time window of another sequence could inappropriately be interpreted as ‘co-active’, therefore introducing artifacts to the inferred effective connectivity. Although such events of accidental participation were rare (by 2%), we carried out a statistical significance test to discard them in a formal way. Additionally, this test provided an efficient way to normalize the weights. Normalization is a fundamental step to compare for instance different network conditions or experimental realizations. The significance test was carried out by considering surrogates formed by a random reshuffling of the time events of activation (see Section 3.4.3) while preserving the total number of firings per cluster. A total of 500 surrogates were considered per network. The final weights were then normalized using the  $z$ -score test. Since our first interest is to disregard linear correlations, this null model was sufficient.

To better understand the implementation of the significance test, Figure 4.9 shows in detail that analysis for the clustered network ‘B’. First of all, we obtained its initial (raw) effective weights’ distribution (Figure 4.9A) together with its respective random weights’ distribution from the 500 surrogates (red dashed line). We can first notice that the initial weights’ distribution resembles an exponential-like or a power law, with a high number of links with nearly negligible weights and few ones with high weights (inset of Figure 4.9A). The random model gives rise to a Gaussian weight distribution with a mean corresponding to the one of the actual data. The  $z$ -score test compares the random data with the actual one, and provides a new, normalized dataset in units of standard deviation with respect to the null model (Figure 4.9B). Those links with a high weight score appeared frequently and therefore their clusters were strongly connected. At the other extreme, negative weight scores reflected those links that were less connected than in a random configuration and therefore had to be disregarded. By setting to

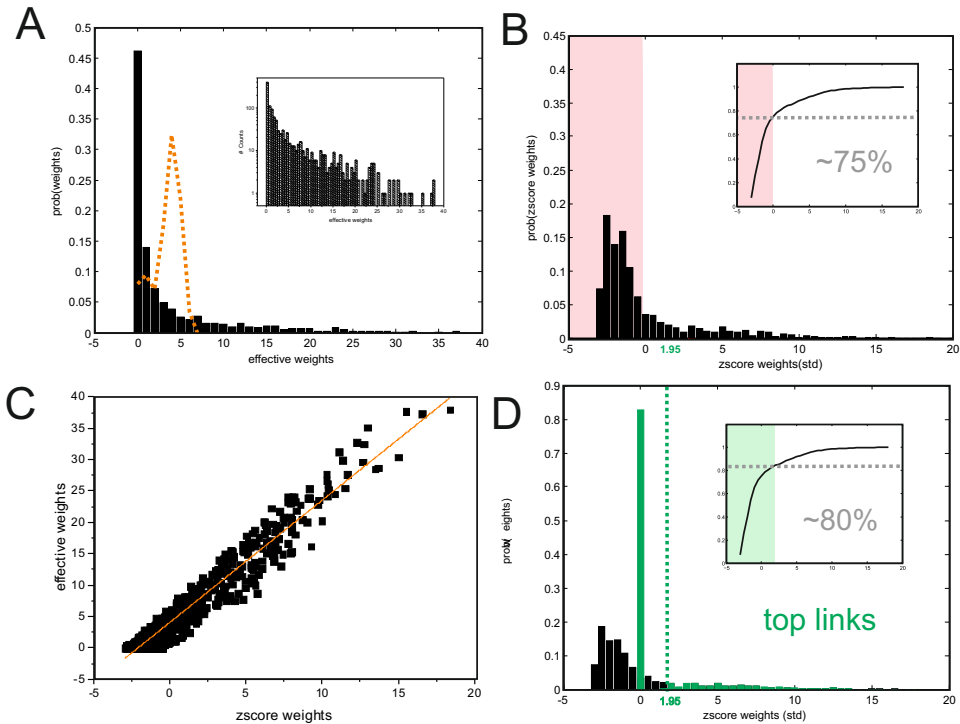


**Fig. 4.9 Effective and  $z$ -score weight distributions.** **A**, Weights' distribution of the links from network 'B' (black) compared to the distribution obtained after a reshuffling of the activation times of the clusters (500 surrogates, red). The inset shows the original dataset with the y-axis in logarithmic scale. **B**, The same weights' distribution after the  $z$ -score normalization. The weights are now shown in standard deviation units. Negative weight values (pink region) reflect those links that were less connected than in a random configuration and were therefore not statistically significant. The inset shows the cumulative weight distribution. About 70% of the weights' scores appeared negative after the  $z$ -score normalization and hence disregarded. **C**, Correlation between the effective initial weights' values and the normalized ones. The relation is linear with  $r = 0.97$ . **D**, Top links (highlighted in green) are those above  $1.95\sigma$  (95% confidence interval).

zero solely these negative values we pruned around 75% of the connections (Figure 4.9B). In general, weight scores before and after normalization scaled linearly (Figure 4.9C), and indicates that normalization does not change the structure of the effective connectivity. For the particular dataset shown, Pearson correlation provided  $r = 0.97$ , and for all inferred networks it was  $r = 0.95$  on average. Those effective links with weight values above  $1.95\sigma$  (95% confidence, Figure 4.9C) were the *top links* of the network, shaped the ‘skeleton’ of the effective connectivity and comprised about 15 – 20% of all normalized links (Figure 4.9D).

### Effective networks in homogeneous cultures

As we described in Chapter 2, the seeding of neurons in cover glasses previously coated with poly-l-lysine gave rise to neuronal cultures with a quasi-homogeneous distribution of neurons. Spontaneous activity in these homogeneous cultures was typically recorded at 100 frames/s, which sufficed to extract the time delays between consecutive neuronal activations. The analysis of their spontaneous activity traces was analyzed in the context of our effective connectivity model, finally procuring their map and topological properties. A representative homogeneous culture and its corresponding effective network is shown in Figure 4.10.

Our interest to study homogeneous neuronal networks was to compare clustered networks with others with a radically different network architecture. As we will see in other parts of the thesis, topological measures such as assortativity, or the resilience of the networks to damage, highly contrasted in the two kind of configurations.

#### 4.3.2 Assortativity

Table 4.1 summarizes the major topological properties of the studied clustered networks. We found of particular importance the assortativity measure given

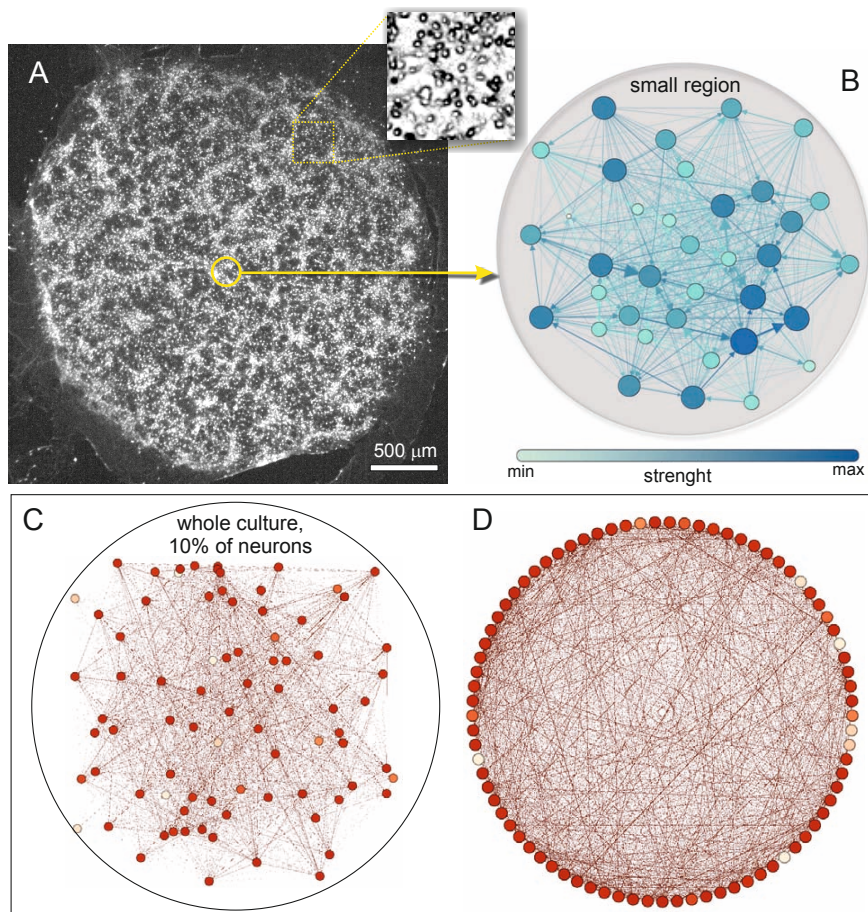


**Fig. 4.10 Analysis of homogeneous cultures.** **A**, A typical culture 3 mm in diameter containing  $\simeq 3000$  neurons, which that can be well identified either as bright spots in the fluorescence recordings or as circular objects in bright-field images (small panel on the right). The particular experiment shown here corresponds to network ‘P’ in Table 4.1, with a total of 814 neurons manually selected over the images and monitored along 45 min. **B**, Given the large number of nodes analyzed and the high average degree of the resulting network ( $\sim 550$  effective connections per neuron), a representation of the complete functional network is unpractical. As an example of the obtained functional networks, we show only the functional links within a small region at the center of the culture and containing 40 neurons. Connections are both color and thickness coded according to their weight. Nodes are color coded according to their strength. **C**, As an alternative representation, we show a 10% of the population (81 neurons randomly chosen), each neuron showing the 10% of its links. Nodes and links are color coded according to their strength and weight, respectively. **D**, A ring graph of the same neurons shows that most of them display a similar connectivity, in contrast to the strong modularity and variability in connectivity exhibited by the clustered networks.

its importance in the context of network resilience. Since our networks are directed and weighted, we extended the definition of assortativity to take into account both characteristics, as described in Section 3.4.5).

Culture type	E+I	DIV	burst rate (min-1)	Number of nodes	Number of edges	Average degree	Average strength	Assortativity Pearson	Assortativity Spearman
<b>Clustered</b>									
	<b>1</b>	5	1.82	32	612	19.125	33.77	0.376±0.058	0.378±0.056
	<b>2</b>	5	2.04	34	692	20.35	38.33	0.519±0.062	0.487±0.052
	<b>3</b>	7	2.43	27	680	24.28	82.84	0.590±0.050	0.470±0.061
	<b>4</b>	8	4.82	32	929	29.96	238.71	0.345±0.027	0.327±0.031
	<b>5</b>	8	4.06	35	1214	31.11	196.69	0.365±0.040	0.341±0.041
	<b>6</b>	9	1.79	31	772	24.90	64.57	0.332±0.041	0.286±0.044
	<b>7</b>	9	2.93	28	562	20.07	95.24	0.636±0.045	0.531±0.049
	<b>8</b>	14	0.50	26	36	5.23	5.43	0.690±0.082	0.720±0.060

**Table 4.2 Network measures of ‘E+I’ clustered networks.** The table shows the major topological descriptors of 8 effective networks of clustered cultures recorded with both excitation and inhibition active (‘E+I’ networks). 4 of the shown experiments, labeled with capital letters, correspond to the same networks measured in ‘E-only’ conditions listed in Table 4.1. Experiments covered almost 10 days of development *in vitro*. All ‘E+I’ networks were also strongly assortative.

For our experiments, we computed the Pearson  $\rho^{PW}$  and the Spearman  $\rho^{SW}$  correlations of the weight-to-weight data. Both correlations provide values in the range  $[-1, 1]$ . Positive values of the weighted assortativity indicate that nodes with similar strength tend to connect to one another, while negative values mean the preferred interconnectivity of nodes with different strength. In Table 4.1 we can observe that all clustered networks (labeled ‘A’-‘O’) exhibited a positive weighted assortativity, in the range  $0.32 < \rho^{PW} < 0.73$  for the Pearson construction and  $0.29 < \rho^{PW} < 0.7$  for the Spearman one. Although the values fluctuate across different cultures, the two assortativity measures provided the same value within statistical error, and reflect that network size corrections provided by the Spearman’s treatment have little influence in strongly assortative networks.

An example is provided in Figure 4.11. The data corresponds to the clustered network ‘B’, and plots, for every functionally linked between clusters  $(i, j)$ , the relation between the out-strength of node  $i$  and the in-strength of node  $j$  (Figure 4.11C). In the plot, the size of the dots is proportional to the

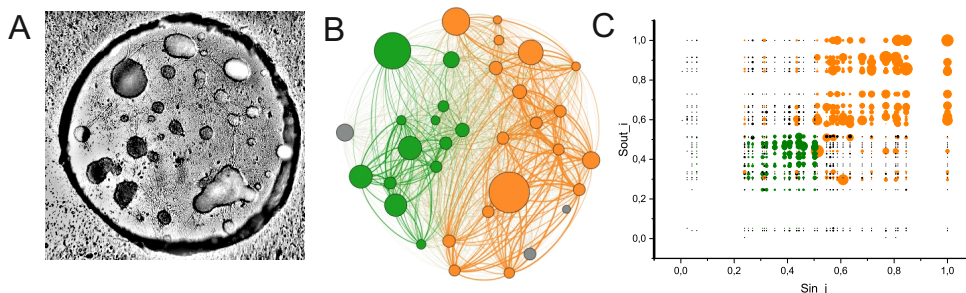


**Fig. 4.11 Assortativity measure in clustered networks.** **A**, Bright field image of the representative clustered network shown in Figure 4.4. **B**, The resulting effective network using our method based on activation delays. Arrows in the links are not shown for simplicity. Nodes and links are colored coded according to their encompassment in the communities shown in Figure 4.4. **C**, The weighted assortativity measure accounts for the correlation between the out- and in-strengths of every pair of linked nodes  $(i, j)$  in the network, and taking into account the weight of the link  $w(i, j)$ . For every pair of connected nodes, the out-strength of node  $i$  and the in-strength of node  $j$  are plotted as a dot. Nodes belonging to the same community are drawn with the same color as the community. Otherwise, they appear black. The size of the dots is proportional to the weight of the link  $w(i, j)$ .

weight of the corresponding link. By examining the plot one can easily observe a positive slope, i.e. an assortative connectivity mixing among clusters. When both nodes  $i, j$  belong to the same module the corresponding dot in the plot is colored coded according to their module color. This coding is convenient and shows that the positive correlation mainly raised from the out- and in- connections confined within the modules and with a wide spectrum of strength values.

For completeness, the above network measures were also analyzed in experiments with a homogeneous distribution of neurons (labeled ‘P’ – ‘U’). The results are summarized in Table 4.1. Interestingly, the assortativity values were much lower (by an order of magnitude on average) than the ones for clustered cultures, in the range  $0.04 < \rho^{PW} < 0.11$  for the Pearson’s and  $0.04 < \rho^{PW} < 0.12$  for Spearman’s.

Finally, to investigate the generality of the assortative traits in the clustered networks, we analyzed effective networks derived from experiments in which both excitation and inhibition were present (‘E+I’ networks). We note that in

our standard experiments we considered only excitation ('E-only' networks) to simplify the biochemical complexity of the system, blocking inhibition with bicuculine. Interestingly, the dynamics was qualitatively similar in either condition, and the topological traits were also comparable. Table 4.2 shows the major topological properties of 8 experiments in 'E+I' conditions. All networks presented strongly assortative values.

### 4.3.3 Rich-Club properties

To assess the importance of the measured assortativity values, we also computed the weighted rich-club (see Section 3.4.6). The rich-club phenomenon refers to the tendency of nodes with high degree to form tightly interconnected communities, compared to the connections that these nodes would have in a null model that preserves the node's degree but otherwise is totally random. Given the positive assortativity found, we analyzed whether this finding was also reinforced by the existence of rich-club structures.

The weighted formulation for the rich-club takes into account the node's strength instead of the degree. The evaluation of the rich-club  $\phi^{\text{unc}}(s_T)$  (relative to the uncorrelated null case) is performed by computing the ratio between the connectivity strength of highly connected nodes and its randomized counterpart, and for gradually higher values of the strength threshold  $s_T$ . The detailed calculation is described in the Section 3.4.6, and the results of the analysis for representative networks are shown in Figure 4.12. Ratios larger than 1 indicate that higher strength nodes are more interconnected to each other than what one would expect in a random configuration. On the contrary, a ratio less than 1 reveals an opposite organizing principle that leads to a lack of interconnectivity among high-degree nodes. After the calculation of the ratios for all the studied clustered networks, we found positive ratios in a wide range of  $s_T$  values, reflecting a tendency towards the creation of rich-clubs (Figure 4.12). On the contrary, homogeneous cultures exhibited a

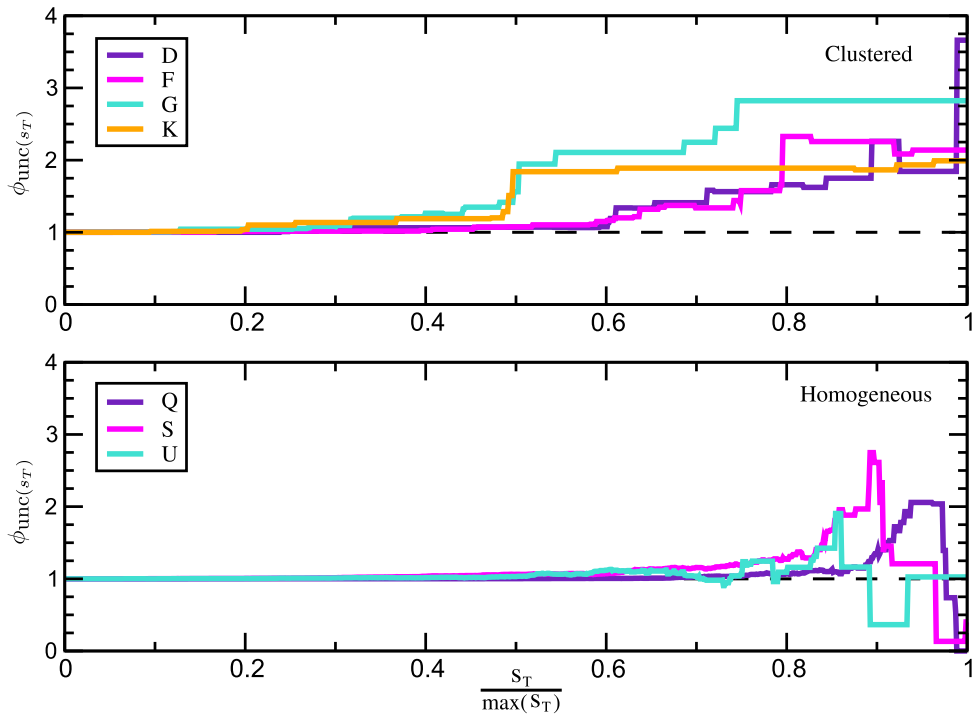


**Fig. 4.12 ‘Rich-club’ analysis.** The evaluation of the rich-club  $\phi^{\text{unc}}(s_T)$  is carried out by computing the ratio between the connectivity strength of highly connected nodes and its randomized counterpart,  $\phi^{\text{unc}} = W_{s_T} / W_{s_T}^{\text{unc}}$ , and for gradually larger values of the strength threshold  $s_T$ . The figure shows the rich-club analysis for 4 representative clustered and 3 homogeneous cultures. Clustered networks exhibit values of  $\phi^{\text{unc}}$  systematically higher than 1 for a wide range of values of the strength threshold  $s_T$ , evidencing the existence of a rich-club core of highly connected clusters in the network. On the contrary, homogeneous cultures display a mixture of positive and negative values, and with an average around 0, ruling out the existence of the rich-club property.

neutral assortativity, with ratios slightly increasing as  $s_T$  grew, but rapidly decreasing and fluctuating afterwards (Figure 4.12).

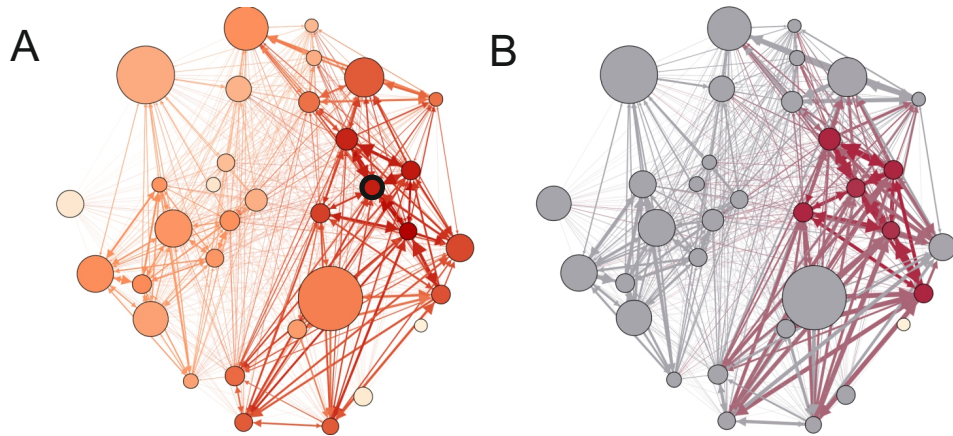


**Fig. 4.13 Identification of the ‘Rich Club’ in a clustered network.** **A**, Effective network of the ‘B’ culture, where nodes are color coded following the node total strength. The darker the colors, the higher the strength. Arrows depict the in-, and the out-weights. The node with the highest strength is encircled in black. **B**, The same effective network but highlighting in purple the subset of highly connected clusters that shape the Rich Club core. Around 20% of the clusters formed part of the Rich Club.

To illustrate the location of the Rich Club within a network, Figure 4.13 shows in detail the nodes that shape the Rich Club core for clustered culture ‘B’. Figure 4.13A pictures the effective network where the nodes’ color is associated to the node total strength. Darker colors correspond to higher strengths, with the arrows depicting the in-, and the out- weights. By examining the data along the Rich Club analysis (Figure 4.12) one can extract the subset of nodes that form it, which is actually obtained at the maximum value of  $s_T$ . The corresponding clusters are colored in purple in Figure 4.13B. The fraction of clusters that shape the Rich Club is about 17% for this particular example. These clusters are indeed linked with the majority of the other clusters in the network. In general, all the clustered networks investigated

presented the Rich Club phenomenon, and its core was encompassed the 15 – 30% of the clusters in the network.

#### 4.3.4 Hubs

As we have commented in Chapter 3, different definitions exist regarding the concept of hub. To assess whether they exist or not in our networks we used the methodology followed in Refs. (Schroeter et al., 2015; van den Heuvel et al., 2010) and that introduce the concept of *hubness score*. This score takes into account 4 topological parameters: ‘nodal strength’, ‘betweenness’, ‘local efficiency’ and the ‘participation coefficient’. The top 20% nodes within each category receive 1 score. Then, we defined as hubs those clusters that have a ‘hubness score’  $\geq 3$ .

Such an analysis is complex. In general we observed that a node with the highest value within a given category do not necessary scores well in other categories. For instance, the node with the highest strength in culture ‘B’, and that we used to illustrate the ‘Rich Club’ concept (Figure 4.13A), is neither the node with the highest betweenness nor the one with the highest local efficiency. On the other hand, the participation coefficient was calculated using the Guimera and Amaral definition ((Guimera and Amaral, 2005)) but extended to all possible moduli arrangement found. Figure 4.14 shows the difference between applying the Guimera and Amaral method to the optimal partition and screening all the possible partitions. By applying the first approach, the difference in moduli sizes overestimates the participation coefficient for the clusters that form part of smaller communities. It is precisely to overcome this effect that we calculated the participation coefficient using the second approach. Indeed, this approach reveals those clusters that both belong to an important module and strongly participate in others.

For culture ‘B’, the detailed analysis of the four network properties and their inter-relation is shown in Figure 4.15. One can notice that the different measures can correlate to one another, but in general their mutual relation is

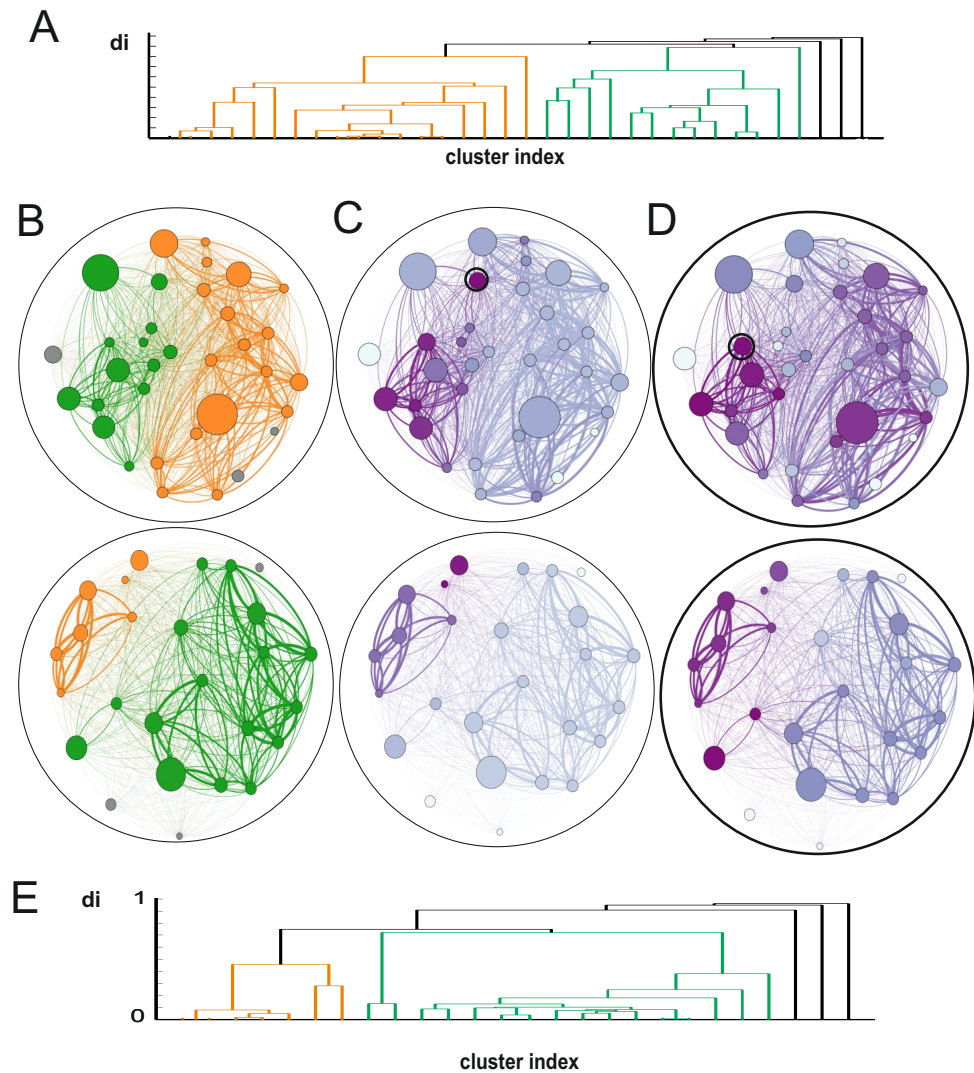


**Fig. 4.14 Participation coefficient.** **A**, Dendrogram of culture 'B'. **B**, The effective network of culture 'B', where nodes are colored according to their dynamical modules. **C**, The nodes are colored following the participation coefficient value applying the Guimera and Amaral method (for the final single partition). **D**, The participation coefficient was calculated following also the Guimera and Amaral method but averaging for the all possible partitions. **E**, Illustrative dendrogram for another experiment where the size of the final modules were more differentiated.

obscure. However, and more importantly, there are very few nodes that score particularly high, making them very attractive candidates to be hubs.

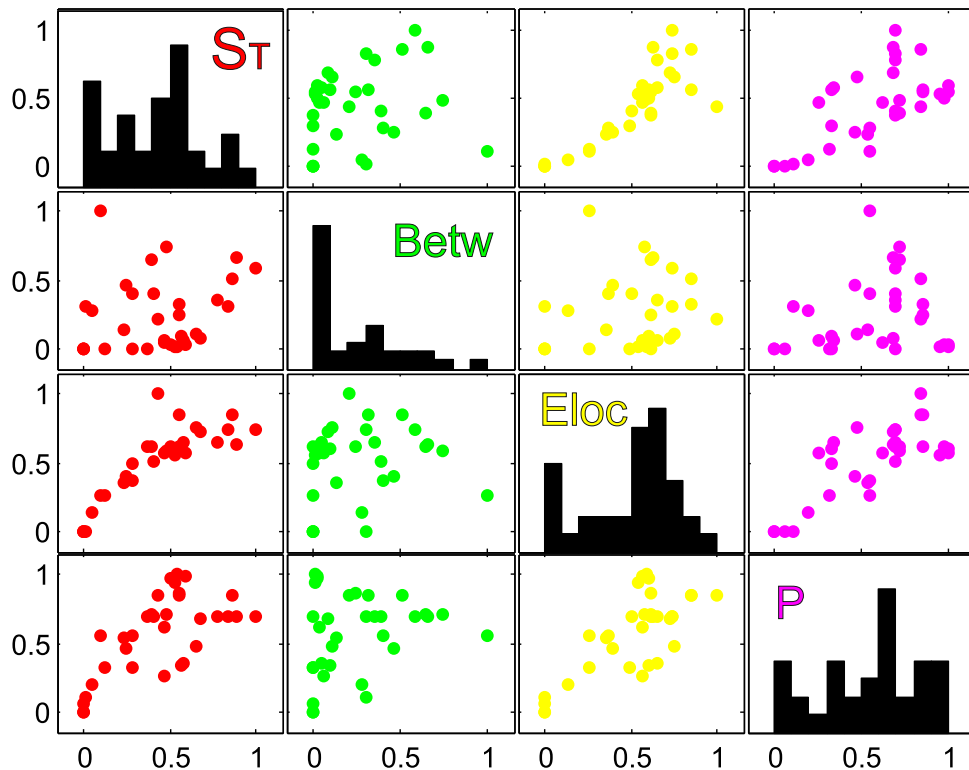


**Fig. 4.15 Analysis of the different network measures for culture ‘B’.** The plots show the relative importance of four quantities used to define a hub: total strength of the node ( $S_T$ ), betweenness (Betw), local efficiency (Eloc) and the participation coefficient (P). The diagonal shows the histograms of the normalized probability of these network properties, while their corresponding pair-wise plots are shown outside the diagonal. Some of these measures correlate to one another, e.g. the total strength and the local efficiency. Some histograms, such as the betweenness or the local efficiency, exhibit a tail of low occurrence probability at high scoring values, indicating that just few nodes score high. These “rare” high scoring nodes are the most favorable candidates to be the hubs of the network, as shown in Figure 4.16.

Top scoring nodes that coincide in the four categories are rare. Such a dispersion in scoring is illustrated in Figures 4.17 and 4.16 for the representative clustered network ‘B’. Figure 4.17A shows all the four measures that

set the ‘hubness score’, i.e. the strength, betweenness, local efficiency and participation coefficient. The four quantities finally set the hubness score, shown in Figure 4.17B at a network level. Two clusters (outline in boxes) score similarly and therefore they are both considered hubs according to our definition. The fact that the two hubs can be well characterized indicates that such a study can be extended to all networks studied.

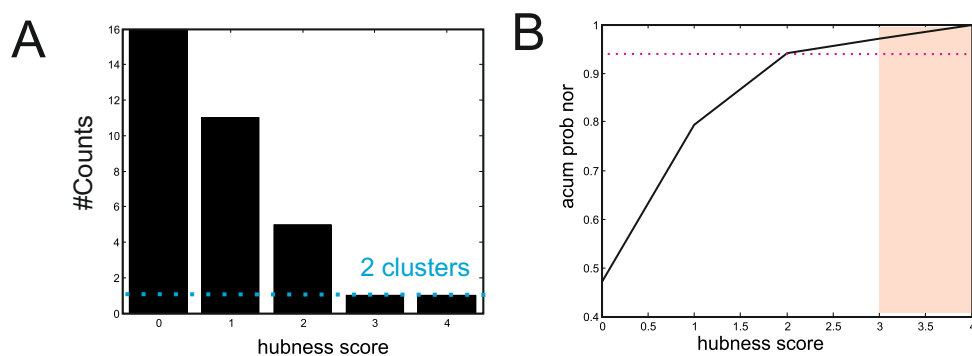


**Fig. 4.16 Hubness score.** A Histogram of the number of clusters with a given hubness score (left), and cumulated probability distribution (right). The majority of the clusters have hubness score equal to 0 indicating that these clusters do not have any relevant topological trait. Clusters with ‘hubness score’ equal to 4 correspond to the ones that belong to the top of the ranking within each category. In the experiment ‘B’, one cluster showed score = 3, and one score = 4, totaling 3% of the network. The other 97% of the clusters did not exhibit high values in three of these categories.

It is important to note that, to simplify these analyses, clusters that fired independently and therefore formed a unique moduli were considered to have a null participation.

### 4.3.5 Robustness of our effective connectivity inference method

#### Sensitivity of the results to the cut-off time

To examine whether the choice of the cut-off does or does not affect the features of the generated effective network, we performed a sensitivity analysis on this parameter. As the process of generating the network from the

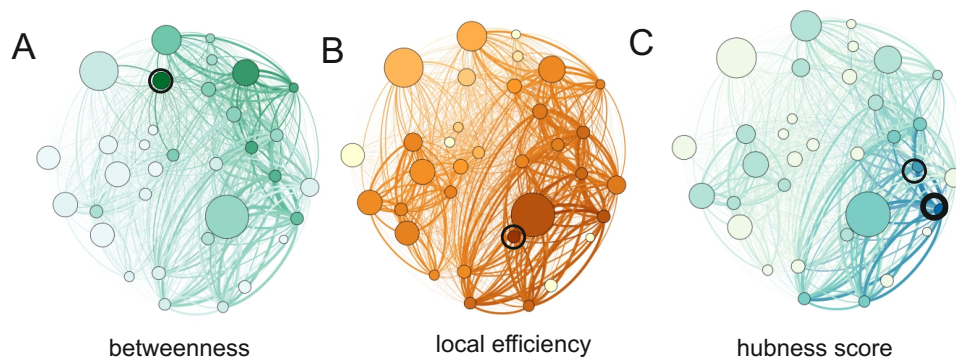


**Fig. 4.17 Summary of network measures for culture ‘B’.** A, ‘betweenness’. B, ‘Local efficiency’. C, ‘Hubness score’. The darker the color of a node, the higher the value of the corresponding measure. Links are both color and thickness coded proportionally to their weight. Black circles indicate the cluster with the highest value of the measure. Squares indicate those clusters that scored the highest and therefore identified as hubs.

sets of firing sequences is deterministic, we analyzed the influence of the cut-off value on the formed groups of firings. To quantify the variation on the firing sequences generated for different values of the cut-off, we calculated the variation of information between the grouping of bursts at a certain cut-off value and the previous one as a measure to assess their difference. We screened the cut-off values from 0 to 1000 ms (Figure 4.3) for the 15 clustered cultures (‘A’-‘O’) and for the homogeneous ones (‘P’-‘U’). In the case of clustered cultures, we found that for our cut-off value of  $200 \pm 50$  ms the variation of information was  $\sim 10^{-2}$ . In the homogeneous case, for a cut-off value of  $10 \pm 5$  ms, the variation of information provided  $\sim 10^{-3}$ . Hence, the modification of the cut-off values within these regions do not substantially change the grouping of the bursts, and therefore the generated networks are equivalent.

### Dependence of the parameter $c$ on cultures properties

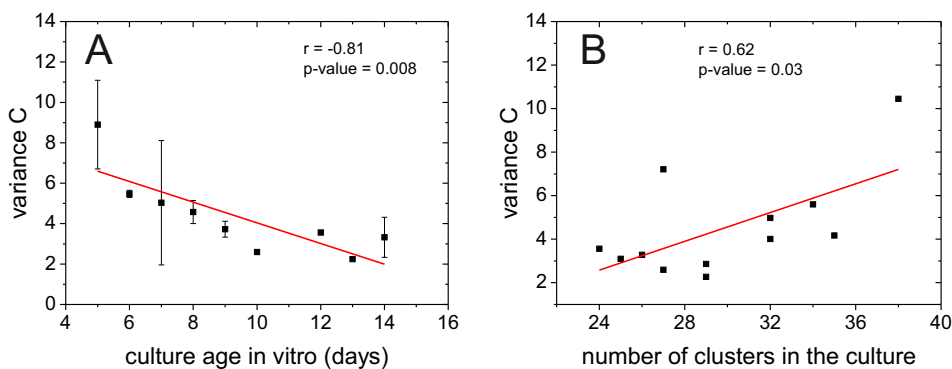
The parameter  $c$  arises from the fitting of the delay times between consecutive clusters’ activations  $\Delta t$  to a Gaussian decay, with  $\Delta t \sim e^{-x^2/c}$  (see

Section 3.4.2). Hence, different values of  $c$  would in principle affect the weights between clusters and therefore an understanding of its dependence on the culture properties is important. Although  $c$  was similar in cultures of the same size and developmental time *in vitro*, we observed that  $c$  did vary in cultures of different developmental stages. For this reason we used a specific value of “ $c$ ” for each culture.

Overall, as depicted in Figure 4.18, two major dependencies were identified, namely the day *in vitro* (DIV) and the number of clusters  $N$  in the network. The plot  $c(DIV)$  shows a very strong correlation that is caused by the changes in network dynamics during maturation. We note that  $c$  is obtained from the statistics of time delays between all pairs of clusters. Young cultures (DIV 5 – 8) had a slightly higher time delays than maturer ones, and therefore the  $\Delta t$  distribution (and in turn  $c$ ) shifted towards higher values in young cultures (Figure 4.18). On the other hand,  $c$  had a tendency to increase with the number of clusters  $N$ , although data is sparse and the significance of the correlation is not very strong.

### **Sensitivity of the effective networks to random or periodic clusters**

Random activation of isolated clusters within a culture can screen actual firing sequences of the network and therefore alter the weights between clusters. To analyze the importance of such an effect, we carried out a numerical test in which we incorporated two clusters ‘ad hoc’ in culture ‘B’, a first one firing randomly, and a second one firing periodically. Figure 4.19 shows the implementation and results of the analysis. The cluster that fires with a random distribution has the mean firing value equal to the mean firing rate of all the clusters in the culture, while the cluster that activates periodically follows the same mean inter-firing sequence as in the culture. The behavior of these ‘fake’ clusters is shown in the raster plot of Figure 4.19A. In both cases, the effect of the artificial activations was to alter the pattern of firing sequences (Figure 4.19B) and that resulted in the emergence of weak links that connected

Dependence of the variance  $C$  on culture properties

**Fig. 4.18 Variance  $c$  and culture properties.** **A**, The variance  $c$  is obtained from the Gaussian fit of the activation delays between pairs of clusters. The plot shows that  $c$  decreases with the culture age *in vitro*, indicating that young cultures display a slower dynamics (larger delay times and therefore larger variance) than mature cultures. **B**, The variance  $c$  increases with the number of clusters in the culture, indicating a broader and richer distribution of time delays as more clusters participate in the dynamics of the network. Errors bars in **A** show standard deviation.

the artificial clusters with the rest of the network (Figures 4.19C and 4.19D–left). The  $z$ –score test pruned the raw effective network and removed these insignificant spurious connections (Figure 4.19D–right). Moreover, from the detailed inspection of the dendrogram, we can observe that these clusters do not appear in any of the characteristic dynamical modules (Figure 4.19C), altogether reinforcing the importance of  $z$ –score test on the Jaccard similarity matrix.

### Comparison with other approaches for effective network inference

To assess the goodness of our construction in inferring the effective connectivity of the clustered networks, we compared our connectivity maps with those procured by information theoretic measures, specifically Mutual Information and Generalized Transfer Entropy, as described in Section 3.4.4. The analyses were directly carried out on the original fluorescence signal. The obtained

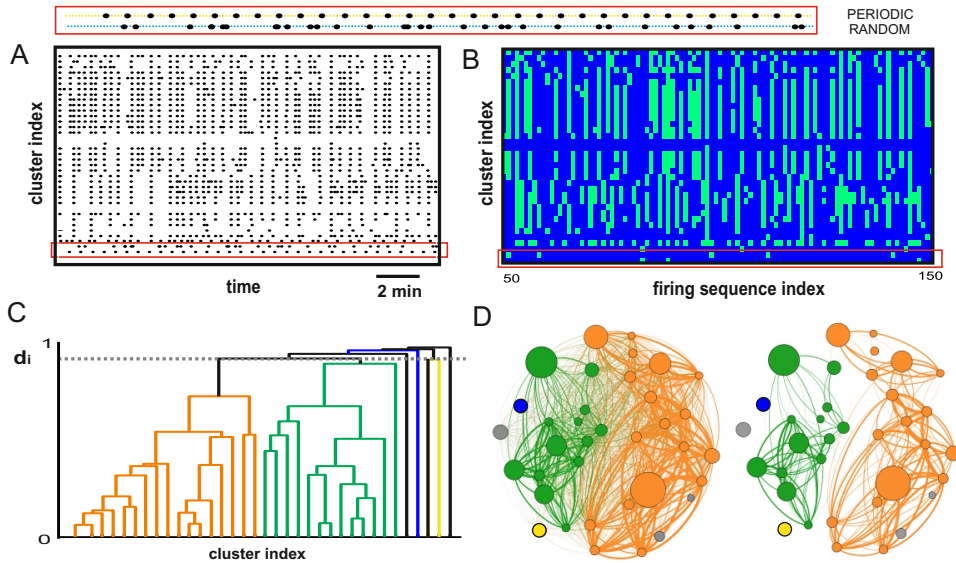


**Fig. 4.19 Influence of periodic and random clusters on network functional organization.**

**A,** Raster plot of the clustered culture ‘B’ with the last two clusters included ‘ad hoc’ (highlighted with a red box), one firing periodically and the other randomly. A zoom of the red box can be seen at the top level of the figure. The first cluster fires periodically with an inter burst interval equal to the mean inter firing sequence in the network. The second cluster fires with a Gaussian distribution with the mean equal to the mean cluster firing rate in the network. **B,** Representation of the total number of clusters that participate in different firing sequences. Each row shows the activity history of each cluster (green for activation, blue for silent). From this matrix one can calculate either the pairwise similarity between clusters’ activity (rows) to find the functional organization, or the effective connectivity network by looking at the time delays between clusters within each firing sequence (columns). Some activations of both ‘fake’ clusters form part of the firing sequences. **C,** Dendrogram of the pairwise similarity distance using the Jaccard distance between the clusters’ activity histories. Once the threshold is applied, the random (blue line) and the periodic (yellow line) clusters appear independent from the main dynamical moduli. **D,** The raw effective network of the representative experiment in to the left. We can notice few, weak links between the periodic (yellow node) and the random (blue node) clusters with the other ones, which are color coded according to their main characteristic modules. A  $z$ -score statistical test eliminates these weak links, as shown in the right network where only the top links are mapped.

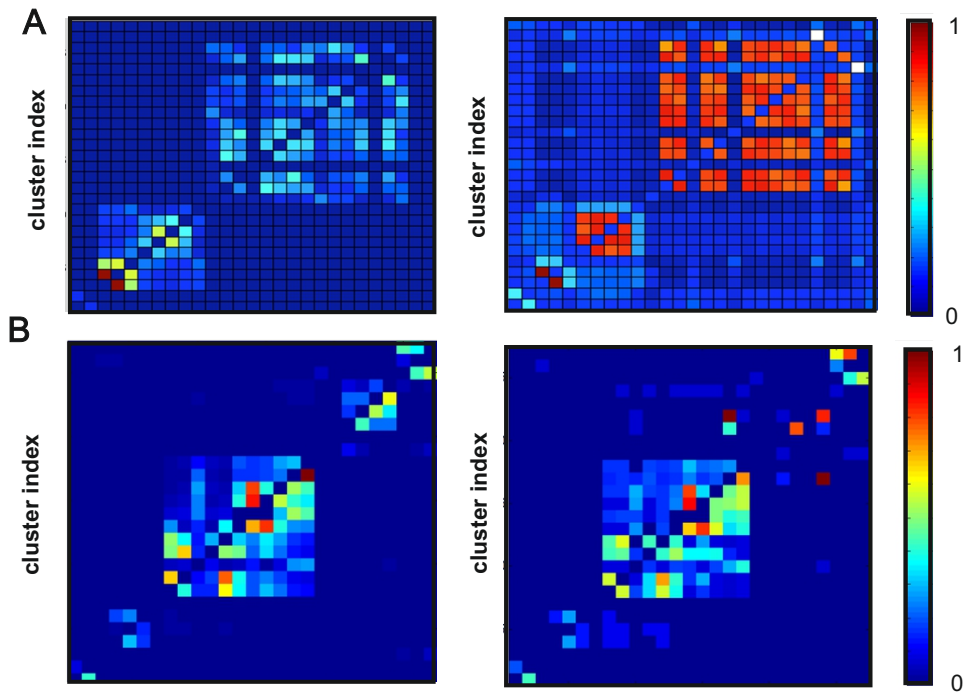


**Fig. 4.20 Effective connectivity inference using MI and GTE.** **A**, On the left we show the connectivity matrix of a typical experiment obtained using our time delays approach. On the right, the network is inferred using MI. Since MI provides bi-directional links, both matrices are symmetric and therefore the networks provide functional maps. The most important functional links in the MI reconstruction appeared also in our construction. **B**, On the right, another representative experiment in which we computed the effective connectivity using our method. On the right, the same experiment analyzed through GTE. Again, both networks are equivalent, and with few variations in the weight of the links.

results were totally in agreement with the effective connectivity map obtained through our time delays approach, as illustrated in Figure 4.20.

### **Robustness of network topology on the recording time**

Fluorescence recordings in clustered networks typically lasted for 1 h and contained between  $\simeq 50$  bursts in the quietest networks and  $\simeq 450$  bursts in the most active ones. To quantify the robustness of our effective connectivity analysis and derived topological measures, we tested whether 50 bursts sufficed to draw the effective networks. We carried out a control experiment in which we monitored spontaneous activity along 2 h (in the limit of our storage capabilities) in a clustered network at DIV 12 that containing 42 nodes (Figure 4.21). We then analyzed the data using two different procedures. In the first one we drew the effective connectivity using the data extracted from the entire recording, and determined its assortativity value. In the second procedure, we separated the recorded sequence in three blocks, each 40 min long, built the functional connectivity for each block, and computed the respective assortative values. The studied culture fired in a sustained manner at a rate of 1.12 bursts/min, and procured a total of 134 bursts. Thus, each data block typically contained about 45 bursts.

The results are shown in Figure 4.21 and provided two major conclusions. First, that the effective connectivity maps are very similar among the data blocks, and between any of the blocks and the entire recording, giving rise to assortativity values that are compatible within statistical error. And second, that the first 40 min of recording (with 45 bursts only) sufficed to shape the major traits of the effective network, therefore validating our strategy of using 1h of acquisition to procure a reliable estimate of the effective connectivity of the network and its topological traits.

## Analysis of a 2h experiment in blocks of 40 min each

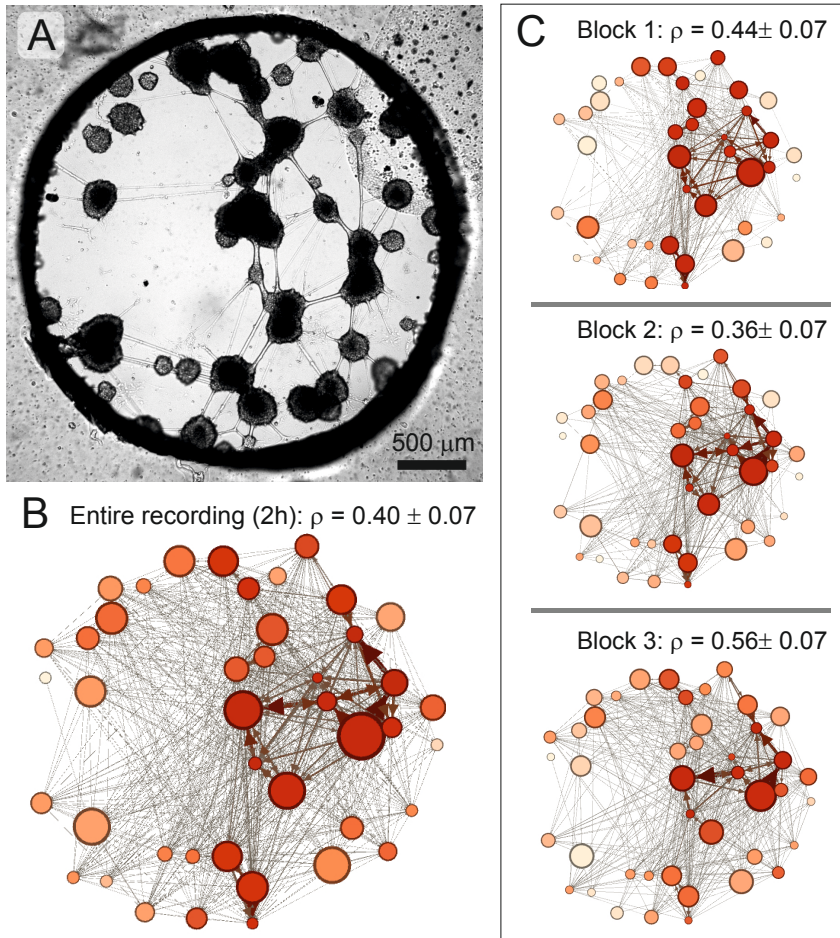


**Fig. 4.21 Assortativity robustness experiment.** **A**, Bright field image of a clustered network whose spontaneous activity has been recorded for 2 h. The average firing rate of the network is 1.12 activations/min. **B**, Corresponding functional network. The size of the nodes is proportional to the size of the actual clusters, and their color is proportional to their strength. The weights of the links are both color and thickness coded. The darker the color, the higher the value of the observable. **C**, Analysis of the 2h recording in three blocks, 40 min in duration each, and containing 45 sequences. The blocks show very similar traits between them, as well as with the entire recording. The blocks exhibit similar assortativity values, and share both the most important links and nodes' strengths.  $\rho^W$  indicates the assortativity value of the depicted network.

### 4.3.6 Topological and dynamical modules

As we described in Chapter 3, the concept of modules, i.e. the grouping of clusters according to some common traits, could be understood as either *dynamical* modules or *topological* ones. Dynamical modules, on the one hand, were inferred from the Jaccard similarity matrix, grouping those clusters that systematically appeared in the same firing sequences, i.e. shared a similar history. Topological modules, on the other, were derived from the effective connectivity and therefore the communities were shaped by those clusters that shared a similar distribution of links.

To clarify whether this definitions led to very different configurations of communities, we analyzed the representative culture ‘B’ by computing its topological modules using the ‘Louvain’ method (Figure 4.22A-B), and next contrasted the inferred topological communities with the dynamical ones. As shown in Figure 4.22C, the two communities constructions give almost identical results. By evaluating in a similar manner several other experiments, we concluded that the dynamical and topological communities were in general very similar in organization, and with VI values between them in the range 0 – 0.25. Such a good agreement is somehow expected since both the similarity the effective connectivity matrices are drawn from the same dynamical information, i.e. the fluorescence traces, and both are therefore ‘proxies’ of the dynamics of the network.

### 4.3.7 Top links mapping and small world properties

Here we analyze further the normalized effective matrices but taking solely into account the top links, i.e. those with 95% confidence as compared to a null model. In a first analysis, we calculated the total,  $S_{out} + S_{in}$  strength distribution, and extended to all the 15 clustered networks. The results are represented in Figure 4.23A. The total strength distribution is more homogeneous than the one obtained without normalization (Figure 4.8A). Additionally, here

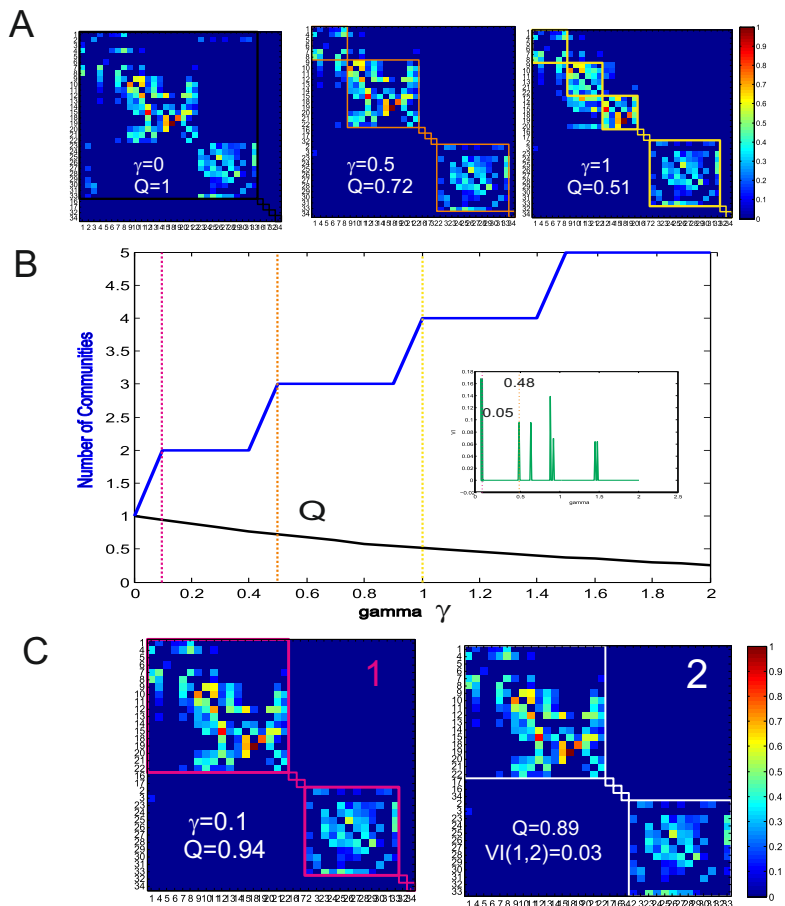


**Fig. 4.22 Topological and dynamical modules.** The plots show the ‘Louvain’ computation of the number of communities and the modularity index  $Q$  for gradually higher thresholds  $\gamma$  in the clustered network ‘B’. The index  $Q$  is a network property that quantifies the set of nodes that more densely connected among each other than with nodes in other modules. **A**, Derived communities (colored boxes on the effective connectivity matrices) and  $Q$  value for three different  $\gamma$  values. For  $\gamma = 0$ , all clusters are comprised within the same community. More communities appear as  $\gamma$  grows. For  $\gamma = 1$  there is a large number of communities, and for  $\gamma \gg 1$  each cluster would form a single community by itself. **B**, Dependence of the number of communities and  $Q$  on  $\gamma$ . The optimal threshold  $\gamma = 0.1$  provides the minimum number of communities with the highest modularity index, and excluding the trivial case of a single community (thick pink line). Thin dashed colored lines are a guide to the eye to illustrate the location of the above inferred communities. The inset shows the evaluation of VI between two consecutive partitions for gradually higher  $\gamma$ . The optimal threshold range would correspond to  $0.05 < \gamma < 0.5$ . **C**, Panel 1 shows the topological modules given by the optimum threshold  $\gamma = 0.1$  and that provides  $Q = 0.94$ ; panel 2 shows the dynamical modules previously obtained in Section 4.2.1, which give  $Q = 0.89$ . The similar modularity index quantifies the almost identical functional organization in the two constructions. Their VI value is 0.03.

we observed a tail that reflect the existence of a small fraction of clusters with a very high strength. By considering the two strength distributions separately, we observed that  $S_{out}$  and  $S_{in}$  have a similar trend (Figure 4.8B). Interestingly, we computed the difference between them,  $\delta D = S_{out} - S_{in}$ , and, as observed in the inset of Figure 4.8B, the distribution is centered at 0, but with a skewness of 0.15. This observation indicates that a small fraction of the clusters in the network exhibit more outputs than inputs, and therefore they have a tendency to act as sources ( $S_{out} > S_{in}$ ) rather than as a sinks ( $S_{out} < S_{in}$ ) of connectivity.

Since these clustered networks present a hierarchical modularity, they should also show a balance between integration and segregation. Indeed, this balance has become really crucial for network efficiency and robustness (Downes et al., 2012). The networks that present this balance are called ‘small world’ networks. This architecture shows a short path length and a high clustering coefficient. Based on this feature, one could hypothesize that the rapid interaction between clusters is mediated by few links between locally connected groups of clusters.

To quantify the degree of small–worldness in our clustered networks we computed the clustering coefficient  $CC$  and the characteristic path length  $L$ . To proceed, we should first note that the evaluation of these topological properties requires the comparison with random models, and the weighted and directed versions of the null models of both  $CC$  and  $L$  are not yet well established. Hence, we used an *undirected* and *binary* versions of our networks, which was achieved by symmetrizing and binarizing our effective matrices. As shown in Figure 4.23C, despite the reduction of information (the weight and the directionality of the links is lost) the total degree distribution in these ‘simplified’ networks retains fundamentally the same features as the total strength distribution shown before in Figure 4.23A, and indicates that the main information is preserved. Furthermore, our objective is not to deepen in the study of small–worldness (Watts and Strogatz, 1998), but to evaluate the

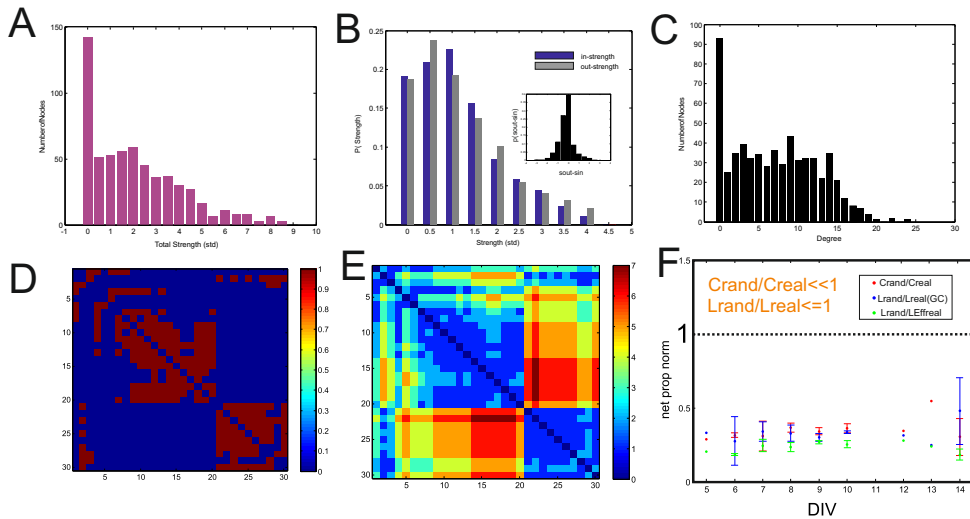


**Fig. 4.23 Strength, degree distributions and small-world properties.** **A**, Histogram of the total strength (inset: the probability in logarithmic scale) for 15 experimental realizations. The distribution shows a long tail and corresponds to a few number of clusters exhibiting high strength. **B**, The in- and out- strengths distributions. The inset stresses the good symmetry of the out-going and in-going connections,  $\delta D = S_{out} - S_{in}$ . **C**, The total degree distribution once the directed and weighted networks are converted into an undirected and binary graphs (inset: the probability in logarithmic scale). The networks considered for the small-world evaluation are the giant component of the  $z$ -score pruned networks. **D**, The final directed and binary network for the clustered culture 'B'. **E**, The path length distance matrix, where the distances are the number of links needed to navigate from one cluster to another. **F** Ratio between randomized versions of  $CC$ ,  $L$  and  $G_{eff}$  and the actual measures, analyzed in experiments at different days *in vitro* (DIV).

present or not of this signature for the simplest scenario, i.e. undirected and unweighted links, and the most significant network, i.e. top links only.

All our undirected and unweighted networks present a degree  $k$  that verifies  $k > \log(N)$  (with  $N$  the number of clusters), a condition that must be satisfied in order to properly compute the small world feature (Bassett and Bullmore, 2006; Bullmore and Bassett, 2011). Thus, density of links is within the ideal cost range (approximately 0.01 – 0.30) where the sparseness of the network is considered optimal, because within this range many graph theory metrics, including the small-worldness, are maximal.

The characteristic path length  $L$  is calculated on the giant component of a the network, , i.e. the sub-connected graph with the most significant links and that represents the 80 – 90% of the network. The giant component of the binary and symmetric connectivity network of the clustered culture ‘B’ is pictured in Figure 4.23D. We note that the ‘independent’ clusters are disconnected from the network and therefore they do not form part of the giant component. To finally calculate  $L$  in the network we define first a distance matrix, which is taken as the inverse of the binary connectivity network. Next, we calculate the path length distance matrix where each element  $(i, j)$  corresponds to the required number of links to navigate from  $i$  to  $j$ . Figure 4.23E shows the path length distance matrix for the clustered culture ‘B’. Moreover, we also compute the clustering coefficient  $CC$  and the global efficiency,  $G_{\text{eff}}$ . The latter gives a similar information as the characteristic path length. All these quantities are later compared to their random counterparts, i.e.  $L^r$  and  $CC^r$ .

In network theory, the necessary condition to ensure the existence of small-worldness is  $CC^r/CC \ll 1$ ,  $L^r/L \lesssim 1$ , and  $G_{\text{eff}}^r/G_{\text{eff}} \lesssim 1$ . Our results, however, shown in Figure 4.23F for cultures studied at different days *in vitro*, do not completely fulfill these conditions. We can notice that the  $CC_r/CC$  is sufficiently small, i.e. there is more segregation in the actual networks than one would expect at random. However,  $L_r/L$  is also very small rather

than close to 1, meaning that the characteristic path length is higher than one would expect at random.

Summarizing, our networks exhibit both a high segregation and high characteristic path length. For small-worldness to fulfill the latter should be smaller. Hence, we conclude that our networks are not small-world, although they share some traits. We explain the lack of agreement to the important loss of connections due to the  $z$ -score test for pruning and normalization. The original, pre-pruned networks—and even the pruned with a less severe reduction in connections—exhibit a higher characteristic path length  $L$  and therefore they are closer to be declared small-world. We would need several more experiments and analyses to achieve more conclusions.

### 4.3.8 Identification of the clusters that initiate spontaneous activity

In the experiments we observed that the spontaneous activity was predominantly initiated by one or two clusters. Interestingly, the number of clusters that actually initiated the spontaneous activity seems to be conditioned by the number of the characteristic dynamical modules. This feature can be seen in two representative experiments, shown in Figures 4.24A–B, and where the functional organization of the networks (left panels) is compared with the ignition scoring of the clusters (right panels). The darker the color of a cluster, the higher the number of times that it has triggered a cluster's activation sequence. While in Figure 4.24A there is only a predominant cluster initiating activity (encircled in black), in Figure 4.24B two clusters were identified, and each of them clearly sitting in different modules. Hence, we hypothesize that these *initiators* might be responsible for starting the activity in their own modules. To make the problem more complex (and fascinating), we observed that initiators had nothing particularly special. They were not the bigger in size, and neither those with the highest strength nor highest clustering coefficient. A deeper study would be needed in order to unravel not only the

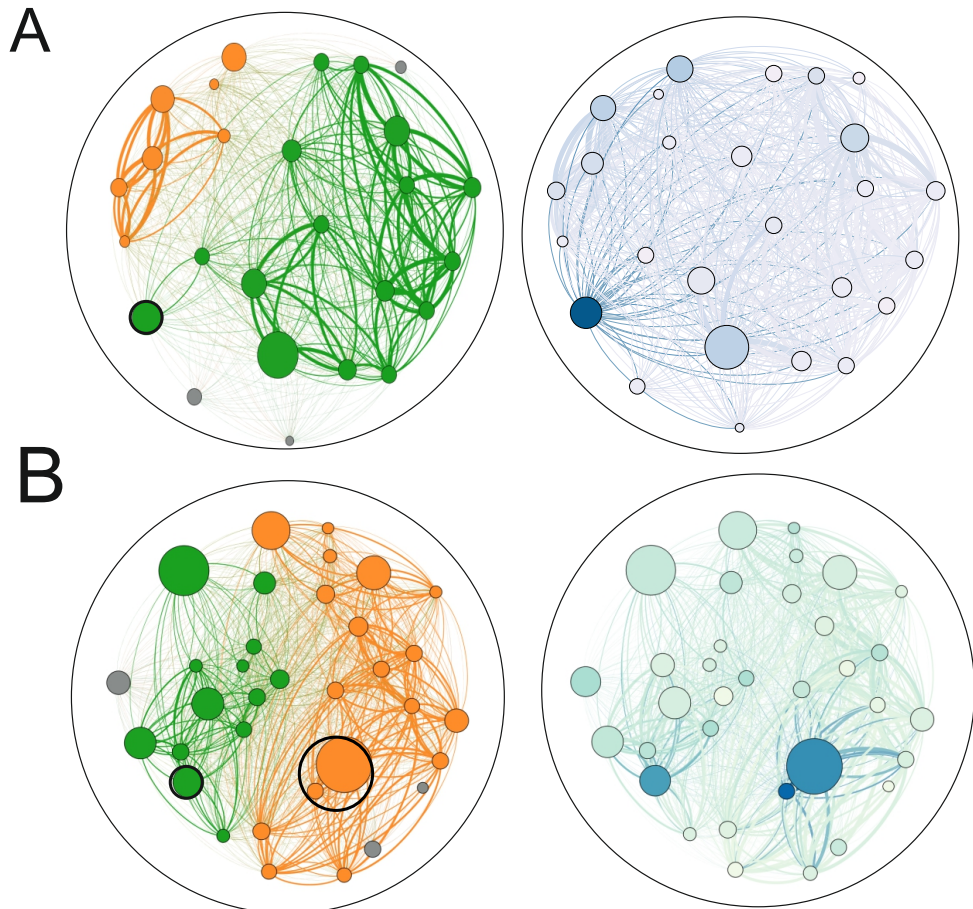


**Fig. 4.24 Functional organization and initiation clusters.** The graphs show two representative experiments with clear ‘initiator’ clusters, and comparing the functional organization of the network (left panels) with the initiation score of the clusters (right). For the latter, clusters are color coded according to their scoring. **A**, Example where only one cluster scored markedly higher than the others. **B**, Example where two clusters scored similarly.

biochemical and wiring hallmarks that make those clusters so special, but also which are mechanisms that could shape different propagation patterns of activity throughout the culture, e.g. wave propagation or avalanches in addition to our observed sequential activations.

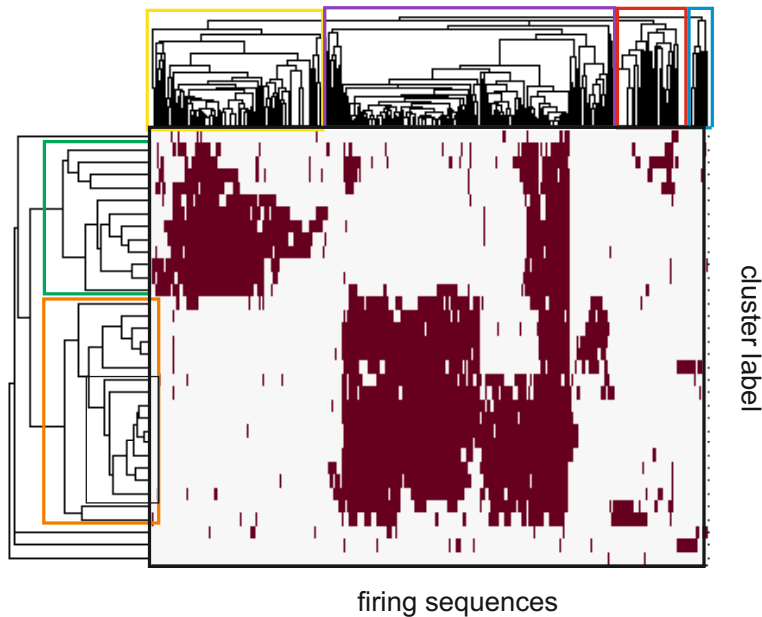


**Fig. 4.25 Structure of firing sequences.** The plot shows the hierarchical construction for the transpose of the co-activation matrix, and that corresponds to the arrangement of similarity between firing sequences. Four different families of likely repeating sequence patterns are found, highlighted with color boxes.

The existence of these ‘few’ initiators naturally implies that the upstream clusters’ activations that we called firing sequences occur in a repeated, patterned manner in which clusters at varied spatial locations fire with similar delays relative to each other. Indeed, if we evaluate not only the similarity between the activity histories (rows of the co-activation matrix  $A$ ) but also the similarity between the clusters that have participated in each firing sequences

(columns of the matrix), we can unveil the set of characteristic firing sequence patterns. This idea is shown in Figure 4.25. There, we show on the top the hierarchical construction for the transpose of the co-activation matrix, and that corresponds to the arrangement of similarity between firing sequences. For the particular culture analyzed, the dynamics present 4 different families of likely repeating sequence patterns, marked with color boxes. However, a deeper study needs to be carried out in order to ensure that these families of firing sequences always follow the same temporal structure of activations.

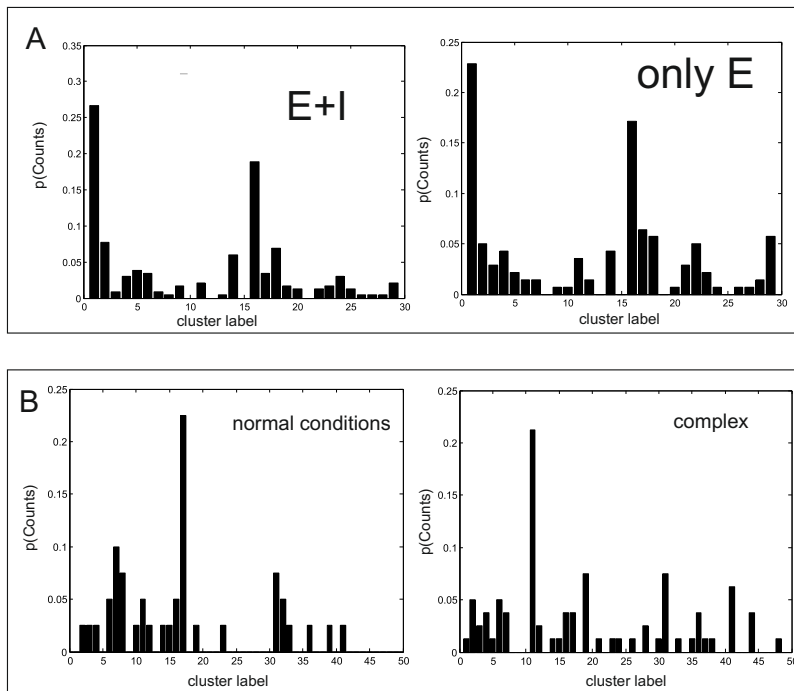


**Fig. 4.26 Presence of ‘initiator’ clusters for different experimental conditions.** The graphs show the probability that a cluster in the network initiated activity in a firing sequence. Two representative experiments are shown, and comparing the behavior of the clusters in the same network before (left panels) and after (right panels) a given action. **A**, Experiment in which the connectivity of the network is modified by the blockade of inhibition, altering connectivity from an initial ‘E+I’ condition to an ‘E-only’ one. The ‘initiators’ (clusters #1 and #16) remain the same. **B**, Experiment in which a culture is dosed with a chemical agent that damages connections. The ‘initiator’ switches from #17 to #11.

A final interesting observation is that the ‘initiation’ clusters are the same in both ‘E+I’ and ‘E-only’ conditions, as shown in Figure 4.26A. Given the robustness of the initiator to the presence or absence of inhibition, it is enlightening to explore under which conditions the number and location of the initiators in a network change. Addressing such exploration is challenging, but we started by considered two major scenarios, namely biochemical perturbation and direct physical destruction of clusters through a laser beam. These experiments are exposed in detail in Chapters 5 and 6, but we can here delineate the two major conclusions. First, that initiators *do change* when network connectivity is degraded. This is exemplified in Figure 4.26B. And, second, that the destruction of a cluster that is far from the initiator has little effect on the latter; whereas the destruction of the initiator itself causes that another, nearby cluster takes its role.

## 4.4 Discussion of the Results

The set of experiments presented in this chapter show that clustered neuronal cultures exhibit a unique self-organizing potential. Dissociated neurons develop towards a clustered network, i.e. dense assemblies of neurons connected between them, a structure that is formed in a few days and that is preserved until the degradation of the culture. However, in our opinion, the most remarkable feature of these cultures is that this self-organizing process drives the network towards specific dynamic states, which shape a modular, assortative effective connectivity with the presence of a rich club.

The exhibited modular behavior of all these clustered cultures seems to be hierarchical, encompassing modules within modules, a characteristic property also seen in the brain and many other complex systems. In general, modularity (or hierarchical modularity) has been claimed to be advantageous for a greater robustness, adaptivity, and development of network function (Meunier et al., 2010). Modular networks also optimize time-scale separation, i.e.,

combine fast intra–modular processes with slow inter–modular ones (Pan and Sinha, 2009; Shein-Idelson et al., 2011). This feature helps maintaining a fine balance between integration and segregation, ultimately promoting the network’s dynamical complexity (Shanahan, 2008). An additional feature of modular networks is the emergence of a master–slave relationship, and where a module drives another one (Baruchi 2008, Shein 2008). Such a feature may be useful to control propagation directionality in the network. On the other hand, hierarchical modularity has been ascribed to enhance dynamical re–connectability, i.e. marginally stable networks can be combined or divided while preserving stability (Robinson et al., 2009). We believe that the rich and flexible repertoire of activity patterns exhibited by the clustered networks is a consequence of their modular nature.

Another important aspect to highlight is that modular networks tend to present a high number of nodes densely connected within the module (leading to high clustering), while the existence of a few links between nodes in different modules plays the role of topological shortcuts in information processing (leading to short path length). Thus, this modular architecture naturally tends to shape a small–world configuration (Pan and Sinha, 2009). However, in our preliminary findings we have found that these clustered networks present, when compared to random networks, both a higher ‘clustering coefficient’ and a higher ‘short path lengths’. Those concurrently high values make difficult to conclude the existence of small world features in clustered networks. Such a difficulty can be a consequence of our unweighted and undirected analysis to find these small world features, since we operated with the top functional links only (corresponding to a pruning of about 75% of the network) and therefore our networks were excessively sparse. As a future work we could use an optimal connectivity threshold for the weighted and directed calculations that would likely lead to a decrease in the short path length, possibly matching the observed modularity with a small–worldness trait.

The inferred effective connectivity maps in our study are built upon the use of time delays to provide a direct measure of causality,. This approach naturally shapes effective networks that is both directed and weighted, with the weights given by a decaying function that follows the frequency of the delay between pairs of clusters. Our formulation is simple and derives from the intrinsic dynamics of the network. Moreover, the comparison of our method with other theoretic measures such as MI or TE showed that the identified effective links were fundamentally the same, with small quantitative differences associated to the particular weighting procedures.

The resulting effective networks consistently maintained high assortativity values, along a wide range of days *in vitro*, and independently of the balance between excitation and inhibition. We also observed that, by contrast, the assortativity analysis in homogeneous cultures procured neutral values, a result that is supported by other studies in homogeneous networks similar to ours Bettencourt et al. (2007). Interestingly, the most fundamental dynamical difference among these two cultures' type resides in the modular activation in clustered cultures that contrasts with the coherent activity in homogeneous ones. Given the acute differences in assortativity between clustered and homogeneous cultures, we hypothesize that the modular dynamics by itself might be highly related to the increase or reinforcement of assortative traits in the effective networks.

In conclusion, the measured positive assortative mixings and the presence of rich clubs in clustered networks is highly remarkable observation, since these traits may facilitate redundancy in the information processing that ultimately reinforce and stabilize network activity. The concurrent presence of these properties has indeed been hypothesizes to confer higher network resilience upon damage compared to other configurations.

The importance of these results for network resilience motivated us to devise and explore perturbative actions in clustered networks. As we will in the next chapter, we used chemical action and physical damage to probe

the resilience of clustered networks, and even investigate possible network recovery mechanisms to cope with degradation.



# Chapter 5

## Results II: Network resilience

The rationale behind the experiments and results presented in this chapter is the debate around the importance of assortativity and ‘rich club’ features on network robustness. Indeed, several studies ascribed these features to network resilience upon damage (Fornito et al., 2015; Rubinov and Sporns, 2010a). In particular, it was shown numerically (Newman, 2002, 2003) that networks exhibiting these features were more robust to random error (random node deletion) and targeted attack (high-degree node deletion) than disassortative or neutral networks. Hence, given the strong assortativity of our clustered networks, we devoted a substantial effort along the thesis to investigate whether the clustered networks exhibited resilient traits, either in a global or local manner.

We investigated network resilience in our networks using two different experimental approaches, namely global damage and local injury. The first category comprised experiments carried out in our laboratory, and we used either chemical agents or photo-damage as main disrupting actions. The second category comprised experiments in which a single cluster of the network was destroyed through a laser beam.

Both categories are described in Chapter 2, but for sake of clarity we describe the main experimental procedure here for an easier comprehension of the results.

For the *global damage* category, the two set of experiments were as follows. In the first one, we continuously exposed a culture to strong fluorescence light, therefore inducing photo-damage to the neurons. This action resulted in random neuronal death across the network and hence a progressive failure of its spontaneous activity. In the second one, the excitatory network connectivity was gradually weakened by means of the AMPA–glutamate receptor antagonist CNQX. The weakening caused the silencing of connections and therefore a progressive reduction of activity. Both actions were simultaneously carried out in clustered (assortative) and homogeneous (dissortative or neutral) networks, and the rate of spontaneous activity decay provided an estimation of the resistance of the networks to global damage.

For the *local damage* category we used the experimental setup at the Institute of Photonic Sciences (ICFO) to destroy clusters through laser damage. These results are still preliminary, but they are presented here given the enormous effort invested along two years to bring them to light. For clarity, we only present three illustrative examples. In each experiment, a ‘target’ cluster was selected for annihilation depending on its initial topological properties. By comparing the activity before and after the physical damage we aimed at assessing some important traits on network resilience and topology. By the end of the chapter, and by considering a total of  $N = 12$  experiments, we will discuss which topological descriptor best described the ‘vulnerability’ of a clustered network.

## 5.1 Global network damage

In this section we describe the results on the photo-damage experiments, to later show the ones with CNQX. Finally, and for the latter group, we will show

in more detail the changes in network functional organization as degradation of neuronal circuitry progressed.

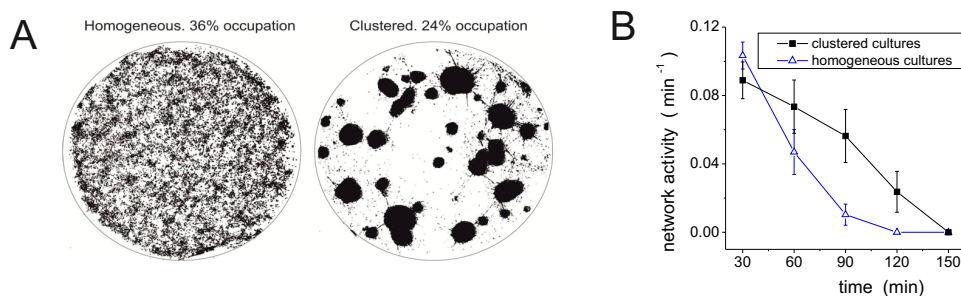


**Fig. 5.1 Photo–damage experiments.** **A**, For each culture monitored in the photo-bleaching experiment, we first converted the images to a black and white pattern by applying a threshold to the acquired bright–field images, as illustrated in the figure. We next counted the ratio between the black pixels and the total number of pixels within the 3 mm diameter circular area. We repeated the analysis for all the 6 cultures of each type monitored, and observed that, on average, homogeneous cultures covered  $(34 \pm 4)\%$  of the available area, while clustered ones covered  $(26 \pm 5)\%$ . Clustered cultures occupy a smaller area ( $1.9 \text{ mm}^2$ ) than their homogeneous counterparts ( $2.3 \text{ mm}^2$ ). **B**, Spontaneous activity is measured in cultures that are continuously exposed to strong fluorescence light, causing gradual neuronal degradation and ultimately the death of the entire network. The total radiation received by the neurons is calculated as the duration of the exposure times the area covered by the neurons in the culture. The spontaneous activity in homogeneous cultures decays at a much faster rate than in the clustered counterparts, pinpointing the general resistance of clustered cultures to structural failure. Data is averaged over 6 network realization of each type. Error bars show standard deviation.

## Photo-damage

We first considered a clustered culture and measured its spontaneous activity uninterruptedly along 2 hours, and with neurons continuously exposed to a light radiation 4 times stronger than normal. We then divided the sequence in blocks of 30 min, and determined, for each block, the average network activity by counting the number of firing sequences within the block. Next, we switched to a homogeneous culture from the same batch (i.e. identical nominal density and age) and carried out the same protocol. In total we

carried out 6 measurements for each kind of culture, and finally analyzed the decay in activity as a function of time. Although the radiation over the culture was homogeneous, the actual area occupied by the neurons was different between homogeneous and clustered cultures. Neurons in homogeneous cultures formed a monolayer that covered  $(34 \pm 4)\%$  of the available area, corresponding to about  $2.4 \text{ mm}^2$  for the 3 mm diameter wells (Figure 5.1A, left). In clustered cultures, neurons were tightly packed in slightly three-dimensional structures, giving rise to a lower spatial coverage of  $(26 \pm 5)\%$ , i.e. about  $1.8 \text{ mm}^2$  (Figure 5.1A, right). Hence, homogeneous cultures were effectively more exposed to light than their clustered counterparts. To take this spatial variability into account, the ‘total radiation’ received by the neurons in a given experiment was quantified as the duration of the light exposure multiplied by the area occupied by the neurons in the studied culture. We then averaged the results over the 6 different culture realizations of each type, and binned nearby values for clarity. Figure 5.1 shows the data of activity level as a function of radiation for the two network types, and evidences that homogeneous cultures decayed in activity much faster than the clustered ones. Overall, we concluded that the clustered architecture and its assortative traits could increase its resistance to damage.

### Chemical degradation

Here we compared the change in activity between a clustered and a homogeneous culture during gradual weakening of neuronal connectivity (Section 2.5.2). The weakening was achieved by progressive application of CNQX, an AMPA-glutamate receptor antagonist in excitatory neurons. We first measured the clustered network and thereafter the homogeneous one. In both cases, we first recorded spontaneous activity at  $[\text{CNQX}] = 0 \text{ nM}$ , measured the activity  $\gamma_i^0$  of each cluster  $i$ , and used the average firing rate of the network  $\Phi_0 = \sum_i \gamma_i^0 / N$  as reference for the subsequent steps. We then increased the concentration of the drug to a preset value, waited 5 min for the drug to take

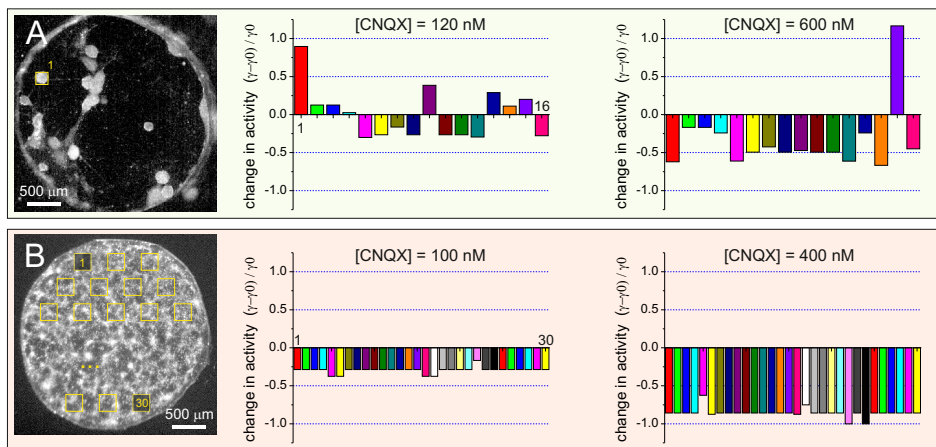


**Fig. 5.2 Chemical-degradation damage.** Examples of the degradation of neuronal activity in clustered and homogeneous cultures due to the gradual weakening of excitatory connectivity. Both culture types were investigated at the same *day in vitro* 14 and contained a similar density of neurons. The weakening of connections is achieved by gradually increasing the concentration of CNQX, an AMPA-glutamate receptor antagonist in excitatory neurons. Network response upon weakening is quantified through the relative change in activity  $(\gamma - \gamma_0)/\gamma_0$  between a given [CNQX] application and the unperturbed state. Activity variations are indicated separately for each cluster, and shown according to the cluster labeling number. **A**, Clustered cultures show a mixed response upon weakening, with some clusters increasing activity and others reducing it. Only for relatively high concentrations of CNQX ( $\gtrsim 600$  nM) the activity systematically decays up to the full silencing of the network. **B**, In homogeneous cultures, activity is analyzed in 30 regions that cover in a regular manner the entire network. Activity decays almost equally in all regions. Relatively small drug concentrations of [CNQX]  $\simeq 400$  nM practically suffice to fully stop activity.

effect and measured again for 15 min, computing the new firing rate  $\gamma_i$  for each individual cluster. We next switched to a second preset values, and repeated the procedure until activity ceased.

We first computed the relative changes in activity respect to the unperturbed case as  $\Gamma_i = (\gamma_i - \Phi_0)/\Phi_0$  for each cluster individually, and provided a network-average measure as  $\Phi = \sum_i \Gamma_i/N$ . Two illustrative examples of the action of CNQX on network activity are provided in Figure 5.2. In a clustered cultured and for weak CNQX applications ( $\simeq 100$ nM) the activity in some clusters increased, while in some other decreased, and on average the

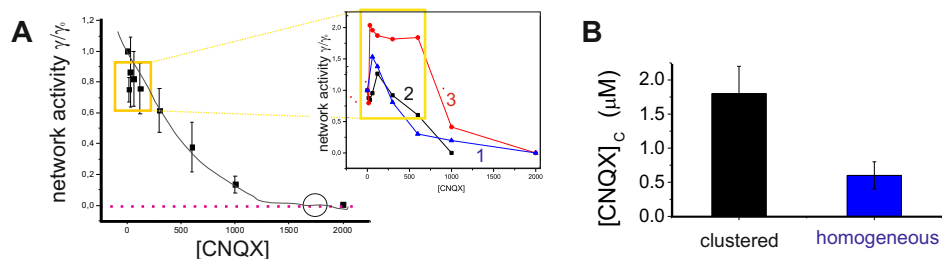


**Fig. 5.3 Chemical-degradation damage.** **A**, The degradation of neuronal activity,  $(\gamma - \gamma_0)/\gamma_0$ , for gradually application of [CNQX]. ( $N = 10$  clustered cultures). The error bars correspond to the standard error. Both curves followed an exponential-like decay but the progressive fall in activity was faster in homogeneous than in clustered cultures. The inset shows three clustered experiments that exhibited an unexpected increase in the firing rate at low range of [CNQX] in the range  $60 - 300\text{nM}$ . **B**, The critical concentration  $[\text{CNQX}]_c$  at which activity complete ceased was  $1.6\mu\text{M}$  for clustered and  $0.5\mu\text{M}$  for homogeneous networks.

network firing rate remained stable ( $\Gamma \simeq 0$ ). As CNQX increased to  $600\text{nM}$ , we observed that most of the clusters reduced their activity, although there were still some that maintained a high activity or even increased it. This different behavior from cluster to cluster suggests that clustered networks are highly flexible, and that they may have mechanisms to preserve activity even with strong weakening of the connectivity. Conversely, homogeneous cultures (Figure 5.2B) lose activity in a more regular and faster way. These networks are characterized by a highly coherent dynamics, and therefore all neurons in the network reduced activity similarly as CNQX was applied. Interestingly, for  $[\text{CNQX}] \simeq 400\text{nM}$  the shown homogeneous culture turned almost completely silent ( $\Gamma \simeq -1$ ), while the clustered culture was still highly active.

We repeated this study for 10 different realizations of each culture type. On average, both network activities respect to the unperturbed case,  $\Phi/\Phi_0$ , followed an exponential-like decay under gradually higher applications of CNQX, as shown in Figure 5.3A. The progressive fall in activity was again much faster in homogeneous than in clustered networks. Indeed, the critical

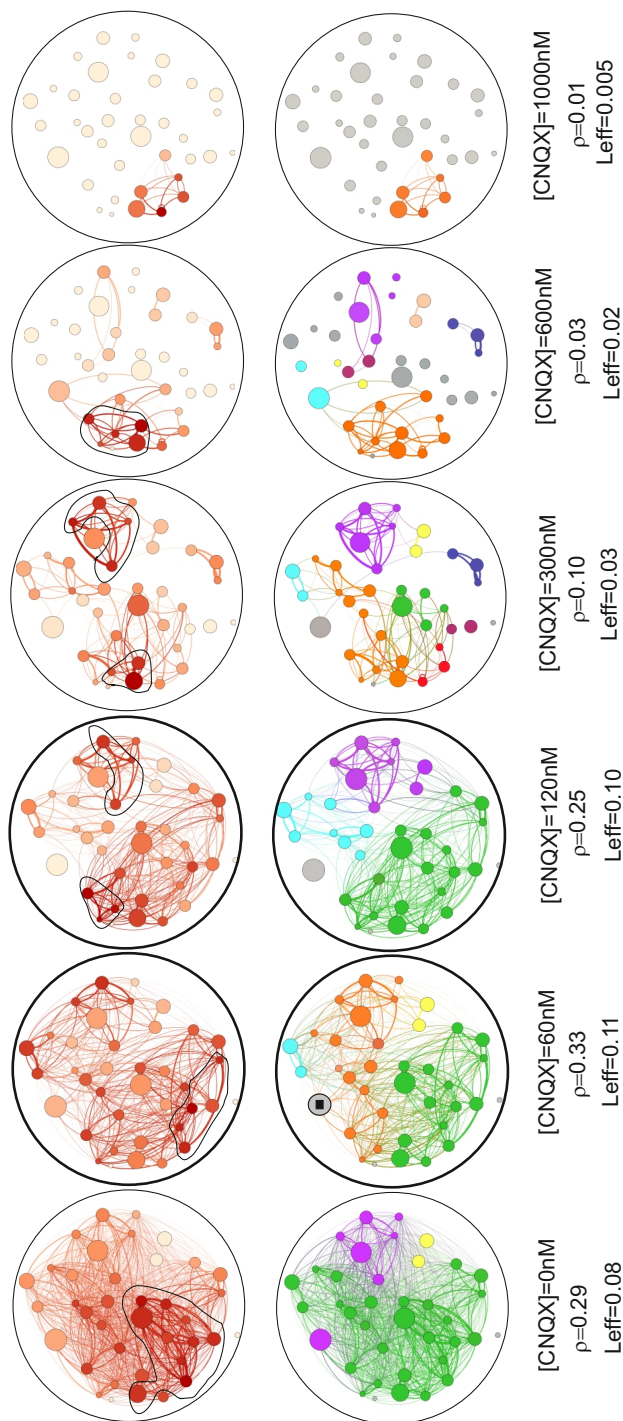


**Fig. 5.4 Chemical degradation** At the top, the functional networks for different applications of [CNQX] of a representative experiment (marked as '1' in the inset of Figure 5.3A). The colors of the nodes and their links correspond to their strength, and the black outline surround the rich club core. At the bottom, the same functional networks, but color coding the nodes and the links according to their community assignment. For every application of [CNQX], the density of the links  $\rho(k)$ , and the global efficiency,  $G_{eff}$  was calculated. We observed, in general, the gradual disruption in the connectivity strength and modularity, together with a reorganization of the rich club, as connectivity failed.

concentration  $[\text{CNQX}]_C$  at which activity completely ceased was  $1.6\mu\text{M}$  for clustered and  $0.5\mu\text{M}$  for homogeneous networks (Figure 5.3B).

An interesting observation is that some clustered networks experienced an increase in their firing rate for  $60 \lesssim [\text{CNQX}] \lesssim 300\text{nM}$ . The inset of Figure 5.3A illustrates such an unexpected behavior for 3 networks. This increase of activity upon weakening of the excitatory circuitry can be seen as a compensatory effect, i.e. a network response to counterbalance the perturbation.

To highlight the intricacy of this increased activity puzzle, we compared the network changes that we observe experimentally with a ‘toy model’ based on percolation in which the effective connections of the original, unperturbed network were gradually suppressed by applying a progressive threshold to the weights, mimicking a disintegration scenario. Interestingly, we observed that the experimental and percolative disintegrations were very different, indicating that the real process is much more complex than just a gradual and homogeneous removal of effective connections.

To illustrate the changes in the network during disintegration and possible network recovery response, we considered one of the cultures and analyzed its functional organization. We studied the network marked as ‘1’ in Figure 5.3A (shown in blue line). Figure 5.4 shows the resulting networks for increasing applications of CNQX. The effective connectivity is shown at the top of the figure, with the nodes and links color coded according to their strength and weight, respectively. The corresponding dynamical modules are drawn at the bottom. The nodes are colored according to their belonging to a given community. In general, we observe a disruption in strength and modularity as connectivity fails. However, for  $[\text{CNQX}] = 60$  and  $120$  nM, the weight of the links among distant nodes slightly increased, giving rise to more homogeneous values of total strength. This characteristic is also reflected in the gain of global efficiency,  $G_{eff}$ , as well as in the density of the links,  $\rho(k)$ . However, although at this stage the network appears to be more globally

connected, we can also note that more communities emerged in the network at those disintegration values.

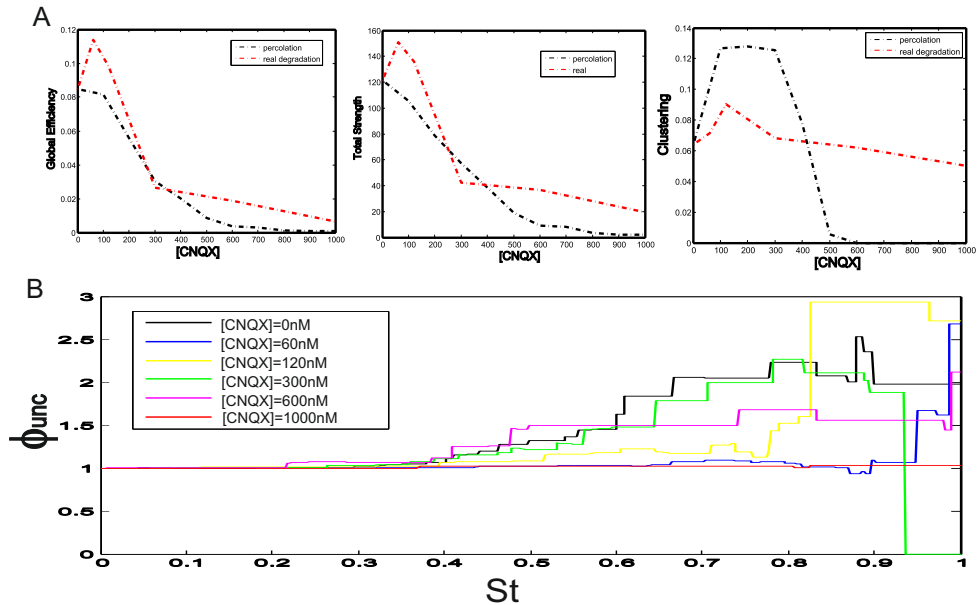


**Fig. 5.5 Chemical real degradation compared with an artificial percolation process.** Comparison of some topological properties for the experiment of Figure 5.4A under real chemical degradation and under simulated percolation. **A**, The global efficiency firstly increases at lower [CNQX] whereas by applying the percolation method it does not appear any peak in activity. The same results also appear calculating the total strength of the nodes. On the other hand, the clustering coefficient using the percolation analysis is higher at these low applications of CNQX than the clustering coefficient obtained in the actual degradation, suggesting that inter-modular connections are not the first ones to be lost. Recovery mechanisms related with continuous functional reorganization appeared in order to preserve global network activity. At high concentrations of the chemical drug, the three topological parameters fall at slower rate than in the percolation process, indicating that the final network is more resilient than one would expect through a linear weight degradation. **B**, The evaluation of the rich club for different CNQX applications (marked with different colors). The subset of strongly interconnected clusters constantly changes as the excitatory connections are being reduced.

In order to understand better these surprising changes, we compared the topological properties of the actual connectivity matrices for distinct applications of [CNQX] with the thresholded ones using the ‘percolation’ approach.

The results are shown in Figure 5.5. First, the global efficiency increases during the initial [CNQX] applications as compared with the values obtained by percolation (Figure 5.5A). The total strength of the nodes exhibit a similar trend (Figure 5.5B). However, at a given CNQX concentration the global efficiency and the total strength decay abruptly, and reach the same level as the percolation case. Thus, we hypothesize that the real degradation may sustain inter-module connections, which maintain the network more globally connected, until a critical value of [CNQX]  $\simeq 300$  nM. Above this value, the disruption is sufficiently high to impede any ‘recovery’, and the network abruptly degrades, although at a lower pace as compared to percolation.

Another surprising result is the different behavior of the clustering coefficient between the real and the percolative scenarios, as shown in Figure 5.5C. The clustering coefficient is lower than the expected from percolation at low CNQX levels, stabilizes at the critical concentration and finally drops again, though less abruptly than the percolative counterpart. Indeed, we note that, in the percolation scenario, the linear decrease in weight causes the network to quickly lose inter-modular links (i.e. a decay in integration) while the underlying sub-modular structures emerge (i.e. a gain in segregation). Conversely, modules in the real network may reorganize in other modules, altogether reinforcing not only the connections within the modules but also among modules. These changes are reflected by a sudden increase in the clustering coefficient and total strength, and that maintain the entire network connected, i.e. exhibiting a higher global efficiency and link density. At the end, one could think that the complex functional reorganization upon disintegration is driven by an effort towards maintaining network’s global activity, readapting network’s topological configuration up to a critical point at which a significant breakdown in connectivity occurs, leading to a cease in activity. This critical point could correspond to the moment in which the clusters that acted as ‘integrators’ (inter-module connectors) are functionally

disconnected from the network (see e.g. the gray cluster with a black square in Figure 5.4B).

Another topological aspect that apparently continuously changes in every application of CNQX is the subset of clusters that shape the ‘Rich Club’, as shown in Figure 5.4. In normal conditions,  $[\text{CNQX}] = 0$ , closer strongly connected clusters form a unique rich club, whereas at higher CNQX more groups of clusters highly connected emerge at relatively large distances. Hence, network degradation may lead to physically disconnected submodules, and the presumably reinforcement of these submodules can derive into the creation of other rich club backbones to preserve the global network activity. Higher inspection of the evolution of the rich clubs is provided in Figure 5.5D. First, we can observe that for  $[\text{CNQX}] = 60\text{nM}$  (blue line) the rich club is formed by a very small subset of clusters. For  $[\text{CNQX}] = 120\text{nM}$  a high number of clusters are noticeably strongly connected, appearing different rich club cores in distance areas. For higher concentrations, the rich club remains stable, disappearing solely at  $[\text{CNQX}] = 1000\text{nM}$  when activity ceases. We should note that the subset of nodes that seems to form the Rich Club are functionally changing and readapting at any step of disintegration, indicating that they do not have an endogenous role, i.e. their behavior seems not to be established biologically.

## 5.2 Local physical damage

As we described in Chapter 2, we developed experiments at ICFO and that were inspired by the work of Albert and Barabasi on vulnerability, Ref.(Albert et al., 2000). Experiments consisted in damaging a neuronal cluster with an infrared ultrashort pulsed laser beam, finally comparing the dynamical changes before and after the physical nodal insult.

Three different procedures were carried out depending on the topological role of the neuronal cluster targeted. The first one consisted in destroying at

random a neuronal cluster; the second one consisted in targeting the cluster with the highest strength; and the third one resided in silencing the ‘initiator’, i.e. the cluster that initiates the spontaneous activity in the network.

Experiments were carried out at  $DIV = 9 - 14$ , in networks with 30 – 40 clusters, rich spontaneous activity —about  $2 \pm 1$  firing/min per cluster on average—, and under ‘E+I’ conditions. We must note that in our experimental system two or more cultures were placed on the same glass, and therefore we could monitor with the same optical system the behavior of a control culture while targeting a neighboring one. Indeed, in all the experiments a control culture was always recorded in parallel with the targeted one. Good experiments were those in which controls remained unaltered in behavior after action on the target cultures.

### 5.2.1 Random cluster deletion

In these experiments the spontaneous activity of the control and target cultures was first recorded along 30 min. Then, we randomly destroyed a cluster by laser ablation and recorded again for another 30 min. The functional connectivity matrices before and after the random cluster’ removal of a representative experiment are pictured in Figure 5.6A-B. The targeted cluster is shown in black. Before damage, two main modules (highlighted in green and orange) governed the activity of the culture. After the injury, a small group of clusters of the green module (contoured in yellow) were now part of the other module, reflecting a functional reorganization. Figure 5.6B better pictures this rearrangement, where the branches in the tree of the dendrogram are colored according to the dynamical modules, and the black circle marks the location of the deleted cluster. The new cluster’s distribution in the modules slightly changed (yellow lines). Interestingly, the few clusters that switched community were the ones weakly linked to the deleted cluster within its community before damage. The VI between the two partitions before and

after damage was around 25%, and the major variations in connectivity weights occurred within the modules (Figure 5.6C).

The latter observation has two implications. First, the local damage affects the network globally, since the changes affect not only the affected module, but also its neighboring one. Second, variations are mostly intra-modular, with little disruption of the inter-modular connectivity, i.e. integration is preserved. This is illustrated in Figure 5.6D, which shows the distribution of the weight differences  $\delta w = w_{\text{after}} - w_{\text{before}}$ . The balance between reinforced links ( $\delta w > 0$ ) and weakened links ( $\delta w < 0$ ) shapes an asymmetric distribution with negative skewness, i.e. a higher number of weakened connections.

In addition of the changes in functional organization, we studied the possible leadership role of the affected cluster by calculating its main initial topological properties. We evaluate its total strength  $S_i$ , betweenness  $B_i$ , local efficiency  $Loc_i$ , and participation coefficient  $P_i$ . These measures are the set of relevant topological properties that configure our definition of ‘hub’. In the diagonal of Figure 5.7 we plot the histograms of these quantities as well as their corresponding pair-wise relations. The histograms include all the clusters in the network, but the deleted cluster is shown in a different color to highlight its properties. We can observe that the deleted node did not show any noticeable topological trait ( $S_i = 0.3, B_i = 0.4, Loc_i = 0.3, P_i = 0.5$ ).

A general feature that can be extracted from these plots is that network properties apparently do not correlate linearly to one another. For instance, the cluster with the highest strength neither exhibits a higher participation with other modules, nor shows a higher betweenness. If we also pay attention to the strength–local efficiency plot we can see that for each dynamical module (marked with its respective color module code) some exponential distributions appear, and that can reflect the hierarchy within modules (Ravasz and Barabási, 2003). Another interesting plot is the strength–participation that exhibits in some way the distinct role nodes in the network. The nodes encircled in light blue could be assigned as provincial hubs (i.e. nodes that

participate mainly with nodes within its own module), whereas the dark blue ones could presumably act as connector hubs (i.e. nodes that tend to participate with nodes from other modules).

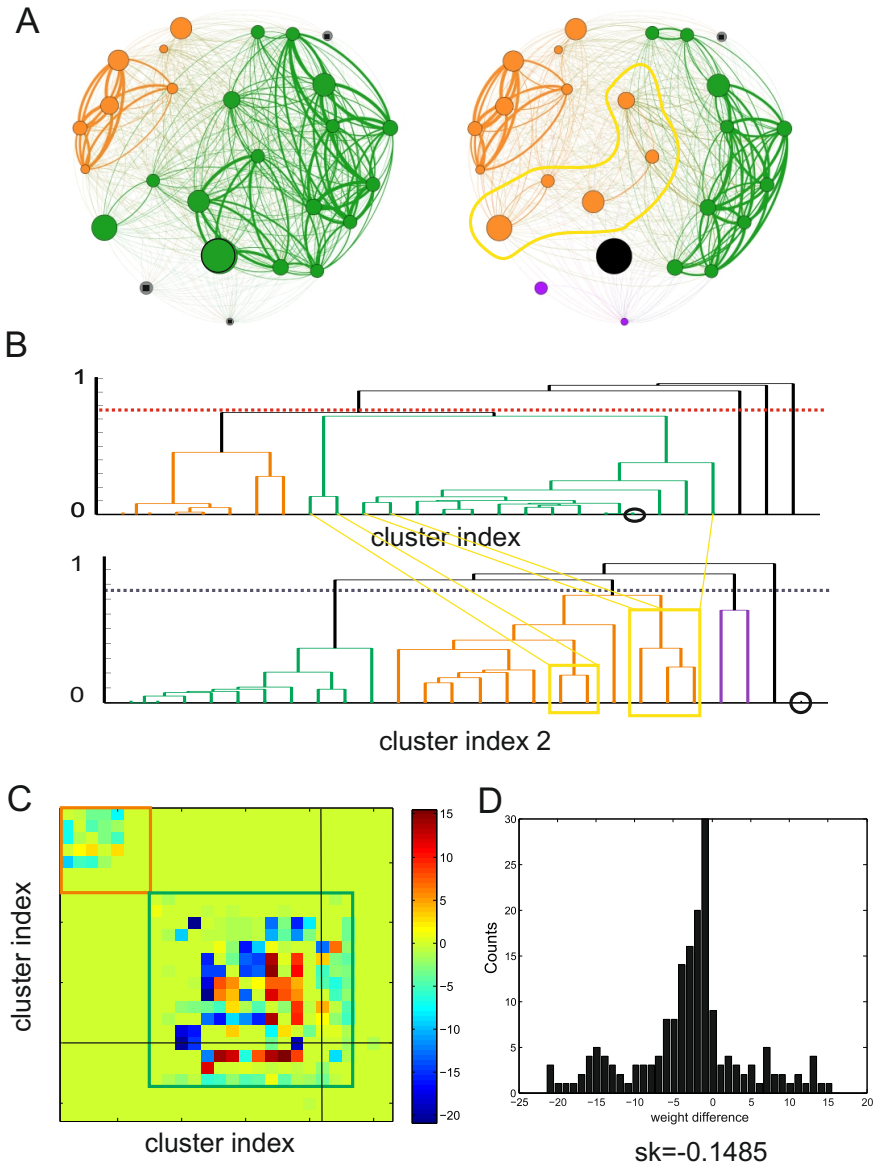


**Fig. 5.6 Random node deletion experiment.** **A**, Functional connectivity matrices before and after random silencing of a neuronal cluster (black circle). In the initial conditions two modules (green and orange) regulate the spontaneous neuronal dynamics. After damage, 5 nodes of the green module (yellow outline) switched to the orange module, and two independent clusters (gray) created a new module (purple). **B**, The functional reorganization examined by the hierarchical tree construction. The cluster indexing is different before and after the physical damage to highlight the new arrangement. The yellow boxes mark the neuronal clusters that have changed their activity and are comprised within the other community. **C**, The matrix difference between the link weights after and before damage. Initial modular structure is shown in color boxes. The black dashed line shows the location of the damaged cluster. The local damage mostly affected intra-modular connectivity. **D**, Corresponding histogram of this weight differences. The values ranged from highly negative to highly positive, highlighting the weakening and reinforcing of the connections. The asymmetry towards negative values of the distribution (skewness  $sk = -0.14$ ) indicates that the network connections were weaker after the damage.

The strength before and after the cluster damaged, are shown in the form of networks in Figure 5.8A. First, we can observe a rearrangement in strength after the random node deletion together with a rearrangement of the rich club core (black outline). We can notice that the targeted cluster is the biggest one in physical size but not in strength, indicating that size and strength are in principle unrelated.

Figure 5.8B illustrates the variation in betweenness, which naturally depicts the crucial paths for activity to pass through. Since betweenness is a measure of centrality, one would expect that the node with high betweenness has a special location in the network, like in the center of it (i.e. physically connected to the majority of nodes). However, in this experiment, the node with the highest centrality (shown in dark green) appeared to be distant from the spatial center. Thus, it is not possible to guess the functional role of a node by its spatial location in the network. Figure 5.8C shows the participation coefficient, and illustrates that the deleted node has indeed a score similar to the average of the network. It therefore, in principle, has no role in the integration of the network.

As a final remark, we note that the mean firing rate decreased by half  $\Gamma/\Gamma_0 \simeq 0.5$  after damage, the link density fell by 10% and the global efficiency declined by 24%. The only topological properties that were nearly

the same before and after damage were the clustering coefficient and the local efficiency, reflecting the maintenance of the modular behavior of the network. Hence, although the damage inflicted a severe, 50% fall in activity, the network seemed to remain globally connected by a reshaping its modular structure.

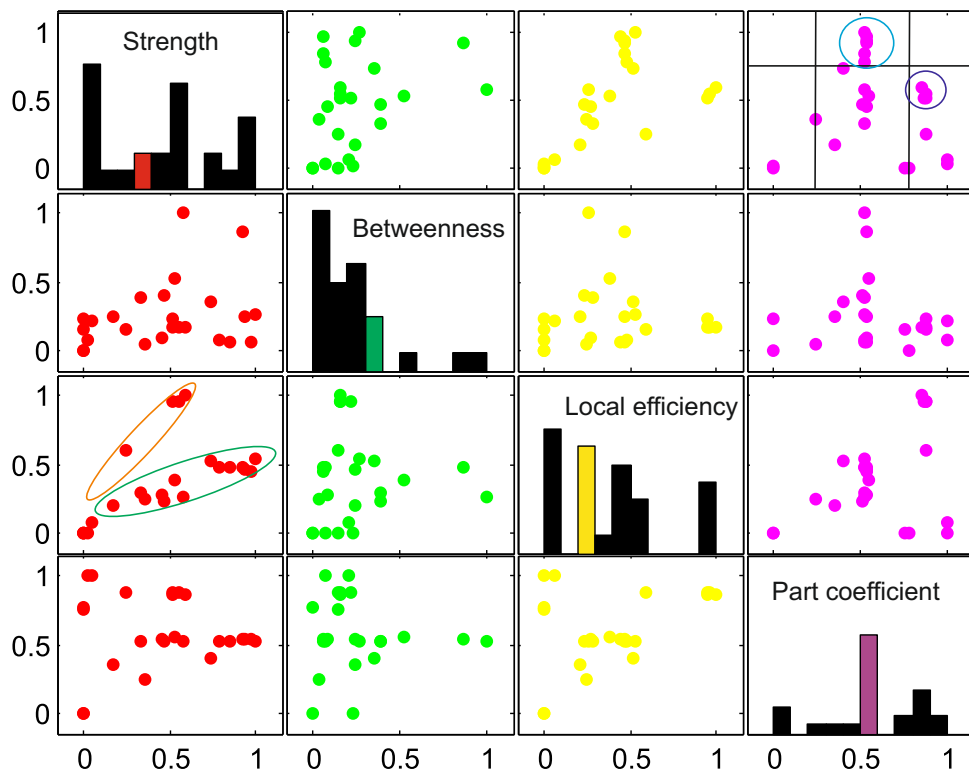


**Fig. 5.7 Major topological properties for the random damage experiment.** The total strength, betweenness, local efficiency and participation coefficient before the physical damage are depicted in the diagonal, while their corresponding pair-wise plots are shown outside. These quantities are normalized respect to the sum and quantify probability distributions. The histograms comprise all the clusters in the network. The color bars highlight the properties of the deleted cluster after damage, ruling out any ‘hub’ trait. The participation coefficient as a function of the strength (top-right corner) provide the ‘provincial’ (encircled in light blue) and ‘connector’ hubs (encircled in dark blue) in the network, which are not the future deleted one. The dashed lines separate the regions with 20% highest scoring.

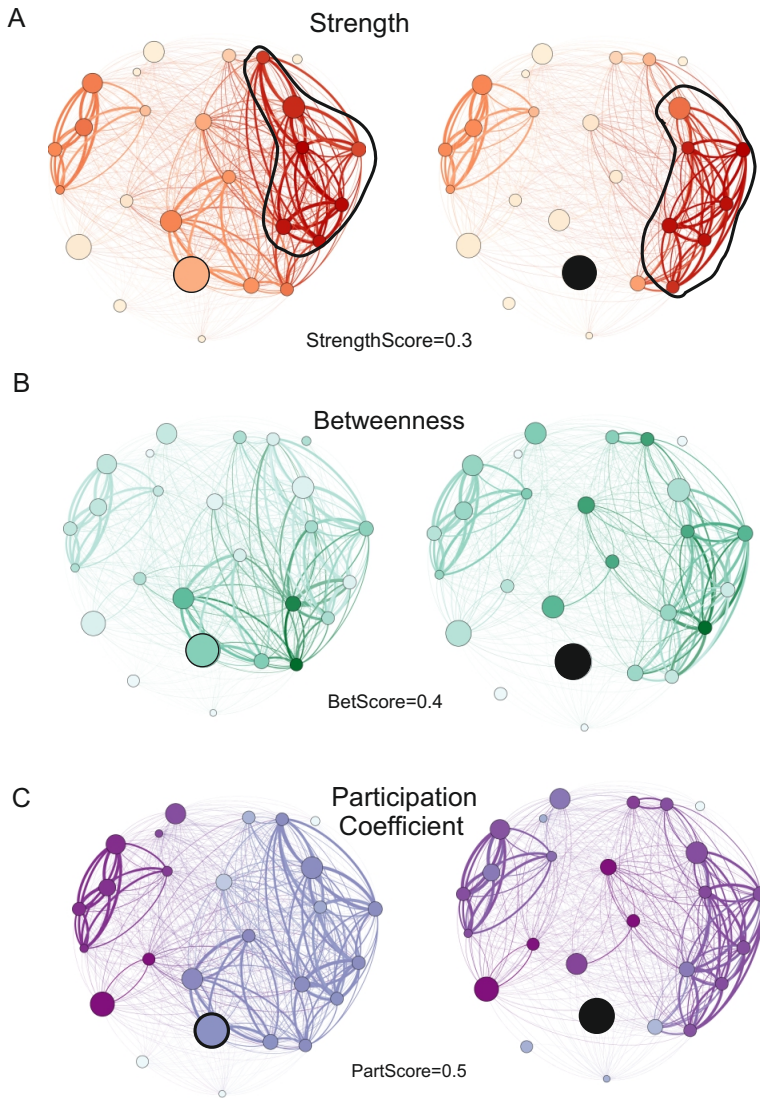


**Fig. 5.8 Changes in strength and betweenness of the random physical damage experiment.** **A**, Functional networks with the node and the connections colored according to the total nodal strength before and after the random neuronal cluster removal (black spot) of the illustrative experiment. **B**, The same functional networks, with the colors indicating the scoring of node betweenness. **C**, The same functional networks, with the color coding indicating the nodal participation coefficient.

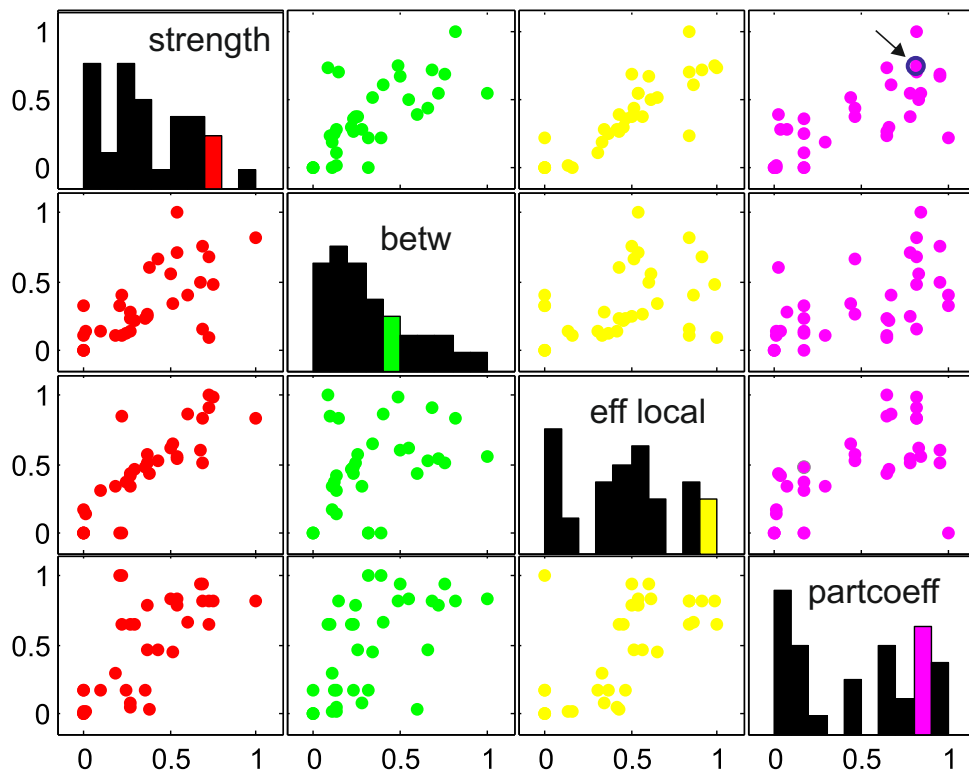


**Fig. 5.9** Evaluation of the initial topological properties in the hub damage experiment. The total strength, betweenness, local efficiency and participation coefficient histograms *before* the physical damage are shown in the diagonal and their corresponding pair-wise correlations outside of it. The colored bars indicate the location of the targeted neuronal cluster. This neuronal cluster can be considered as a one of the hubs in the network, being the second highest one in strength terms as well as in local efficiency, and with elevated participation coefficient (the 6th). Considering these functional networks as modulars, in the strength–participation coefficient plot we can observe that the actual damaged hub (black arrow) has a high strength but also a high participation coefficient, taking part to the integration-segregation game. Interestingly, here most of these network measures show linear correlations.

### 5.2.2 ‘Hub’ deletion

In these experiments we proceeded in two steps. In the first one we recorded activity for 30 min, but at the 10th minute we retrieved the corresponding data and swiftly analyze it to identify the clusters with the highest strength.

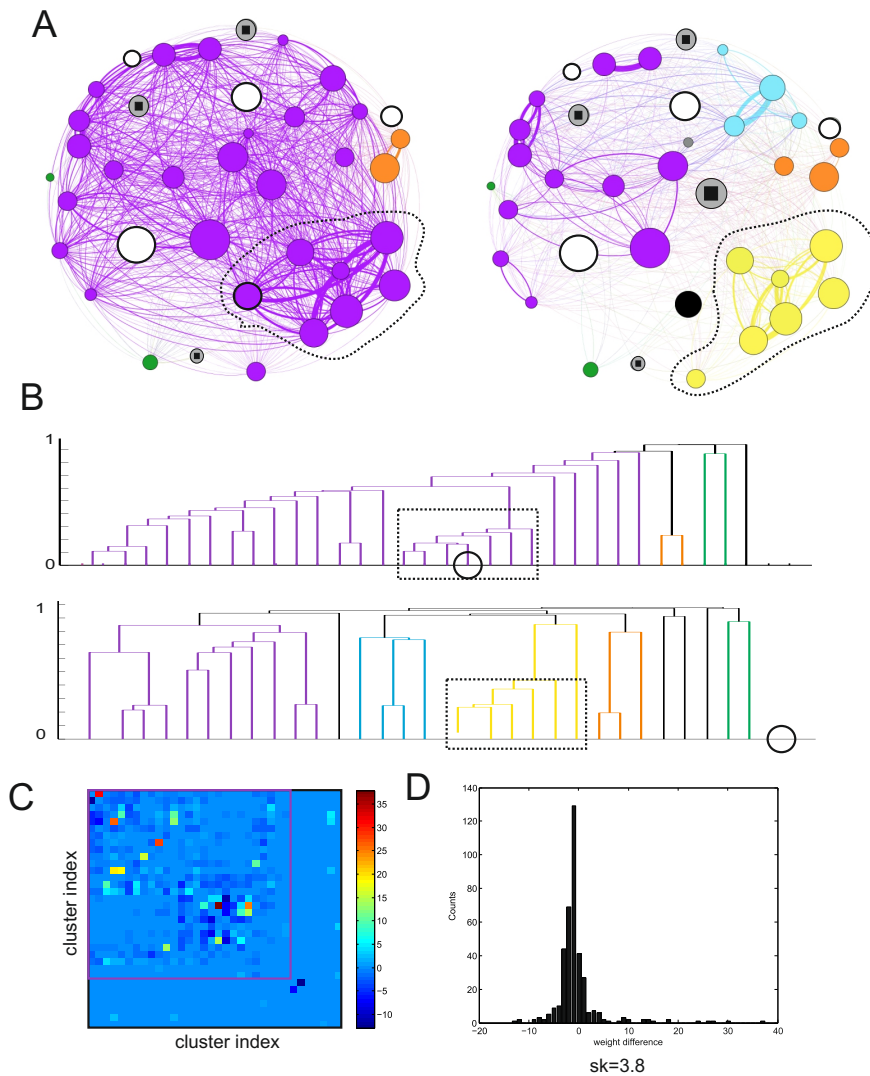
In the second step, we destroyed the candidate cluster with the laser beam and recorded again for another 30 min. These top–strength scoring clusters were good candidates to be hubs, and our aim was to inquiry whether a major network failure could be triggered as a consequence of a such a targeted attack.

Figure 5.10A shows the functional organization of the network before and after the deletion of the hub candidate, and the corresponding dendrograms are shown in Figure 5.10B. The dynamical community structure varied after damage, with a breakdown of the major community (purple colored) in three smaller ones (yellow, blue and purple). The dendrogram construction shows that the destruction of the ‘hub’ did not severely altered the intra–module organization of the new formed communities (e.g. the yellow one, marked with a dashed outline). However, the widespread damage on network structure is important, as reflected by a substantial decrease in global efficiency of 70%. Additionally, the major variations in the weight of the links occurred within the modules (Figure 5.10C) and a large number of connections increased their weights after damage (Figure 5.10D). The latter result can be quantified through the asymmetry of the weights’ differences distribution, which shows a remarkably high skewness of  $sk=3.8$ , and that can point at the emergence of compensatory mechanisms of the clustered networks under hub deletion.

The decrease in firing rate after hub removal was about 50%, similar as the random deletion experiment. Hence, we hypothesized that actual damage occurred in integration terms, i.e a major disruption of the main community, but still all clusters maintained activity within their modules.

The distributions of the main topological properties (in basis of our hub definition) are shown in Figure 5.9. We note that the targeted cluster ranked second in strength, with  $S_{rel_i} = 0.75$ . This cluster also was the second with the highest local efficiency,  $Loc_{rel_i} = 0.98$ , presenting a high participation score  $P_{rel_i} = 0.81$  and normal betweenness  $B_{rel_i} = 0.48$ . Using our hubness score measure, we firmly categorized the cluster as a hub, with a hubness score= 3,

since it was within the top 20% of the clusters with high strength, local efficiency and participation coefficient. Finally, by observing the pair-wise topological relations of the figure, we can note that in this experiment some of the network properties strongly correlate, facilitating the identification of hubs. Such a different behavior illustrates the dynamic richness of our cultures.



**Fig. 5.10 Changes in functional organization in the targeted physical damage experiment.** An illustrative experiment where the physical damage was done in the neuronal cluster that initially was second in high strength. **A**, Functional connectivity matrices before and after the neuronal cluster was injured (black spot) where the colors correspond to the functional communities and the dashed black curve pictures the submodule which shape one of the rich clubs in the network (see next Figure 5.11A). Before the targeted attack a big main community (purple depicted) governs the spontaneous neuronal dynamics. After the impairment, a disruption of the global community occurs, arising a submodular dynamical structure (yellow and blue colors). The gray clusters with a black square in the middle correspond to ‘independent’ clusters that do not form part of any community; the white nodes are inactive clusters. **B**, This strong functional reorganization is illustrated by the dendrograms. The black dashed boxes mark the preservation of the module where the affected cluster pertained (corresponding to the dashed black curves in A). **C**, The matrix difference between the weight of the links after and before applying the local damage. The local damage (the black lines indicate the injured cluster) was restricted to the modular functional structure (marked as color boxes). **D** The corresponding weight difference distribution showing a high asymmetry towards positive values ( $sk = 3.8$ ) indicating the high reinforcement of the connections after the physical insult to this ‘hub’.

The variations in total strength of every neuronal cluster from this experiment can be examined in Figure 5.11A. First, it is interesting to point out the existence of two rich clubs (black outlines). This trait tends to appear when the network is fragmented into different submodules physically disconnected, giving rise to high–strength interconnected clusters at distant locations. Interestingly, we can observe that the initial subset of clusters that formed the rich club was practically unaltered after damage.

Finally, Figure 5.11 B shows the ‘hubness score’ across the network. Just four clusters appeared to be the hubs, three with  $Hub_{sc} = 3$  and one with  $Hub_{sc} = 4$ . Considering the modular architecture shown, one can qualitatively assign these four hubs to the category of ‘connector’ and ‘provincial’ hubs. Based on the participation coefficient and taking into account their higher strength, one hub (highlighted with a star in Figure 5.11B) can be assigned as a provincial hub since it is totally embedded within its own submodule, i.e. all its connections are intra–submodular ones. We can also identify three connector hubs (highlighted with diamonds) that present a number of out–going connections within other submodules higher than in–going connections within their submodules. Of these connectors hubs, one actually corresponds

to the damaged cluster and formed part of the rich club. We remark that these hubs indeed connect with other clusters within its submodule, but also project strong connections to other submodules, being potential mediators between segregation and integration. Therefore, their destruction can cause—as we have observed—a severe disruption of the balance between these two properties.

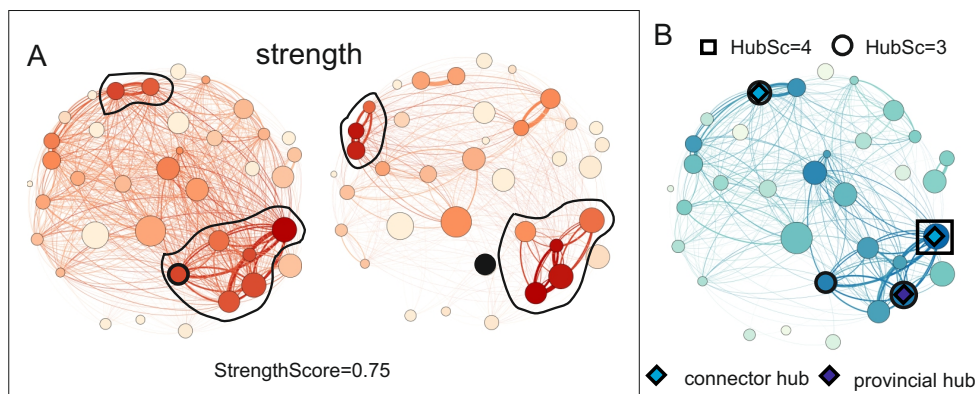


**Fig. 5.11 Changes in strength and hubness score.** **A**, Functional networks with the node and the connections colored according to the total nodal strength before and after one of the hubs was removed (dark spot). The black outline surrounds the subset of nodes that participate in the rich club. Two rich clubs appear, pinpointing the high robustness of these networks. **B**, The functional network before the attack (showing the top link connections) colored according to the mean ‘hubness score’. Four nodes were identified as ‘hub’ following the ‘hubness score’ evaluation. The square boxes mark the hubs with  $Hub_{sc} = 4$  whereas circles stamp the hubs with  $Hub_{sc} = 3$ . Two connector (dark blue within the diamond) and one provincial hub (light blue within the diamond) are qualitatively identified taking into account the internal modular hierarchy of the neuronal clustered dynamics. The attacked hub is embedded within a ‘submodule’ resembling other provincial hub, but projecting few but strong connections to other submodule, being therefore also important as integrator node.

### 5.2.3 Initiators damage

As we commented in Section refinitiators, spontaneous activity in the clustered networks is typically initiated by few number of clusters, and whose downstream activations shape the firing sequences. Given the clear impor-

tance of these clusters, we studied the effect of permanently silencing them through laser damage.

The experimental procedure that we carried out was similar to the previous one. We recorded spontaneous activity in two steps, before and after damage, and using a fraction of data from the first block to determine the initiators. We found the detection of the initiator difficult. In the preliminary results that we present in Figures 5.12 and 5.13 we observed that the damaged cluster actually did not have the highest initiation score, it was just strongly linked to it. We therefore used this experiment to shed light on the importance of the neighboring clusters to understand and quantify the final damage effect.

The functional organization of a representative network before and after the physical damage is shown in Figure 5.12A. Before damage, activity was nearly coherent, and a big community shaped the structure of the network (highlighted in orange). After damage, the community broke off and smaller ones merged. Interestingly, not only the damaged cluster (black circle) became silent, but also some of its neighbors (black circles with red outline), while other nearby clusters started to fire in an independent manner (gray circles with red outline). Altogether, these changes indicate a highly local connectivity disruption.

The corresponding dendrograms (Figure 5.12B) show these dynamical changes in detail. An interesting feature is the emergence of a neat hierarchical community structure after damage, which was not present before. The black circles at the bottom of the dendrogram point out the clusters that became silent or fired independently after damage. We note that, by inspecting the arrangement of these clusters in the dendrogram, it is not possible to deduce any relation with the final dynamical clusters' arrangement. Simply, these clusters are physically close to the damaged one, but they are not functionally neighbors (as we can observe in the dendrogram). This observation highlights the crucial role that the structural connectivity plays in shaping the functional organization of the network. It also reveals that the structural connectivity is

strongly local, as evidenced by a 25% of network affectionation —understood as clusters either silenced or disconnected— after damage.

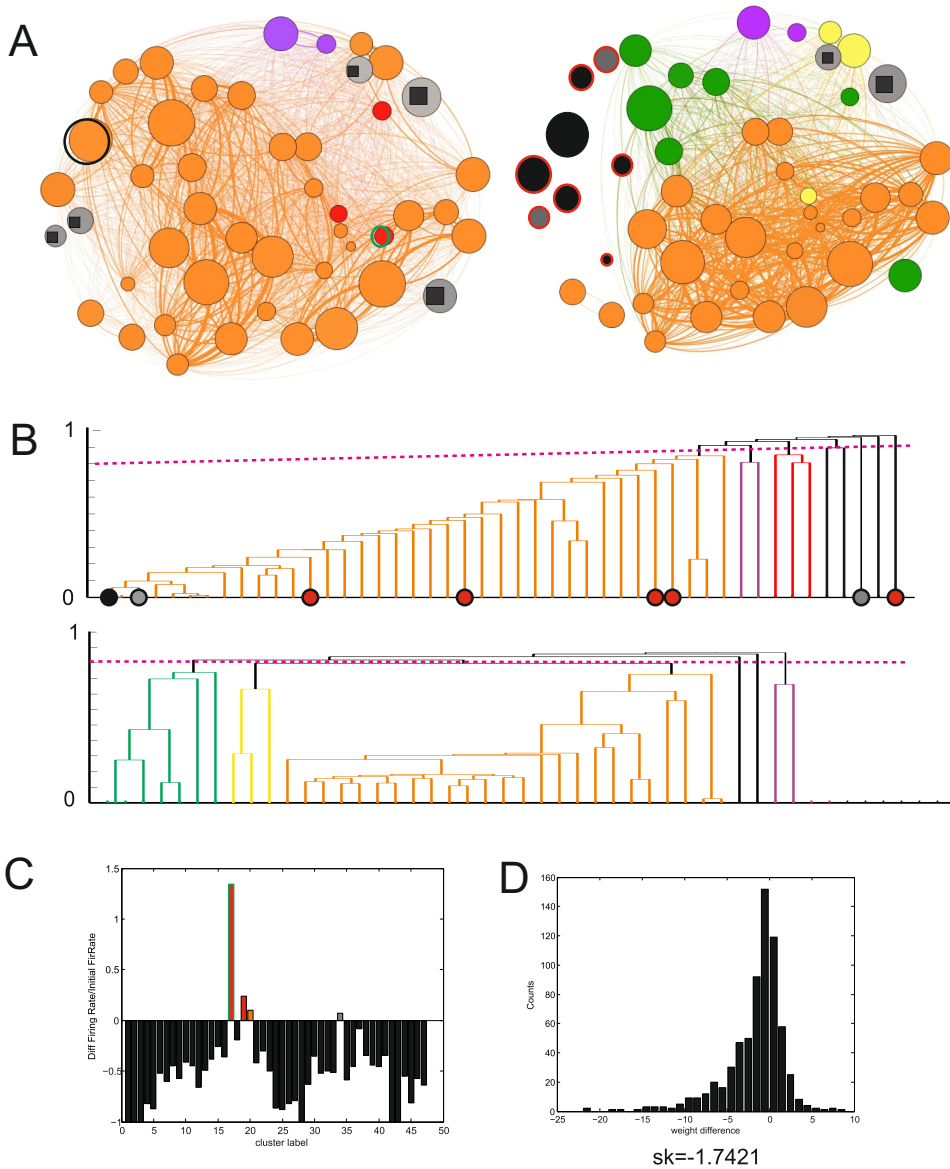


**Fig. 5.12 Changes in functional organization when the local damage affects the initiator of activity.** **A**, Functional structures before and after the neuronal cluster was injured (black spot) where the color corresponds to the functional communities (orange, red and purple). The gray nodes with a black square are the ‘independent’ clusters that do not belong to any community, the dark cluster corresponds to the initial damaged cluster, the dark ones encircled with red color are clusters that in consequence ceased completely their activity after the cluster impairment, and the gray ones also encircled with red color kept on firing but in an independent way that might have disconnected from the network. Again, after the lesion, this global dynamics was disrupted and gave rise a more modular dynamics that shaped new communities. **B**, This changes in dynamics are illustrated by the dendrograms, where the circles depicted at the bottom are colored using the same node color pattern that appears in the functional network after the cluster has been damaged. The died clusters does not correspond to the clusters that were more similar in activity histories of the injured node. **C**, Ratio of the firing rate of each cluster after and before the attack. Practically all the clusters reduced their firings events indicating the high damaged received except few clusters (colored following their community initial colors) that slightly increase their activity and especially one neuronal cluster increased substantially its firing rate (red colored surrounded by a green circle in A). **D**, The corresponding weight difference distribution showing a high asymmetry towards negative values ( $sk = -1.74$ ) indicating the high weakening of the connections when the initiator cluster is affected.

In principle, network damage is widespread. By plotting, for each cluster, the ratio between the activity after and before damage (Figure 5.12D) one can observe that the firing rate notably decreased for most of the clusters, except for one that boosted in activity. Moreover, this damage is also evidenced by the distribution of links’ weight differences  $\delta w$  (Figure 5.12 E), which exhibits a strong left-skewness with  $sk = -1.74$ . However, this general deterioration does not affect the global integration of the network since the global efficiency value remains similar with  $G_{\text{eff}}^{\text{after}}/G_{\text{eff}}^{\text{before}} = 1.08$ . Apparently, the damage is significant but mainly affects locally clearly exhibited by the number of died or disconnected clusters closely in space.

By evaluating the topological properties of the targeted node before damage we observed that it did not excel in any significant topological property, with  $S_{\text{rel}_i} = 0.17$ ,  $B_{\text{rel}_i} = 0.12$ ,  $Loc_{\text{rel}_i} = 0.35$ ,  $P_{\text{rel}_i} = 0.66$ . As an example of the distribution of these properties across the network, Figure 5.13A-B shows the total strength before and after damage. We note that the rich club was relatively far from the damaged cluster and was largely unaffected. Addition-

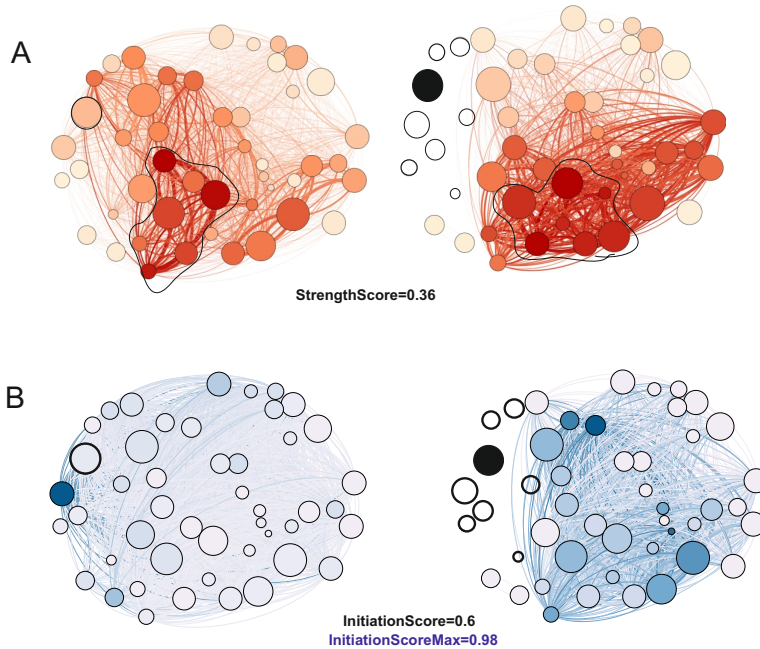


**Fig. 5.13 Changes in strength and initiator cluster scores.** **A**, Functional networks with the node and the connections colored according to the total nodal strength before and after the cluster deletion (dark spot). The black curve surrounds the subset of nodes that form the rich club. After the local damage, some cluster stopped firing or went on firing but disconnected from the rest of the network (white nodes) highlighting the harmful consequences when the damage affects to the initiator cluster. **B**, The same functional networks where here the color coded depicts the number of times that one cluster has initiated the spontaneous activity (initiator cluster scores). One can easily observe that the highest initiator cluster was spatially closer to the initial damaged cluster. After the injury different clusters spatially distant started to initiate the spontaneous activity.

ally, as commented before, the damaged cluster had a powerful initiator of activity as neighbor, with  $\text{InitScore} = 0.98$  (Figure 5.13C-D). Interestingly, the initiator became silent after damage but others emerged to take its role, and spread homogeneously across the network.

## 5.3 Discussion

### 5.3.1 Assortativity, resilience, and network circuitry

Global network deterioration experiments through photo-damage and chemical degradation showed that the clustered cultures exhibit a higher resilience to damage as compared to the homogeneous ones. We ascribe this contrast in behavior to the difference in the functional architecture of both networks, and that is mainly related with their structural topological configuration. In particular, in the previous chapter we observed that clustered networks exhibited assortative traits while homogeneous networks were nearly disassortative. However, the link between assortativity and resilience in our experiments is based on the comparison between the response of clustered and homogeneous cultures upon the same perturbation. To obtain conclusive evidences that assortativity confers resilience traits exclusively from topology, we would require an experimental protocol in which we could ‘rewire’ at will the connectivity between clusters, or shape in a control manner different circuitries while preserving the number of nodes in the network. Although these strategies are certainly enlightening, they are of difficult development and a major experimental challenge that goes far beyond the scope of this thesis.

It is important to point out, however, that the shown resilience may result from other factors directly linked to biological aspects of the clustered networks, for instance a larger number of gap junctions as compared to homogeneous networks or differences in CNQX perfusion into the neurons. Thus, the best set of experiments would be those where cultures of a specific type (i.e. homogeneous or clustered) could be prepared with very different connectivity configurations, therefore giving rise to a broad range of assortativity levels. The major experimental difficulty in developing such an idea in clustered networks is that we lack the engineering resources to favor assortative or disassortative traits. Based on our experience along the last 5 years, we think that the physical organization of the clusters (for instance self-organized net-

works versus engineered ones) or their dynamics (coherent versus modular) are parameters that may modulate assortativity. Such investigation is one of our future research projects.

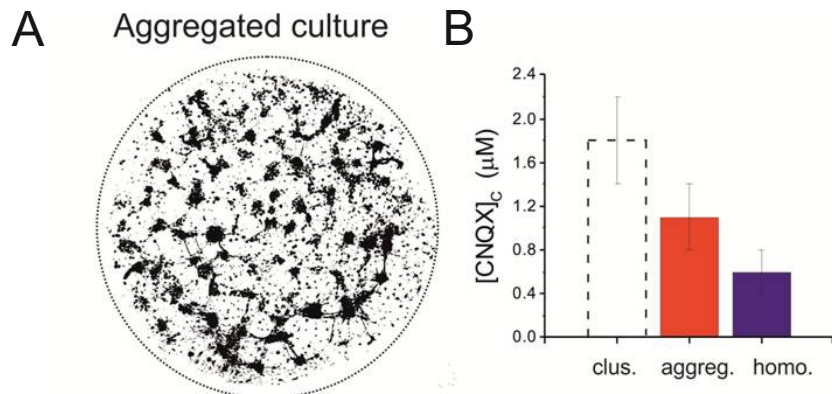


**Fig. 5.14 Aggregate culture.** **A**, Example of an aggregated culture. The culture is 3 mm in diameter. Image is highly contrasted to show the neurons as black pixels over a white background. Note the strong aggregation and interconnectivity of a part of the network. **B**, Critical concentration of CNQX at which activity ceased, comparing the behavior of clustered cultures (strongly assortative), aggregated (assortative), and homogeneous (weakly assortative or neutral). Each bar is an average over 4 – 6 cultures.

On the other hand, considering homogeneous cultures, we can use recent theoretical developments (Schmeltzer et al., 2014) that show that assortativity can be favored in spatial networks by combining areas of high density of connections with areas of much lower density. Experimentally, this can be achieved in homogeneous cultures by allowing aggregation in the culture, resulting in areas of high density of neurons (and strongly interconnected) with areas of relatively poor population. Despite aggregation, the culture maintains a monolayer of neurons, so CNQX application or photo-damage affects all neurons equally. An example of such a configuration is shown in Figure 5.14A. The analysis of effective connectivity shows that this kind of aggregated cultures exhibit higher assortativity values than standard homogeneous cultures. Additionally, by analyzing the activity in the aggregated networks upon CNQX application, we observed a tendency for activity to

cease at higher concentrations of CNQX compared to their homogenous equivalents (Figure 5.14B). Interestingly, these aggregated networks present positive assortativity values, in the range 0.18 – 0.25, in between the homogeneous and clustered networks. These experiments strengthen the link between assortativity and resistance to damage. However, more experiments are required to confirm the drawn conclusions.

### **5.3.2 On recovery mechanisms upon CNQX degradation**

The unexpected increase in firing rate at specific CNQX dosages may hint at the emergence of some sort of network mechanism to compensate for damage. In these experiments, and only upon blockade of a small fraction of the excitatory connections, there was a characteristic increase in the global efficiency, suggesting network compensation to preserve activity. However, above some specific level, network damage took over and functional organization rapidly deteriorated, disrupting the structure in multiple submodules until activity finally ceased. By comparing these results with a percolation process in which the first links to be lost were the inter-modules ones, one can hypothesize that the actual network reorganized in a set of new, more robust communities that resulted in a slower degradation.

These adaptive or recovery traits of the network upon weak damage, as well as the particular damage level at which rapid disruption starts, may strongly depend on how rapidly the rich club is compromised upon damage progression. The integrity of the rich club is indeed our hypothesis to explain a higher resistance to damage. Such an idea has been also suggested in Alzheimer's disease, where acute brain's deterioration occurs when the affected regions are the ones associated to the rich club (Palop et al., 2006; Stam, 2014).

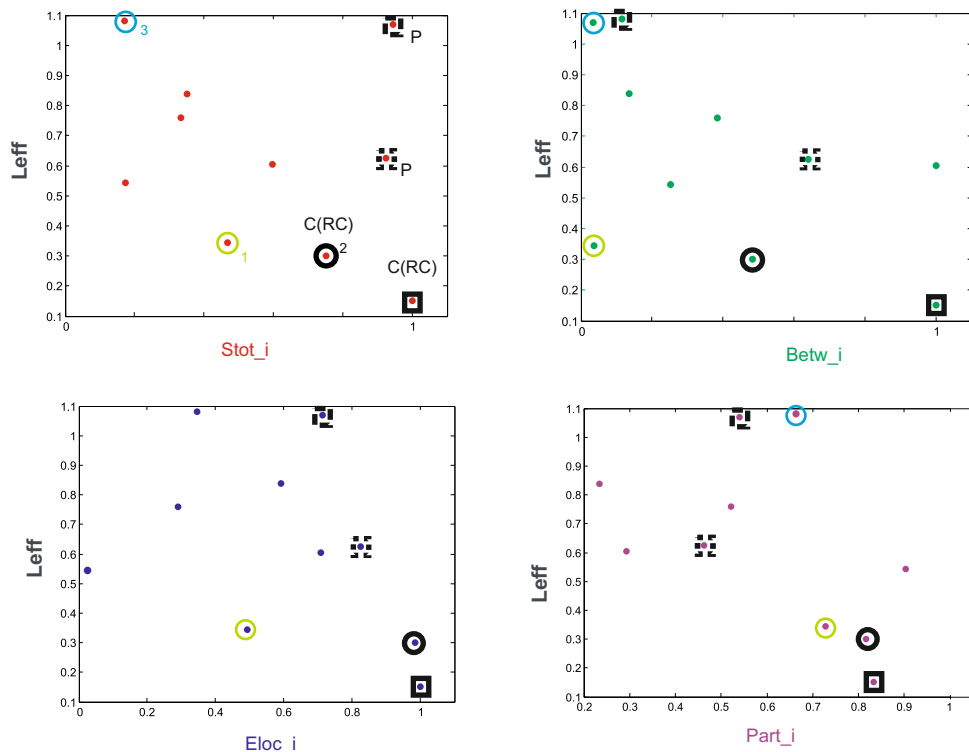


**Fig. 5.15 Global damage versus initial topological properties of the impaired cluster**  
 The global efficiency ratio is evaluated to distinct topological properties of the damaged neuronal cluster for 10 experiments. The global damaged caused on the network after the removal of the neuronal cluster in principle does not depend on its initial total nodal strength or betweenness.

### 5.3.3 The importance of the hubs in our experiments

We have completed so far 10 experiments (including the random, hub and initiator actions). Despite the relatively poor number of experiments we can infer a set of interesting features on network resilience. Although only a node is deleted in our experiments, we can quantify the extent of damage using the ‘global efficiency’ measure  $G_{\text{eff}}$  for every damaging action.

The plots in Figure 5.15 show the relationship between  $G_{\text{eff}}$  and some topological measures of the targeted nodes before actual damage, namely total strength, betweenness, local efficiency and participation coefficient. At a

first look, the global extent of damage does not directly correlate on the initial characteristics of the targeted cluster. However, if we inspect the hub-targeted experiments (black outlines) we can observe some interesting patterns. First, the four hubs have high strength and high local efficiency; two of them have a high participation coefficient and can be assigned as connectors C., while the others have lower participation coefficient and are therefore can be ascribed as provincial (P) hubs. Interestingly, we can observe that the connectors that also form part of the Rich Club core (RC) caused more global disruption than the provincial ones. Indeed, the nodal total strength correlates with the loss in global efficiency except for these provincial hubs.

This analysis indicates that the connectivity surrounding the node can be important. The hub can therefore be embedded within a module, be part of the RC, or operate independently. This analysis also points out that not only the hub with the highest strength will cause the highest damaging upon failure, but also its position in the modular network.

### 5.3.4 Network performance upon random and targeted damage

From our preliminary results on laser ablation, we can conclude that clustered networks are presumably resilient to random failure. This is quantified through the ratio of the global efficiency after and before damage,  $G_{\text{eff}}^{\text{ratio}} = G_{\text{eff}}^{\text{after}} / G_{\text{eff}}^{\text{before}} \simeq 0.7$ , relatively high. However, under ‘hub’ destruction, the damage extended globally throughout the network, with  $G_{\text{eff}}^{\text{ratio}} \simeq 0.3$ , ultimately causing the fragmentation of the network in multiple submodules. On the other hand, the damage of the ‘initiator’ did not cause a cascade of global failure (in integration terms), with  $G_{\text{eff}}^{\text{ratio}} \simeq 1$ , although the damage inflicted at a local level was substantial and caused the silencing or disconnection of the clusters surrounding the targeted one.

Indeed, the set of damaging actions can be conceptualized in terms *integration–segregation*. Integration deals with overall network functionality,

whereas segregation deals with the functionality at a cluster or community scale. It is important to note that both characteristics can be independent. A network can decrease in segregation as a result of weaker communities, but remain integrated since all communities are operational. Conversely, a network can be less integrated as a consequence of *inter-moduli* failure, but remain richly segregated as far as *intra-moduli* connectivity is maintained.

Hence, in the context of our experiments, global damage corresponds to a decrease in integration, i.e. a loss in network performance as a whole; while local damage corresponds to a reduction in segregation, i.e. a loss in the performance of the communities. This integration–segregation interplay that we observe is fascinating, and illustrates the complexity of clustered networks, their organization, and the intricate role of recovery mechanisms.

### 5.3.5 Network damage and the brain

Studies on network resilience to insult in the brain have typically focused on the global extent of damage upon network failure (Achard et al., 2006; Alstott et al., 2009; Honey and Sporns, 2008). Computational models of brain failure considered the Albert and Barabasi approach (Albert et al., 2000), which quantifies the global damage using the global efficiency and the giant component. With these two components, the studies evaluated the fall in network performance upon progressive deletion of nodes, to later compare different topological configurations, e.g. scale-free or random, to assess the resilience degree of the network. The fact that these studies centered on the global damage in integration terms is because specific circuit degradation in the brain may ultimately affect whole brain processes such as behavior and cognition. A failure in integration, hence, may give rise to several neurological pathologies (Fornito et al., 2015; Stam, 2014). (Local damage, on the contrary, seemed to produce specific deficits that do not have a prominent effect in behavior). In particular, it has been shown that this global disintegration is the first critical step towards an irreversible deterioration and

death, as occurs in highly aggressive neurodegenerative disorders, such as Alzheimer disease. For this reason, it is of vital importance to unveil as soon as possible vulnerable brain regions that, once affected, initiate a cascade of miscommunication and ultimately total failure.

The mechanisms that lead to widespread brain damage are complex and highly non-linear, and strongly depend on the topological role of the affected brain regions. Some studies have claimed that the the role of connector and provincial hubs, and ultimately the participation coefficient, are extremely correlated with the global impact of the focal lesion. In particular, it has been hypothesized that damage on connector hubs is more harmful than on provincial hubs, simply because the failure of the inter-modular connections quickly triggers global network breakdown(Fornito et al., 2015; Gratton et al., 2012; He et al., 2009; Honey and Sporns, 2008; Warren et al., 2014). On the other hand, other studies Alstott et al. (2009); He et al. (2009) have pinpointed a higher dramatic effect on the performance of brain's functional network when nodes that occupy a high central position on the network (i.e. high betweenness) are removed.

These studies reflect the importance of the different hub categories, i.e. high centrality, high strength, or high inter-modular participation. Clearly, the role of these hubs is crucial since they govern network integration. A pending issue, however, is the understanding of which category causes the highest global network damage upon removal.

In this sense, our neuronal clustered networks offer an ideal platform to study in an easy and accessible manner the effect of removing these hubs in the functional connectivity, as well as procuring information on their role in integration and segregation. Indeed, it would be very interesting to target all kind of hubs (such as high strength, degree, provincial, connectors, or high betweenness) in order to get pivotal information on their importance upon removal.

### 5.3.6 Network response upon attack and resilience

The degree of global damage is strongly linked to the local connectivity. Hence, the ability of the network to maintain some sort of activity and functional connectivity upon damage greatly depends on the location of the targeted clusters. As observed for the random- and hub-targeted experiments, the silencing of the cluster did not cause the loss of the module in which it participated. This observation is somehow surprising since one could expect that the removal of a high-strength node within a module could trigger the collapse of the whole community, but the experiments show that this is not the case.

The apparently general trend is that functional connectivity reorganizes to retain the structure of the modules as much as possible. The weaker connections within modules are typically the first to vanish, while the strongest ones prevail. Experiments also show that when a cluster is removed from the rich club core, the network exhibits a major reinforcement, as revealed by a strongly positive skewness  $sk$  of the weight differences distribution,  $sk \simeq 3.8$ .

On the other hand, an interesting observation derived from our experiments is that those networks lacking a modular structure are much less capable to retain the integrity of the network, with  $sk \simeq -1.8$  in a typical experiment. Hence, such a modular structure seems pivotal to resilience. Since modularity and assortativity are related, this observation strengthens again the importance of assortative traits for a resilient network. In this sense, it was suggested that brain networks can confront the loss of nodes placed within modules much better than in other configurations (Meunier et al., 2010). For instance, it has been claimed that the recovery of function in the brain is higher when the affected regions exhibit a high clustering coefficient; whereas the recovery is less likely after damage of topological central areas with low clustering, such as bridge nodes (Fornito et al., 2015).

### 5.3.7 Potential descriptor of network damage

We have seen that the skewness,  $sk$ , of the distribution of weight differences provides a quick evaluation of the presumably network's ability to resist upon attack. Thus, the skewness measure appears as an additional potential descriptor to detect the effect of damage in local connectivity (loss of segregation) as well as the global one (loss of integration).

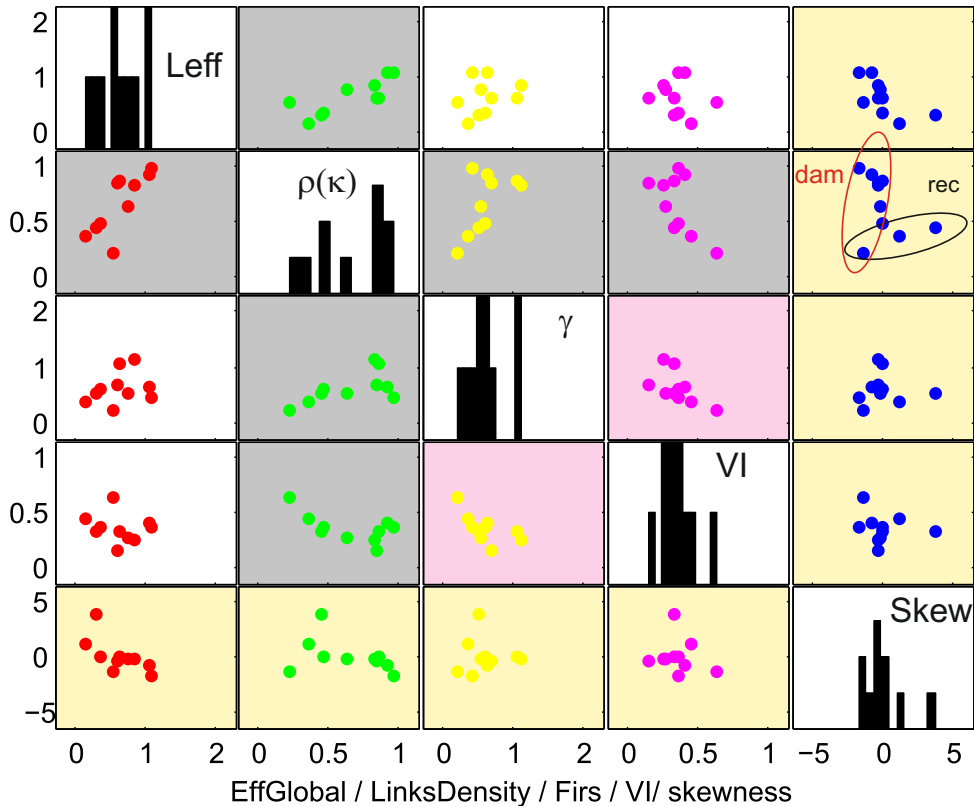


**Fig. 5.16 Potential descriptors.** The graphs show different descriptors used in the literature to quantify the global damage, namely the global efficiency ratio, the ratio of density links  $\rho(k)$ , the ratio of mean firing rates, the variation of information of community structures, and the skewness. Although some of these measures correlate to one another, the skewness is the only measure that captures the recovery ('rec') and the damaging ('dam') effects.

To stress the interest of the skewness measure and other, we have studied the relationship between five measures, namely the skewness itself, the ratio between the global efficiency after and before damage  $G_{\text{eff}}^{\text{ratio}}$ , the ratio in density of the links  $\rho$ , the ratio between the mean firing rate ( $\gamma/\gamma_0$ ), and the VI between the partitions after and before damage, considering the 10 experiments.

The results are shown in Figure 5.16. Interestingly, most of the measures correlate between them (highlighted in the figure with gray colored background). For instance, a lower density of links after damage correlates well with a lower global efficiency, a lower number of firings and higher VI. The latter indicates a higher segregation in different modules. However, the skewness has a more complex relationship with the other magnitudes and interestingly, we can distinguish a double role, namely damaging (‘dam’) and recovering (‘rec’) effect. This apparently double behavior can be easily seen in the plot of the loss in density links a function of the skewness. This observation reinforces the idea that this skewness measure can identify the local and global vision, i.e. the segregation–integration balance. It can therefore distinguish the recovery or the deterioration on the network, becoming a powerful estimator to predict the final damage, becoming useful for a ‘prognosis’ of the future network state.

# Chapter 6

## Results III: Clustered networks as an *in vitro* model for Alzheimer

We here use the developed tools and experience from previous results to apply our clustered neuronal networks to tackle specific medical problems. Specifically, we aim at quantifying the damaging action of three major agents observed in Alzheimer's (AD) disease pathogenesis: magnetite (M), amyloid- $\beta$  ( $A\beta$ ), and magnetite-amyloid- $\beta$  complex (M- $A\beta$ ).

As we have seen in previous chapters, our neuronal network fire collectively in small groups forming *dynamical moduli* or *communities*, and that shape what we call the *functional organization* of the network. The coherence within and between communities is tied to the clusters' interconnectivity, and therefore a loss in coherence can be ascribed to actual changes in the network's underpinned circuitry due to damage. Therefore, we simultaneously monitored networks dosed with each of the three agents (together with a control network) and studied the variations in spontaneous activity and functional organization. The results show first that, of the three chemical actions studied, only the M- $A\beta$  complex caused severe network deterioration; and, second, that the clustered networks offer a unique platform for pharmacological studies.

## 6.1 Biochemical context

AD is a neurodegenerative disorder characterized by a widespread functional deterioration of the human brain. Among the diverse factors involved in AD pathogenesis, it has been suggested that the high accumulations of  $A\beta$  fibrils that constitute the observed senile plaques (Hardy and Selkoe, 2002; Hardy and Higgins, 1992; Tsai et al., 2004), as well as the high levels of iron concentration (Castellani et al., 2012; Goodman, 1953), are primary actors. The origin of these abnormal overproductions, their interrelation and actual action on brain's circuitry are still unsettled questions and a major focus of research.

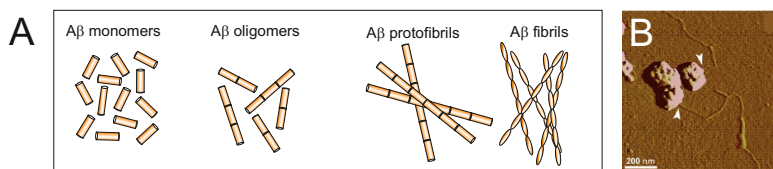


**Fig. 6.1 Different conformational states of  $A\beta$ , compared to *in vitro* complex M- $A\beta$ .** (A) Qualitative representation of the different conformational states of  $A\beta$ . From left to right,  $A\beta$  monomers,  $A\beta$  oligomers (comprising two, and three monomers),  $A\beta$  protofibrils (intermediate state),  $A\beta$  fibrils (stable final configuration that form the  $A\beta$  senile plaques). (B), The *in vitro* complex M- $A\beta$ ) prepared at IBEC. The white arrowheads mark  $A\beta$  protofibrils attached to magnetite nanoparticles.

A high number of recent studies indeed showed that the intermediate states of the final conformation of  $A\beta$  plaques, specifically  $A\beta$  protofibrils (Lannfelt et al., 2014; Lashuel et al., 2002; Mucke, 2009), appear to be directly related to neuronal damage (see Figure 6.1A). Indeed, several studies demonstrated that these protofibrillar  $A\beta$  states alter signal-transduction cascades and cause high neurotoxicity (Demuro et al., 2005, 2010; Kawahara et al., 2011), while monomeric states of  $A\beta$  were considered non-toxic. On the other hand,  $Fe^{2+}$ , a redoxactive and highly damaging valence state of iron, has been reported in abundant quantities in AD brains (Everett et al., 2014; Smith et al., 1997). These abnormal quantities of iron have been linked in turn to

magnetite, the only stable iron oxide that contains  $\text{Fe}^{2+}$  (Collingwood et al., 2005; Hautot et al., 2003; Pankhurst et al., 2008). The concurrent presence of magnetite and  $\text{A}\beta$  in AD brains raised the hypothesis that magnetite itself could be non-toxic and even protective against  $\text{Fe}^{2+}$ , but its formation in the presence of  $\text{A}\beta$  could stabilize protofibrillar  $\text{A}\beta$  states, lethally reinforcing its accumulation and damaging role.

Despite the advances towards an understanding of key molecular mechanisms in AD, the complexity of the pathology and the inherent difficulty to study the progression of the disorder *in vivo*, have motivated the development of more accessible *in vitro* approaches. Studies using cell cultures have established a connection between fibrillar  $\text{A}\beta$  plaques and neurotoxic effects (Dahlgren et al., 2002b; Hartley et al., 1999); and in slices from mouse hippocampus it was reported local neuronal damage upon presence of protofibrillar  $\text{A}\beta$  structures (O’Nuallain et al., 2010).

The experimental platform that we developed and the results that we obtained follow this spirit of developing new *in vitro*, multidisciplinary approaches to tackle neurological disorders.

## 6.2 Experimental system

We studied the influence of the three chemical perturbations on the activity of clustered networks, studied at DIV 5 – 15. As core experimental platform, we used the *Specific, perturbative biochemical environment experiments* configuration, i.e. the simultaneous monitoring of 4 mini-cultures as described in Chapter 2. In summary, this experimental configuration consisted in an array of  $2 \times 2$  cavities pierced on a PDMS mold, each cavity 3.5 mm in diameter and 4 mm deep. Figure 6.2A shows this experimental platform. Neurons were seeded with identical nominal density in each cavity, and the entire system cultured as a single unit in a multi-well culture plate to ensure identical development. Although each cavity gave rise to different network designs

—as also seen in previous chapters— the dynamics of these clustered networks was qualitatively very similar. under identical biochemical conditions. In total we investigated 15 networks, and all experiments were carried out at room temperature.

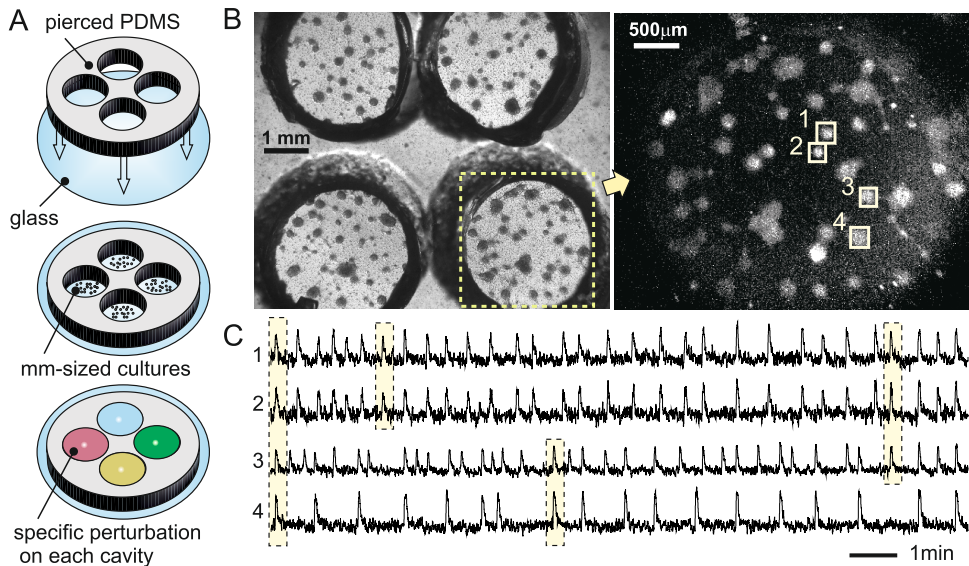


**Fig. 6.2 Experiments and data acquisition.** (A), Sketch of the experimental setup and procedure. A pierced PDMS layer was attached to a glass coverslip to shape a  $2 \times 2$  grid of cavities, each 3.5 mm in diameter and 4 mm deep. Neurons were plated on these cavities forming independent, mm-sized neuronal networks, and cultured in identical conditions. For measurements, one of the cavities was left as control, while the others were dosed with specific chemical agents. (B), Left: Bright field image of a typical preparation at *day in vitro* 8, showing the 4 cavities containing the neuronal networks. Dark circular objects are the clusters connected to one another through bundles of neurites. Right: Fluorescence image of the bottom-right culture. Firing clusters appear as bright spots on the images. (C), Representative fluorescence traces of the 4 clusters highlighted in B, and along 15 min of recording. The yellow boxes illustrate different combinations of co-activations, that ultimately shape the final communities.

Active clusters appeared as bright spots upon activation (Figure 6.2B, right), and the monitoring of all the clusters for about 1 h provided the main data for quantifying network activity. Typical fluorescence traces for 4

representative clusters are shown in Figure 6.2C, and exhibit the distinctive firing in groups that delineate the characteristic communities.

The novelty of the presented system is the ability to simultaneously monitor the changes in spontaneous activity in all 4 cavities, and upon administration of a specific chemical agent in each of them. To proceed, we first measured spontaneous activity on each cavity for 30 min before applying the chemical perturbation. Then, one of the cavities was always left as control, while the others were doped either with 2  $\mu$ l of magnetic nanoparticles (M), A $\beta$  solution, or M-A $\beta$  complex (see Section 2.5.3, for details on their preparation). The cavities were next left in darkness for 10 min for the compounds to dissolve and take effect, and spontaneous activity resumed for another 30 min.

Changes in the temperature of the well or medium evaporation can cause variations in the spontaneous activity of all cavities from the first to the second recording. Such a drift is an artifact that masks actual chemical damage, and is quantified as the ratio  $\Phi_C^P/\Phi_C^0$ , with  $\Phi_C^0$  and  $\Phi_C^P$  the average activity in the control cavity along the first and second recordings, respectively. Of the 15 experiments studied, this ratio ranged between 0.9 and 1.2.

Data analysis in the context of activity variability, modular organization and functional (effective) connectivity provided a quantification of the influence of each chemical agent on network behavior.

## 6.3 Results

### 6.3.1 Spontaneous activity upon M-A $\beta$ action

Examples of the collected data (in the form of raster plots) before and after the chemical intervention are shown in Figure 6.3. The control case effectively consisted in two identical, consecutive measurements, and its raster plots indeed exhibit nearly the same features. The network is characterized by rich spontaneous activity with the existence of two distinct firing sequences,

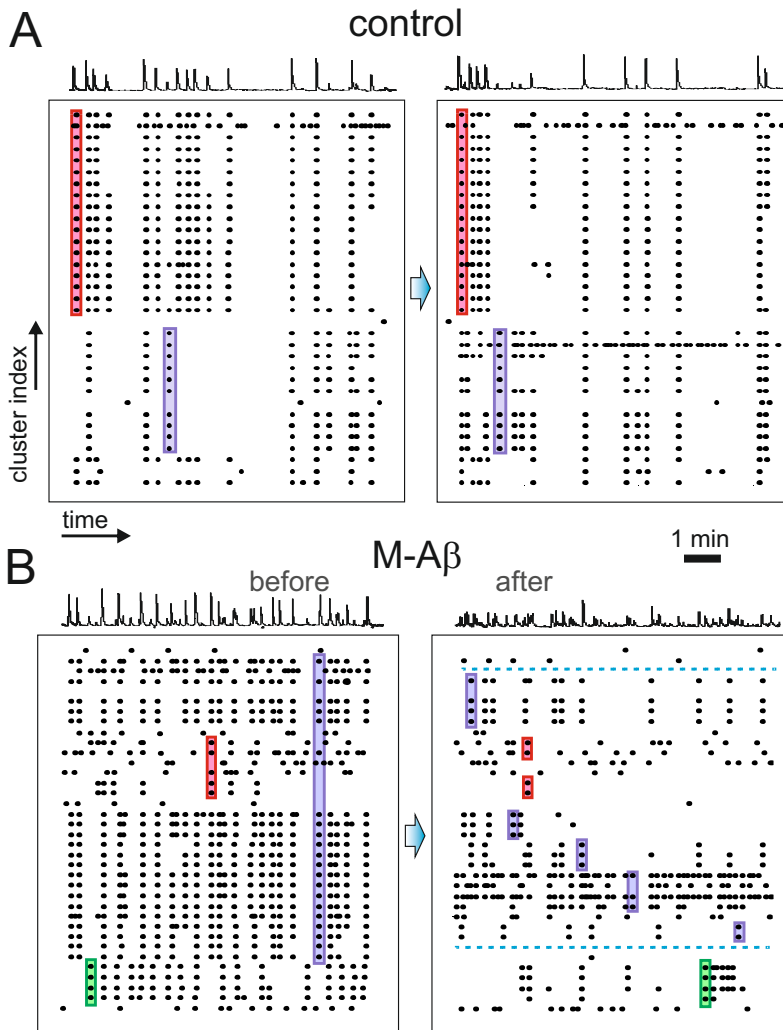


**Fig. 6.3 Analysis of the spontaneous activity.** (A)-(B) Representative raster plots of spontaneous activity and average fluorescence signal, comparing the behavior of the clustered neuronal networks in control conditions (top) and under perturbation with M-A $\beta$  complex (bottom). The left panels show the first 10 min of recording before perturbation, while the right panels show the last 10 min of recording upon perturbation. For the control case, the network activity and the structure of the different firing sequences (outlined boxes) are preserved, while for the M-A $\beta$  case both traits degrade, with a rupture of the biggest sequence in sub-sequences and the silencing of clusters (dotted horizontal lines).

highlighted as color boxes. Both network activity and the pattern of the repeating firing sequences are well preserved along the two recordings. The stability of the control measurement contrasts with the behavior of the M-A $\beta$  cavity. Spontaneous activity is rich before chemical application, with 3 distinct repeated firing sequences, but substantially decays after dosage, with a rupture of the pattern of the firing sequences in smaller subsequences. For instance, a firing sequence highlighted in blue on the left panel —and that encompassed the majority of the clusters— broke off into 4 new, uncorrelated subsequences. One can also observe that some clusters became completely silent (dotted lines), while others boosted in activity.

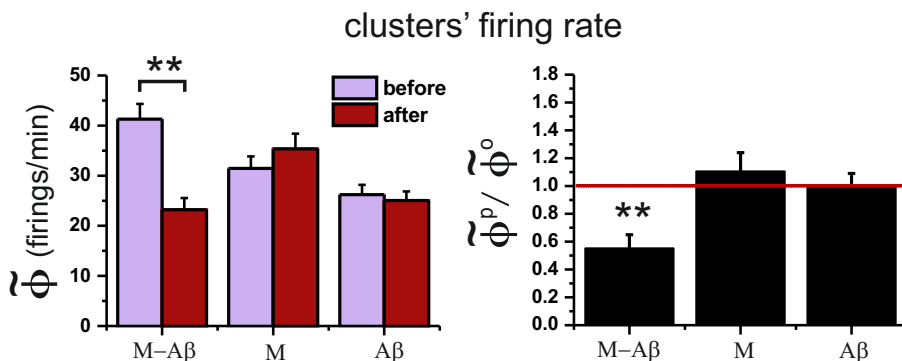


**Fig. 6.4 Activity changes** Variation of the mean clusters' firing rate  $\tilde{\Phi}$  upon perturbation, and comparing the action of M, A $\beta$  and M-A $\beta$ . The left panel shows the values before and after application, and corrected by the control measurement; the right panel shows the corresponding ratios. Each dataset is an average over 15 experimental realizations, and is represented as mean  $\pm$  standard error of the mean. (\* $p < 0.05$ , \*\* $p < 0.005$ , Student's t-test.) The red horizontal line is a guide to the eye for the control condition.

A first, crude evaluation of the changes in the dynamics of these networks, for the different actions and along the 15 experiment, was carried out by computing the average clusters' firing rate  $\tilde{\Phi}$ . As shown in the left panel of Figure 6.4A,  $\tilde{\Phi}$  significantly decayed by about a factor 2 upon M-A $\beta$  action (p-value  $p = 8 \times 10^{-6}$ ), while it remained unaltered within statistical error

for both M and  $A\beta$  perturbations. To compare the variability in behavior between chemical actions, we computed the ratio between the spontaneous activity after and before perturbation,  $\tilde{\Phi}^P/\tilde{\Phi}^0$ . As shown in the right panel of Figure 6.4A, activity significantly dropped upon M- $A\beta$  action when compared with either the M or  $A\beta$  cases, but no significant differences were observed between M and  $A\beta$ .

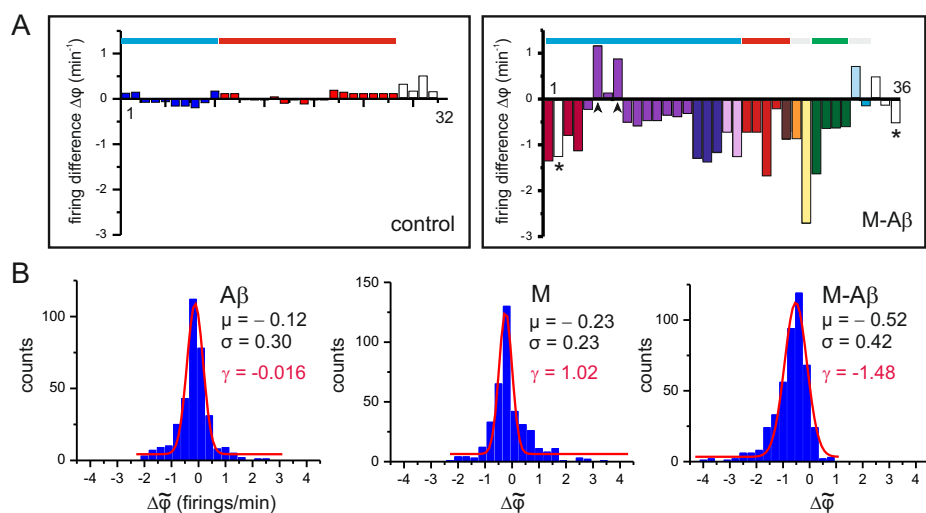


**Fig. 6.5 Cluster's activity and network coherence.** (A), Difference in cluster's firing rate between the perturbed ( $\phi^P$ ) and the unperturbed ( $\phi^0$ ) activities, and comparing a control cavity (left, 32 clusters) with one targeted with M- $A\beta$  complex (right, 36 clusters). Data corresponds to the experiments shown in Figure 6.3. Each bar represents a cluster of the network. Clusters are color coded and ordered in the horizontal axis according to their participation in a co-activated group. White bars depict clusters that fire independently. Bars marked with asterisks indicate the clusters that became silent after perturbation, and the ones marked with arrowheads highlight those that boosted in activity. The top horizontal color boxes show the structure of co-activations before perturbation, and color coded according to the sequences shown in Figure 6.3. Grey boxes are sequences that were not indicated in Figure 6.3B. (B), Distributions of the firing rate differences  $\Delta\tilde{\phi}$  for 15 experimental realizations upon action of the different chemical agents. The red curve shows a Gaussian fit to the distributions, with mean  $\mu$  and standard deviation  $\sigma$ .

To deepen in the understanding of the M-A $\beta$  damage on network dynamics we analyzed in detail the representative experiment of Figure 6.3B, and computed the difference in spontaneous activity before and after perturbation for each individual cluster,  $\Delta\varphi = \varphi^P - \varphi^0$ . As shown in Figure 6.5A, clusters in the control case slightly varied in activity due to the natural fluctuations in such a biological system, but the overall population activity along the two measurements remained stable, with  $\langle\Delta\varphi\rangle \simeq 0$ . The structure of clusters' co-activations was characterized by the two major communities outlined in the raster plot of Figure 6.3A together with few clusters that fired independently. This dynamical organization was the same for both measurements, and illustrates the stability of the clusters' coherence in control conditions.

For the M-A $\beta$  case, however, there was a remarkable drop in the activity of most of the clusters together with a rupture of the initial co-activation patterns. The biggest community of coherent clusters indeed divided into 5 smaller groups upon perturbation. Some clusters also became totally silent (marked with asterisks) while others boosted in activity (arrowheads). Although this particular experiment exhibited two clusters with boosted activity, such a feature was in general rare.

We extended this analysis to the M and A $\beta$  cases, and included all the 15 experimental realizations. Figure 6.5B shows the distribution of normalized clusters' activity differences  $\Delta\tilde{\varphi}$  for all the data. For the A $\beta$  case, all clusters were active along the recording and their activity varied moderately, with an overall symmetric distribution centered at 0 (mean  $\mu_{A\beta} \simeq 0$ , skewness  $\gamma_{A\beta} \simeq 0$ ). The M case shared similar characteristics except for a higher presence of boosted activations, as reflected by its right-skewed distribution ( $\gamma_M = 1.02$ ). Such a potentiation of activity by the magnetic nanoparticles is an interesting observation that needs further studies to be understood. Conversely, the M-A $\beta$  case exhibited a prominent widespread loss in clusters' activity (often caused by clusters that became silent), with a remarkable shift

of the distribution towards negative values ( $\mu_{M-A\beta} = -0.52$ ,  $\gamma_{M-A\beta} = -1.48$ ), and the almost absent presence of clusters with boosted activity.

These results suggest that M-A $\beta$  complex damaged the connectivity between clusters, the clusters themselves, or both. Such an action caused a deterioration of the individual clusters' activity and the overall network collective behavior.

### 6.3.2 Disruption of the structure of network communities due to M-A $\beta$ complex

We illustrate the damage in the collective dynamics of the network by considering another representative experiment in which all clusters displayed activity after M-A $\beta$  perturbation. Figure 6.6A shows the identification of the network communities. By setting a threshold in the dendrogram (dotted horizontal lines) the most representative communities in the network can be established. For the control case we obtained 2 characteristic communities that encompass around 15-20 clusters each. These communities are well preserved along the two consecutive recordings, although with variations in their internal structure due to fluctuations in clusters' dynamics. For the M-A $\beta$  case, however, the structure of communities markedly changed, with 3 main communities separating into 6. Figure 6.6B shows an alternative representation of the communities in the form of the similarity matrices  $J_S$ . The control experiment retained the main structure of the communities despite fluctuations, while for the M-A $\beta$  case the reorganization of the network in smaller communities was well manifested.

We combined the analysis of the communities' structure with the effective connectivity of the network to better quantify the changes in the coupling between clusters upon perturbation. Figure 6.7A depicts the functional maps for the control and M-A $\beta$  experiments. Two levels of representation are shown. In a first one, all functional connections between clusters are drawn as gray links, effectively shaping a homogeneous area that evinces the widespread

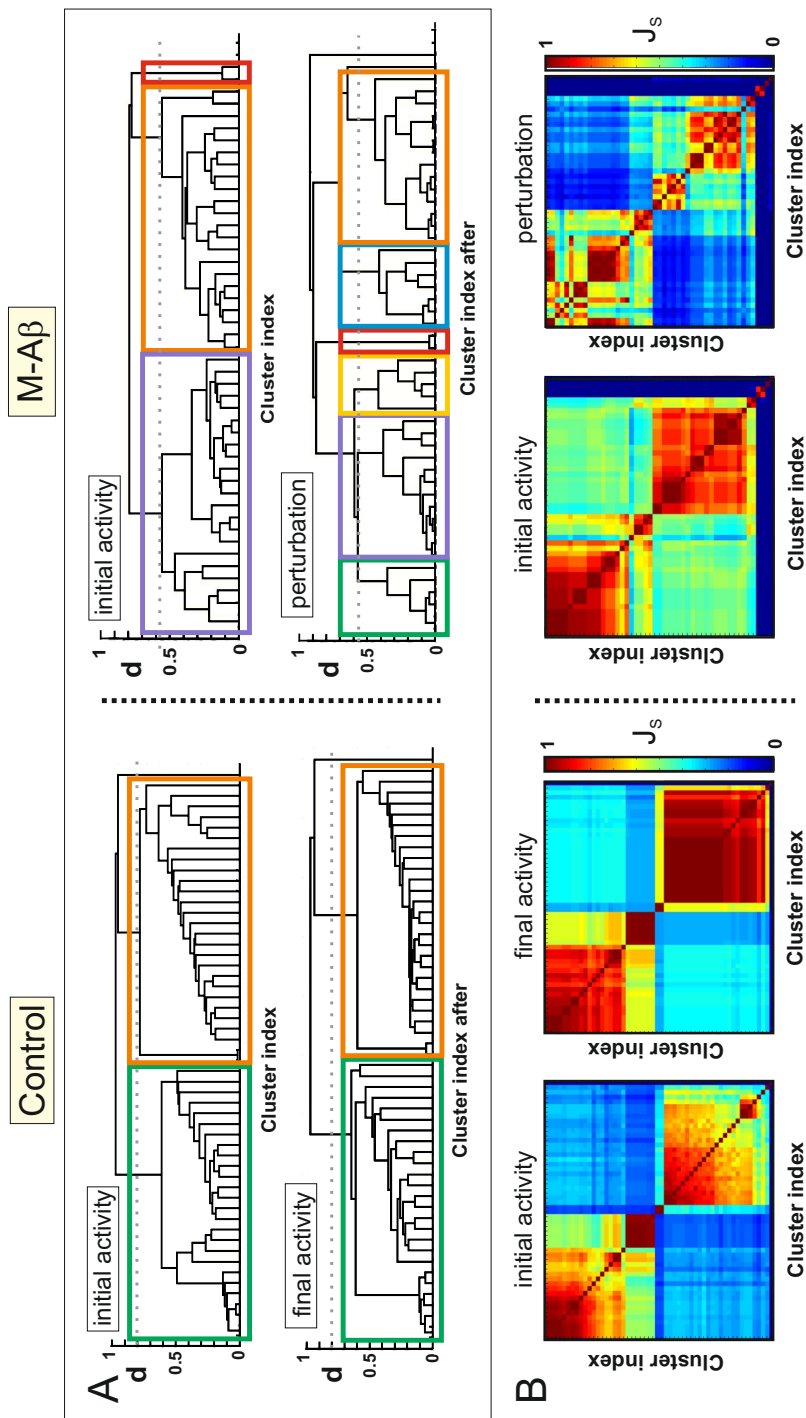


**Fig. 6.6 Communities analysis.** (A) Corresponding dendrograms and Jaccard similarity matrices. For the control case (left), the dendrograms compare the network's communities (color boxes, set with a threshold  $d_{th} = 0.80$ ) in two consecutive measurements, which exhibit similar traits and the maintenance of the two main communities. For the M-A $\beta$  case (right), the dendrograms compare the standard and the perturbed measurement ( $d_{th} = 0.58$ ), and reflect the rupture of the two main communities and the formation of smaller ones. Boxes are color coded according to the distinct communities. (B) Corresponding Jaccard similarity plots drawn using the clusters' indexes provided by the dendrogram, highlighting the deterioration of the network upon M-A $\beta$  action.

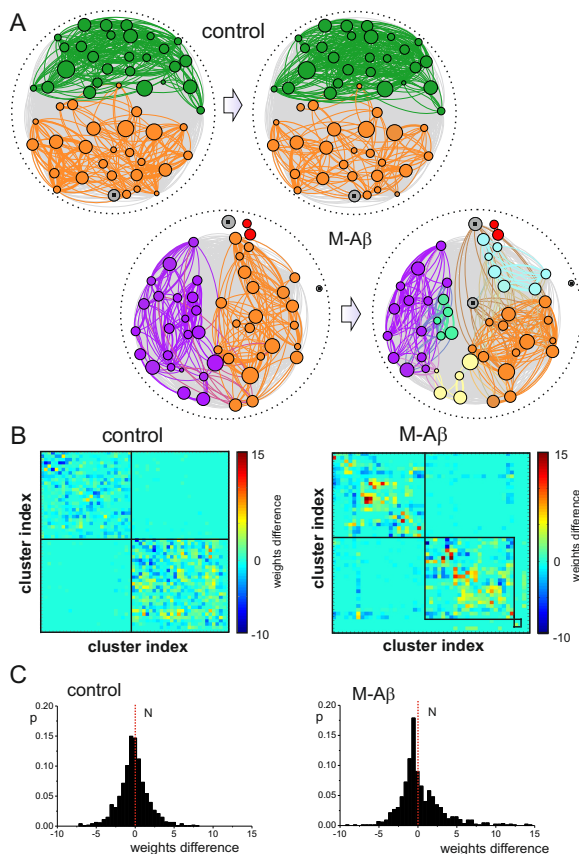


**Fig. 6.7 Functional connectivity and damage.** (A) Effective networks for the control and M-A $\beta$  experiments shown in Figure 6.6. Gray links show all functional connections, and color links correspond to the top functional connections ( $z$ -score  $> 1.95$ , 500 surrogates). The direction of the links is not shown for clarity. The control network reflects the stability of the network in two consecutive measurements. The M-A $\beta$  network exhibits strong connectivity changes and reorganization of the network moduli, which are color coded according to the hierarchical tree information of Figure 6.6. Grey clusters with a square in their center are those that fired independently or that participated equally in different communities. (B) Matrices of weight differences  $w_d$  of the functional links. The clusters' index order is the same as in Figure 6.6, and corresponds to the unperturbed condition. The square boxes outline the moduli before perturbation. (C) Corresponding distributions of weight differences for the control and M-A $\beta$  experiments.  $\gamma$  indicates the skewness of the distributions. The red vertical line is a guide to the eye to show the symmetry of the distribution in the control case.

clusters' functional interconnectivity. In a second one, only the top functional links ( $z$ -score  $> 1.95$ , 500 surrogates) are shown, with clusters and

their connections color coded according to their participation in the above inferred communities. For the control case, we observed that the overall structure of the network was well preserved along the two recordings, with small variations in the effective links that reflect the fluctuations observed in the dendrograms. For the M- $A\beta$  case, the rupture of the 3 initial communities into 6 smaller ones was clear, and the clusters that remained in a given community experienced important variations in functional connectivity. However, a number of the strongest links were preserved, hinting at the maintenance of some sort of internal organization in the network. Another example of a M- $A\beta$  perturbation is provided in Figure 6.8A, and corresponds to the data shown in Figures 6.3B and 6.5A. In addition, representative experiments for the M and  $A\beta$  cases are shown in Figures 6.8B-C, and highlight the maintenance of the network features in both cases.

To quantify in more detail the changes in the functional connectivity we computed the weights' differences  $w_d$  of the functional links between the perturbed condition and the initial one. As shown in Figure 6.7B, the weights fluctuated in the control case, but variations occurred within the communities and with few extreme values. For the M- $A\beta$  case, however, extreme variations were abundant, and with a large presence of negative values outside the two main original communities. This broad network weakening ultimately caused the emergence of the smaller communities and the overall degradation of network activity. Such a deterioration can also be illustrated by plotting the distribution of weights' differences. As shown in Figure 6.7C, the control case led to a symmetric, narrow distribution centered at zero (skewness  $\gamma_C = -0.10$ ). Conversely, the M- $A\beta$  displayed an asymmetric distribution with two main features. First, the peak of the distribution appeared at negative values, which signatures an overall network weakening; and second there was an emergence of extreme positive differences ( $\gamma_{M-A\beta} = 1.41$ ) that possibly reflect the activation of network mechanisms to stop activity degradation by reinforcing specific links. Such a behavior is also maintained across the

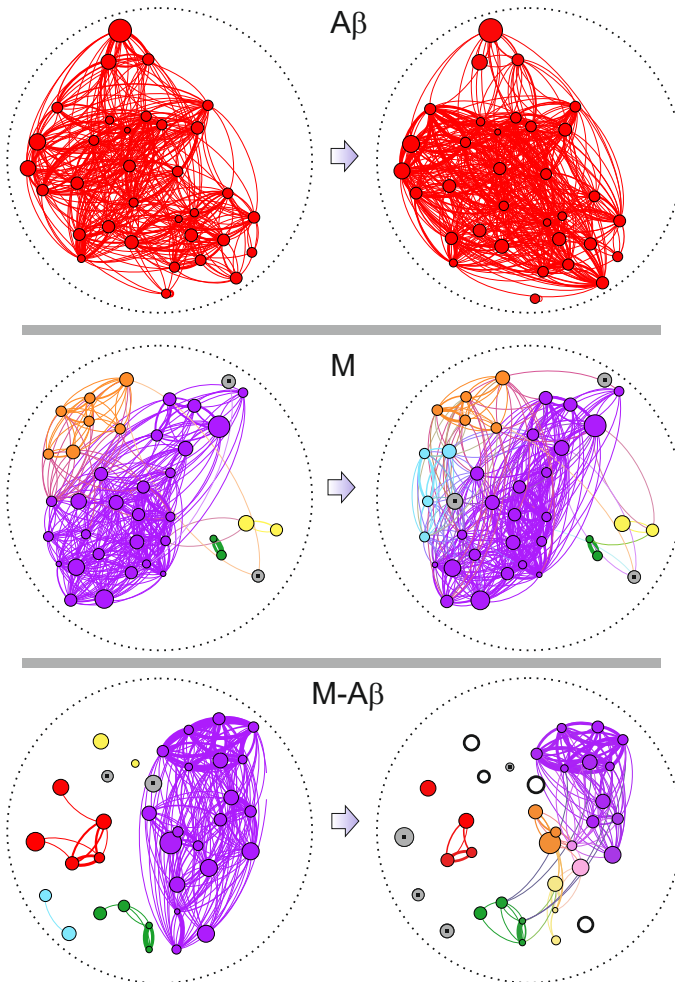


**Fig. 6.8 Comparison of the functional networks for M,  $A\beta$  and M- $A\beta$**  The graphs illustrate the stability of the network moduli and functional connectivity for the M and  $A\beta$  cases. Although functional links change in strength and target, the variability is similar to the control measurements. An additional M- $A\beta$  experiment is shown for comparison. Links between clusters correspond to the top functional connections ( $z$ -score  $> 1.95$ , 500 surrogates), with the thickness proportional to the weight of the link. Their direction is not shown for clarity. Clusters and links are color coded according to their participation in a given community, with the thickness of links proportional to their importance. Grey clusters with a square in their center are those that fired independently or that participated equally in different communities. Clusters with thick outlines are those that ceased activity after chemical application.

15 experimental realizations studied (Figure 6.9A). However, we must note that network response to damage and functional reorganization is complex. Remarkably, if we analyze in detail the M-A $\beta$  distribution of Figure 6.9A, we observed that a substantial number of positive weight differences ( $wd > 0$ ) correspond to intra-moduli reinforcement, as shown in Figure 6.9B). However, as shown in the same figure, weights' loss after M-A $\beta$  action ( $wd < 0$ ) are more similar for both inter-moduli and intra-moduli links.

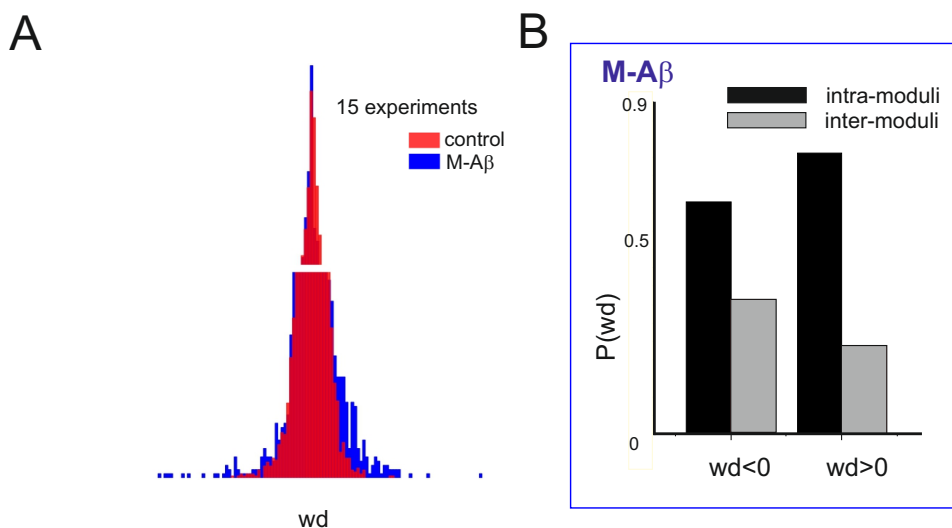


**Fig. 6.9 Intra and inter-moduli connections** (A) Comparison of the weight difference distributions between control and M-A $\beta$  including all 15 experimental realizations. The M-A $\beta$  distribution is broader and contains both strongly weakened and strongly strengthened functional links. (B) Probability of negative and positive weight differences for intra-moduli and inter-moduli connections for all 15 M-A $\beta$  experiments.

To complete the analysis of the functional organization of the network upon M-A $\beta$  action, we also analyzed high-order topological features such as the efficiency, clustering, and assortativity. The results are summarized in Figure 6.10, and are presented as the ratio between the condition of the network after M-A $\beta$  application and before it. The *strength* substantially decayed after perturbation and reflects the widespread loss of connectivity density seen in the effective maps. The *global efficiency* indicates that the

perturbation affected the global integration among the communities. This is supported by the increase of the *local efficiency*, overall pinpointing a scenario where the information flow shifted towards local areas. The fall of the *clustering coefficient*, on the other hand, indicated the emergence of a sparser connectivity, i.e. a switch towards a more random network.

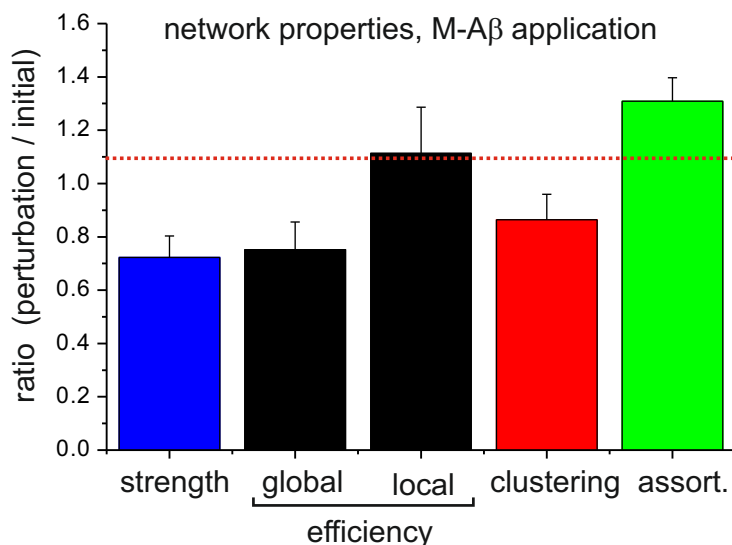


**Fig. 6.10 Changes in network topology upon M-A $\beta$  perturbation.** Ratio of five topological descriptors, namely network strength, global and local efficiencies, clustering coefficient, and assortativity, after and before the application of M-A $\beta$ . The descriptors are computed from the directed and weighted functional connectivity graphs, and averaged over 15 network realizations. Error bars indicate mean  $\pm$  standard error of the mean. The red horizontal line is a guide to the eye for the control condition.

The combination of a decreased global efficiency with an increased local one strengthens the observation that M-A $\beta$  action caused the partition of the biggest moduli. This community disruption is also reflected by an increase of the *assortativity*. We must note that modular networks are in general assortative and, as we have seen, these clustered networks already exhibit this property. Hence, the observed increase in assortativity indicates that the networks maintain the modular organization despite deterioration, a feature

that in turn favors the preservation of activity, though local, in the system (see e.g. Figure 6.3B).

### 6.3.3 Loss of integration-segregation balance upon M-A $\beta$ damage

In order to better understand the decrease in global efficiency (associated to the degree of integration) and clustering coefficient (associated to the degree of segregation), we compared the networks deteriorated upon M-A $\beta$ , at the time point corresponding to the end of the experiment, with the initial undamaged network but explored along gradually higher weakening steps carried out through a percolation process. In principle, if M-A $\beta$  action acts equally in all connections, we would expect that at some ‘percolation threshold’ both networks (the real and the percolated ones) reach a maximum in similarity. To compare both networks (real and percolated at a given threshold), we first binarized the weights of the connectivity matrices, so the matrix reflects solely the presence or absence of links. Next, we computed the correlation and the Jaccard distance between them along the progression of ‘percolative damage’. We used the two measures since correlation estimates the ‘similarity’ using the entire connectivity matrix (i.e. ‘0’ for absence and ‘1’ for presence of connections), while the Jaccard distance quantifies the number of links (i.e. ‘1’ values) that are present in both networks. Figure 6.11A shows the results, which are averaged over 10 experiments in which most of the clusters were active at the end of the measurement. The black curve depicts the correlation distance and the red curve the Jaccard one. We can observe that no peak appears. Instead, the similarity between both networks decreases monotonically since the beginning of disintegration, meaning that the network behavior after the chemical damage strongly differs from a percolation case. The result implies that the M-A $\beta$  action do not simply reduces the integration of the network as a consequence of inter-modular failure of connectivity. Rather, more complex mechanisms are at play.

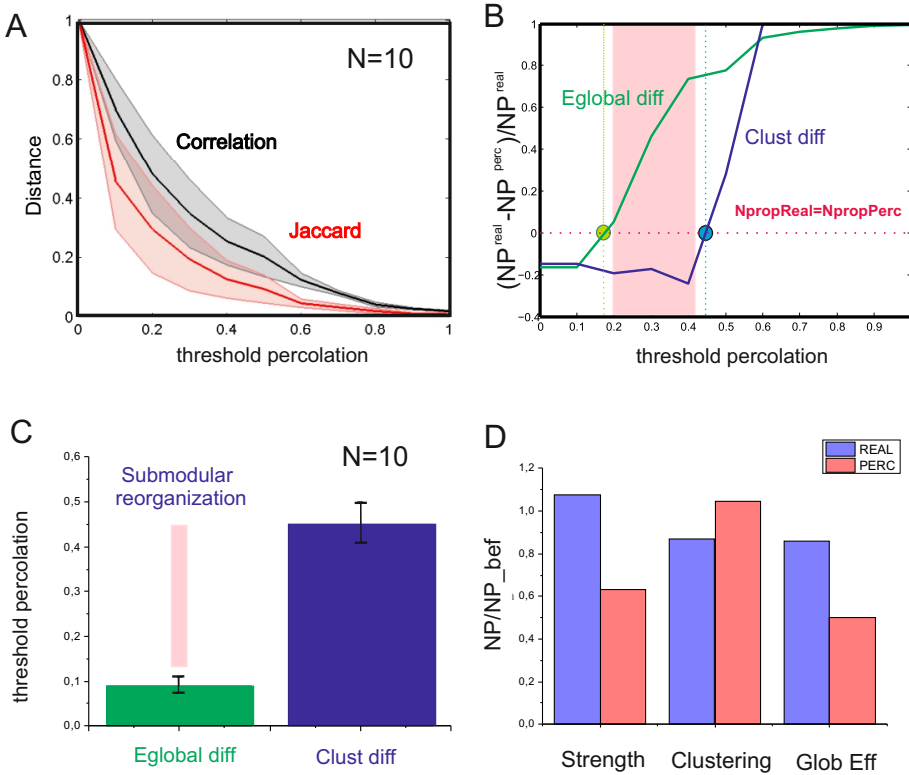


**Fig. 6.11 Comparison of actual M-A $\beta$  damage with a percolation model. (A)** Comparison of the functional connectivity matrices between the actual M-A $\beta$  network and the percolated one for different thresholds, averaged over 10 experimental realizations. No maximum is observed for any ‘percolative threshold’. The shading around the curves marks standard error. **(B)** Difference between two network properties (NP), namely global efficiency and clustering, of the representative clustered network after M-A $\beta$  application (denoted as ‘real’) and the initial network altered through a percolation process (‘perc’). The circles mark the ‘percolation threshold’ at which the two network properties for the ‘real’ case are equal to the ‘percolated’ one. The difference between the two thresholds imply that, after global disintegration, the functional modules reorganize to new ones compared to the initial ones. The pink box marks this range. **(C)** A 10% of the links need to be pruned from the initial network to obtain the same decrease in the global disintegration as the network after actual M-A $\beta$  damage. On the other hand, both networks appear with the same clustering coefficient when the 45% of the links (weights gradually removed) are taken off. **(D)** The strength, the clustering coefficient and the global efficiency for the networks after the M-A $\beta$  application compared to the ‘percolated’ network, and averaging across the threshold range that comprise the ‘pink’ range in **B**.

To explore this difference in more detail, and for a particular experiment, we compared the global efficiency  $G_{\text{eff}}$  and the global clustering  $CC$  of the initial network percolated for different thresholds with the real, M- $A\beta$  damaged one. We note that, in this analysis, the weights of the links were included. We used the data of the the experiment shown in Figures 6.6 and 6.7. The results of this comparison are shown in Figure 6.11B, where we plotted the relative difference of these network properties NP, i.e.  $(NP^{\text{real}} - NP^{\text{perc}})/NP^{\text{real}}$ , where  $NP^{\text{real}}$  corresponds to the measure for the M- $A\beta$  network and  $NP^{\text{perc}}$  for the percolated one at different thresholds. First, one can observe that the relative differences are initially negative, reflecting the damage of the M- $A\beta$  network with respect to its initial condition. As percolation commences, both measures approach the corresponding value of the real network and, at some threshold, they coincide and the relative difference is zero. Interestingly, this coincidence occurs at different threshold for each measure. The ‘percolation threshold’ for  $G_{\text{eff}}$  is about 0.18, whereas for  $CC$  is about 0.42. The substantial difference between both values indicates that the real network quickly disintegrates as a whole, switching to a new scenario where the containing modules become predominant, which in turn strongly reorganize as compared to the initial modular structure.

Similar results were found for the rest of experiments. The averaged results are shown in Figure 6.11C. The global efficiency of the real ( $G_{\text{eff}}^{\text{real}}$ ) and percolated ( $G_{\text{eff}}^{\text{perc}}$ ) networks coincide when the initial network is pruned by about 10%, while a 45% of decimation is required in the original network for the clustering measures  $CC$  to concert. This result implies, first, that integration and segregation behave very differently in the real network, i.e. M- $A\beta$  damage is *not* equivalent to a percolative process of gradual failure of connections. Indeed, in the percolation case, the links that disappear first are the weakest ones and that mostly correspond to the inter-moduli connections, causing a reduction in integration, the emergence of the sub-modular structure, and an increase in integration. In the real case, however,

integration is also reduced, but it is not followed by an immediate rise in segregation, which requires more damage to be important. We hypothesize that the positive weights' differences  $w_d$  for both the intra- and inter-modular connections shown in Figure 6.9A, appear once integration starts to fail in order to reorganize the functional modular structure of the network and maintain it globally connected as much as possible.

An alternative approach for the above analysis consist in constructing an 'average percolated network', i.e. the disintegrated network averaged over a range of thresholds. In our case, we average over the obtained networks in the region that extends from the threshold in which  $G_{\text{eff}}^{\text{real}} \simeq G_{\text{eff}}^{\text{perc}}$  to the threshold in which  $CC^{\text{real}} \simeq CC^{\text{perc}}$ . This averaged network is then compared with the real, M- $A\beta$  damaged one in terms of major topological properties. The results, for the same experiment presented in Figure 6.11B, are shown in Figure 6.11D. We can first observe that the strength is higher in the real network than in the average-percolated one, suggesting that a reinforcement of the connections takes place upon damage. The global efficiency is also higher, revealing that this reinforcement helps preserving integration. Finally, both networks exhibit a similar level of clustering, indicating that segregation is maintained. This is reflected in the organization of the modules and the emergence of new ones (e.g., Figure 6.7A).

### 6.3.4 Clustered networks exhibit higher resistance to M- $A\beta$ damage compared to homogeneous ones.

As a final analysis, we studied the sensitivity of homogeneous cultures to damage. It was shown in the previous Chapter that while the assortative, clustered networks were resilience to the weakening of connections, the weakly disassortative, homogeneous ones were not (Teller et al., 2014). Thus, the rationale behind this comparison is the existence of these assortative traits can mark difference in the resilience of the networks.

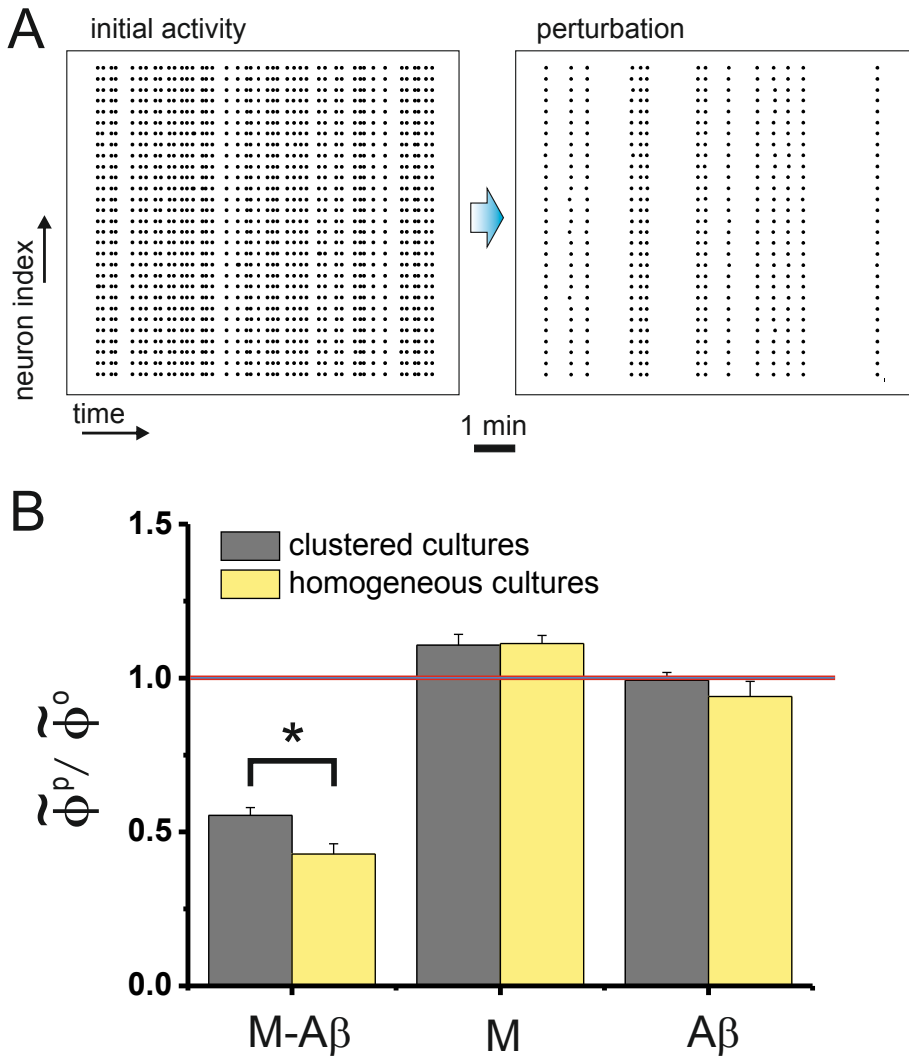


**Fig. 6.12 Homogeneous cultures.** **A** Raster plots of spontaneous activity before (left) and after (right) application of M-A $\beta$  complex. Spontaneous activity fell by 65% on average. **B** Ratio of the normalized firing rate for homogeneous (averaged over 5 experiments with the respective standard error of the mean) and clustered cultures (15 experiments), and comparing the behavior of the two kind of cultures for the M, A $\beta$  and M-A $\beta$  perturbations. Both culture types behaved similarly except for the M-A $\beta$  condition, where the homogeneous cultures exhibited a significantly higher decay in activity. (\* $p < 0.05$ , Kolmogorov-Smirnov test.)

Figure 6.12A shows a typical raster plot of activity before and after application of M-A $\beta$ . Network coherence was preserved upon perturbation, but the frequency and regularity of bursting episodes were substantially reduced. The number of bursting episodes kept decreasing as the damage progressed until activity ceased. This behavior contrasted with the one observed in clustered networks, where whole network activity switched to a modular yet highly rich one that lasted for long time. In general we observed that homogeneous cultures became silent much earlier than clustered ones, a result that provides a qualitative evidence for a higher resistance of the latter to damage.

To quantify the differences between the two culture types, we analyzed the ratio in the normalized spontaneous activity of either individual neurons (for the homogeneous preparations) or clusters,  $\tilde{\Phi}^P/\tilde{\Phi}^0$ , and compared the action of M-A $\beta$  with the other perturbations. As shown in Figure 6.12B, homogeneous cultures exhibited a significantly higher drop in spontaneous activity than clustered ones ( $p = 0.04$ ), while for the M and A $\beta$  cases both culture types behaved similarly within statistical error.

## 6.4 Discussion

Given the diverse hypothesis for AD, our work aimed at introducing a new experimental platform and analysis tools for understanding the role of the compounds that seem pivotal in neuronal damage. We centered our efforts in the combined effect of magnetite and A $\beta$ . Our results indicate that A $\beta$  manifests a damaging role only when acting in synergy with magnetite, which possibly acts as a stabilizer for a protofibril M-A $\beta$  complex. Although other studies have shown that A $\beta$  itself induces apoptosis in neuronal cultures similar to ours, in the time frame and conditions of our study we could not find evidences for neuronal damage due to the action of either A $\beta$  or magnetite. It may occur that long exposures to these agents induce neuronal

damage and broad alterations in network function, but our results clearly show the aggressiveness of M-A $\beta$ , which acts quickly and broadly.

The paramount result that evince the M-A $\beta$  damage is the combined loss of neuronal activity and the deterioration of network's functional organization. This was quantified by an average fall of the spontaneous activity, a rupture of the dynamic communities, and widespread changes in the functional connectivity of the culture. Neuronal apoptosis was reflected in our networks by the gradually higher presence of silent clusters. However, network functional deterioration occurred much earlier than actual neuronal death, and suggests that M-A $\beta$  acts first on connections and, at longer stages, on the cells themselves. Despite the degree of damage, the partition of the network into smaller communities has two interesting features. First, the new moduli are constituted by clusters that are spatially close (see e.g. Figure 6.7A), and reveals that clusters tend to connect to their nearest neighbors rather than establishing long-range paths. And second, the damage preserves most of the intra-modular organization, picturing a network with a core of strongly connected nodes. Altogether, the clustered networks effectively configure a *network of networks*, a hierarchical organization that may explain their higher resistance to damage as compared to homogeneous networks.

Clustered networks upon M-A $\beta$  action switch from a global dynamics to a local one and, as far as few modules are active, the network maintains some degree of operation that can help activating response mechanisms. This switching scenario has been also observed in AD (Delbeuck et al., 2003; Wang et al., 2013) and mild cognitive impairment (Buldú et al., 2011). Structural and functional neuroimaging techniques revealed that the first clinical manifestations of AD were associated with a loss of the integration capacity between brain regions, while the segregation, i.e. the reinforcement within neuronal modules, increased (Bai et al., 2013; Shu et al., 2012). In this direction, an enlightening result of our study is the capacity of the clustered networks to respond to damage. Indeed, the functional connectivity

analysis pinpoints a strong reorganization, with the reinforcement of existing functional paths and the formation of new ones. This behavior shows the intrinsic ability of the network to compensate or restore for damaged function. We conjecture that this plasticity provides mechanisms for response and adaptation against external attacks. Such a fast response is a well known observation in brain recordings (Pascual-Leone et al., 2011). For instance, along the intermediate stages of AD there have been observed episodes of partial recovery of cognitive tasks and memory (Borge-Holthoefer et al., 2011; Dickerson et al., 2005), and that possibly reflect broad neuronal circuit response to damage.

Our work provides an innovative and versatile tool to unveil the action of molecular agents in network activity and function. We believe that it is a unique experimental model system for neurodegeneration that may help uncovering universal processes for functional reorganization upon damage. Our system can not only help understanding the role of magnetite,  $A\beta$  or M- $A\beta$  complex in Alzheimer's, but can also help addressing the role of other pivotal players such as the Tau protein. It can also help developing innovative therapeutics for AD. Indeed, given the importance of the combined effect of magnetite and  $A\beta$ , it has been suggested to use transcranial magnetic stimulation to target magnetite accumulation, with promising advances. Magnetic stimulation could be incorporated in our experimental system given its accessibility and easy manipulation, and could help exploring in a control manner the benefits of such an action. Also, our system could be useful to test specific drugs at a network level, providing a valuable tool for pharmacological studies focused on AD and other disorders.

# Chapter 7

## Work in progress

Along the previous chapters we studied the effective connectivity in the clustered networks, and used a number of topological descriptors to characterize it, both in standard conditions and upon perturbation or damage. Several aspects were left unexplored during our investigations, or were underway at the moment of writing this thesis. This chapter aims at introducing this major unfinished studies and important ideas that were “left in the fridge” waiting to be explored in detail.

One of the aspects to be comprehended is the relation between the anatomical, physical connectivity between clusters and the effective one derived from activity. Since we cannot extract the directionality of the anatomical links, we have to disregard the directionality of the effective links if we want to compare both networks. Hence we will use the term *functional connectivity* all along this chapter instead of effective one.

### 7.1 Anatomical and functional connectivities

The interplay between the anatomical circuitry and the functional connectivity is one of the most interesting questions in neuroscience. It is considered that the anatomical connectivity shapes the different patterns of activity gener-

ated by neuronal circuits, both *in vitro* and *in vivo*. These morphological connections constraint the flow of activity throughout the culture, but in turn the resulting activity can reciprocally affect the architecture of the structural connectivity at long-term. Moreover, it has been seen that a specific anatomical circuit can give rise to a rich repertoire of activity patterns while a given functional connectivity can arise from different underlying circuitries. This rich spectrum of possibilities highlights the beautiful and complex activity-connectivity relationship.

In particular, macroscopic studies in the *resting state* brain have suggested that structural connections predict in great measure the functional ones (Deco et al., 2011; Honey et al., 2007a, 2009). However, a number of functional links are observed without a direct mapping to anatomical ones. Such indirect connections can lead to discrepancies between anatomical and functional connectivity, although wide evidence have demonstrated that the topological organization in both networks are generally conserved.

## 7.2 Mapping structural connectivity in clustered networks

In general, mapping the anatomical connections in neuronal cultures is extremely difficult despite the relative simplicity of small networks *in vitro*. Indeed, the majority of the studies in neuronal cultures have focused on inferring the functional or effective connectivity, but few ones have achieved to unveil all the physical connections in these ‘simple’ microcircuits. In particular, mapping the anatomical connections in our clustered networks should be easy since the number of elements and connections are substantially smaller than in other *in vitro* preparations. However, the connections among these clusters present some features that highly increase their complexity. First, these clusters are composed by a several hundred of neurons, meaning that the connections between clusters are formed by axons and dendrites

that arrive from —or exit towards— different neurons, making challenging their examination. Moreover, in some cultures these connections are not well defined at all. Instead of thinner, neat processes connecting pair-clusters in a clean culture, they appear as a homogeneous tangle of connections that spread throughout the culture, effectively connecting with several clusters. Finally, even the neatest physical connections can travel across different clusters, making very complicated to establish if a clustered has connected to its nearest neighbor, its next-nearest one, or further away.

Different experimental techniques were applied along the course of this thesis in order to identify the internal structure of the clusters and their connections. Some of these procedures were carried out in collaboration with Dr. Marta Nieto's group in the Centro Nacional de Biotecnología (CNB, Madrid) or with the group of Dr. Juan Mena Segovia at the Anatomical Neuropharmacology Unit (Medical Research Council, Oxford University). Later on, these protocols were incorporated to our laboratory, but without reaching yet satisfactory results. Next, we briefly explain these techniques and their adaption to our neuronal clustered networks.

### 1) *Immunostaining techniques (Immunohistochemistry).*

This method allows to label specific proteins of the cell tissue taking advantage of the use of the antibody–antigen binding in the biological tissue. By using primary and/or secondary antibodies one can stain, for instance, neurons, axons or dendrites with high specificity. A wide spectrum of different markers exists in the market.

In particular, we used a primary and a secondary antibodies to mark neurons, their neurites and glial cells. First, we used the primary marker *anti-beta-Tubulin* to target the neurons and their neuronal processes and *anti-GFAP* to mark the glia cells. Afterwards, we introduced the secondary marker *Alexa* to label neurons and glia in different colors. Representative examples are shown in Figure 7.1, where neurons and their neurites are stained in green,

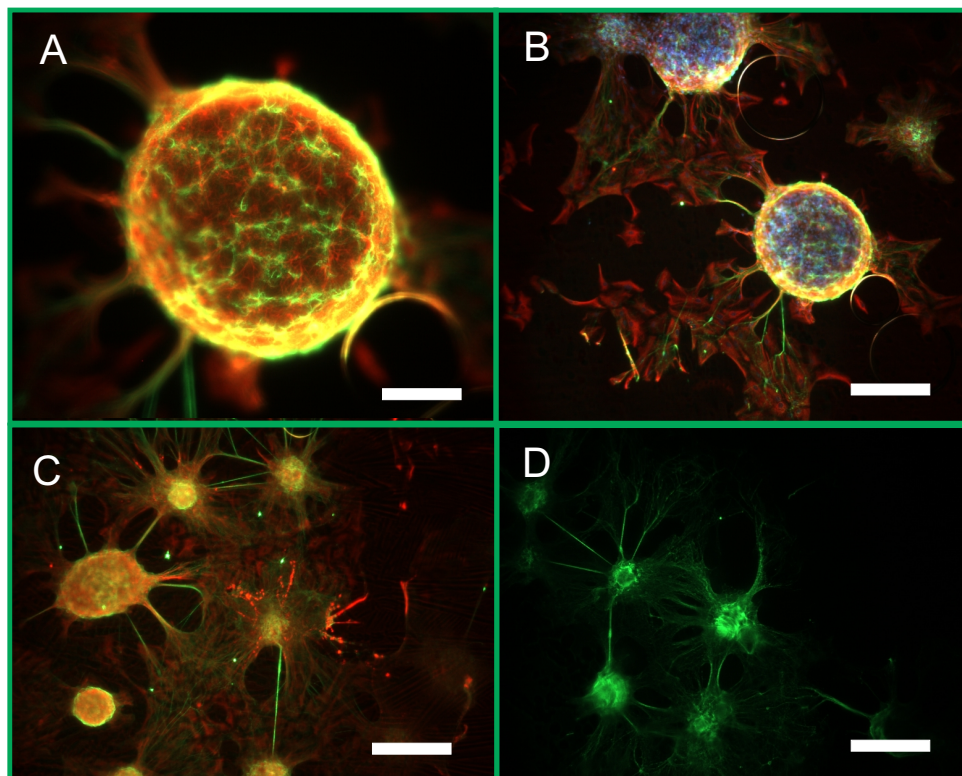


**Fig. 7.1 Immunostaining technique in clustered networks.** **A**, Neuronal cluster, where glia are marked in red, neurons and neurites in green. A neuronal cluster is composed by an underlying glial layer with hundred of neurons on the top. The spatial resolution is  $50\mu\text{m}$ . **B**, Two connected neuronal clusters where the connections between them appear as a homogeneous tangle that spread throughout the culture, being difficult their examination. The red color labels the glia, the green one stains the neurons and their connections, and the blue color marks the soma cells. The spatial resolution is  $200\mu\text{m}$ . **C-D**, Two representative examples of clustered networks following the same color pattern. The spatial resolution is at  $300\mu\text{m}$ .

while glial cells appear in red.

## 2) *GFP transfection*

Transfection enables the introduction the genetic material —a *green fluorescence protein* (GFP) in this case— within the targeted cells, ultimately promoting the expression of the fluorescence protein. GFP has been widely

used to visualize different elements of the neuronal tissue. We attempted different methods to introduce the genetic material, for instance by means of liposomes (lipofectamine transfection); or by viral infection, using promoters with distinct efficiency such as hSyn, CAG or CamKIIa to label neurons and/or their connections. Our results showed that lipofectamine is highly aggressive for the neurons, whereas viral injection presents more satisfactory viability and transfected efficiency (independently of the promoter).

### 3) *Retrograde and anterograde tracing techniques*

This method is based on the detection of biological processes that are involved in the axonal transport, finally enabling the axonal path visualization. Retrograde tracers mark the path from the axonal terminal (synapse) to the soma of the neuron, while anterograde tracers acts in the reverse direction, i.e. tracing from the neuron's soma to the synaptic terminal. We adapted, with the invaluable assistance of Segovia's group at Oxford, the protocols used for *in vivo* studies in rats to our *in vitro* clustered networks. In particular, we used *FluoroGold* marker as retrograde tracer and *BDA* as anterograde tracer. We investigated different methods to inject the retrograde tracer inside the clusters, such as iontophoresis or electrophoresis, but without sufficient success. In general, these injection techniques appeared to be very aggressive for the neurons. On the other hand, the anterograde injection was carried out using a virus, being this method less invasive for the clusters and then obtaining better results. However, these protocols still needed intense tuning in our cultures to achieve good results.

In general, the experimental preparation of all these methods is highly complicated. These difficulties include not only to an expensive, extensive and meticulous experimental procedure, but also a continuous control of neuronal health conditions once the labeling markers have been introduced. Regarding the last aspect, it is important to point out that the introduction of

the fluorescent markers in techniques (2) and (3) is carried out at initial stages of the culture development, whereas the first technique is implemented once the culture has been previously fixated with paraformaldehyde. In addition, these techniques are commonly combined with one another to achieve a richer final connectivity labeling, although greatly increasing the complexity of the entire experimental procedure.

These difficulties have indeed compromised the feasibility of these studies in our laboratory. To date, the majority of collected data—including the one shown here—comes from our collaborators. From these ‘few number’ of results we have discovered interesting features on the internal organization of the clusters, as well as about their interconnectivity.

Figure 7.1A shows a stained neuronal cluster using immunostaining techniques. One can clearly appreciate the characteristic arrangement of neurons and glia, i.e. glia cells arranged as a base layer with sparse neuronal network on top. Two connected clusters are shown in Figure 7.1B, where the neurons’ soma were also marked in blue by using the fluorescent marker DAPI. This picture, together with the images from Figures 7.1C-D, illustrate the complex connectivity among the clusters, where one can observe well defined connections in combination with a tangle of connections that spread over the neuronal clusters. These fuzzy connections extremely complicate the extraction of the structural connectivity map. Moreover, from these immunostaining results we calculated (by filtering the pictures and counting the number of pixels) the number of glia and neurons within the neuronal clusters. First, the number of neurons within a cluster typically ranges between 100 and 300, and strongly linearly varies with cluster size (Pearson’s correlation  $r = 0.99$ ). In addition, the glia/neurons ratio was around 1.5, i.e. 60% glia and 40% neurons in a cluster.

On the other hand, from the GFP transfection we observed that axons projected from neurons within a cluster could extend several hundreds of microns, easily crossing 3 or more clusters in their way. A representative

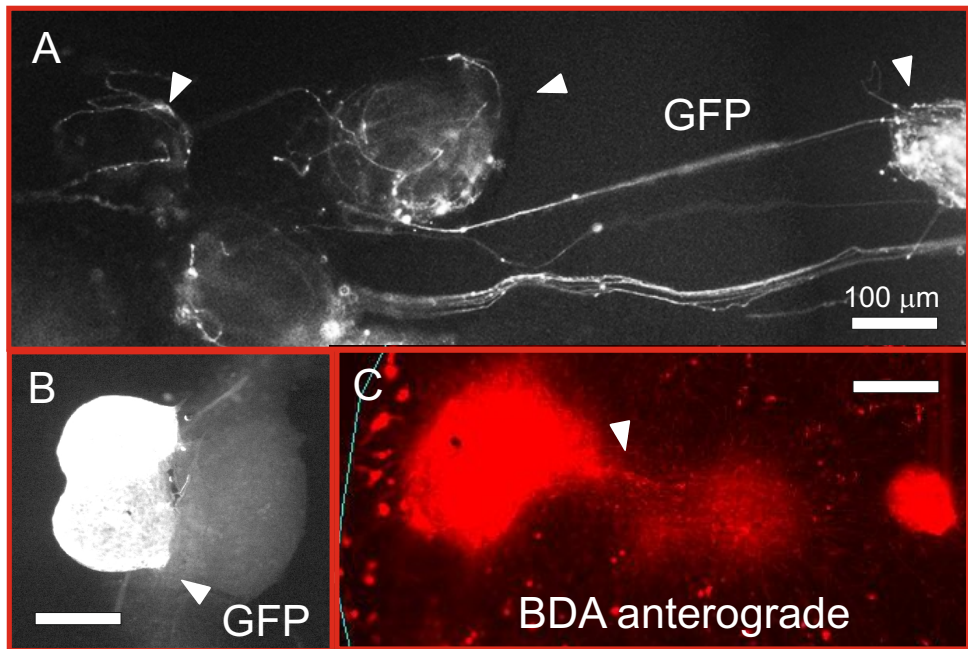


**Fig. 7.2 GFP transfection and anterograde tracing in clustered networks.** **A**, Detail of a GFP transfection in a clustered culture. Thin white filaments are axons. The picture reveals a long projection of a single axon, which interconnects with 3 clusters along its way. The arrow indicates the clusters that are interconnected by the same axon. **B**, Merging between a cluster previously transfected with GFP (marked with an arrow) and a non-transfected one. **C**, The left cluster shows the BDA anterograde, and connects with a non-transfected cluster on the right. The white arrow highlights some ‘blurred’ connections labeled with the anterograde tracer.

image is shown in Figure 7.2A. This observation indicates that clusters are interconnected beyond a simple two-neighbors coupling. In this sense, immunostaining techniques are not able to draw this non-local connectivity since all the culture is 100% stained. The advantage of using GFP is that we can either completely mark all the culture or adjust the efficiency transfection to label, for instance, just a 30% of the connections. Since this fluorescence protein is transfected in alive neurons one can develop new strategies for labeling, for instance just a 30% of the connections. A way of achieving that is mixing in the same culture transfected clusters with non-transfected ones.

To proceed, we took transfected neuronal cultures at DIV= 5 – 6 and very gently broke their inter-connections off. Afterwards, the single-transfected clusters were transferred onto a culture at DIV= 0, i.e. just plated neurons. At DIV= 5 – 6 the two types of clusters connected to each other. An example of this mixture can be seen in Figure 7.2B. The same procedure was applied to retrotracers, but it was much for difficult (Figure 7.2C).

These preliminary results are not sufficient to get good statistics, and therefore we could not use them so far to extract the anatomical map. Nevertheless, in parallel, we tried other options to gain knowledge on the structure–function of these clustered cultures, as described next.

### 7.3 Functional vs. cluster-to-cluster structural connectivity

As a general remark, we first note that in order to precisely map the entire physical structure of the clustered networks, one would require the labeling of all the synaptic connections, their weight and the corresponding pre- and post-synaptic neurons. As we have seen in the previous section, that level of identification is unfeasible with our current experimental knowledge (and actually economical resources). Nevertheless, as a first attempt to relate the anatomical and functional connections, we used the bright field images of our networks and *manually inferred* the existence of physical connections from cluster to cluster, ultimately building a binary connectivity matrix. Finally, this matrix was compared with a symmetrized and binarized version of the functional connectivity.

In the majority of the comparisons we found a 80% match between the structural connections and the functional connections. A representative example of this analysis is shown in Figure 7.3. In particular, Figure 7.3A–top shows the bright field image of a clustered network. Red lines mark the physical connections that one can easily visualize from the picture. Color

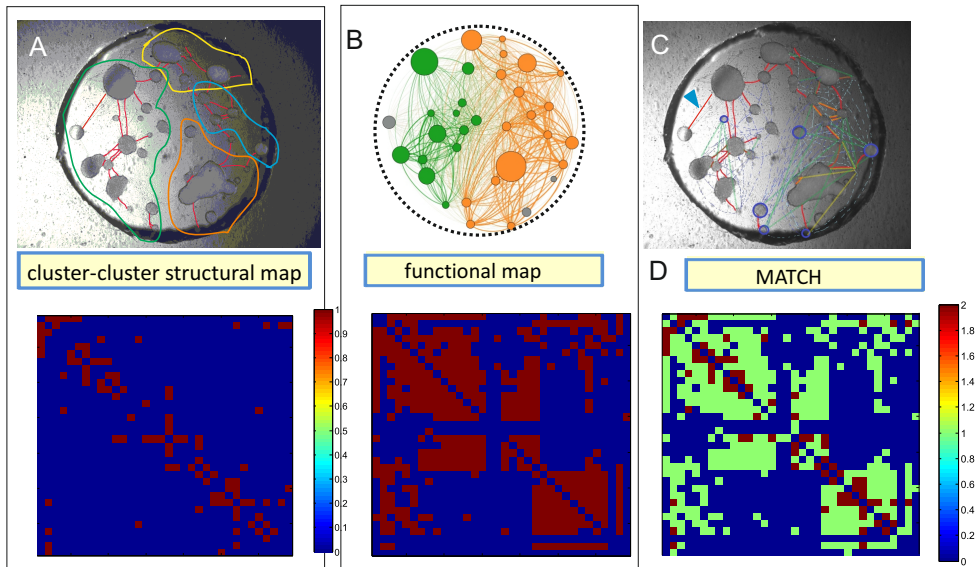


**Fig. 7.3 Functional vs. cluster-to-cluster structural connectivity.** **A**, On the top, the bright field image of a clustered network (3mm in diameter). Red lines mark the seen anatomical connections (cluster-to-cluster). The characteristic modules of this structural connectivity are encircled in different colors. On the bottom, the matrix representation of the cluster-to-cluster structural connectivity. It should be noted that the connectivity matrix is undirected (symmetric) and unweighted (binary). **B**, The functional organization of the same representative culture (top). The unweighted and undirected version of the functional connectivity map (bottom). **C**, The same bright field image as in **A** illustrating in blue dashed lines the functional links and in different colors the top functional links. In particular, links with weight in the range of  $0.4 < w_{i,j} < 0.6$  are drawn in yellow and links with weight,  $w(i,j) > 0.6$  are colored in green (with  $w_{max}(i,j) = 1$ ). Some of these top links overlap with the actual structural links, although others —particularly those linking distant clusters— do not appear in the cluster-to-cluster structural map. **D**, The resulting sum of two matrices (A,bottom and B, bottom). Values equal to 2 correspond to the concurrent existence of both connection types (a match). The percentage of matching is about 82%.

outlines identify the major topological modules of this structural network using the Louvain method. The structural connectivity matrix is shown in Figure 7.3A—bottom. Figure 7.3B shows at the top the functional network with the characteristic modules marked in different colors, and at the bottom the binarized and symmetrized functional connectivity map.

To compare both networks, the top image of Figure 7.3C marks both the structural (in red) and the ‘top’ functional links in (blue dashed lines). The thicker colored lines correspond to the strongest top links:  $0.4 < w(i, j) < 0.6$  (yellow),  $w(i, j) > 0.6$  (green), with  $w_{max}(i, j) = 1$ . We observe that some of these top links overlap with the actual structural links, although others—particularly those linking distant clusters—do not appear in the cluster-to-cluster structural map. On the other hand, there are also some structural links that do not have its corresponding top functional connection (orange arrows). Finally, clusters circled in blue correspond to presumably ‘independent’ or ‘connector’ nodes of the functional connectivity, and that could influence the assessment of functional links among distant clusters since they fire randomly or integrate different modules, respectively. At the bottom of Figure 7.3C the structural and functional matrices are compared. Comparison is simply carried out by summing up both matrices. Then, a value of 2 (red) corresponds to the concurrent existence of both connection types, a coincidence of about 82% for the particular experiment shown.

To explore in more detail the overlap between structural and functional connections, we repeated the same comparative analysis but using solely the top functional links. Surprisingly, the matching between structural and top-functional is only around 50%, substantially different as compared with the previous analysis. Three examples of these comparisons are shown in Figure 7.4, the first one (Figure 7.4A) corresponding to the previous example shown in Figure 7.3.

This finding suggests that neither the top functional links can predict the direct (cluster-to-cluster) structural connectivity nor the cluster-to-cluster connectivity is a good predictor of the functional one. Such a result is interesting and cumbersome alike: strong functional links can appear without sharing a direct structural path, and functionally weakly coupled clusters appear to be linked by a thick structural connection.

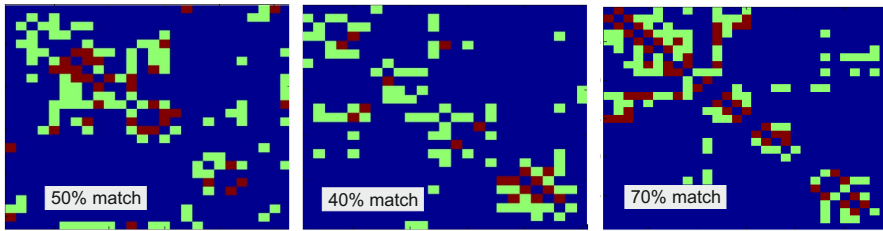


**Fig. 7.4 Functional and structural connectivity.** The matrices show three examples of functional and structural connectivity matrices. Functional links are shown in green, and structural ones in red.

The presence of functional links without an structural cluster-to-cluster analogous can be ascribed to two main possibilities. The first, and simplest, is that there are several physical connections that cannot be identified directly in the bright field images. We can indeed only see a minor fraction of all the connections, and therefore such a ‘photographic inspection’ may not suffice to dissect the real structural connectivity. As we have seen, the axons projecting from the neurons within a cluster may extend several hundreds of microns, establishing connections to distant clusters. The second possibility is the existence of ‘spurious’ functional connections. These ‘spurious’ links can be related to those connections associated to independent, randomly firing clusters, or ‘connectors’ clusters. However, these links in principle are infrequent and generally weak, and disappear when treating with the top,  $z$ -score thresholded functional maps. Additionally, special cases may occur when a cluster  $i$  is driving at the same time the dynamics of clusters  $j$  and  $k$  and that are not connected to each other, giving rise to a functional link between  $(j, k)$ . Such a relation can often take place since  $j$  and  $k$  are driven by the same dynamics even if there is a lack of direct causality relationship between them.

To further examine possible dependencies between functional and cluster-to-cluster traits we computed the following correlations.

### A) Correlation between morphological and functional parameters

In this analysis, we considered experiments in which we first measured spontaneous activity in a culture to obtain its functional network. We then took high resolution images of the physical connections, and measured their weight in microns. We then plotted the weight of functional links as a function of the physical thickness for those pairs of clusters that exhibited a neat physical connection. The results are shown in Figure 7.5A. For clarity, we binned the data for similar physical widths. The plot shows the large dispersion in functional weights, and the lack of correlation between neighbor-to-neighbor structure and function ( $r = 0.040$ ).

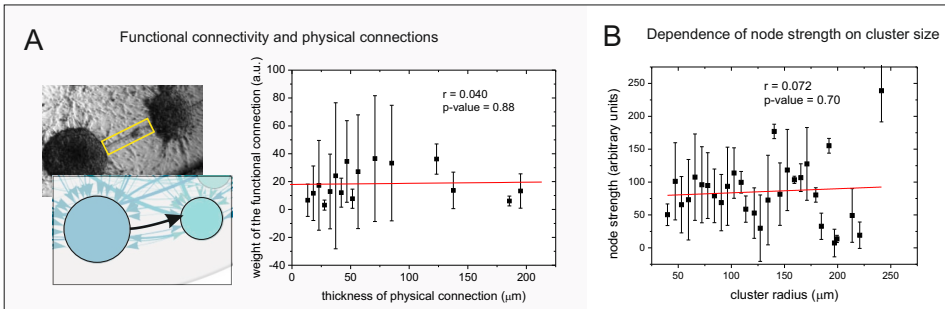


**Fig. 7.5 Correlation between morphological and functional parameters.** The functional connectivity of the clustered networks does not seem to depend on direct physical traits of the culture. **A**, Dependence of the weight of the functional connections on the width of physical connections between directly connected clusters. The sketch conceptually shows the comparison between structural and functional links. The plot represents the analysis of 102 pairs of clusters, with data binned for similar widths. No significant correlation is observed. **B**, The dependence of the nodal strength on cluster size shows no correlation, indicating that the functional connectivity cannot be assessed from the size of the clusters. Data is based on the analysis of 537 clusters. Error bars show standard deviation.

Similarly, we carried out an analysis in which we studied the correlation between the nodal strength and the size of the physical cluster. The data was binned to average over similar cluster sizes. The results are shown in Figure 7.5B. Again, we observed strong fluctuation in the values of the strength, and no correlation between strength and cluster size ( $r = 0.072$ ).

B) Correlation between cluster's activity and size

In addition of investigating the relation between physical traits and functional ones, we studied the relation between the physical size of the clusters and their dynamic characteristics. Thus, we investigated whether the activity of the clusters is related to their size. We measured for all clusters their average activity along the recordings and plotted it as a function of their radius. We used all available data (537 measurements) and binned similar sizes. We also observed that the size of the clusters did not correlate with their average activity ( $r = 0.14$ ), as shown in Figure 7.6A, i.e. small and big clusters displayed similar firing frequencies, and of 1 firing/min on average. However, since some clusters are initiators of activity and others just followers, we also computed the relative contribution of a given cluster size to initiate activity in the network. We found no significant correlation between initiation and cluster size ( $r = 0.38$  Figure 7.6B). These results strengthen the conclusion that one cannot predict the clusters that will initiate activity, or the most persistent sequences, by just a visual inspection of cluster sizes and their distribution over the network.

These analyses are important in the context of the work by Shein-Idelson and coworkers (Shein Idelson et al., 2010), who studied the dynamics of *isolated* clusters similar to ours, and observed that their firing rate increased from 0.7 to 8 firings/min as the clusters' radii escalated from 30 to 130  $\mu\text{m}$ . We also investigated isolated clusters as a control in our analysis and observed a similar trend. Hence, the remarkable difference in behavior between isolated and 'networked' clusters highlights the importance of the connectivity –rather than the cluster's themselves– in dictating the dynamics of the network.

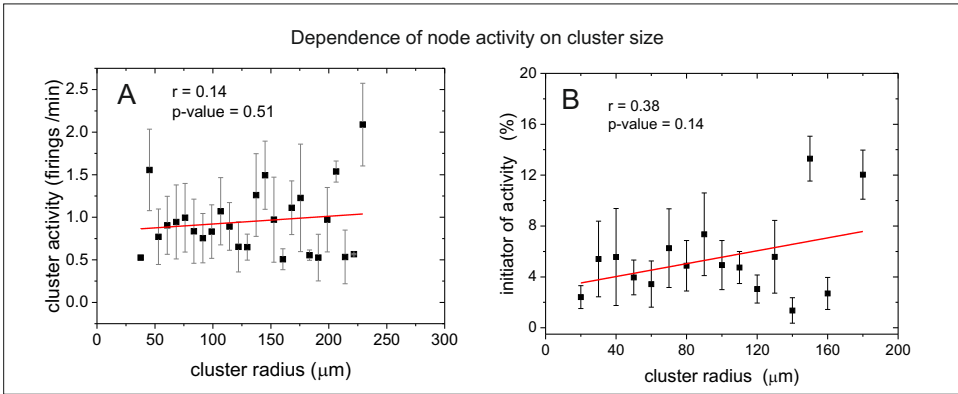


**Fig. 7.6 Dependence of the clusters' activity on their size.** **A**, For the same clusters of Figure 7.5B, this plot shows that the activity of a cluster is independent of its size. **B**, Activity within a burst is always initiated by a particular cluster, which triggers the sequential activation of all the downstream clusters. To quantify the importance of these 'initiators of activity' in network dynamics we computed the number of times that a cluster of a given size initiates a sequence of activations. The plot shows that there is no significant correlation between initiation and size. The analysis is based on the study of 1800 bursts. All these results indicate that the functional connectivity cannot be drawn from a visual inspection of the neuronal culture. Errors bars show standard deviation.

## 7.4 Towards engineering clustered neuronal networks

All our clustered networks are shaped solely by a self-organizing process. An initial ensemble of isolated neurons evolves towards a network of clustered neurons that, from culture to culture, varies both in layout and number of clusters. From an experimental perspective, two main questions arise: can we design networks that are reproducible? How different are self-organized networks from engineered ones?

To address these questions, we attempted several times in the last five years to devise 'patterned' networks, i.e. physical designs to control both the position of nodes and connections, and following a number of strategies developed by others (Gabay et al., 2005; Macis et al., 2007; Shein et al., 2009; Sorkin et al., 2006; Soussou et al., 2007; Wheeler and Brewer, 2010). Interest-

ingly, the majority of these studies used also neuronal clusters as nodes of a designed network given their easy manipulation and high viability. However, the idea seems simple but its actual development very hard, and the majority of these works describe the diverse problems and cumbersome strategies for placing neuronal clusters in predefined locations. One therefore finds a large number of possibilities in this difficult field, but none of them really simple or cheap. Nevertheless, the idea to force the underlying connectivity to follow, for instance, well-known topologies such as random, scale-free or small-world—and then study the resulting functional connectivity—makes these studies fascinating. More importantly, they confer a powerful opportunity to unveil important aspects of the structure–function relationship in an (ideally) easy and systematic manner.

At the beginning of this thesis we tried very hard to create ‘patterned’ clustered networks, but the difficulties turned out to be important, and none of the strategies provided satisfactory results. However, at the moment of writing this thesis, we are still working hard to find a good strategy. Next, we summarize the two attempted techniques, highlighting which one provided the most promising results for future work.

The idea behind both techniques is the use of photolithography to design circuits where the clusters sit (Figure 7.7). These circuits were printed in PDMS molds, and with assistance of the Technical Services from the Barcelona Science Park. The two different techniques consisted in printing the circuit either as *topographical pattern* in the mold or as a *pierced* layout, i.e. a hollow mask.

The methodology used for *topographical patterning* is shown in Figure 7.7A, and illustrative printed patterns are shown in Figure 7.8B. This technique provided top areas (‘mountains’ of the topographical pattern) combined with down areas (‘valleys’) where neurons would ideally sit. Obviously, in this approach neurons grow over a PDMS substrate, which turned out to be not very favorable for healthy neuronal development. After several attempts,

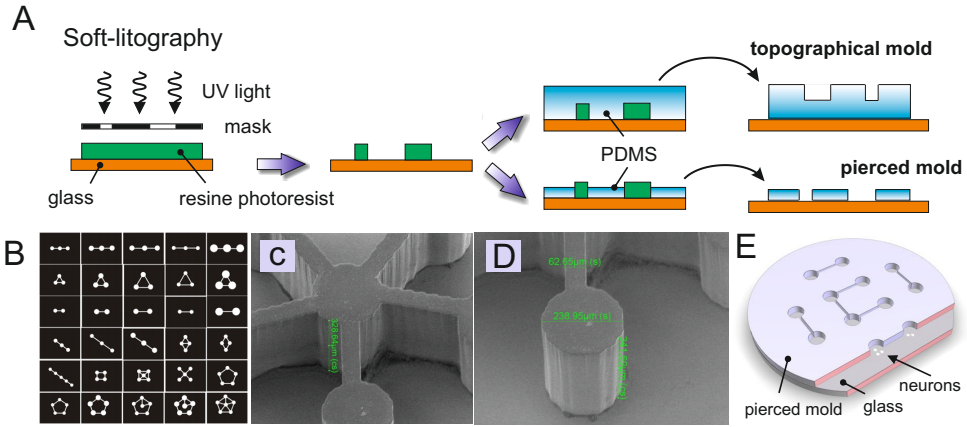


**Fig. 7.7 Soft lithography and patterned networks.** **A**, Detail of the soft-lithography process. First, the photomask with the pattern prototype (typically printed on transparency film) is placed on a glass with a photoresist resin above. Then, the photoresist resin is irradiated with UV light through the photo-mask to engrave the desired pattern on the substrate (black areas of the pattern are protected, while the transparent ones are exposed). This process induces cross-linking in the irradiated parts, and after development one obtains a resin mold with the negative relief of the photo-mask. PDMS is next poured over the relief and cured to get the final mould, where the white areas of the original design correspond to the valleys of the PDMS topography. One typically obtains topographical structures that are 50 – 100  $\mu\text{m}$  deep. In addition to topographical molds, one can also prepare resins 300 – 400  $\mu\text{m}$  high and pour the PDMS just below the resin level. In this way one can design pierced PDMS molds with complex shapes. Neurons are then plated with the mold in contact with the substrate, thus confining the neurons solely in the mold openings. **B**, An example of a photomask with our desired patterns. **C-D**, One example of high resin mold (350  $\mu\text{m}$ ) resulted applying the 'pierced mold' method. The diameter of the nodes in the pattern (adapted for clusters) is around 200  $\mu\text{m}$  and the connecting tunnels of 65  $\mu\text{m}$ . **E**) Confinement of neurons using a pierced PDMS mold.

we realized that clusters were not developing well. Moreover, the relatively small difference in height between mountains and valleys in the PDMS mold favored the creation of two networks, one at the top and one at the bottom, that connected to one another.

For *pierced* patterns, our idea was to generate hollow masks to grow the neurons over glass, with the masks containing very high walls to prevent possible neurons growing in the top to connect with the bottom ones (Figure 7.7C-E). We used a new resin (SU8-2100) that just appeared in the

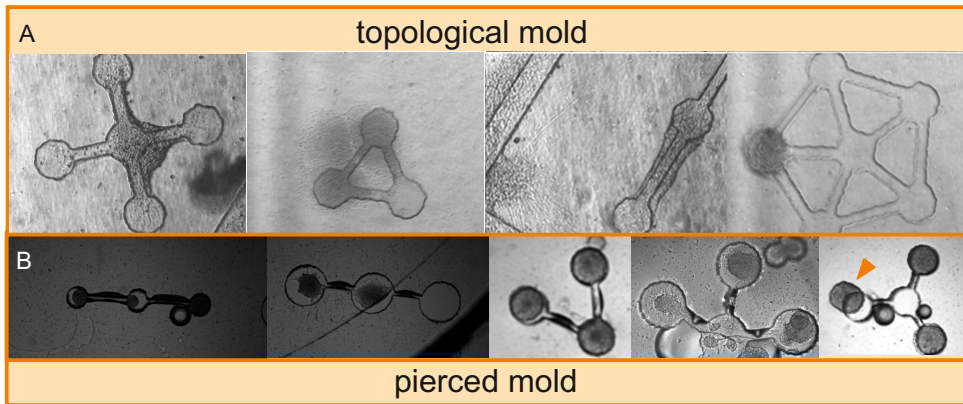


**Fig. 7.8 Topographical and pierced mold examples.** **A**, Representative examples using the topographical mold. Neurons are above of the PDMS. In this surface neurons difficult survive and cannot create well defined sphere aggregation. Moreover, PDMS high in this method was around  $100\ \mu$  leading to the neurons on the mountains and the valleys of the PDMS to connect among them. **B**, Illustrative results using the pierced mold. Here, neurons are in touch with the glass favoring the neuron-neuron attachment and ultimately the cluster formation. Moreover, the height of the PDMS here was around  $300\ \mu\text{m}$ , avoiding two-level network contact. However, the clusters' motility (see cluster marked with a white arrow) made highly difficult to achieve the final patterned networks.

market to achieve such goal. The final PDMS structure was around  $300\ \mu\text{m}$  in height, drastically reducing the possibility for top–bottom interconnectivity. Despite solving these two initial problems, the neurons' and clusters' natural motility turned out to be a problem. Simply, the neurons at the bottom aggregated as a giant cluster in a corner of the pattern, or clusters growing at the top 'jump' into the bottom structure. Although for the latter problem we tried to cover the PDMS with a glass, such a strategy damaged all the circuits by the turbulence created in the fluids. Hence, our best strategy at the end was to transfer previously individual clusters from self–organizing cultures at  $\text{DIV} = 5 - 6$  to the patterns, and waiting next to re–connect to one another. After few days, clusters created new connections —although not always— and did not move significantly, obtaining better outcomes.

Illustrative examples of the results for both techniques are shown in Figure 7.8. For the topographical pattern (Figure 7.8A) we can observe that

neurons tend to form a giant cluster or a continuum of neurons, making the pattern totally useless. For the pierced mold (Figure 7.8B) the results are better, but clearly require more tuning. For the latter, it is worth mentioning that we explored different ranges to optimize the structures, optimized the width and length of the corridors and the diameter of the circular traps. In some cases we even managed to record spontaneous activity for 30 min, but the richness and reproducibility of the experiments was poor. Overall, and despite some successes, the balance between effort and good statistics was in general bad. Thus, we finally put aside this research line and concentrated our efforts on the more rewarding self-organizing neuronal clustered networks.

As a final remark, and as we have seen, the rewarding aspect of working with free self-organizing networks is that their structural as well as functional organization is driven towards optimizing biological survival, a fundamental reason by itself to characterize them.

# Chapter 8

## Conclusions

Clustered neuronal cultures arise from a self-organizing process. An initially isotropic ensemble of individual neurons swiftly attach to one another to shape a stable configuration of interconnected clusters of tightly packed neurons that exhibit rich spontaneous activity. The formation of these clustered networks seems to be driven by the neurites' tension that overcomes the substrate adhesion. Aggregation occurs even in the absence of glial cells and neuronal activity (Segev et al., 2003b), and we observed that it is maintained up to the degradation of the culture (de Santos-Sierra et al., 2014; Segev et al., 2003b; Shefi et al., 2002). In this thesis we investigated in detail the dynamics of this kind of neuronal networks and, by using tools from complex network theory, we drew their *effective connectivity* maps and pictured their overall *functional organization*.

These clustered cultures display a distinct spontaneous activity characterized by the cascaded activation of groups of clusters in a short time window, an event that we termed *firing sequence*. Some clusters often fire together along the entire measurement, shaping strong *modules* or communities. By applying community detection tools we examined the modular structure of the clustered networks. It appeared to be hierarchically modular, i.e. with big modules containing other, smaller modules.

We also inferred the effective connectivity of these clustered cultures from the analysis of the firing sequences. Although different information–theoretic methods could be applied to carry out such an analysis, we developed in collaboration with Alex Arenas’ group (U. Rovira i Virgili, Tarragona) a new approach that naturally captures the intrinsic dynamics of our clustered cultures. Our method is based on the use of the time delays between cluster’s activations to weight the connections among clusters as well as their directions. Our results, in comparison to previous methods such a transfer entropy, provided similar results, although our method is much simpler from a computational perspective. Additionally, by deeply exploiting different complex network theory tools, we unveiled that these clustered networks are assortative, i.e. nodes with high strength tend to be connected, and that all the studied networks presented a Rich Club core and hubs. All these network features were observed along different days *in vitro* and independently of the balance between excitation and inhibition. Conversely, when examining the topological properties of homogeneous cultures, we observed that they exhibited a nearly disassortative connectivity and without a rich club.

These results are important since, first, it has been claimed that a hierarchical modularity can enhance robustness, adaptivity, and evolvability of network function (Meunier et al., 2010). And, second, different studies have highlighted the importance of assortativity and rich club traits to facilitate redundancy mechanisms that ultimately reinforce and stabilize network activity.

We must note that the number of clusters and their distribution is initially random. Therefore, a wide spectrum of physical circuitries and functional topologies are in principle possible. However, in all the studied cultures, the network drives itself towards a hierarchical modular configuration, assortative connectivity traits and the presence of a rich club. Hence, we concluded in the first part of the Results of this thesis that the self–organizing aggregation of neurons and their interconnection, together with the resulting robust func-

---

tional organization, could emerge as a survival mechanism to ensure a robust architecture and a sustained network activity.

This first set of results were fascinating for us. These clustered cultures indeed seem to exhibit key brain-related network features, particularly a hierarchical modularity and the existence of assortativity traits and a rich club core. Thus, in our view, these clusters shape networks with spatio-temporal dynamics that truly resemble a ‘brain in a dish’, offering a great potential to study not only major topological features, but also to tackle network resilience and response to damage.

The presumably robust architecture of the clustered networks, together with our interest in exploring resilience traits, launched us to study network resilience upon different chemical and physical damages. In the second part of the Results, we applied *global* and *local* damages to the clustered networks and studied the changes in their functional organization. In particular, we globally attacked neurons through photo-damage and by blocking their excitatory connections. We always compared the resulting network degradation with identical actions on homogeneous cultures, which are disassortative. In all these studies, clustered networks retained a higher network activity, and therefore higher resilience to damage, than the homogeneous analogs. We concluded that this difference in network response could be ascribed to their different functional organization, thus reinforcing the message that assortative traits are related to resilience. Interestingly, depending on the level of network deterioration, these clustered networks seem to present compensatory mechanisms that tend to preserve the global network connectivity while reorganizing the internal modular structure.

This rich interplay between integration and segregation was also seen upon local damage. In particular, we applied local damage—and in a highly controlled manner—into a single neuronal clusters by using a laser adapted for ablation at the Institute for Photonic Sciences (ICFO). Substantial efforts were poured into this idea, and we needed about two years to design and

tune the experimental system before achieving good results. The results were classified depending on the topological role of the targeted cluster before damage. We observed that these clustered networks presented a high resilience under *random attack*, but under *hub attack* the network globally disintegrated. From these preliminary results, we concluded that depending on the topological role in the modular architecture of the targeted neuronal cluster, as well as on the position that it occupies in the network, the global damage can be stronger or weaker. We also observed that topological role and location are features that in turn can favor or not the presence of recovery mechanisms to maintain network activity.

Once we exposed the potential of these clustered networks to link network functional traits with resilience to damage, we used them as a platform to study the damaging effects of different chemical compounds involved in Alzheimer's disease. In collaboration with the Institute for Bioengineering of Catalonia (IBEC), the experiments showed that the concurrent presence of magnetite and Amyloid- $\beta$  leads to the formation of a biochemical complex that causes a major disruption in the structure of the communities in the network together with a decrease in the weight of its connections. In particular, network upon biochemical damage lost their integration and an increase in segregation, i.e. the emergence of a submodular structures. Interestingly, depending on the level of damage in the network, compensatory effects emerged in order to preserve network activity. Concretely, networks tended to maintain global connectivity by reinforcing their inter-connections, but also tended to preserve their modular structure by locally increasing their intra-moduli connections. These findings suggest that the modular behavior—that can be related in turn with their assortative traits— can be favorable to prevent network degradation. This work confirms that these clustered networks provide an innovative and versatile tool to unveil the action of molecular agents in network activity and function. We believe that it is

---

a unique experimental model system for neurodegeneration that may help uncovering universal processes for functional reorganization upon damage.

A final study in this thesis, still in progress, was motivated by several studies in brain networks which advocate that the functional connectivity reflects the underlying structural organization Deco et al. (2011); Honey et al. (2007a, 2009). To shed light on this interrelation in our cultures, we would need the identification of all the physical links between clusters. From bright field pictures some structural connections could be identified by simple visual inspection. However, we observed that only a small fraction of the entire structural layout were directly accessible, and therefore a complete description of the physical circuitry must be carried out before comparing the structural and functional networks. Such a detailed identification is difficult, and requires the use of a number of connectivity-labeling techniques. Nevertheless, for the connections that we could visualize, we draw two major conclusions. First, that neither the width of the physical connections nor the size of the clusters were related to a particular trait of the functional links, such as the weight of the connections or the strength of the nodes. And, second, that our construction inferred strong functional links between clusters that were not directly connected in a physical manner, highlighting the importance of indirect paths in the flow of activity.

Hence, for future work, the identification of the full set of structural connections would certainly provide invaluable information to investigate the interplay between structure and function in our networks. In this context, the recent work by Santos-Sierra *et al* de Santos-Sierra et al. (2014) is enlightening. They analyzed some major structural connectivity traits in clustered networks similar to ours, and observed that the networks were also strongly assortative. Assortativity emerged at early stages of development, and was maintained throughout the life of the culture. Hence, in clustered cultures, the combined evidences of this study and ours hints at the existence of assortative properties in both structure and function.

As an overall conclusion, we have presented in this thesis powerful constructions to draw the effective connectivity and delineate the functional organization of clustered neuronal cultures. The construed networks exhibit assortativity and ‘rich club’ features, which are present concurrently with resilience traits. Our analysis has been based on spontaneous activity data, and may certainly vary from evoked activity. Hence, the combined experimental setup and functional construction can be viewed as a model system for complex networks studies, specially to understand the interplay between structure and function, and the emergence of key topological traits from network dynamics. Also, the spatial nature of our experiments have procure invaluable data to understanding the role of short– and long–range connections in network dynamics; or to investigate the targeted deletion of the hub nodes that shape the backbone of the network. The latter is a powerful concept that may assist in a detailed exploration of resilience in neuronal circuits, for instance to model circuitry–activity damage in neurological disorders.

This thesis gave rise to the following publications:

- J.G. Orlandi, E.Alvarez-Lacalle, S. Teller, J.Casademunt, J.Soriano. *The role of connectivity and noise in the emergence of spontaneous activity in cultured neuronal networks*. Nonlinear Theory and Its Applications, IEICE Conf.Proc. 547 (2012).
- J.G. Orlandi, E.Alvarez-Lacalle, S. Teller, J.Casademunt, J.Soriano, *The emergence of spontaneous activity in neuronal cultures*. AIP Conf. Proc. **1510**, 25 (2013).
- E. Tibau, C. Bendiksen, S. Teller, N. Amigó, J. Soriano. *Interplay Activity–connectivity: Dynamics in Patterned Neuronal Cultures*. AIP Conf. Proc.**1510**, 54 (2013).

- S. Teller and J. Soriano. *Experiments on Clustered Neuronal Networks*, in *Physics, Computation, and the Mind – Advances and Challenges at Interfaces*, AIP Conf. Proc. **1510**, 244 (2013).
- J.G. Orlandi, J. Soriano, E. Alvarez-Lacalle, S. Teller, and J. Casademunt. *Noise focusing and the emergence of coherent activity in neuronal cultures*. Nature Physics. **9**, pp. 582 – 590 (2013).
- S. Teller, C. Granell, M. De Domenico, J. Soriano, S. Gomez, and A. Arenas. *Emergence of assortative mixing between clusters of cultured neurons*. PLoS Computational Biology **10**, e1003796 (2014).
- S. Teller, I. B. Tahirbegi, M. Mir, J. Samitier, J. Soriano. *Magnetite–Amyloid- $\beta$  deteriorates activity and functional organization in an in vitro model for Alzheimer’s disease*. Scientific Reports **5**, article 17261 (2015).
- S. Teller and J. Soriano. *Experiments In Clustered Neuronal Networks: A Paradigm for Complex Modular Dynamics*. AIP Conf. Proc (in press).



# Chapter 9

## Resumen en castellano

### 9.1 Introducción

Desvelar el mapa de conexiones del cerebro, así como de todos los procesos dinámicos que se dan en él, es una de los mayores objetivos de la neurociencia moderna (Bullmore and Sporns, 2009). Además, comprender como funciona un cerebro sano, y asignar qué clase de deficiencias presenta un cerebro con patologías neurológicas, es de vital importancia (Stam, 2014). Sin embargo, alcanzar hoy en día dicho objetivo es sumamente difícil, y por varias razones. Por un lado, la tecnología actual en imagen y electrofisiología no permite medir con precisión y simultáneamente todas las neuronas del cerebro, aparte de que se generaría tal volumen de datos cuyo tratamiento sería extremadamente costoso y complejo. Y, por otro lado, los modelos biofísicos y matemáticos para entender y contextualizar los datos aun están en desarrollo o son poco eficientes.

Por estas razones, la neurociencia y biofísica han buscado alternativas que permitan investigar las fenomenologías fundamentales de redes neuronales a una escala más tratable, y tanto en sistemas sanos como enfermos. Así, las escalas mesoscópicas (del orden del mm), han adquirido gradualmente más protagonismo como un punto intermedio entre la escala microscópica

(neurona y procesos moleculares) y la macroscópica (áreas funcionales del cerebro o el propio cerebro). Esta escala mesoscópica permite el desarrollo de modelos teóricos relativamente sencillos que describen correctamente los procesos fundamentales, así como la preparación de experimentos de fácil preparación y manipulación (Orlandi et al., 2013). Estos modelos más sencillos no sólo facilitan la comprensión entre las conexiones físicas de una red neuronal y la dinámica a la que puede dar lugar, sino que también permiten explorar de manera accesible fenómenos colectivos importantes. Estos fenómenos se generan a nivel de circuito neuronal mesoscópico y, en general, se dan también a mayor escala en el cerebro.

Esta tesis doctoral se enmarca dentro del esfuerzo de usar sistemas mesoscópicos para ayudar a entender fenómenos fundamentales que ocurren en redes neuronales y el propio cerebro. La herramienta de trabajo principal de mi estudio ha sido neuronas cultivadas en pequeñas cavidades, una herramienta experimental que se conoce como *cultivos neuronales*

Los cultivos neuronales son uno de los sistemas modelos más utilizados por su gran versatilidad y fácil manipulación. Un cultivo neuronal no es más que una red bidimensional de neuronas o agregaciones de neuronas interconectadas, cultivadas sobre un sustrato de vidrio, y mantenidas en un medio bioquímico adecuado. Estos cultivos presentan una actividad espontánea rica, lo que permite estudiar una gran cantidad de fenomenologías. Los cultivos utilizados son primarios, es decir derivados de neuronas de un tejido neuronal específico. En nuestro caso hemos trabajado con tejido cortical, el cual ha sido disociado en neuronas individuales y éstas sembradas en el vidrio. La disociación lleva a tener un cultivo donde, inicialmente, las neuronas están totalmente desconectadas, formando conexiones y un circuito *de novo* a medida que el cultivo madura.

Existen varios tipos de cultivos neuronales dependiendo de la preparación del sustrato previa a la siembra de neuronas. Cuando el sustrato ha sido recubierto con proteínas adhesivas, las neuronas quedan ancladas en su posición

inicial, generando una red con neuronas homogéneamente distribuidas en el espacio. Estos cultivos son llamados *cultivos homogéneos* y su utilización ayudado a entender aspectos tan importantes como el aprendizaje, la memoria, o la transmisión de información a través de la red (Madhavan et al., 2006, 2007; Segev et al., 2004). Cuando la restricción de la motilidad de las neuronas es específica, es decir siguiendo un patrón que guía las conexiones, entonces se habla de *cultivos dirigidos*. Estudios con este tipo de cultivo (Gabay et al., 2005; Macis et al., 2007; Shein et al., 2009; Shein-Idelson et al., 2011; Sorkin et al., 2006) son clave para explorar de forma controlada que tipo de patrones de actividad emergen en la red dependiendo del mapa de conectividad o topología subyacente. Finalmente, cuando no existe ningún tipo de restricción en las neuronas o su conectividad, éstas tienden de forma natural a agregarse entre ellas, dando lugar a una red de agregados de neuronas (*clústeres*) interconectados por grupos de axones. Estos cultivos auto-organizados, que llamamos *cultivos de neuronas clusterizadas* (*clustered neuronal cultures* en inglés) constituyen la preparación experimental básica bajo la que se ha desarrollado esta tesis. Como veremos, nuestro objetivo principal ha sido entender las propiedades de la actividad espontánea que presentan estos cultivos, y como ésta se liga a la conectividad de la red.

Los principios organizativos a nivel de dinámica que exhiben estos cultivos clusterizados son muy similares a los del cerebro. Muchos de estos rasgos son presentes en redes que demuestran ser robustas a diferentes tipos de ataques tanto químicos como físicos. En definitiva, estos cultivos clusterizados representan un sistema modelo muy apropiado para estudiar aspectos relacionados con la resistencia y/o vulnerabilidad en circuitos neuronales.

## 9.2 Métodos experimentales

Las neuronas que utilizamos son de la corteza cerebral de ratas embrionarias con 17 – 18 días de gestación. Las neuronas una vez disgregadas mediante

pipeteo son depositadas en vidrios circulares de 13 mm de grosor, y que tienen acoplado un molde de plástico transparente conocido como PDMS. Dicho molde presenta 4 cavidades circulares de 3 mm de diámetro, permitiendo que las neuronas formen mini-redes encima del vidrio de tan sólo 3 mm de diámetro. Las dimensiones de estos mini-cultivos fueron las ideales para optimizar al máximo las condiciones experimentales.

La actividad espontánea de estas mini redes de neuronas es medida a los 7 – 16 días *in vitro* mediante la técnica de fluorescencia de calcio (Grienberger and Konnerth, 2012). En concreto, utilizamos Fluo-4 como marcador, el cual emite luz cada vez que la neurona se activa. Combinando esta técnica con un microscopio y una cámara digital optimizada para fluorescencia, podemos detectar las activaciones espontáneas (*bursts*) producidas por los clústeres de neuronas. La cámara digital permite grabar a unas 80 – 100 imágenes por segundo y con una alta resolución espacial, lo que nos permite seguir la dinámica de la red con gran calidad. Tras analizar estas imágenes con un software propio programado en Matlab, podemos obtener de forma bastante precisa el momento en que tienen lugar los eventos de actividad.

La actividad espontánea en estos clústeres viene caracterizada por una activación consecutiva de disparos, que llamamos ‘secuencias de disparo’, y en donde participan dos o más clústeres. Algunos clústeres siempre participan en las mismas secuencias, formando *módulos dinámicos* bien definidas, mientras que otros clústeres participan a veces en una comunidad, a veces en otra. Estas ‘secuencias de disparo’ se observan alrededor de un centenar de veces en un experimento típico, lo que permite inferir los distintos módulos dinámicos con buena precisión.

Durante la tesis se ha realizado diferentes tipos de experimentos. El experimento estándar consiste en grabar el mini-cultivo en condiciones normales a lo largo de 1h. En otros experimentos perturbamos químicamente el cultivo añadiendo diferentes fármacos, o físicamente, destruyendo diferentes clústeres de neuronas mediante un laser.

## 9.3 Métodos teóricos

El conjunto de herramientas utilizadas para caracterizar la dinámica neuronal son básicamente dos: ‘teoría de redes’ (*complex networks*) y ‘algoritmos de clusterización’ (*community detection*).

En teoría de redes, los elementos (nodos) y sus interacciones (conexiones) son representadas en forma de red. En nuestro caso particular, los nodos corresponden a los agregados de neuronas, mientras que las conexiones pueden definirse de distintas formas dependiendo de la naturaleza de las interacciones. Existen tres tipos de conexiones: anatómicas, funcionales y efectivas. Las conexiones anatómicas hacen referencia a las conexiones físicas de la red. En nuestro caso, serían el conjunto de axones y dendritas que conectan a los agregados de neuronas entre ellos. Las conexiones funcionales provienen de las dependencias estadísticas entre actividades neuronales. Existen diferentes métodos para obtener la red funcional, como la correlación cruzada (Garofalo et al., 2009) o la información mútua (Hlavácková-Schindler et al., 2007). Por último las conexiones efectivas evalúan la influencia que un nodo tiene sobre otro, es decir la relación de ‘causalidad’ en la actividad entre el par de nodos. Existen pocas herramientas estadísticas para generar la red efectiva, ya que es un campo aun en desarrollo. La más utilizada, aunque a nivel computacional es muy costosa, se conoce como transferencia de entropía (Schreiber, 2000; Stetter et al., 2012). Determinar la conectividad efectiva de las redes clusterizadas ha sido uno de los objetivos de la tesis.

Una vez definida la red se aplican parámetros topológicos (también conocidos como descriptores estadísticos) que permiten la caracterización de la red —en nuestro caso efectiva— en condiciones normales o bajo diferentes acciones químicas o físicas.

La primera parte de mi tesis consistió en diseñar junto con el grupo del Prof. Álex Arenas (Universidad Rovira i Virgili, Tarragona) un modelo matemático para extraer la conectividad efectiva de la red. Este modelo utiliza básicamente el retraso temporal entre los disparos dentro las secuencias de

disparo para estimar la influencia de un clúster en otro. En otras palabras, si dentro de la secuencia de disparo un clúster ha disparado antes que otro, consideramos que el clúster que responde después ha sido causalmente activado por el primero, viéndose conectados de manera *efectiva* el uno con el otro, y con una fuerza de conexión que depende del retraso entre las dos activaciones. Así, cuanto menor es el tiempo entre disparos, mayor es la fuerza de la conexión. Por otro lado, utilizamos el método jerárquico de clustering para mirar la similitud en la participación de los clústeres en estas secuencias de disparo, y usando la ‘distancia de Jaccard’ como medida de tal similitud, para finalmente detectar las comunidades o módulos dinámicos que presenta la red.

## 9.4 Resultados y conclusiones

La tesis se compone de tres partes. La primera parte, y que dio fruto a una primera publicación (Teller et al., 2014), explica la caracterización de la red efectiva a partir del modelo matemático previamente explicado. El análisis de estas redes efectivas mostró que existe *asortatividad positiva* en estas redes, entendida como la tendencia que tienen los clústeres con número similar de conexiones a conectarse entre ellos. Además, descubrimos que clústeres con un gran número de conexiones —también llamados ‘hubs’— están interconectados entre sí formando una estructura robusta en la red que se conoce como ‘rich club’. Estas dos propiedades topológicas parecen conferir resistencia a la red y estabilidad en la actividad neuronal (Sporns, 2013; van den Heuvel and Sporns, 2011). Por otro lado, también calculamos la red efectiva para cultivos homogéneos, y observamos que presentan una asortatividad prácticamente nula y sin ‘rich club’, evidenciando una configuración de red más vulnerable.

Una de las conclusiones que derivamos a partir de estos resultados es que el proceso natural de auto-organización característico de las redes clusterizadas lleva al cultivo a conectarse de la manera más robusta posible para

preservar su actividad, es decir se podría ver como un mecanismo de supervivencia. Por otro lado, también vimos a partir del análisis de comunidades, que estos cultivos presentan una dinámica modular jerárquica, compuesta por módulos y sub-módulos. La presencia de módulos bien definidos se asocia a una segregación del sistema, mientras que la interconexión entre ellos se asocia a una integración.

En la segunda parte de la tesis utilizamos estos cultivos como plataforma para estudiar diferentes daños, globales y locales, en la actividad y conectividad efectiva de la red, haciendo seguidamente un estudio detallado de la resistencia de la misma a daño. Los daños globales fueron clasificados en dos grupos que se describen seguidamente, y la significancia del daño en la red la comparamos con los resultados obtenidos para cultivos homogéneos bajo las mismas perturbaciones. Así, en el primer daño, dejamos el cultivo expuesto a una intensa luz de fluorescencia hasta su degradación total. Midiendo el nivel de actividad respecto el tiempo de exposición concluimos que los cultivos homogéneos perdieron su actividad antes y a un ritmo mayor que los cultivos con clústeres. En el segundo daño, se degradó la red con un fármaco que bloquea las conexiones excitadoras. A mayores concentraciones la red tiene menos conexiones, con lo que le cuesta más disparar, hasta que a una concentración crítica el cultivo está totalmente silenciado. De nuevo vimos que los cultivos homogéneos decaían en actividad mucho más rápidamente que los clusterizados, y que por lo tanto la concentración crítica para silenciar los cultivos clusterizados era mucho mayor que para los homogéneos. Estos experimentos de daño global evidenciaron la robustez de las redes clusterizadas frente a las homogéneas. Como conclusión, lanzamos la hipótesis de que las propiedades asortativas y de ‘rich club’ de estas redes son el pilar que sustenta de su mayor resistencia.

En esta segunda parte de la tesis también realizamos un daño local a los clusteres de neuronas mediante un laser. Este estudio, aún en un estadio preliminar, se realizó en colaboración con el grupo del Prof. Pablo Loza

(Instituto de Ciencias Fónicas, Castelldefels). Tres diferentes experimentos representativos son mostrados en la tesis, clasificados según el 'nodo' dañado. Hasta el momento concluimos que la repercusión del daño tanto global (pérdida de integración) como local (pérdida en segregación) en la red depende fuertemente de las propiedades topológicas del nodo, es decir de su rol a nivel global y en donde está embebido a nivel local. También pudimos comprobar que las redes clusterizadas presentan diferentes mecanismos de compensación para perseverar la actividad.

Finalmente, en la tercera parte de la tesis, se explica un estudio, publicado recientemente, en el que utilizamos los cultivos clusterizados como sistema *in vitro* para estudiar diversos agentes químicos involucrados en la enfermedad de Alzheimer, en concreto un complejo formado por magnetita y *beta*-amiloide. Estos cultivos mostraron una declinación importante de la actividad, una desintegración de la red efectiva, y una notable pérdida de conexiones. Además, esta desintegración afecta al equilibrio entre integración y segregación, con una importante pérdida de la primera y un notable aumento de la segunda con la presencia de nuevos sub-módulos. En estos experimentos también se observaron mecanismos de recuperación ante la pérdida en conectividad, como por ejemplo el reforzamiento de conexiones, hecho que remarca la robustez y complejidad de estos cultivos.

La tesis, conjuntamente con todos los estudios y aplicaciones desarrollados, evidencia la gran utilidad de estos cultivos neuronales. La organización dinámica que presentan —asortatividad positiva, 'rich club' y la modularidad jerárquica— son características que también se han visto en el cerebro. Así, nuestro sistema modelo biológico vivo presenta un gran potencial para ayudar a entender mecanismos fundamentales que se generan también a otras escalas. Además, en nuestros cultivos, el número de nodos y conexiones son tan accesibles, que es un sistema ideal para mapear su conectividad anatómica, compararla con la efectiva y, así, ampliar el conocimiento sobre la relación estructura-función en circuitos neuronales.

# References

- A. Abbott. Solving the brain. *Nature*, 499(7458):272–274, 2013.
- S. Achard, R. Salvador, B. Whitcher, J. Suckling, and E. Bullmore. A resilient, low-frequency, small-world human brain functional network with highly connected association cortical hubs. *The Journal of neuroscience*, 26(1): 63–72, 2006.
- M. B. Ahrens, M. B. Orger, D. N. Robson, J. M. Li, and P. J. Keller. Whole-brain functional imaging at cellular resolution using light-sheet microscopy. *Nature methods*, 10(5):413–420, 2013.
- R. Albert and A.-L. Barabási. Statistical mechanics of complex networks. *Reviews of modern physics*, 74(1):47, 2002.
- R. Albert, H. Jeong, and A.-L. Barabási. Error and attack tolerance of complex networks. *nature*, 406(6794):378–382, 2000.
- U. Alon. Network motifs: theory and experimental approaches. *Nat Rev Genet*, 8(6):450–461, June 2007. ISSN 1471-0056. doi: 10.1038/nrg2102. URL <http://dx.doi.org/10.1038/nrg2102>.
- J. Alstott, M. Breakspear, P. Hagmann, L. Cammoun, and O. Sporns. Modeling the impact of lesions in the human brain. *PLoS Comput Biol*, 5(6): e1000408–e1000408, 2009.
- L. Bai, M. Zhang, S. Chen, L. Ai, M. Xu, D. Wang, F. Wang, L. Liu, F. Wang, and L. Lao. Characterizing acupuncture De Qi in mild cognitive impairment: relations with small-world efficiency of functional brain networks. *Evid-Based Compl Alt*, 2013:304804, 2013.
- A.-L. Barabási and R. Albert. Emergence of scaling in random networks. *science*, 286(5439):509–512, 1999.

- A.-L. Barabási and E. Bonabeau. Scale-free networks. *Scientific American*, 288(5):50–59, 2003.
- A. Barrat, M. Barthélemy, and A. Vespignani. *Dynamical processes on complex networks*. Cambridge University Press, New York, NY, USA, 2008.
- D. S. Bassett and E. Bullmore. Small-world brain networks. *The neuroscientist*, 12(6):512–523, 2006.
- D. S. Bassett and E. T. Bullmore. Human brain networks in health and disease. *Current opinion in neurology*, 22(4):340, 2009.
- J. M. Beggs and D. Plenz. Neuronal avalanches in neocortical circuits. *The Journal of neuroscience*, 23(35):11167–11177, 2003.
- J. M. Beggs and D. Plenz. Neuronal avalanches are diverse and precise activity patterns that are stable for many hours in cortical slice cultures. *The Journal of neuroscience*, 24(22):5216–5229, 2004.
- T. E. Behrens and O. Sporns. Human connectomics. *Current opinion in neurobiology*, 22(1):144–153, 2012.
- Y. Ben-Ari. Developing networks play a similar melody. *Trends in neurosciences*, 24(6):353–360, 2001.
- L. Berdondini, M. Chiappalone, P. van der Wal, K. Imfeld, N. de Rooij, M. Koudelka-Hep, M. Tedesco, S. Martinoia, J. van Pelt, G. L. Masson, and A. Garenne. A microelectrode array (mea) integrated with clustering structures for investigating in vitro neurodynamics in confined interconnected sub-populations of neurons. *Sensors and Actuators B: Chemical*, 114(1):530 – 541, 2006. ISSN 0925-4005. doi: <http://dx.doi.org/10.1016/j.snb.2005.04.042>. URL <http://www.sciencedirect.com/science/article/pii/S0925400505004624>.
- M. J. Berridge, P. Lipp, and M. D. Bootman. The versatility and universality of calcium signalling. *Nature reviews Molecular cell biology*, 1(1):11–21, 2000.
- L. M. Bettencourt, G. J. Stephens, M. I. Ham, and G. W. Gross. Functional structure of cortical neuronal networks grown in vitro. *Physical Review E*, 75(2):021915, 2007.

- G.-q. Bi and M.-m. Poo. Synaptic modification by correlated activity: Hebb's postulate revisited. *Annual review of neuroscience*, 24(1):139–166, 2001.
- G. M. Bishop and S. R. Robinson. Human A $\beta$ 1-42 reduces iron-induced toxicity in rat cerebral cortex. *J Neurosci Res*, 73(3):316–323, 2003. ISSN 1097-4547. doi: 10.1002/jnr.10661.
- V. D. Blondel, J.-L. Guillaume, R. Lambiotte, and E. Lefebvre. Fast unfolding of communities in large networks. *Journal of Statistical Mechanics: Theory and Experiment*, 2008(10):P10008, 2008.
- S. Boccaletti, V. Latora, Y. Moreno, M. Chavez, and D.-U. Hwang. Complex networks: Structure and dynamics. *Physics reports*, 424(4):175–308, 2006.
- P. Bonifazi, M. Goldin, M. A. Picardo, I. Jorquera, A. Cattani, G. Bianconi, A. Represa, Y. Ben-Ari, and R. Cossart. Gabaergic hub neurons orchestrate synchrony in developing hippocampal networks. *Science*, 326(5958):1419–1424, 2009. doi: 10.1126/science.1175509.
- J. Borge-Holthoefer, Y. Moreno, A. Arenas, and M. Perc. Modeling abnormal priming in Alzheimer's patients with a free association network. *PLoS One*, 6(8):e22651, 2011.
- M. Bottlang, M. B. Sommers, T. A. Lusardi, J. J. Miesch, R. P. Simon, and Z.-G. Xiong. Modeling neural injury in organotypic cultures by application of inertia-driven shear strain. *Journal of neurotrauma*, 24(6):1068–1077, 2007.
- I. Breskin, J. Soriano, E. Moses, and T. Tlusty. Percolation in living neural networks. *Physical review letters*, 97(18):188102, 2006.
- R. L. Buckner, J. Sepulcre, T. Talukdar, F. M. Krienen, H. Liu, T. Hedden, J. R. Andrews-Hanna, R. A. Sperling, and K. A. Johnson. Cortical hubs revealed by intrinsic functional connectivity: mapping, assessment of stability, and relation to alzheimer's disease. *The Journal of Neuroscience*, 29(6):1860–1873, 2009.
- J. M. Buldú, R. Bajo, F. Maestú, N. Castellanos, I. Leyva, P. Gil, I. Sendiña Nadal, J. A. Almendral, A. Nevado, F. Del-Pozo, and S. Boccaletti. Reorganization of functional networks in mild cognitive impairment. *PLoS One*, 6(5):e19584, 2011.

- E. Bullmore and O. Sporns. Complex brain networks: graph theoretical analysis of structural and functional systems. *Nature Reviews Neuroscience*, 10(3):186–198, 2009.
- E. Bullmore and O. Sporns. The economy of brain network organization. *Nature Reviews Neuroscience*, 13(5):336–349, 2012.
- E. T. Bullmore and D. S. Bassett. Brain graphs: graphical models of the human brain connectome. *Annual review of clinical psychology*, 7:113–140, 2011.
- G. Buzsáki and A. Draguhn. Neuronal oscillations in cortical networks. *science*, 304(5679):1926–1929, 2004.
- C. Carmeli, P. Bonifazi, H. P. Robinson, and M. Small. Quantifying network properties in multi-electrode recordings: spatiotemporal characterization and inter-trial variation of evoked gamma oscillations in mouse somatosensory cortex in vitro. *Frontiers in computational neuroscience*, 7, 2013.
- L. Carrillo-Reid, F. Tecuapetla, D. Tapia, A. Hernández-Cruz, E. Galarraga, R. Drucker-Colin, and J. Vargas. Encoding network states by striatal cell assemblies. *Journal of neurophysiology*, 99(3):1435–1450, 2008.
- R. J. Castellani, P. I. Moreira, G. Perry, and X. Zhu. The role of iron as a mediator of oxidative stress in Alzheimer disease. *Biofactors*, 38(2): 133–138, 2012.
- Y. Chen, B. Stevens, J. Chang, J. Milbrandt, B. A. Barres, and J. W. Hell. Ns21: re-defined and modified supplement b27 for neuronal cultures. *Journal of neuroscience methods*, 171(2):239–247, 2008.
- D. W. Choi, M. Maulucci-Gedde, and A. R. Kriegstein. Glutamate neurotoxicity in cortical cell culture. *The Journal of neuroscience*, 7(2):357–368, 1987.
- D. Cohen and M. Segal. Network bursts in hippocampal microcultures are terminated by exhaustion of vesicle pools. *Journal of neurophysiology*, 106(5):2314–2321, 2011.
- E. Cohen, M. Ivenshitz, V. Amor-Baroukh, V. Greenberger, and M. Segal. Determinants of spontaneous activity in networks of cultured hippocampus. *Brain Research*, 1235(0):21 – 30, 2008. ISSN 0006-8993. doi: 10.1016/j.brainres.2008.06.022. <ce:title>Brain Oscillations in Cognition and Cognitive Disorders</ce:title>.

- O. Cohen, A. Keselman, E. Moses, M. R. Martínez, J. Soriano, and T. Tlusty. Quorum percolation in living neural networks. *EPL (Europhysics Letters)*, 89(1):18008, 2010.
- J. Collingwood, A. Mikhaylova, M. Davidson, C. Batich, W. Streit, J. Terry, and J. Dobson. In situ characterization and mapping of iron compounds in Alzheimer's disease tissue. *J Alzheimers Dis*, 7(4):267–272, 2005.
- N. A. Crossley, A. Mechelli, J. Scott, F. Carletti, P. T. Fox, P. McGuire, and E. T. Bullmore. The hubs of the human connectome are generally implicated in the anatomy of brain disorders. *Brain*, 137(8):2382–2395, 2014.
- P. Crucitti, V. Latora, M. Marchiori, and A. Rapisarda. Error and attack tolerance of complex networks. *Physica A: Statistical Mechanics and its Applications*, 340(1):388–394, 2004.
- D. K. Cullen and M. C. LaPlaca. Neuronal response to high rate shear deformation depends on heterogeneity of the local strain field. *Journal of neurotrauma*, 23(9):1304–1319, 2006.
- K. N. Dahlgren, A. M. Manelli, W. B. Stine, L. K. Baker, G. a. Krafft, and M. J. LaDu. Oligomeric and fibrillar species of amyloid-beta peptides differentially affect neuronal viability. *J Biol Chem*, 277:32046–32053, 2002a.
- K. N. Dahlgren, A. M. Manelli, W. B. Stine, L. K. Baker, G. A. Krafft, and M. J. LaDu. Oligomeric and fibrillar species of Amyloid- $\beta$  peptides differentially affect neuronal viability. *J Biol Chem*, 277(35):32046–32053, 2002b.
- W. de Haan, K. Mott, E. Van Straaten, P. Scheltens, and C. J. Stam. Activity dependent degeneration explains hub vulnerability in alzheimer's disease. *PLoS Comput Biol*, 8(8):e1002582–e1002582, 2012.
- D. de Santos-Sierra, I. Sendiña-Nadal, I. Leyva, J. A. Almendral, S. Anava, A. Ayali, D. Papo, and S. Boccaletti. Emergence of small-world anatomical networks in self-organizing clustered neuronal cultures. *PloS one*, 9(1), 2014.
- F. De Vico Fallani, M. Corazzol, J. Sternberg, C. Wyart, and M. Chavez. Hierarchy of neural organization in the embryonic spinal cord: Granger-causality graph analysis of calcium imaging data. 2014.

- G. Deco, V. K. Jirsa, and A. R. McIntosh. Emerging concepts for the dynamical organization of resting-state activity in the brain. *Nature Reviews Neuroscience*, 12(1):43–56, 2011.
- J. DeFelipe, H. Markram, and K. S. Rockland. The neocortical column. *Frontiers in neuroanatomy*, 6, 2012.
- X. Delbeuck, M. Van der Linden, F. Collette, and M. V. D. Linden. Alzheimer’s disease as a disconnection syndrome? *Neuropsychol Rev*, 13(2):79–92, 2003.
- A. Demuro, E. Mina, R. Kaye, S. C. Milton, I. Parker, and C. G. Glabe. Calcium dysregulation and membrane disruption as a ubiquitous neurotoxic mechanism of soluble amyloid oligomers. *J Biol Chem*, 280(17):17294–17300, 2005.
- A. Demuro, I. Parker, and G. E. Stutzmann. Calcium signaling and amyloid toxicity in Alzheimer disease. *J Biol Chem*, 285(17):12463–12468, 2010.
- B. C. Dickerson, D. H. Salat, D. N. Greve, E. F. Chua, E. Rand-Giovannetti, D. M. Rentz, L. Bertram, K. Mullin, R. E. Tanzi, D. Blacker, M. S. Albert, and R. A. Sperling. Increased hippocampal activation in mild cognitive impairment compared to normal aging and AD. *Neurology*, 65(3):404–411, 2005.
- S. N. Dorogovtsev and J. F. Mendes. Evolution of networks. *Advances in physics*, 51(4):1079–1187, 2002.
- S. N. Dorogovtsev and J. F. F. Mendes. *Evolution of Networks: From Biological Nets to the Internet and WWW*. Oxford University Press, 2003.
- J. H. Downes, M. W. Hammond, D. Xydas, M. C. Spencer, V. M. Becerra, K. Warwick, B. J. Whalley, and S. J. Nasuto. Emergence of a small-world functional network in cultured neurons. *PLoS Comput. Biol*, 8(5):e1002522, 2012.
- J. C. Doyle, D. L. Alderson, L. Li, S. Low, M. Roughan, S. Shalunov, R. Tanaka, and W. Willinger. The “robust yet fragile” nature of the internet. *Proceedings of the National Academy of Sciences of the United States of America*, 102(41):14497–14502, 2005.
- J.-P. Eckmann, O. Feinerman, L. Gruendlinger, E. Moses, J. Soriano, and T. Tlusty. The physics of living neural networks. *Physics Reports*, 449(1): 54–76, 2007.

- J.-P. Eckmann, S. Jacobi, S. Marom, E. Moses, and C. Zbinden. Leader neurons in population bursts of 2d living neural networks. *New Journal of Physics*, 10(1):015011, 2008.
- J.-P. Eckmann, E. Moses, O. Stetter, T. Tlusty, and C. Zbinden. Leaders of neuronal cultures in a quorum percolation model. *Frontiers in computational neuroscience*, 4, 2010.
- B. Efron. Computers and the theory of statistics. *S I a M r e*, 21:1.
- V. M. Eguíluz, D. R. Chialvo, G. A. Cecchi, M. Baliki, and A. V. Apkarian. Scale-free brain functional networks. *Phys. Rev. Lett.*, 94:018102, Jan 2005. doi: 10.1103/PhysRevLett.94.018102.
- E. Estrada. *The Structure of Complex Networks*. Oxford University Press, Oxford, 2011a.
- E. Estrada. *The structure of complex networks: theory and applications*. Oxford University Press, 2011b.
- J. Everett, E. Céspedes, L. R. Shelford, C. Exley, J. F. Collingwood, J. Dobson, G. van der Laan, C. A. Jenkins, E. Arenholz, and N. D. Telling. Evidence of redox-active iron formation following aggregation of ferrihydrite and the Alzheimer's disease peptide  $\beta$ -amyloid. *Inorg Chem*, 53(6):2803–2809, 2014.
- O. Feinerman, M. Segal, and E. Moses. Signal propagation along unidimensional neuronal networks. *Journal of neurophysiology*, 94(5):3406–3416, 2005.
- O. Feinerman, M. Segal, and E. Moses. Identification and dynamics of spontaneous burst initiation zones in unidimensional neuronal cultures. *Journal of neurophysiology*, 97(4):2937–2948, 2007.
- O. Feinerman, A. Rotem, and E. Moses. Reliable neuronal logic devices from patterned hippocampal cultures. *Nature Physics*, 4(12):967–973, 2008.
- S. Feldt, P. Bonifazi, and R. Cossart. Dissecting functional connectivity of neuronal microcircuits: experimental and theoretical insights. *Trends in neurosciences*, 34(5):225–236, 2011.
- A. Fornito, A. Zalesky, and M. Breakspear. The connectomics of brain disorders. *Nature Reviews Neuroscience*, 16(3):159–172, 2015.

- S. Fortunato. Community detection in graphs. *Physics Reports*, 486(3): 75–174, 2010.
- M. D. Fox and M. E. Raichle. Spontaneous fluctuations in brain activity observed with functional magnetic resonance imaging. *Nature Reviews Neuroscience*, 8(9):700–711, 2007.
- A. M. Fraser and H. L. Swinney. Independent coordinates for strange attractors from mutual information. *Physical review A*, 33(2):1134, 1986.
- M. Frega, V. Pasquale, M. Tedesco, M. Marcoli, A. Contestabile, M. Nanni, L. Bonzano, G. Maura, and M. Chiappalone. Cortical cultures coupled to micro-electrode arrays: a novel approach to perform in vitro excitotoxicity testing. *Neurotoxicology and teratology*, 34(1):116–127, 2012.
- T. Gabay, E. Jakobs, E. Ben-Jacob, and Y. Hanein. Engineered self-organization of neural networks using carbon nanotube clusters. *Physica A: Statistical Mechanics and its Applications*, 350(2–4):611 – 621, 2005. ISSN 0378-4371. doi: 10.1016/j.physa.2004.11.007. URL <http://www.sciencedirect.com/science/article/pii/S037843710401413X>.
- K. Ganguly, A. F. Schinder, S. T. Wong, and M.-m. Poo. Gaba itself promotes the developmental switch of neuronal gabaergic responses from excitation to inhibition. *Cell*, 105:521–532, 2001.
- M. Garofalo, T. Nieuws, P. Massobrio, and S. Martinoia. Evaluation of the performance of information theory-based methods and cross-correlation to estimate the functional connectivity in cortical networks. *PloS one*, 4(8): e6482, 2009.
- K. R. Gee, K. Brown, W. U. Chen, J. Bishop-Stewart, D. Gray, and I. Johnson. Chemical and physiological characterization of fluo-4 ca 2+-indicator dyes. *Cell calcium*, 27(2):97–106, 2000.
- G. Gong, Y. He, L. Concha, C. Lebel, D. W. Gross, A. C. Evans, and C. Beaulieu. Mapping anatomical connectivity patterns of human cerebral cortex using in vivo diffusion tensor imaging tractography. *Cerebral cortex*, 19(3):524–536, 2009.
- L. Goodman. Alzheimer’s disease: a clinico-pathologic analysis of twenty-three cases with a theory on pathogenesis. *J Nerv Ment Dis*, 118(2):97–130, 1953.

- C. W. Granger. Investigating causal relations by econometric models and cross-spectral methods. *Econometrica: Journal of the Econometric Society*, pages 424–438, 1969.
- C. Gratton, E. M. Nomura, F. Pérez, and M. D’Esposito. Focal brain lesions to critical locations cause widespread disruption of the modular organization of the brain. *Journal of cognitive neuroscience*, 24(6):1275–1285, 2012.
- C. Grienberger and A. Konnerth. Imaging calcium in neurons. *Neuron*, 73(5): 862–885, 2012.
- M. G. Grigorov. Global properties of biological networks. *Drug discovery today*, 10(5):365–372, 2005.
- G. W. Gross and J. M. Kowalski. Origins of activity patterns in self-organizing neuronal networks in vitro. *Journal of Intelligent Material Systems and Structures*, 10(7):558–564, 1999.
- R. Guimera and L. A. N. Amaral. Cartography of complex networks: modules and universal roles. *Journal of Statistical Mechanics: Theory and Experiment*, 2005(02):P02001, 2005.
- P. Hagmann, L. Cammoun, X. Gigandet, R. Meuli, C. J. Honey, V. J. Wedeen, and O. Sporns. Mapping the structural core of human cerebral cortex. *PLoS Biol*, 6(7):e159, 07 2008. doi: 10.1371/journal.pbio.0060159.
- M. I. Ham, L. M. Bettencourt, F. D. McDaniel, and G. W. Gross. Spontaneous coordinated activity in cultured networks: analysis of multiple ignition sites, primary circuits, and burst phase delay distributions. *Journal of computational neuroscience*, 24(3):346–357, 2008.
- J. Hardy and D. J. Selkoe. The Amyloid hypothesis of Alzheimer’s disease: Progress and problems on the road to therapeutics. *Science*, 297(5580): 353–356, 2002.
- J. A. Hardy and G. A. Higgins. Alzheimer’s disease: the amyloid cascade hypothesis. *Science*, 256(5054):184–185, 1992.
- L. Harriger, M. P. Van Den Heuvel, and O. Sporns. Rich club organization of macaque cerebral cortex and its role in network communication. 2012.
- R. E. Harris, M. G. Coulombe, and M. B. Feller. Dissociated retinal neurons form periodically active synaptic circuits. *Journal of neurophysiology*, 88 (1):188–195, 2002.

- D. M. Hartley, D. M. Walsh, C. P. Ye, T. Diehl, S. Vasquez, P. M. Vassilev, D. B. Teplow, and D. J. Selkoe. Protofibrillar intermediates of amyloid beta-protein induce acute electrophysiological changes and progressive neurotoxicity in cortical neurons. *J Neurosci*, 19(20):8876–8884, 1999.
- D. Hautot, Q. Pankhurst, N. Khan, and J. Dobson. Preliminary evaluation of nanoscale biogenic magnetite in Alzheimer’s disease brain tissue. *P Roy Soc B - Biol Sci*, 270(Suppl 1):S62–S64, 2003.
- Y. He, Z. J. Chen, and A. C. Evans. Small-world anatomical networks in the human brain revealed by cortical thickness from mri. *Cerebral cortex*, 17(10):2407–2419, 2007.
- Y. He, J. Wang, L. Wang, Z. J. Chen, C. Yan, H. Yang, H. Tang, C. Zhu, Q. Gong, Y. Zang, et al. Uncovering intrinsic modular organization of spontaneous brain activity in humans. *PloS one*, 4(4):e5226, 2009.
- S. Herculano-Houzel. The human brain in numbers: a linearly scaled-up primate brain. *Frontiers in human neuroscience*, 3, 2009.
- A. Hierlemann, U. Frey, S. Hafizovic, and F. Heer. Growing cells atop microelectronic chips: interfacing electrogenic cells in vitro with cmos-based microelectrode arrays. *Proceedings of the IEEE*, 99(2):252–284, 2011.
- C. C. Hilgetag and M. Kaiser. Clustered organization of cortical connectivity. *Neuroinformatics*, 2(3):353–360, 2004.
- C.-C. Hilgetag, G. A. Burns, M. A. O’Neill, J. W. Scannell, and M. P. Young. Anatomical connectivity defines the organization of clusters of cortical areas in the macaque and the cat. *Philosophical Transactions of the Royal Society of London B: Biological Sciences*, 355(1393):91–110, 2000.
- K. Hlaváčková-Schindler, M. Paluš, M. Vejmelka, and J. Bhattacharyya. Causality detection based on information-theoretic approaches in time series analysis. *Physics Reports*, 441:1–46, 2007.
- P. Holme, B. J. Kim, C. N. Yoon, and S. K. Han. Attack vulnerability of complex networks. *Physical Review E*, 65(5):056109, 2002.
- C. J. Honey and O. Sporns. Dynamical consequences of lesions in cortical networks. *Human brain mapping*, 29(7):802–809, 2008.

- C. J. Honey, R. Kötter, M. Breakspear, and O. Sporns. Network structure of cerebral cortex shapes functional connectivity on multiple time scales. *Proceedings of the National Academy of Sciences*, 104(24):10240–10245, 2007a. doi: 10.1073/pnas.0701519104. URL <http://www.pnas.org/content/104/24/10240.abstract>.
- C. J. Honey, R. Kötter, M. Breakspear, and O. Sporns. Network structure of cerebral cortex shapes functional connectivity on multiple time scales. *Proceedings of the National Academy of Sciences*, 104(24):10240–10245, 2007b.
- C. J. Honey, O. Sporns, L. Cammoun, X. Gigandet, J. P. Thiran, R. Meuli, and P. Hagmann. Predicting human resting-state functional connectivity from structural connectivity. *Proceedings of the National Academy of Sciences*, 106(6):2035–2040, 2009. doi: 10.1073/pnas.0811168106. URL <http://www.pnas.org/content/106/6/2035.abstract>.
- Y. Ikegaya, G. Aaron, R. Cossart, D. Aronov, I. Lampl, D. Ferster, and R. Yuste. Synfire chains and cortical songs: temporal modules of cortical activity. *Science*, 304(5670):559–564, 2004.
- T. R. Insel, S. C. Landis, and F. S. Collins. The nih brain initiative. *Science*, 340(6133):687–688, 2013.
- S. Ito, M. E. Hansen, R. Heiland, A. Lumsdaine, A. M. Litke, and J. M. Beggs. Extending transfer entropy improves identification of effective connectivity in a spiking cortical network model. *PloS one*, 6(11):e27431, 2011.
- S. Ito, F.-C. Yeh, E. Hiolski, P. Rydygier, D. E. Gunning, P. Hottowy, N. Timme, A. M. Litke, and J. M. Beggs. Large-scale, high-resolution multielectrode-array recording depicts functional network differences of cortical and hippocampal cultures. 2014.
- S. Jacobi, J. Soriano, and E. Moses. Bdnf and nt-3 increase velocity of activity front propagation in unidimensional hippocampal cultures. *Journal of neurophysiology*, 104(6):2932–2939, 2010.
- I. Jolliffe. *Principal component analysis*. Wiley Online Library, 2002.
- H. Kamioka, E. Maeda, Y. Jimbo, H. P. Robinson, and A. Kawana. Spontaneous periodic synchronized bursting during formation of mature patterns of connections in cortical cultures. *Neuroscience letters*, 206(2):109–112, 1996.

- T. Kanungo, D. M. Mount, N. S. Netanyahu, C. D. Piatko, R. Silverman, and A. Y. Wu. An efficient k-means clustering algorithm: Analysis and implementation. *Pattern Analysis and Machine Intelligence, IEEE Transactions on*, 24(7):881–892, 2002.
- B. Karrer, E. Levina, and M. E. Newman. Robustness of community structure in networks. *arXiv preprint arXiv:0709.2108*, 2007.
- L. Kaufman and P. J. Rousseeuw. *Finding groups in data: an introduction to cluster analysis*, volume 344. John Wiley & Sons, 2009.
- M. Kawahara, I. Ohtsuka, S. Yokoyama, M. Kato-Negishi, and Y. Sadakane. Membrane incorporation, channel formation, and disruption of calcium homeostasis by alzheimer’s  $\beta$ -amyloid protein. *Int J Alzheimers Dis*, 2011: 304583, 2011.
- P. J. Keller, A. D. Schmidt, J. Wittbrodt, and E. H. Stelzer. Reconstruction of zebrafish early embryonic development by scanned light sheet microscopy. *science*, 322(5904):1065–1069, 2008.
- S. Kirkpatrick. Optimization by simulated annealing: Quantitative studies. *Journal of statistical physics*, 34(5-6):975–986, 1984.
- T. Knöpfel. Genetically encoded optical indicators for the analysis of neuronal circuits. *Nature Reviews Neuroscience*, 13(10):687–700, 2012.
- S. Kullback and R. A. Leibler. On information and sufficiency. *The annals of mathematical statistics*, pages 79–86, 1951.
- Y.-M. Kuo, M. R. Emmerling, C. Vigo-Pelfrey, T. C. Kasunic, J. B. Kirkpatrick, G. H. Murdoch, M. J. Ball, and A. E. Roher. Water-soluble A $\beta$ (N-40, N-42) oligomers in normal and Alzheimer disease brains. *J Biol Chem*, 271(8):4077–4081, 1996.
- Y. Lai, K. Cheng, and W. Kisaalita. Three dimensional neuronal cell cultures more accurately model voltage gated calcium channel functionality in freshly dissected nerve tissue. 2012.
- L. Lannfelt, C. Möller, H. Basun, G. Osswald, D. Sehlin, A. Satlin, V. Logovinsky, and P. Gellerfors. Perspectives on future Alzheimer therapies: amyloid- $\beta$  protofibrils – a new target for immunotherapy with BAN2401 in Alzheimer’s disease. *Alzheimers Res Ther*, 6:article 16, 2014.

- M. C. LaPlaca, V. N. Vernekar, J. T. Shoemaker, and D. K. Cullen. Three-dimensional neuronal cultures. *Methods in Bioengineering: 3D Tissue Engineering*. Artech House Publishers, London, 2010.
- H. A. Lashuel, D. Hartley, B. M. Petre, T. Walz, and P. T. Lansbury. Neurodegenerative disease: amyloid pores from pathogenic mutations. *Nature*, 418 (6895):291–291, 2002.
- V. Latora and M. Marchiori. Efficient behavior of small-world networks. *Phys. Rev. Lett.*, 87:198701, Oct 2001. doi: 10.1103/PhysRevLett.87.198701.
- M. S. Lewicki. A review of methods for spike sorting: the detection and classification of neural action potentials. *Network: Computation in Neural Systems*, 9(4):R53–R78, 1998.
- J. W. Lichtman, H. Pfister, and N. Shavit. The big data challenges of connectomics. *Nature neuroscience*, 17(11):1448–1454, 2014.
- N. Litvak and R. Van Der Hofstad. Uncovering disassortativity in large scale-free networks. *Physical Review E*, 87(2):022801, 2013.
- G. Lohmann, D. S. Margulies, A. Horstmann, B. Pleger, J. Lepsien, D. Goldhahn, H. Schloegl, M. Stumvoll, A. Villringer, and R. Turner. Eigenvector centrality mapping for analyzing connectivity patterns in fmri data of the human brain. *PLoS one*, 5(4):e10232–e10232, 2010.
- E. Macis, M. Tedesco, P. Massobrio, R. Raiteri, and S. Martinoia. An automated microdrop delivery system for neuronal network patterning on microelectrode arrays. *Journal of Neuroscience Methods*, 161(1):88 – 95, 2007. ISSN 0165-0270. doi: 10.1016/j.jneumeth.2006.10.015. URL <http://www.sciencedirect.com/science/article/pii/S0165027006005115>.
- E. Z. Macosko, N. Pokala, E. H. Feinberg, S. H. Chalasani, R. A. Butcher, J. Clardy, and C. I. Bargmann. A hub-and-spoke circuit drives pheromone attraction and social behaviour in *c. elegans*. *Nature*, 458(7242):1171–1175, 2009.
- R. Madhavan, Z. C. Chao, D. Wagenaar, D. J. Bakkum, S. M. Potter, et al. Multi-site stimulation quiets network-wide spontaneous bursts and enhances functional plasticity in cultured cortical networks. In *Engineering in Medicine and Biology Society, 2006. EMBS'06. 28th Annual International Conference of the IEEE*, pages 1593–1596. IEEE, 2006.

- R. Madhavan, Z. C. Chao, and S. M. Potter. Plasticity of recurring spatiotemporal activity patterns in cortical networks. *Physical biology*, 4(3):181, 2007.
- E. Maeda, H. Robinson, and A. Kawana. The mechanisms of generation and propagation of synchronized bursting in developing networks of cortical neurons. *The Journal of neuroscience*, 15(10):6834–6845, 1995.
- E. Marconi, T. Nieuws, A. Maccione, P. Valente, A. Simi, M. Messa, S. Dante, P. Baldelli, L. Berdondini, and F. Benfenati. Emergent functional properties of neuronal networks with controlled topology. 2012.
- H. Markram. The blue brain project. *Nature Reviews Neuroscience*, 7(2):153–160, 2006.
- H. Markram. The human brain project. *Scientific American*, 306(6):50–55, 2012.
- H. Markram, E. Muller, S. Ramaswamy, M. W. Reimann, M. Abdellah, C. A. Sanchez, A. Ailamaki, L. Alonso-Nanclares, N. Antille, S. Arsever, et al. Reconstruction and simulation of neocortical microcircuitry. *Cell*, 163(2):456–492, 2015.
- T. Martin, X. Zhang, and M. Newman. Localization and centrality in networks. *Physical Review E*, 90(5):052808, 2014.
- A. Mason, A. Nicoll, and K. Stratford. Synaptic transmission between individual pyramidal neurons of the rat visual cortex in vitro. *The Journal of Neuroscience*, 11(1):72–84, 1991.
- A. Mazzatenta, M. Giugliano, S. Campidelli, L. Gambazzi, L. Businaro, H. Markram, M. Prato, and L. Ballerini. Interfacing neurons with carbon nanotubes: electrical signal transfer and synaptic stimulation in cultured brain circuits. *The Journal of neuroscience*, 27(26):6931–6936, 2007.
- A. Mazzoni, F. D. Broccard, E. Garcia-Perez, P. Bonifazi, M. E. Ruaro, and V. Torre. On the dynamics of the spontaneous activity in neuronal networks. *PloS one*, 2(5):e439, 2007.
- A. Mechelli, C. J. Price, U. Noppeney, and K. J. Friston. A dynamic causal modeling study on category effects: bottom–up or top–down mediation? *Journal of cognitive neuroscience*, 15(7):925–934, 2003.

- M. Meilă. Comparing clusterings by the variation of information. In *Learning theory and kernel machines*, pages 173–187. Springer, 2003.
- D. Meunier, R. Lambiotte, and E. T. Bullmore. Modular and hierarchically modular organization of brain networks. *Frontiers in neuroscience*, 4, 2010.
- Y. Mishchencko, J. T. Vogelstein, and L. Paninski. A bayesian approach for inferring neuronal connectivity from calcium fluorescent imaging data. *The Annals of Applied Statistics*, pages 1229–1261, 2011.
- B. Morrison III, B. S. Elkin, J.-P. Dollé, and M. L. Yarmush. In vitro models of traumatic brain injury. *Annual review of biomedical engineering*, 13: 91–126, 2011.
- V. B. Mountcastle. The columnar organization of the neocortex. *Brain*, 120 (4):701–722, 1997.
- L. Mucke. Neuroscience: Alzheimer’s disease. *Nature*, 461(7266):895–897, 2009.
- M. Newman. *Networks: an Introduction*. Oxford University Press, Oxford, 2010.
- M. E. Newman. Assortative mixing in networks. *Physical review letters*, 89 (20):208701, 2002.
- M. E. Newman. Mixing patterns in networks. *Physical Review E*, 67(2): 026126, 2003.
- M. E. Newman. Modularity and community structure in networks. *Proceedings of the National Academy of Sciences*, 103(23):8577–8582, 2006.
- M. E. Newman. Communities, modules and large-scale structure in networks. *Nature Physics*, 8(1):25–31, 2012.
- B. O’Nuallain, D. B. Freir, A. J. Nicoll, E. Risse, N. Ferguson, C. E. Herron, J. Collinge, and D. M. Walsh. Amyloid  $\beta$ -protein dimers rapidly form stable synaptotoxic protofibrils. *J Neurosci*, 30(43):14411–14419, 2010.
- J. G. Orlandi, J. Soriano, E. Alvarez-Lacalle, S. Teller, and J. Casademunt. Noise focusing and the emergence of coherent activity in neuronal cultures. *Nature Physics*, 9(9):582–590, 2013.

- J. G. Orlandi, O. Stetter, J. Soriano, T. Geisel, and D. Battaglia. Transfer entropy reconstruction and labeling of neuronal connections from simulated calcium imaging. 2014.
- B. Pakkenberg, D. Pelvig, L. Marnier, M. J. Bundgaard, H. J. G. Gundersen, J. R. Nyengaard, and L. Regeur. Aging and the human neocortex. *Experimental gerontology*, 38(1):95–99, 2003.
- J. J. Palop, J. Chin, and L. Mucke. A network dysfunction perspective on neurodegenerative diseases. *Nature*, 443(7113):768–773, 2006.
- R. K. Pan and S. Sinha. Modularity produces small-world networks with dynamical time-scale separation. *EPL (Europhysics Letters)*, 85(6):68006, 2009.
- Q. Pankhurst, D. Hautot, N. Khan, and J. Dobson. Increased levels of magnetic iron compounds in Alzheimer’s disease. *J Alzheimers Dis*, 13(1):49–52, 2008.
- R. M. Paredes, J. C. Etzler, L. T. Watts, W. Zheng, and J. D. Lechleiter. Chemical calcium indicators. *Methods*, 46(3):143–151, 2008.
- A. Pascual-Leone, C. Freitas, L. Oberman, J. C. Horvath, M. Halko, M. El-daief, S. Bashir, M. Vernet, M. Shafi, B. Westover, et al. Characterizing brain cortical plasticity and network dynamics across the age-span in health and disease with tms-eeG and tms-fMRI. *Brain Topogr*, 24(3):302–315, 2011.
- V. Pasquale, P. Massobrio, L. Bologna, M. Chiappalone, and S. Martinoia. Self-organization and neuronal avalanches in networks of dissociated cortical neurons. *Neuroscience*, 153(4):1354–1369, 2008.
- T. P. Patel, S. C. Ventre, and D. F. Meaney. Dynamic changes in neural circuit topology following mild mechanical injury in vitro. *Annals of biomedical engineering*, 40(1):23–36, 2012.
- S. Pautot, C. Wyart, and E. Y. Isacoff. Colloid-guided assembly of oriented 3d neuronal networks. *Nature methods*, 5(8):735–740, 2008.
- G. R. Poudel, G. F. Egan, A. Churchyard, P. Chua, J. C. Stout, and N. Georgiou-Karistianis. Abnormal synchrony of resting state networks in premanifest and symptomatic huntington disease: the image-hd study. *Journal of psychiatry & neuroscience: JPN*, 39(2):87, 2014.

- J. Pu, H. Gong, X. Li, and Q. Luo. Developing neuronal networks: Self-organized criticality predicts the future. *Scientific reports*, 3, 2013.
- N. Raichman and E. Ben-Jacob. Identifying repeating motifs in the activation of synchronized bursts in cultured neuronal networks. *Journal of neuroscience methods*, 170(1):96–110, 2008.
- E. Ravasz and A.-L. Barabási. Hierarchical organization in complex networks. *Physical Review E*, 67(2):026112, 2003.
- A. Riecker, K. Gröschel, H. Ackermann, S. Schnaudigel, J. Kassubek, and A. Kastrup. The role of the unaffected hemisphere in motor recovery after stroke. *Human brain mapping*, 31(7):1017–1029, 2010.
- P. Robinson, J. Henderson, E. Matar, P. Riley, and R. Gray. Dynamical reconnection and stability constraints on cortical network architecture. *Physical review letters*, 103(10):108104, 2009.
- N. L. Rochefort, H. Jia, and A. Konnerth. Calcium imaging in the living brain: prospects for molecular medicine. *Trends in molecular medicine*, 14(9):389–399, 2008.
- J. D. Rolston, D. A. Wagenaar, and S. M. Potter. Precisely timed spatiotemporal patterns of neural activity in dissociated cortical cultures. *Neuroscience*, 148(1):294–303, 2007.
- M. Rubinov and O. Sporns. Complex network measures of brain connectivity: uses and interpretations. *Neuroimage*, 52(3):1059–1069, 2010a.
- M. Rubinov and O. Sporns. Complex network measures of brain connectivity: uses and interpretations. *Neuroimage*, 52(3):1059–1069, 2010b.
- E. Salinas and T. J. Sejnowski. Correlated neuronal activity and the flow of neural information. *Nature reviews neuroscience*, 2(8):539–550, 2001.
- N. Sato, M. Okochi, Y. Taniyama, H. Kurinami, M. Shimamura, D. Takeuchi, H. Hamada, A. Fukumori, K. Kiyosue, T. Taguchi, T. Tanaka, M. Miyasaka, M. Takeda, T. Ogihara, and R. Morishita. Development of new screening system for Alzheimer disease, in vitro Abeta sink assay, to identify the dissociation of soluble Abeta from fibrils. *Neurobiol Dis*, 22(3):487–495, 2006.

- D. Saur, R. Lange, A. Baumgaertner, V. Schraknepper, K. Willmes, M. Rijntjes, and C. Weiller. Dynamics of language reorganization after stroke. *Brain*, 129(6):1371–1384, 2006.
- S. Saxena and P. Caroni. Selective neuronal vulnerability in neurodegenerative diseases: from stressor thresholds to degeneration. *Neuron*, 71(1):35–48, 2011.
- J. W. Scannell, C. Blakemore, and M. P. Young. Analysis of connectivity in the cat cerebral cortex. *The Journal of Neuroscience*, 15(2):1463–1483, 1995.
- C. Schmeltzer, J. Soriano, I. M. Sokolov, and S. Rüdiger. Percolation of spatially constrained erdős-rényi networks with degree correlations. *Phys. Rev. E*, 89:012116, Jan 2014. doi: 10.1103/PhysRevE.89.012116. URL <http://link.aps.org/doi/10.1103/PhysRevE.89.012116>.
- M. M. Schoonheim and M. Filippi. Functional plasticity in ms friend or foe? *Neurology*, 79(14):1418–1419, 2012.
- T. Schreiber. Measuring information transfer. *Physical review letters*, 85(2):461, 2000.
- M. S. Schroeter, P. Charlesworth, M. G. Kitzbichler, O. Paulsen, and E. T. Bullmore. Emergence of rich-club topology and coordinated dynamics in development of hippocampal functional networks in vitro. *The Journal of Neuroscience*, 35(14):5459–5470, 2015.
- R. Segev, M. Benveniste, Y. Shapira, and E. Ben-Jacob. Formation of electrically active clusterized neural networks. *Phys. Rev. Lett.*, 90:168101, Apr 2003a. doi: 10.1103/PhysRevLett.90.168101. URL <http://link.aps.org/doi/10.1103/PhysRevLett.90.168101>.
- R. Segev, M. Benveniste, Y. Shapira, and E. Ben-Jacob. Formation of electrically active clusterized neural networks. *Physical review letters*, 90(16):168101, 2003b.
- R. Segev, I. Baruchi, E. Hulata, and E. Ben-Jacob. Hidden neuronal correlations in cultured networks. *Physical Review Letters*, 92(11):118102, 2004.
- M. Á. Serrano. Rich-club vs rich-multipolarization phenomena in weighted networks. *Physical Review E*, 78(2):026101, 2008.

- S. Seung. *Connectome: How the brain's wiring makes us who we are*. Houghton Mifflin Harcourt, 2012.
- M. Shanahan. Dynamical complexity in small-world networks of spiking neurons. *Physical Review E*, 78(4):041924, 2008.
- O. Shefi, I. Golding, R. Segev, E. Ben-Jacob, and A. Ayali. Morphological characterization of in vitro neuronal networks. *Physical Review E*, 66(2):021905, 2002.
- M. Shein, V. Volman, N. Raichman, Y. Hanein, and E. Ben-Jacob. Management of synchronized network activity by highly active neurons. *Physical biology*, 5(3):036008, 2008.
- M. Shein, A. Greenbaum, T. Gabay, R. Sorkin, M. David-Pur, E. Ben-Jacob, and Y. Hanein. Engineered neuronal circuits shaped and interfaced with carbon nanotube microelectrode arrays. *Biomedical microdevices*, 11(2):495–501, 2009.
- M. Shein Idelson, E. Ben-Jacob, and Y. Hanein. Innate synchronous oscillations in freely-organized small neuronal circuits. *PLoS ONE*, 5(12):e14443, 12 2010. doi: 10.1371/journal.pone.0014443.
- M. Shein-Idelson, E. Ben-Jacob, and Y. Hanein. Engineered neuronal circuits: A new platform for studying the role of modular topology. *Frontiers in Neuroengineering*, 4(10), 2011. ISSN 1662-6443. doi: 10.3389/fneng.2011.00010. URL <http://www.frontiersin.org/neuroengineering/10.3389/fneng.2011.00010/abstract>.
- M. Shimono and J. M. Beggs. Functional clusters, hubs, and communities in the cortical microconnectome. *Cerebral Cortex*, page bhu252, 2014.
- N. Shu, Y. Liang, H. Li, J. Zhang, X. Li, L. Wang, Y. He, Y. Wang, and Z. Zhang. Disrupted topological organization in white matter structural networks in amnesic mild cognitive impairment: relationship to subtype. *Radiology*, 265(2):518–527, 2012.
- A. Singh and N. A. Lesica. Incremental mutual information: a new method for characterizing the strength and dynamics of connections in neuronal circuits. *PLoS Comput. Biol*, 6:e1001035, 2010.
- D. Smetters, A. Majewska, and R. Yuste. Detecting action potentials in neuronal populations with calcium imaging. *Methods*, 18(2):215–221, 1999.

- M. A. Smith, P. L. Harris, L. M. Sayre, and G. Perry. Iron accumulation in alzheimer disease is a source of redox-generated free radicals. *P Natl Acad Sci USA*, 94(18):9866–9868, 1997.
- J. Soriano, M. R. Martinez, T. Tlusty, and E. Moses. Development of input connections in neural cultures. *PNAS*, 105(37), 2008.
- R. Sorkin, T. Gabay, P. Blinder, D. Baranes, E. Ben-Jacob, and Y. Hanein. Compact self-wiring in cultured neural networks. *Journal of Neural Engineering*, 3(2):95, 2006. URL <http://stacks.iop.org/1741-2552/3/i=2/a=003>.
- W. Soussou, G. Yoon, R. Brinton, and T. Berger. Neuronal network morphology and electrophysiology of hippocampal neurons cultured on surface-treated multielectrode arrays. *Biomedical Engineering, IEEE Transactions on*, 54(7):1309–1320, 2007. ISSN 0018-9294. doi: 10.1109/TBME.2006.889195.
- R. Sperling. Functional mri studies of associative encoding in normal aging, mild cognitive impairment, and alzheimer’s disease. *Annals of the New York Academy of Sciences*, 1097(1):146–155, 2007.
- O. Sporns. The human connectome: a complex network. *Annals of the New York Academy of Sciences*, 1224(1):109–125, 2011.
- O. Sporns. Network attributes for segregation and integration in the human brain. *Current opinion in neurobiology*, 23(2):162–171, 2013.
- O. Sporns and J. D. Zwi. The small world of the cerebral cortex. *Neuroinformatics*, 2(2):145–162, 2004.
- O. Sporns, G. Tononi, and G. M. Edelman. Theoretical neuroanatomy: relating anatomical and functional connectivity in graphs and cortical connection matrices. *Cerebral Cortex*, 10(2):127–141, 2000.
- O. Sporns, D. R. Chialvo, M. Kaiser, and C. C. Hilgetag. Organization, development and function of complex brain networks. *Trends in cognitive sciences*, 8(9):418–425, 2004.
- K. V. Srinivas, R. Jain, S. Saurav, and S. K. Sikdar. Small-world network topology of hippocampal neuronal network is lost, in an in vitro glutamate injury model of epilepsy. *European Journal of Neuroscience*, 25(11):3276–3286, 2007.

- C. Stam, B. Jones, G. Nolte, M. Breakspear, and P. Scheltens. Small-world networks and functional connectivity in alzheimer's disease. *Cerebral cortex*, 17(1):92–99, 2007.
- C. J. Stam. Modern network science of neurological disorders. *Nature Reviews Neuroscience*, 15(10):683–695, 2014.
- C. J. Stam and J. C. Reijneveld. Graph theoretical analysis of complex networks in the brain. *Nonlinear biomedical physics*, 1(1):3, 2007.
- O. Stetter, D. Battaglia, J. Soriano, and T. Geisel. Model-free reconstruction of excitatory neuronal connectivity from calcium imaging signals. *PLoS Comput. Biol*, 8(8):e1002653, 2012.
- J. Streit, A. Tschertter, M. O. Heuschkel, and P. Renaud. The generation of rhythmic activity in dissociated cultures of rat spinal cord. *European journal of neuroscience*, 14(2):191–202, 2001.
- G. Sumbre, A. Muto, H. Baier, and M.-m. Poo. Entrained rhythmic activities of neuronal ensembles as perceptual memory of time interval. *Nature*, 456(7218):102–106, 2008.
- D. A. Sun, S. Sombati, R. E. Blair, and R. J. DeLorenzo. Calcium-dependent epileptogenesis in an in vitro model of stroke-induced “epilepsy”. *Epilepsia*, 43(11):1296–1305, 2002.
- D. A. Sun, S. Sombati, R. E. Blair, and R. J. DeLorenzo. Long-lasting alterations in neuronal calcium homeostasis in an in vitro model of stroke-induced epilepsy. *Cell Calcium*, 35(2):155–163, 2004.
- J.-J. Sun, W. Kilb, and H. J. Luhmann. Self-organization of repetitive spike patterns in developing neuronal networks in vitro. *European Journal of Neuroscience*, 32(8):1289–1299, 2010.
- K. Svoboda and R. Yasuda. Principles of two-photon excitation microscopy and its applications to neuroscience. *Neuron*, 50(6):823–839, 2006.
- H. A. Swadlow. Efferent neurons and suspected interneurons in motor cortex of the awake rabbit: axonal properties, sensory receptive fields, and subthreshold synaptic inputs. *Journal of Neurophysiology*, 71(2):437–453, 1994.

- S. Teller and J. Soriano. Experiments on clustered neuronal networks. *AIP Conference Proceedings*, 1510(1):244–246, 2013. doi: 10.1063/1.4776529. URL <http://link.aip.org/link/?APC/1510/244/1>.
- S. Teller, C. Granell, M. De Domenico, J. Soriano, S. Gómez, and A. Arenas. Emergence of assortative mixing between clusters of cultured neurons. *PLoS computational biology*, 10(9):e1003796–e1003796, 2014.
- C. Tetzlaff, S. Okujeni, U. Egert, F. Wörgötter, M. Butz, et al. Self-organized criticality in developing neuronal networks. *PLoS Comput. Biol.*, 6(12): e1001013, 2010.
- L. Tian, S. A. Hires, T. Mao, D. Huber, M. E. Chiappe, S. H. Chalasani, L. Petreanu, J. Akerboom, S. A. McKinney, E. R. Schreiter, et al. Imaging neural activity in worms, flies and mice with improved gcamp calcium indicators. *Nature methods*, 6(12):875–881, 2009.
- E. Tibau, M. Valencia, and J. Soriano. Identification of neuronal network properties from the spectral analysis of calcium imaging signals in neuronal cultures. *Frontiers in neural circuits*, 7, 2013.
- A. W. Toga, K. A. Clark, P. M. Thompson, D. W. Shattuck, and J. D. Van Horn. Mapping the human connectome. *Neurosurgery*, 71(1):1, 2012.
- J. Tønnesen, A. T. Sørensen, K. Deisseroth, C. Lundberg, and M. Kokaia. Optogenetic control of epileptiform activity. *Proceedings of the National Academy of Sciences*, 106(29):12162–12167, 2009.
- C.-Y. Tsai and M.-C. Chang. Robustness and variability of pathways in the spontaneous synchronous bursting of clusterized cortical neuronal networks in vitro. *Journal of the Physical Society of Japan*, 77(8):084803, 2008.
- J. Tsai, J. Grutzendler, K. Duff, and W.-B. Gan. Fibrillar amyloid deposition leads to local synaptic abnormalities and breakage of neuronal branches. *Nat Neurosci*, 7(11):1181–1183, 2004.
- G. G. Turrigiano and S. B. Nelson. Homeostatic plasticity in the developing nervous system. *Nature Reviews Neuroscience*, 5(2):97–107, 2004.
- M. P. van den Heuvel and O. Sporns. Rich-club organization of the human connectome. *The Journal of neuroscience*, 31(44):15775–15786, 2011.
- M. P. van den Heuvel and O. Sporns. Network hubs in the human brain. *Trends in cognitive sciences*, 17(12):683–696, 2013.

- M. P. van den Heuvel, R. C. Mandl, C. J. Stam, R. S. Kahn, and H. E. H. Pol. Aberrant frontal and temporal complex network structure in schizophrenia: a graph theoretical analysis. *The Journal of Neuroscience*, 30(47):15915–15926, 2010.
- M. P. van den Heuvel, O. Sporns, G. Collin, T. Scheewe, R. C. Mandl, W. Cahn, J. Goñi, H. E. H. Pol, and R. S. Kahn. Abnormal rich club organization and functional brain dynamics in schizophrenia. *JAMA psychiatry*, 70(8):783–792, 2013.
- D. C. Van Essen. A tension-based theory of morphogenesis and compact wiring in the central nervous system. *NATURE-LONDON-*, pages 313–318, 1997.
- J. Van Pelt, M. Corner, P. Wolters, W. Rutten, and G. Ramakers. Longterm stability and developmental changes in spontaneous network burst firing patterns in dissociated rat cerebral cortex cell cultures on multielectrode arrays. *Neuroscience letters*, 361(1):86–89, 2004.
- J. van Pelt, I. Vajda, P. S. Wolters, M. A. Corner, and G. J. Ramakers. Dynamics and plasticity in developing neuronal networks in vitro. *Progress in brain research*, 147:171–188, 2005.
- D. A. Wagenaar, J. Pine, and S. M. Potter. An extremely rich repertoire of bursting patterns during the development of cortical cultures. *BMC Neurosci.*, 7:11, 2006.
- P. Walicke, W. Cowan, N. Ueno, A. Baird, and R. Guillemin. Fibroblast growth factor promotes survival of dissociated hippocampal neurons and enhances neurite extension. *Proceedings of the National Academy of Sciences*, 83(9):3012–3016, 1986.
- J. Wang, L. Wang, Y. Zang, H. Yang, H. Tang, Q. Gong, Z. Chen, C. Zhu, and Y. He. Parcellation-dependent small-world brain functional networks: A resting-state fmri study. *Human brain mapping*, 30(5):1511–1523, 2009.
- J. Wang, X. Zuo, Z. Dai, M. Xia, Z. Zhao, X. Zhao, J. Jia, Y. Han, and Y. He. Disrupted functional brain connectome in individuals at risk for Alzheimer’s disease. *Biol Psychiat*, 73(5):472–481, 2013.
- D. E. Warren, J. D. Power, J. Bruss, N. L. Denburg, E. J. Waldron, H. Sun, S. E. Petersen, and D. Tranel. Network measures predict neuropsychological outcome after brain injury. *Proceedings of the National Academy of Sciences*, 111(39):14247–14252, 2014.

- D. J. Watts and S. H. Strogatz. Collective dynamics of ‘small-world’ networks. *nature*, 393(6684):440–442, 1998.
- B. Wheeler and G. Brewer. Designing neural networks in culture. *Proceedings of the IEEE*, 98(3):398–406, 2010. ISSN 0018-9219. doi: 10.1109/JPROC.2009.2039029.
- O. Yizhar, L. E. Fenno, T. J. Davidson, M. Mogri, and K. Deisseroth. Optogenetics in neural systems. *Neuron*, 71(1):9–34, 2011.
- M. P. Young. The organization of neural systems in the primate cerebral cortex. *Proceedings of the Royal Society of London B: Biological Sciences*, 252(1333):13–18, 1993.
- R. Yuste. From the neuron doctrine to neural networks. *Nature Reviews Neuroscience*, 16(8):487–497, 2015.
- C. Yvon, R. Rubli, and J. Streit. Patterns of spontaneous activity in unstructured and minimally structured spinal networks in culture. *Experimental brain research*, 165(2):139–151, 2005.